Multiple Scattering Effects on the Dynamics and Radiation of Fast Charged Particles in Crystals. Transients in the Nuclear Burning Wave Reactor

Alex Fomin

université PARIS-SACLAY

NNT : 2017SACLS272

Thèse de doctorat

UNIVERSITÉ PARIS SUD

Comprendre le monde, construire l'avenir

1804

Харківський національний університет імені В.Н. Каразіна

Multiple Scattering Effects on the Dynamics and Radiation of Fast Charged Particles in Crystals. Transients in the Nuclear Burning Wave Reactor.

Thèse de doctorat
de l'Université Nationale V.N.Karazin de Kharkiv
et de l'Université Paris-Saclay
préparée à l'Université Paris-Sud

Ecole doctorale n°576 Particules, Hadrons, Énergie et Noyaux: Instrumentation, Images, Cosmos et Simulation (PHENIICS)
Spécialité de doctorat : Physique des Accélérateurs

Thèse présentée et soutenue à Orsay, le 22 septembre 2017, par

OLEKSIY (ALEX) FOMIN

Composition du Jury :

M. Fabien Cavalier Professeur, Université Paris-Sud	Président
M. Ulrik Ingerslev Uggerhøj Professeur, Aarhus University	Rapporteur
M. Konstantin Mikityuk Directeur de Recherche, Paul Scherrer Institut	Rapporteur
M. Alexander Korchin Professeur, V.N.Karazin KhNU	Examinateur
M. Achille Stocchi Professeur, Université Paris-Sud	Directeur de thèse
M. Mykola Shulha Professeur, V.N.Karazin KhNU	Co-directeur de thèse

Contents

Synthèse en français

Comme le titre le reflète, la dissertation est divisée en deux parties principales, la première sur les effets de diffusion multiples sur la dynamique et le rayonnement des particules chargées rapide dans les cristaux (chapitres 1–6), et la seconde sur les transitoires dans le réacteur à onde de combustion nucléaire (OCN) (chapitres 7–12). Chaque partie se termine par un chapitre contenant une conclusion.

Le premier chapitre de la thèse propose une introduction aux principaux thèmes de la première partie et aborde la théorie de la canalisation axiale et planaire, "doughnut scattering", des effets incohérents et des problèmes liés à la déviation du faisceau par un cristal courbé. En général, les effets cohérents dans l'interaction des particules à haute énergie avec les cristaux ouvrent de nouvelles possibilités pour accélérer et détecter les techniques. Les champs électromagnétiques effectifs qui se produisent dans ce cas peuvent dépasser mille fois les champs qui peuvent maintenant être atteints dans les installations expérimentales.

Le chapitre 2 contient une revue de la dynamique des particules se propageant à travers les cristaux. Ici sont présentés divers régimes de mouvement dans le cristal, tels que la canalisation axiale et planaire dans les cristaux droits et courbés, et la réflexion de volume. Dans ce chapitre, un modèle de potentiel continu est utilisé pour expliquer les processus physiques et introduire les principaux paramètres qui seront utilisés plus avant.

Le chapitre 3 donne une description de la base théorique d'un modèle de calcul (approche de Monte-Carlo basée sur le modèle de collision binaire) pour la propagation de particules dans des cristaux droits ou courbés.

Cette approche a la manière la plus organique de prendre en compte la vibration thermique des atomes au niveau des nœuds cristallins. La diffusion multiple sur le sous-système électronique du réseau cristallin est prise en compte en utilisant le modèle des collisions globales.

Des facteurs importants qui décrivent la canalisation dans un cristal de courbure tels que l'angle d'acceptation, la probabilité de déchaînement et le facteur d'acceptation de la canalisation sont obtenus, et l'on obtient une expression phénoménologique de l'efficacité de la canalisation. Basé sur un grand nombre de simulations informatiques, la paramétrisation a été obtenue. Les valeurs des paramètres sont présentées dans des tableaux pour deux matériaux cristallins couramment utilisés (silicium et germanium) à température ambiante, et pour les cristaux de germanium refroidis à des températures cryogéniques.

En utilisant ces formules, on peut prédire si la particule est capturée dans un régime de canalisation, et la probabilité de son décanalisation après une certaine longueur de trajet. Ces résultats peuvent être utilisés aussi bien dans les approches Monte-Carlo que déterministes.

Au chapitre 4, cette paramétrisation est utilisée pour optimiser les paramètres des cristaux courbés pour une mesure potentielle du moment dipolaire magnétique des baryons charmés aux énergies du LHC par l'utilisation de la rotation de spin.

L'un des objectifs de cette étude est de trouver des conditions optimales pour effectuer la mesure du moment magnétique anormal du baryon Λ_c^+ au LHC. En raison de la courte durée de vie de cette particule, la seule façon de fournir une telle mesure est d'utiliser un cristal plié, qui peut imiter le champ magnétique de l'ordre de mille Tesla.

L'optimisation des paramètres pour un montage expérimental a été réalisée sur la base d'une simulation par ordinateur du passage Λ_c^+ à travers un cristal courbé en utilisant le modèle des collisions binaires, prenant en compte la diffusion incohérente des vibrations thermiques des atomes aux n$\frac{1}{2}$uds réticulaires et diffusion sur un sous-système électronique d'un cristal. Les résultats de la recherche menée dans la thèse donnent une prévision optimiste quant à la possibilité de mener une telle expérience au LHC et sont devenus la base de la proposition correspondante.

Le chapitre 5 traite des effets de diffusion multiple sur le rayonnement, et présente une discussion sur le concept de zone de formation pour la génération de rayonnement (aussi appelée longueur de cohérence), et sa pertinence pour les différents régimes de rayonnement.

Les effets de diffusion multiples du rayonnement des électrons et positrons ultra relativistes sont considérés dans les cristaux alignés. Cette étude est réalisée dans le cadre de l'approche électrodynamique classique pour décrire le rayonnement de particules relativistes et la simulation par ordinateur de particules chargées rapidement passant à travers un cristal en utilisant le modèle mentionné ci-dessus.

Il est démontré que, en raison des multiples effets de diffusion, le régime non dipolaire du rayonnement a lieu dans un cristal mince dans une certaine région du spectre d'émission. Il est également démontré que la distribution angulaire spectrale et les caractéristiques de polarisation du rayonnement diffèrent essentiellement des résultats de la théorie de Bethe–Heitler.

Une approche pour atteindre un haut degré de polarisation dans le rayonnement émis par des cibles minces, en utilisant des particules de haute énergie, est présentée. Cette méthode ne semble d'abord pas très prometteuse avec la technologie d'aujourd'hui, mais peut devenir pertinente avec les futures machines linéaires. Les conditions d'observation expérimentale de ces effets sont présentées.

Le chapitre 6 présente les principales conclusions de la partie I.

La deuxième partie de la thèse est consacrée à l'étude des processus transitoires des réacteurs rapides fonctionnant dans un régime d'onde de combustion nucléaire auto-entretenue. C'est un nouveau concept de réacteurs de fission nucléaire avec la soi-disant "sécurité intrinsèque", dans laquelle le développement d'une réaction nucléaire à chaîne incontrôlable est impossible en raison des principes physiques du fonctionnement du réacteur. Les concepts prometteurs du réacteur OCN dans le cas de sa mise en œuvre permettent d'utiliser l'uranium appauvri et fournit le traitement des déchets radioactifs à longue durée de vie.

Le chapitre 7 présente les concepts de base et un bref historique de la recherche et du développement (R&D) du réacteur de OCN, positionne le travail de thèse par rapport à la R&D antérieure et formule les objectifs de l'étude.

Au chapitre 8, le domaine de calcul et les équations transitoires pour la diffusion des neutrons et l'évolution de la composition des matériaux ainsi que la procédure de préparation de la section transversale sont introduits. Cette étude est basée sur la résolution numérique de l'équation de diffusion non linéaire non stationnaire du transport de neutrons avec un ensemble d'équations de combustion pour les composants du carburant et les équations de la cinétique nucléaire pour les noyaux précurseurs des neutrons retardés, en utilisant une approche "effective multigroup". Le modèle du réacteur cylindrique homogène avec le combustible métallique est considéré dans le cadre du concept de flambage.

Le chapitre 9 présente les résultats de calcul pour le fonctionnement de base de OCN dans différents cycles du combustible: U–Pu, Th–U et mixte Th–U–Pu. À la suite de ces études, l'existence du mode OCN dans le cas du combustible mixte Th–U–Pu et de ses avantages essentiels est démontrée.

Dans le cas du mixte Th–U–Pu combustible, il est possible d'obtenir des valeurs des principaux paramètres de fonctionnement du réacteur qui semblent être acceptables pour une utilisation pratique. Par exemple, le flux de neutrons est d'environ $6{\times}10^{15}$ $\mathrm{cm}^{-2}\,\mathrm{s}^{-1}$, la densité de production d'énergie est d'environ 500 $\mathrm{W/cm}^3$, la durée de la campagne du réacteur est égale à environ 60 ans pour la longueur du réacteur de 5 m, la vitesse OCN est d'environ 6 cm/an, la profondeur de combustion du combustible pour ^{238}U et ^{232} Th atteint 45–50 %. Le schéma considéré permet d'impliquer une grande quantité de 232 Th (50-70 % de la fraction du volume de carburant) dans le processus de combustion nucléaire. Après l'extinction finale du réacteur, les concentrations des isotopes fissiles produits du plutonium et de l'uranium, qui pourraient servir de combustible à d'autres réacteurs après un traitement adéquat, atteignent un niveau significatif (6-7 %) dans tout le volume du réacteur.

Le chapitre 10 se concentre sur les réponses du réacteur OCN aux perturbations externes de la composition du combustible et du flux de neutrons pour démontrer la stabilité du réacteur. L'analyse détaillée d'un type spécial de rétroaction négative inhérente au régime OCN et sous-jacente à la "sécurité intrinsèque" d'un tel réacteur est réalisée. Une stabilité notable du régime de OCN relatif aux perturbations du flux de neutrons dans le système et aux irrégularités de la composition du carburant a été démontrée.

Le chapitre 11 présente les résultats de calcul pour le démarrage du réacteur, l'arrêt forcé et le redémarrage subséquent du réacteur OCN. Le comportement non trivial de la réactivité du réacteur dans ces régimes est analysé. On montre qu'un tel réacteur peut être manipulé, mais il est très important de prendre en compte le retour de réactivité négatif.

Les caractéristiques de la phase initiale d'établissement du régime OCN ont été étudiées en détail au moyen de l'examen de diverses compositions de la zone d'allumage du réacteur. La méthode spéciale d'un démarrage en douceur du réacteur OCN qui empêche l'augmentation excessive du flux de neutrons et de la production d'énergie au stade initial est proposée.

Une simulation numérique a été réalisée pour l'arrêt forcé de cette réacteur rapide (RR) en introduisant l'absorbeur de neutrons ^{181}Ta dans une certaine zone axiale de combustion nucléaire active. L'influence du taux d'introduction des absorbeurs sur l'extinction du régime OCN a été considérée. Des études détaillées ont été effectuées sur les processus physiques transitoires dans le RR après sa fermeture et l'évolution de la réactivité du système en raison de la décroissance de ^{239}Np et de la production correspondante de ^{239}Pu, et le montant minimum du tantale introduit, qui est nécessaire pour un arrêt fiable du réacteur, a été estimé.

Le problème du redémarrage ultérieur du régime de OCN dans le RR considéré consiste à assurer une combustion progressive du surplus de plutonium produit après l'arrêt de la RR et à établir les distributions auto-cohérentes des composants du combustible et du flux de neutrons correspondant au régime OCN. Ce processus est réalisé par un retrait progressif de l'absorbeur de tantale avec une création simultanée du champ de neutrons dans le RR en utilisant une source de neutrons externe située dans la zone de combustion active. Sur la base de diverses variantes du redémarrage RR, certains scénarios de redémarrage ont été trouvés qui permettent de fournir un processus stable et régulier de reprise du régime OCN dans ce RR.

Le chapitre 12 présente les principales conclusions de la partie II.

List of publications

Part I

1. A.S. Fomin, S.P. Fomin and N.F. Shul'ga. Multiple scattering effect on angular distribution and polarization of radiation by relativistic electrons in a thin crystal. *Proc. of the SPIE*, 5974:177–184, 2006.
[http://dx.doi.org/10.1117/12.639989],
[http://arxiv.org/abs/1705.03354].

2. A.S. Fomin, S.P. Fomin and N.F. Shul'ga. Fine structure of angular distributions and polarization of radiation by relativistic electrons and positrons in a thin crystal. *J. of KhNU #721, "Nuclei, Particles, Fields"*, 1:39–44, 2006.

3. A.S. Fomin, S.P. Fomin and N.F. Shul'ga. Multiple scattering effect on spectral, angular, and polarization characteristics of bremsstrahlung in a thin amorphous target. *Proc. of the SPIE*, 6634:663406, 2007.
[http://dx.doi.org/10.1117/12.741837].

4. A.S. Fomin, S.P. Fomin and N.F. Shul'ga. Radiation of a relativistic electron with non-equilibrium own Coulomb field. *Nuovo Cim.*, C034N4:45–53, 2011.
[http://dx.doi.org/10.1393/ncc/i2011-10969-7],
[http://arxiv.org/abs/1705.03355].

5. A.S. Fomin, A.Yu. Korchin, A. Stocchi, et al. Feasibility of measuring the magnetic dipole moments of the charm baryons at the LHC using bent crystals. *Journal of High Energy Physics*, 2017(8):120, Aug 2017.
[http://doi.org/10.1007/JHEP08(2017)120].

Part II

1. A.S. Fomin, S.P. Fomin, Yu.P. Mel'nik, V.V. Pilipenko and N.F. Shul'ga. Safe fast reactor based on the self-sustained regime of nuclear burning wave. *Proc. Global 2009, Paris, France*, Paper 9456, 2009.

2. Yu.P. Mel'nik, V.V. Pilipenko, A.S. Fomin, S.P. Fomin and N.F. Shul'ga. Study of self-organized nuclear burning wave regime in fast reactor based on Th-U cycle. *Atomic Energy*, 107:288–295, 2009.
[http://doi.org/10.1007/s10512-010-9235-x].

3. A.S. Fomin, S.P. Fomin, Yu.P. Mel'nik, V.V. Pilipenko and N.F. Shul'ga. Self-sustained regime of nuclear burning wave in safe fast reactor using mixed Th-U-Pu fuel cycle. *Proc. of ICAPP 2010, San Diego, CA, USA*, Paper 10302, 2010.

4. S.P. Fomin, A.S. Fomin, Yu.P. Mel'nik, V.V. Pilipenko and N.F. Shul'ga. Nuclear burning wave in fast reactor with mixed Th-U fuel. *Progress in Nuclear Energy*, 53:800–805, 2011.
[http://doi.org/10.1016/j.pnucene.2011.05.004].

5. O.S. Fomin, S.P. Fomin, Yu.P. Mel'nik, V.V. Pilipenko and N.F. Shul'ga. Nuclear burning wave reactor: smooth start-up problem. *Journal of KhNU #1041, physical series "Nuclei, Particles, Fields"*, 2:49–56, 2013.

6. O.S. Fomin, S.P. Fomin, Yu.P. Mel'nik, V.V. Pilipenko and N.F. Shul'ga. Specific mechanism of negative reactivity feedback in the nuclear burning wave reactor. *S. Monti, editor, International Atomic Energy Agency (IAEA), Vienna: (Proc. IC FR-13, Paris, France, March 03-08, 2013)*, 46091111:01–10, 2015.

7. A.S. Fomin, S.P. Fomin, Yu.P. Mel'nik, V.V. Pilipenko and N.F. Shul'ga. Transient processes in the nuclear-burning-wave reactor. *Proc. of "Global-2015" (Paris, France, September 20-24, 2015)*, Paper 5254, 2015.

Part I

Multiple scattering effects on the dynamics and radiation of fast charged particles in crystals

Chapter 1

Crystals in accelerator physics (Introduction)

Recently there has been a significant increase of interest to the steering of high energy charged particle beams using aligned crystals. Primarily, this is due to the ability to effectively deflect the high energy charged particle beam, or some fraction of the beam, by means of straight or bent crystals instead of a bulky, power-consuming and expensive electromagnetic systems commonly used in accelerators.

One of such example is the use of bent crystals for the so-called slow beam output from cyclic accelerators. This can provide additional beam channels for the fixed target experiments which will operate simultaneously with the main channels practically without affecting their characteristics. First time such a scheme was implemented on the proton synchrotron with an energy of 76 GeV at the Institute of High Energy Physics (Protvino, Russia). Now this technology has been successfully implemented in other cyclic high energy accelerators.

Another example of using bent crystals in accelerator systems is the cleaning of the proton beam halo, which is planning to be implemented at the Large Hadron Collider (LHC) in CERN at the energies up to 7 TeV. It is assumed that the use of bent crystals for this purpose instead of the traditional collimators with amorphous material will significantly improve background conditions at the LHC, which is one of the most important problems at measurements of low cross sections processes, such as the Higgs boson production and others.

One more example of the use of bent crystals as a unique instrument of experimental physics is the measurement of the magnetic moment of ultra short-lived particles. Usually, for the determination of the magnetic moment of an elementary particle, the precession effect of the vector of a magnetic moment in a predetermined

external magnetic field is used. The problem is that in order to obtain a sufficient angle of rotation for this vector and to establish the magnitude of the magnetic moment of a particle, it is necessary that this particle passes a fairly large distance (in order of few meters) in a strong magnetic field.

If considering the measurement of the magnetic moment of short-lived particles, for example, Σ^+ hyperon, whose mean lifetime is $\tau \approx 0.8 \times 10^{-10}$ s [1], that means that the distance overcomed by such a particle from the production point to its decay, even at its moving at a speed of almost the speed of light, is several centimeters only. Therefore, such a measurement is a rather complex problem.

Using the phenomenon of planar channeling of Σ^+ hyperons in a bent silicon crystal of 4.5 cm long made it possible to carry out the measurement of its magnetic moment at the proton accelerator with an energy of up to 800 GeV at the Enrico Fermi National Accelerator Laboratory (Batavia, USA). The bent silicon crystal in that experiment simulated the action of an external magnetic field of about 45 Tesla, which was sufficient to rotate the magnetic moment of Σ^+ hyperons (precession of its spin) by an angle of approximately 60^o [2]. For comparison, superconducting magnets of the Large Hadron Collider achieve magnetic field induction values of up to 8.3 Tesla.

Even more ambitious is the problem of measuring the magnetic moment of charmed Λ_c^+ and Ξ_c^+ hyperons, whose mean lifetimes are $\tau \approx 0.2 \times 10^{-12}$ s and $\tau \approx 0.4 \times 10^{-12}$ s, respectively [1]. To determine the possibility of carrying out such a measurement using a bent crystal, it is necessary to optimize all the parameters of the future experimental setup, based on the beam parameters of a particular particle accelerator and the capabilities of existing detecting systems. However, the main task is to find the optimal parameters of the crystal, which is planned to be used. The latter is one of the tasks that is solved in the first part of this thesis.

Another important example of the use of the features of electrodynamic processes accompanying the passage of fast charged particles through aligned crystals is the radiation of relativistic electrons and positrons. Due to the coherent nature of the interaction of these particles with the atoms of the crystal lattice in such a case, their bremsstrahlung can have a much higher intensity than in an amorphous medium with a chaotic arrangement of atoms. Moreover, the coherent radiation in crystals is possessing a number of features, including quasi-monochromaticity, narrow directivity, high degree of polarization, and others (see, e.g., [3, 4]).

Thanks to these properties, it has been successfully used for many decades in many accelerating centers to create intense beams of polarized gamma quanta for the nuclear physics research needs (see, e.g., [3–8] and references therein). The

possibility of using a single crystal to create an effective positron source for the future electron-positron collider (see, e.g., [9, 10]) is being studied.

With increasing energy of charged particles, the dimensions of the spatial regions that are responsible for the formation of certain electrodynamic processes increase significantly. This leads to an increase in the influence of both coherent and incoherent effects during multiple scattering by the atoms of matter. In the case of an amorphous substance with a random arrangement of atoms, the effect of multiple scattering of ultrarelativistic electrons on atoms leads to the effect of suppression of bremsstrahlung. This is the so-called Landau–Pomeranchuk effect [11, 12]. Even more effects associated with the influence of multiple scattering on radiation are manifested in the case of an ordered arrangement of atoms in the crystal lattice as a result of coherent effects in scattering [4]. These effects must be taken into account in the development of new high-energy accelerators and detectors for them, as well as in the study of cosmic rays of high and ultrahigh energies.

An investigation of the multiple scattering effect on the angular distributions and polarization characteristics of the radiation of ultrarelativistic electrons and positrons in thin amorphous and crystalline targets is also one of the problems solved in the first part of this thesis.

Chapter 2

Dynamics of particles in crystals (Review)

The main precondition for the possibility of using straight and bent crystals as a source of external electromagnetic field of a super power is the fact that the gradients of electromagnetic fields that affect the motion of fast charged particle that propagates through the crystal can by several orders exceed the gradients of fields achieved in the most powerful superconducting electromagnets in modern accelerators. The nature of this phenomenon lies in the existence of significant correlations in collisions of fast charged particle with atoms of the crystal during its motion along the crystallographic axis or plane. In special conditions, these correlations can lead to coherent effects both in scattering and radiation of the particles in the crystal.

One of these effects in coherent scattering of fast charged particles as they pass through the crystal is a phenomenon of channeling. For positively charged particles, it appears as the effect of a full reflection of particles from the crystal plane or axis when the particle is falling at an angle that is less than a critical one. There is an analogy with the effect of a full reflection of rays in optics, but in the case of charged particle channeling in a crystal, the mechanism of this effect is coherent multiple scattering in the Coulomb field of crystal lattice atoms, located along selected crystallographic plane or axis. In the case of negatively charged particles passage through a crystal such coherent scattering leads to a "capture" of particles by the total field of corresponding crystallographic plane or axis, instead of "reflection".

2.1 Channeling phenomenon. Continuous potential.

The theoretical prediction of the phenomenon of channeling as anomalous passage of charged particles along the "open channels" in the crystal, was made in 1912 by a future Nobel Prize winner Johannes Stark [13]. It happened almost immediately after the experimental confirmation of the existence of crystal lattice by observing the diffraction of X-rays, so-called Lauegram. For this, Max von Laue received the Nobel Prize in 1914. Stark proposed an experiment where charged particle beams were used instead of X-rays, but it has not been made at that time. The channeling phenomenon of positively charged particles in the crystal was re-discovered half a century later by Mark T. Robinson and Ordean S. Oen [14] when they did a computer simulation of nuclear reactions initiated by neutrons in the crystal.

Basic theory of the channeling phenomenon was developed in the works of Jens Lindhard (see [15] and references there). He pointed to the importance of correlations in charged particles sequential collisions with crystal lattice atoms for the formation of channeled particle trajectory, and showed that the motion of such particle can be described using classical mechanics. He also suggested the approximation of continuous potential of rows and planes of crystal atoms, which is now widely used to describe the passage of fast charged particles through an aligned crystal and introduced the concept of channeling critical angle — the Lindhard angle [15]. This approach can significantly simplify the problem of describing the motion of fast charged particle in the real 3-dimensional field of crystal lattice and proceed to the problem of particle scattering in the two-dimensional field in case of axial orientation of the crystal and one-dimensional — in planar orientation case.

2.1.1 Axial orientation case

When fast charged particle is falling into a crystal at a small angle to one of the crystallographic axes (axis z in Fig. 2.1), continuous potential approach can be used, if the change of impact parameter between successive collisions with atoms of the lattice is small in comparison with the impact parameter b_i itself. This is because fast particle is scattered on a small angle in the Coulomb field of individual atom. In fact, the so-called "catastrophic" scatterings on a large angle are possible at the frontal collision of particle with an atom, but such events are quite rare.

The continuous potential of an atomic row is the averaged potential of the atoms located along the crystallographic axis (axis z):

$$U_{\mathrm{R}}(\vec{\rho}) = \frac{1}{L_z} \int\limits_{-\infty}^{\infty} dz \sum_i U_{\mathrm{a}}(\vec{\rho} - \vec{\rho}_i, z), \tag{2.1}$$

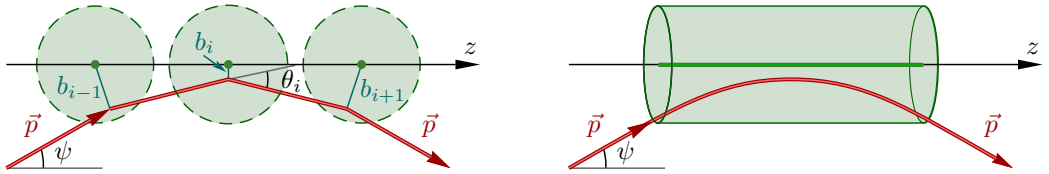

Figure 2.1: The approximation of continuous field of crystal atomic row.

where $\vec{\rho}$ is the coordinate in the plane (x, y) perpendicular to z axis, L_z is the length of a crystal row. The summation is over all atoms of the row, $U_{\rm a}(\vec{r})$ is the potential of individual atom, $\vec{\rho}_i$ is its coordinate. Schematically, this replacement is illustrated in Fig. 2.1. Here ψ is the angle between the particle momentum and the crystal axis.

The position of atoms in the row $\vec{\rho}_i$ has a certain distribution with respect to the equilibrium position. This distribution is due to the thermal vibrations of atoms in a crystal lattice nodes. It can be taken into account by averaging over atom displacement with Gaussian distribution at the calculation of continuous row potential [15, 16]:

$$U_{\rm R}(\rho) = \frac{1}{2\pi \overline{u^2} d_{\rm row}} \int d^2 u_\perp \, \exp\left(-u_\perp^2 / 2\overline{u^2}\right) \int\limits_{-\infty}^{\infty} dz U_a(\vec{\rho} - \vec{u}_\perp, z) \qquad (2.2)$$

where $\rho = |\vec{\rho}|$, $\vec{u}_\perp$ is the thermal displacement of atom in the transverse plane (x, y), $\overline{u^2}$ is the mean square value of $\vec{u}_\perp$, $d_{\rm row}$ is the distance between atoms in the row.

In the field $U_{\rm R}(\rho)$, the particle momentum projection on z axis, p_z, is conserved. Thus, the motion in the orthogonal plane is defined by a two-dimensional equation:

$$\ddot{\vec{\rho}} = -\frac{q}{\varepsilon_\parallel} \frac{\partial}{\partial \vec{\rho}} U_{\rm R}(\rho), \qquad (2.3)$$

where q is the particle charge, $\varepsilon_\parallel = \sqrt{p_z^2 + m^2}$, m and ε are the mass and energy of particle. Here and further we use the units where speed of light $c = 1$. In the relativistic case ($\varepsilon \gg m$): $\varepsilon_\parallel \approx \varepsilon$. Thus, the problem is reduced to a problem of particle movement with "mass" ε in the plane (x, y) in a central potential field $U_{\rm R}(\rho)$ (see Fig. 2.2).

In the field $U_{\rm R}(\rho)$, besides the momentum component p_z, the energy $\varepsilon_\perp$ and momentum $M_\perp$ of particle transverse motion are conserved:

$$\varepsilon_\perp = \frac{\varepsilon \, \dot{\rho}^2}{2} + q \, U_{\rm R}(\rho), \quad M_\perp = p_\perp \, \rho = \varepsilon \, \rho^2 \, \dot{\varphi}, \qquad (2.4)$$

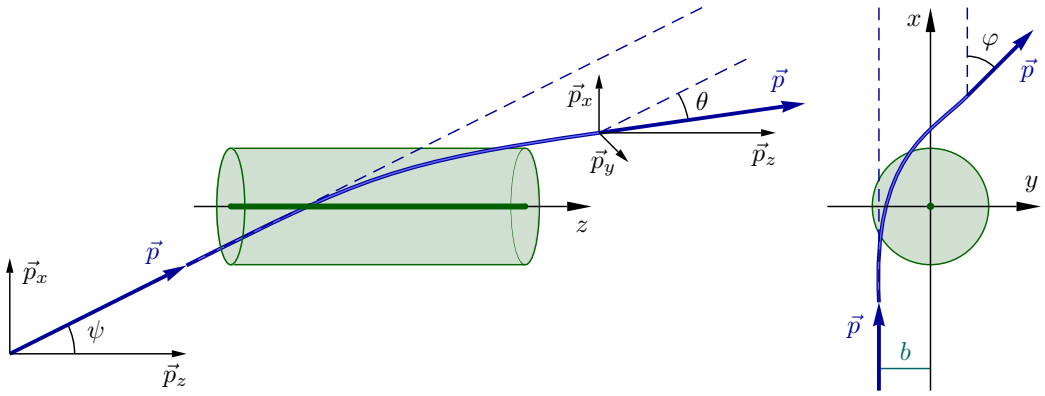

Figure 2.2: Particle scattering by the continuous potential field of crystal atomic row.

where $\varphi = \varphi(t)$ is the azimuthal angle of particle in plane (x, y), see Fig. 2.2. At large distances from the row, where $U_{\mathrm{R}}(\rho) \to 0$, values $\varepsilon_\perp$ and $M_\perp$ are defined by the total energy and incidence angle ψ of the particle with respect to the row:

$$\varepsilon_\perp = \frac{\varepsilon\,\psi^2}{2}, \quad M_\perp = v\,\varepsilon\,b\,\psi \tag{2.5}$$

where b is the particle impact parameter with respect to the row (see Fig. 2.2), v is the particle speed.

Equations (2.4) determine the trajectory of the particle in the field of crystal atomic row in polar coordinates $\rho = \rho(t)$ and $\varphi = \varphi(t)$. The radial dependence of the energy of particle transverse motion has the following form:

$$\varepsilon_\perp = \frac{\varepsilon\,\dot{\rho}^{\,2}}{2} + \frac{M_\perp^2}{2\,\varepsilon\,\rho^2\,v^2} + q\,U_{\mathrm{R}}(\rho), \tag{2.6}$$

Using the equations of particle motion in the field of the continuous potential of the atomic row (2.3), we can determine the particle azimuthal scattering angle in the (x, y) plane as a function of impact parameter b. This relationship has the following form:

$$\varphi(b) = \pi - 2\,b \int\limits_{\rho_0}^{\infty} \frac{d\rho/\rho^2}{\sqrt{1 - \frac{q\,U_{\mathrm{R}}(\rho)}{\varepsilon_\perp} - \frac{b^2}{\rho^2}}}. \tag{2.7}$$

This is the function of the particle deflection in the external field $U_{\mathrm{R}}(\rho)$ in the transverse plane (x, y).

If the energy of particle transverse motion considerably exceeds the atomic row potential $\varepsilon \gg q\,U_{\mathrm{R}}(\rho)$, then the angle between the particle momentum and the

crystal axis $\psi \gg \psi_c$, where ψ_c is the particle critical angle of axial channeling (or the Lindhard angle) [15]:

$$\psi_c = \sqrt{\frac{2|q|U_0}{\varepsilon}} \tag{2.8}$$

where U_0 is the maximal value of row porential, $U_0 = U_R(0)$.

At $\psi \gg \psi_c$ the expansion over the parameter $U/\varepsilon_\perp$ is possible. As a result for all types of functions $U_R(\rho)$ the quantity $\varphi(b)$ is of the order of [17]:

$$\varphi(b) \sim \frac{\psi_c^2}{\psi^2}. \tag{2.9}$$

The full scattering angle of particle scattered by the atomic row, as can be seen in Fig. 2.2 has a following relation with the azimuthal scattering angle (2.7):

$$\theta(b) = 2\,\psi \sin\frac{\varphi(b)}{2}. \tag{2.10}$$

As noted above, the energy of particle transverse motion is conserved in the continuous field of atomic row (2.4), hence the angle between the particle momentum and the crystal axis ψ is also conserved. Therefore, scattering of the particle in such a field is possible only in the azimuthal angle φ and leads to the formation of circular angular distributions of scattered particles along the crystal axis (see Fig. 2.2). This phenomenon is known as "doughnut scattering effect", and it was observed both by computer simulations [18] and experimentally [19]. The theoretical explanation of this effect using the simplest model of atomic row potential $U(\rho) \sim 1/\rho$, can be found, for example, in [20,21]. The detailed study of fast charged particles scattering in the field of atomic chains of a crystal using more realistic models of row potential, including quantum effects at scattering and dynamical chaos phenomenon, was done in [17, 22–24] (see also book [4] and references therein).

When $\psi < \psi_c$, scattering in the crystal is greater with respect to the usual multiple scattering on atoms of amorphous medium. This is because all the atoms of row scatter particles in the same direction (coherent effects in scattering), while the scattering on atoms of amorphous medium has a stochastic nature due to random impact parameter values at successive collisions of particle with atoms of the medium. Note that at high energies, the number of atoms with which this particle interacts effectively at a single act of scattering on atomic row in the crystal can reach tens or hundreds of thousands:

$$N_{\text{eff}} \sim \frac{R_{\text{eff}}}{\psi\, d_{\text{row}}}, \tag{2.11}$$

where R_{eff} is the effective transverse size of the row field.

However, it is necessary to bear in mind that after "closing the ring" of scattered particles angular distribution ($\varphi \sim \pi$), the coherent azimuthal scattering ceases to affect the "full" three-dimensional scattering angle θ (see Eq. 2.10). Therefore, the effect of coherent scattering on atomic rows significantly manifests itself only in relatively thin crystals. Further growth of particle mean square scattering angle with increasing of crystal thickness is caused by incoherent scattering due to thermal vibrations of the crystal lattice atoms. It has a stochastic nature and is similar to multiple scattering in the amorphous medium.

Propagating though a crystal at small angle ψ to of crystallographic axes (axis z), fast charged particle consequently interacts with a number of atomic rows located along this axis. In this case this particle has the multiple scattering on these rows (see Fig. 2.3).

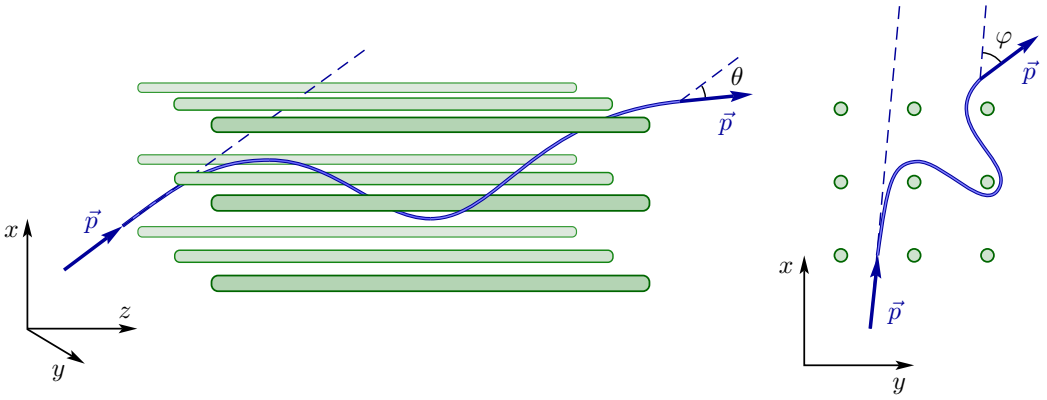

Figure 2.3: Interaction of fast charged particle with atomic rows of the crystal.

The theory of multiple scattering of fast charged particles by atomic rows in aligned crystal is developed in [22, 23, 25]. In contrast to an amorphous medium, the elementary act of multiple scattering in this case is the scattering on atomic row, described by Eqs. (2.7 and 2.8). In these papers, the distribution function of particles over the scattering angle in aligned crystal is obtained on the basis of the kinetic equation approach. The key point of this approach is the use of the assumption of random collisions of scattered particle with atomic rows of a crystal. This approximation is applicable if the angle ψ is small enough, and the azimuthal angle is of the order of unity ($\varphi \sim 1$) [24]. When $\psi \gg \psi_c$, it is necessary to take into account periodical disposition of atomic rows in a crystal lattice (see Fig. 2.4). The field of crystal lattice in transverse plane (x, y) can be represented as a sum of

corresponding atomic rows fields:

$$U(\vec{\rho}) = \sum_j U_{\mathrm{R}}(\vec{\rho} - \vec{\rho}_j), \tag{2.12}$$

where $\vec{\rho}_j$ is the coordinate of atomic row in the plane (x, y), U_{R} is the potential of one atomic row (2.2).

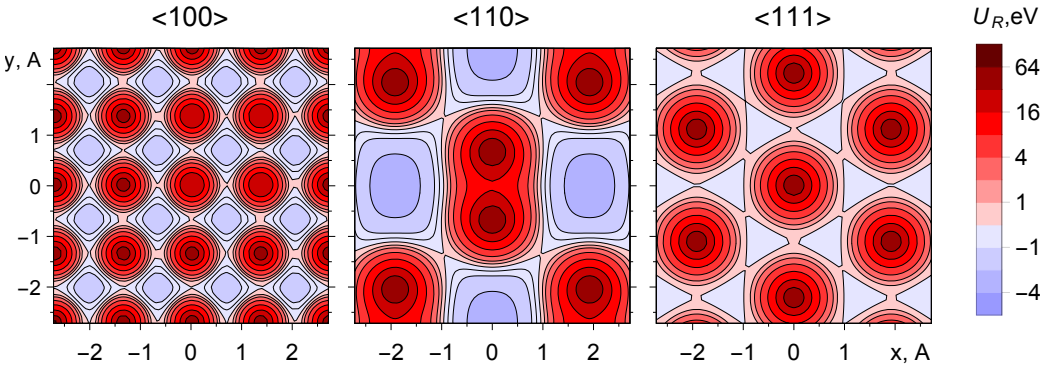

Figure 2.4: Equipotentials of crystal lattice field as a complex of row fields in the transversal plane to the crystallographic axes <100>, <110> and <111> of the silicon crystal. Potentials are set to zero in the middle points between the axes.

Equipotentials of the total field in the transverse plane (x, y) are shown in Fig. 2.4 for a silicon monocrystal, averaging Coulomb potential of individual atoms along the crystallographic axes <100>, <110> and <111>. In such a field the angular momentum of particle with respect to the nearest atomic row conserves only in the region close to the row where its field can be considered as central symmetrical (see Fig. 2.4). Beyond this region the angular momentum $M_\perp$ is not conserved, but the transverse motion energy $\varepsilon_\perp$ is.

Depending on the transverse motion energy the particle motion can be both finite or infinite with respect to the atomic row. For negative charged particles the finite motion ($\varepsilon_\perp < 0$) is possible if the initial angle between particle momentum and crystallographic axis ψ_i is less than critical angle of axial channeling ψ_{c}. In the opposite case, $\psi_i > \psi_{\mathrm{c}}$, the particle motion relative to the atomic rows is always infinite, i.e. above-barrier motion ($\varepsilon_\perp > 0$). The region of axial finite motion of positively charged particles is negligible, because the typical value of potential well depth is of the order of a few eV. Thus, almost all particles are in the above-barrier motion regime. The finite motion of particle in field of atomic rows is often called the axial channeling (or hyper-channeling), see, e.g., [16], though historically channeling

phenomenon was discovered as an abnormal penetration of ions in a crystal in certain directions (crystallographic axes or planes) [14].

2.1.2 Planar orientation case

If the angle between particle momentum and crystallographic axis $\psi \gg \psi_c$, the characteristic values of angle of azimuthal scattering on each atomic row is small $\varphi \ll 1$ (see Eq. 2.9). It means that the particle trajectory in the transverse plane (x, y) is close to the straight line. If at the same time the particle momentum lies in one of crystallographic planes there are correlations in consequent collisions with atoms located along this plane. In this case, the continuous plane potential can be introduced similarly to the continuous axial potential (2.2):

$$U_{\mathrm{P}}(x) = \frac{n\, d_{\mathrm{p}}}{\sqrt{2\pi\, \overline{u_1^2}}} \int d\, u_x \, \exp\left(-u_x^2 / 2\overline{u_1^2}\right) \iint dy\, dz \; U_a(x - u_x, y, z), \tag{2.13}$$

where n is the atom density of crystal, d_{p} is the distance between neighboring crystallographic planes orthogonal to x axis.

The potential energy is a periodic function of the coordinate x. It can be represented as a sum of potential energies of interaction of a particle with individual crystal planes of atoms. In this case, the expression for the potential energy of positively $U^+(x)$ and negatively $U^-(x)$ charged particles is:

$$U^{\pm}(x) = q \sum_k U_{\mathrm{p}} \; (x + k\, d_{\mathrm{p}}) + C^{\pm}. \tag{2.14}$$

Summation is carried out over neighboring planes. The constants C^+ and C^- here are chosen in a way that the minimal potential energies (i.e., in the center between the crystallographic planes $U^+(0)$ and $U^-(d_{\mathrm{p}}/2)$) are zero.

Introduction of the continuous plane potential reduces the problem of particle motion in the crystal lattice field to the one-dimensional one. In this case, the particle momentum components along the z and y axes p_z and p_y are conserved, and the trajectory along the x axis is defined by the following equation:

$$\ddot{x} = -\frac{\nabla\, U^{\pm}(x)}{\varepsilon}. \tag{2.15}$$

The solution of this equation can be expressed in general form in terms of the energy of the particle transverse motion with respect to the crystallographic planes, which is the first integral of the equation of particle motion (2.15):

$$\varepsilon_{\perp \mathrm{p}} = \frac{\varepsilon \dot{x}^2}{2} + U^{\pm}(x). \tag{2.16}$$

The typical trajectories of charged particles in a crystal are presented in Fig. 2.5 on the right. Upper plots (red curves) correspond to the trajectories of positively charged particles and bottom plots (blue curves) — to the negatively charged ones.

The corresponding potential energy of particle interaction with atomic field of crystal planes is shown on the left plots: solid black curve — for a continuous field approximation of crystal atomic planes (2.14) with taking into account the thermal vibrations of atoms in crystal nodes, dashed black curve — the same without thermal vibrations. As one can see, the potential energy $U^{\pm}(x)$ is a set of one-dimensional potential wells of finite depth, located periodically along the x axis.

Dashed green straight lines shows the position of planes, orange curves around them — distribution of atomic density due to thermal vibrations.

On the left plots the lines labeled with numbers represent the energy of particle transverse motion. Depending on its the magnitude, the motion of particle along the x axis in such a field, can be either finite "1" or infinite "2" and "3".

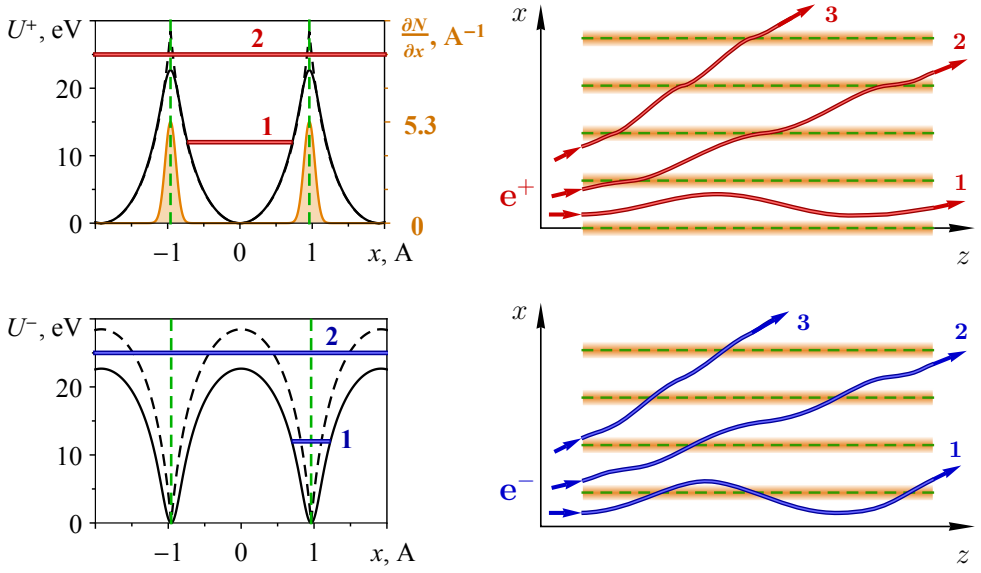

Figure 2.5: Typical trajectories (on the right) of positively (upper plots, red) and negatively (bottom plots, blue) charged particles and corresponding potential energies $U^{\pm}(x)$ of their interaction with atomic field of crystal planes (on the left). 1 — channeled particles $\theta < \theta_{\mathrm{p}}$, 2 — over-barrier particles $\theta > \theta_{\mathrm{p}}$, and 3 — high over-barrier particles $\theta \gg \theta_{\mathrm{p}}$. See more details in text.

The motion of charged particle will be finite if

$$\varepsilon_{\perp \mathrm{p}} < U_0, \tag{2.17}$$

where U_0 is a maximal value of potential energy $U^{\pm}(x)$. By introducing the angle θ between the particle momentum and the crystallographic plane at the position x, where potential energy $U^{\pm}(x) = 0$, this relation has a following form:

$$\theta < \theta_{\mathrm{p}}, \qquad \theta_{\mathrm{p}} = \sqrt{2\,U_0/\varepsilon}, \tag{2.18}$$

where θ_{p} is the plane channeling critical angle of particle [15].

Thus, if condition (2.17) holds, the particle will move in the channel formed by the crystalline planes of atoms, periodically deviating from the atomic plane by a small angle.

At $\theta > \theta_{\mathrm{p}}$, the particle will perform an infinite motion with respect to the crystalline atomic planes, passing from one atomic plane to another. Such a motion is called the above-barrier motion of a particle in the field of the crystal planes of atoms [26].

At $\theta \gg \theta_{\mathrm{p}}$, trajectories of both positively and negatively charged particles are similar to one each other, and are close to a straight line.

The quantity $\varepsilon_{\perp\,\mathrm{p}}$ is determined by the conditions at which the particle enters the crystal, i.e. the angle of its entry θ_0 and the magnitude of impact parameter x_0 with respect to the corresponding crystallographic plane

$$\varepsilon_{\perp\,p} = \frac{\varepsilon\,\theta_0^2}{2} + U^{\pm}(x_0). \tag{2.19}$$

As in the case of the motion in a continuous field of atomic rows (2.2), the energy (2.16) of the transverse motion in a continuous field of atomic planes is also conserved. This means that, if the particle has been caught in the channeling regime when entering a crystal, it must remain in this regime of motion throughout its passage through the crystal. Taking into account the incoherent effects in the scattering of fast charged particles in the crystal lattice field, caused by the thermal fluctuations of atom positions, and scattering on the electronic subsystem of the crystal, leads to a nonconservation of $\varepsilon_{\perp\,\mathrm{p}}$, and thus affects the stability of the channeling regime. This problem will be discussed in more detail in Section 2.2.

Note, that trajectories of positively charged particles in channeling regime are located mainly between densely packed atomic planes, and hence these particles have lower probability of nuclear scattering than in amorphous medium. On the contrary, negatively charged particles (both channeled and above-barrier) periodically pass through atomic planes (see. Fig. 2.5). Due to this effect the channeling regime is much more stable for positively charged particles than for negative ones [27].

2.1.3 Beam deflection by bent crystals

The above described features of fast charged particles motion in the field of aligned crystal lattice can be used for a beam parameters control. The strong correlations in consequent collisions of fast particles with crystal lattice atoms leads to coherent effects in scattering. This opens up a possibility to use the high gradients of atomic Coulomb fields on a macroscopic scale, because the number of such correlated collisions can reach millions.

For example, the bent germanium crystal can deflect 450 GeV protons on the angles about 10 mrad, that is equivalent to magnetic field of about 2000 Tesla [28].

Depending on the crystal orientation (axial or planar) different mechanisms can be used for fast charged particle beam deflection. Below, the main features of each mechanisms are considered in details.

2.1.3.1 Planar channeling

Particles captured in planar channeling regime propagate along the crystal plane oscillating in the plane channel, periodically deviating at a small angle ($\theta < \theta_{\mathrm{p}}$) with respect to the main direction of its motion. If the crystal is slightly bent, the channeled particles will follow the crystal bending direction (see Fig. 2.6).

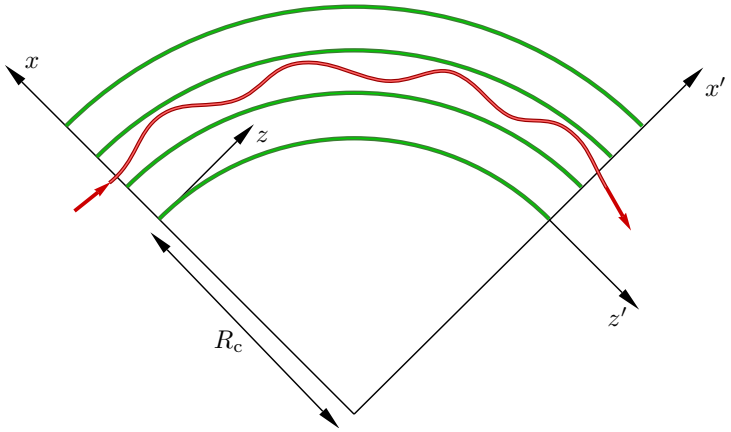

Figure 2.6: Deflection of a positively charged particle by planar channeling in the field of curved crystalline planes.

Due to the crystal curvature, the particle is a subject to a centrifugal force in the direction orthogonal to the bent crystal plane. This can be taken into account

by introducing the effective potential energy of particle interaction with atomic field of curved crystalline plane with the additional centrifugal term [24, 29, 30]:

$$U_{\text{eff}}(x) = U^{\pm}(x) - x\frac{\varepsilon}{R_{\text{c}}} \tag{2.20}$$

where R_{c} is the radius of crystal curvature.

The behavior of $U_{\text{eff}}(x)$ for the positively charged particles is presented in Fig. 2.7. In a straight crystal (see curve "$R_{\text{c}} \gg R_{\text{cr}}$") the motion of particle is

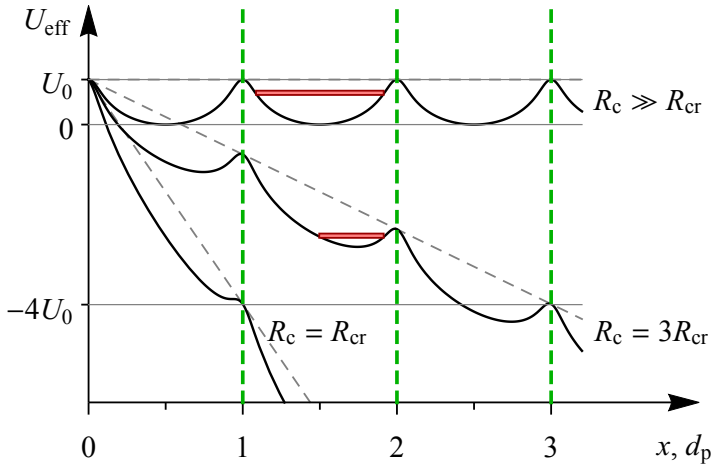

Figure 2.7: Effective potential energy (2.20) of particle interaction with the field of atomic planes in a bent crystal with different radii of curvature: $R_{\text{c}} \gg R_{\text{cr}}$, $R_{\text{c}} = 3R_{\text{cr}}$ and $R_{\text{c}} = R_{\text{cr}}$.

finite, if its transversal motion energy is less then maximal value of potential energy U_0 (2.17). Otherwise, the motion is infinite. In a bent crystal, the centrifugal term leads to the deformation of potential well and decrease of its depth (see curve "$R_{\text{c}} = 3R_{\text{cr}}$"). In this case, the number of particles captured into channeling regime also decreases.

With the curvature radius decreasing the position of potential well bottom shifts along the x axis to the position of the crystal plane. When this shift reaches the value $d/2$ no finite motion is possible (see curve "$R_{\text{c}} = R_{\text{cr}}$" in Fig. 2.7). Corresponding value of the curvature radius is called the critical radius of curvature R_{cr} for the beam deflection by a bent crystal. If the plane potential is approximated by a parabolic function, the expression for the critical radius can be easily obtained [24, 30, 31]:

$$R_{\text{cr}} = d_{\text{p}}\frac{\varepsilon}{4\,U_0}. \tag{2.21}$$

The efficiency of beam deflection by planar channeling mechanism in a bent crystal essentially depends on the stability of the channeling regime. As mentioned in previous section there is a crucial difference between positively and negatively charged particles planar channeling. Due to this difference this mechanism works properly for positively charged particles but is inefficient for negatively charged particles [28]. The nature of instability of the planar channeling regime for both positively and negatively charged particles lies in the thermal vibration of lattice atoms that violates the conservation of transverse energy of these particles (2.16) due to the incoherent scattering. This effect will be discussed in details in the section 2.2.

2.1.3.2 Volume reflection

Besides the planar channeling there is another mechanism of beam deflection by atomic planes of bent crystal. It is based on the phenomenon of total deflection of above barrier positively charged particle by a bent crystal atomic plane. It takes place when the incident angle of the particle to the plane becomes less than critical angle of the planar channeling (see Fig. 2.8).

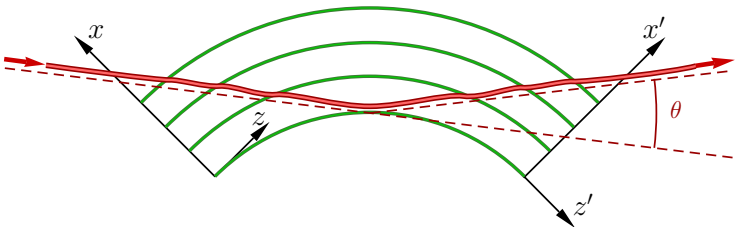

Figure 2.8: Volume reflection.

The benefit of this method in comparison with planar channeling is the extension of the part of initial beam that is deflected. For this deflection mechanism it is not necessary to have the angular divergence of incident beam less than critical angle of planar channeling. Practically all particles of incident beam are deflected by such a bent crystal if the initial divergence of the beam is less than the bending angle of crystal $\Theta = L/R$, where L is the length of the crystal. At high energies this angle can essentially (in orders of magnitude) exceed the critical angle of the planar channeling θ_{p}. However, the effective deflection angle for this mechanism is less than $2\theta_{\mathrm{p}}$, because the coherent scattering of particle by atomic plane on the right angle (the total deflection effect) happens only once during the penetration of the crystal per each particle.

The attempts to increase the deflection angle of this mechanism by using a set of crystals face the problem of additional angular swelling of the beam at each entrance into the next crystal, due to the random impact parameter of a particle relative to a crystal plane. The value of this angular swelling at the particle impact with each crystal is about θ_{p}.

2.1.3.3 Stochastic mechanism

As shown in section 2.1.1, at fast charged particles motion in the field of atomic row the coherent effect in scattering over azimuthal angle φ (see Eq. 2.2) takes place ("doughnut scattering effect" [17–22]). At small angles $\psi \sim \psi_{\mathrm{c}}$ between particle momentum and atomic row axis the value of angle φ can reach big enough values $\varphi \sim \pi$ after the particle passing a certain path along this row. It means that the "doughnut" is closed. In this case, the center of the beam angular distribution coincides with this crystallographic axis. Thus, due to this effect, the particle beam falling at the angle $\psi \sim \psi_{\mathrm{c}}$ to the crystallographic axis is deflected as a whole by the angle ψ.

If the crystal rows are slightly bent, the beam as a hole can follow the crystal curvature consequently scattered by different atomic rows along the crystallographic axis. This effect was predicted by Greenenko and Shul'ga [32] on the basis of computer simulation results. They also developed the original theoretical approach based on recurrence relations in successive collisions of a fast charged particle by different crystal atomic rows located along a given axis (see 2.3), which gave the possibility to describe this effect and to obtain the criteria of its existence [24, 33].

The so-called Greenenko–Shul'ga condition of the stochastic mechanism of fast charged particle deflection by bent crystal rows can be presented in the following form [24, 33]:

$$\frac{lT}{R_{\mathrm{c}}^2} \leq \psi_{\mathrm{c}}^2, \tag{2.22}$$

where l is the length of atomic row, at which the distribution over azimuthal angle φ becomes uniform at $\psi \sim \psi_{\mathrm{c}}$, $l \approx 1/(ndR_{\mathrm{TF}}\psi_{\mathrm{c}})$, n is the atomic density in the crystal, d is the distance between atoms in the row, R_{TF} is the Thomas–Fermi radius of atomic potential screening (see, e.g., [3]), T is the crystal thickness, and R_{c} is the crystal curvature radius for the axis z.

It should be noted, that the beam deflection using the stochastic mechanism of fast charged particle scattering by bent crystal rows, in contrast to the previously considered planar channeling mechanism, is realized for particles that perform infinite motion with respect to atomic rows, and such a deflection of the beam is possible for both positively and negatively charged particles.

2.2 Incoherent effects at multiple scattering in crystal

As it was demonstrated, the continuous potential approximation, proposed in [15], simplifies essentially the description of channeled particle motion in a crystal lattice field both for axial and planar orientation cases, decreasing the spatial dimension of the solving problem to two-dimensional and one-dimensional ones, correspondingly. In [24] it was shown that this approach can be successfully applied also for describing the above-barrier particle scattering and radiation in a crystal, when particle moves at relatively small angle, but greater than Lindhard's critical angle of channeling [15], to one of crystallographic axes or planes: $\psi \geq \psi_c$ and $\theta \geq \theta_p$. Using the continuous potential model, it is possible to describe the main features of coherent effects in scattering and radiation of fast charged particles in aligned crystals.

Nevertheless, this approach has one essential drawback. As mentioned above, the energy of the particle transverse motion in continuous potential $U(\rho)$ and $U(x)$ is conserved (2.4) and (2.16). This means, in particular, that the particle captured in the channeling regime entering the crystal, in theory, should remain its motion in this regime up to leaving the crystal. In reality, the channeling regime of fast charged particles is not completely stable. The particle abandonment of this regime, called the dechanneling process, is due to incoherent stochastic multiple scattering of particles on the atoms of crystal, due to the imperfections of the crystal lattice. In particular, these are the thermal vibrations of atoms relative to their equilibrium positions in the lattice nodes, scattering on the electron subsystem of the crystal, and structural defects of various kinds.

The procedure of taking into account the thermal vibrations of atoms, described in section 2.1 (see Eqs. (2.2) and (2.13)), affects only the form of continuous potential of atomic rows or planes of a crystal. This leads to the reduction of the continuous potential height (see solid and dashed black curves in Fig. 2.5 on the left), and accordingly affects the efficiency of coherent scattering of particles in a corresponding field. However, using the averaged potential of axes or planes when solving the equations of motion (2.3) or (2.15) a priori retains the energy of transverse motion of a particle (see Eqs. (2.4) and (2.16)) in such potentials. Thus, the continuous potential approach with all its advantages disregards incoherent scattering effects, which leads to non-conservation of energy of particle transverse motion and, as a result, the possibility of switching between the motion regimes: dechanneling and reverse effect — rechanneling, i.e. capture of over-barrier particle into finite motion in the field of atomic rows or planes of a crystal.

2.2.1 Differences between positively and negatively charged particles motion in a crystal

When a negatively charged channeled particle is moving in the Coulomb field of crystal atomic rows or planes, it has on average a higher probability of close collision with nuclei of atom than positively charged channeled particle. This is because the trajectory of negatively charged particle due to Coulomb attraction regularly passes through the area of thermal vibrations of atoms of crystal rows or planes. Additionally, the trajectory of this particle lies in the region of higher density of electron subsystem. For this reason, incoherent multiple scattering significantly affects the negatively charged channeled particle motion leading to its relatively rapid dechanneling.

On the contrary, a positively charged channeled particle is pushed off by the averaged field of atomic row or plane, and hence, has a much lower probability of close collision with the lattice atoms compared not only to a negatively charged channeled particle, but also to the probability at motion in the amorphous medium (see Fig. 2.5). This provides significant stability to the motion of positively charged particles in the channeling regime.

The exception is a small region in the energy phase space of transverse motion of charged particles, for which

$$\varepsilon_{\perp\,\mathrm{p}} \approx U_0, \tag{2.23}$$

i.e. close to the potential barrier, but under-barrier states of channeled particles. Such particles regularly (every half period of motion in planar channel) enter the region of thermal vibrations of the atoms of crystallographic plane, which is also the region of higher density of electron subsystem. In addition, positively charged particles spend a significant amount of time in this region, so-called “hang effect”, that leads to their rapid dechanneling.

Note, that for high over-barrier particle there is almost no difference in motion of positively and negatively charged particles, and this motion is close to the one in the amorphous media.

As shown in this chapter, there are significant differences in the dynamics of charged particles as they pass through the oriented crystals depending on the sign of the particle charge and the orientation of the crystal relative to the direction of the particle beam. These differences in the particles dynamics in the field of crystal lattice, obviously, can significantly affect not only the characteristics of particle beam scattering on a crystal, but also the secondary electrodynamic processes accompanying the passage of fast charged particles through a crystal, such as bremsstrahlung,

pair production and others. Therefore, the effect of incoherent scattering on the motion of particles in the crystal is very important.

In general, the kinetics of relativistic beam of charged particles in oriented crystals, i.e. taking into account changes in the energy of transverse motion as a result of incoherent scattering, is quite complicated. This is due to the fact that when the beam propagates through the crystal, its various fractions are in different regimes of motion, finite – infinite, regular – chaotic, axial – planar with constant transitions between them. For a quantitative description of this kinetics there are two essentially different approaches.

2.2.2 Kinetic equation method

The first one is based on a kinetic equation for the probability density in phase space position and momentum of a particle moving in a crystal in the channeling regime. The solution of this kinetic equation is the distribution function of beam particle energy of transverse motion $\varepsilon_\perp$, as a function of the penetration depth of particles in the crystal. An important parameter here is the dechanneling length L_{dech}, i.e. the crystal length, on which the half of the particles, that were originally captured in the channeling regime, dechannels (passes into over-barrier regime of motion)

The kinetic theory of dechanneling at ions propagation through the oriented crystals was developed by Jens Lindhard (see [15] and references there) based on the diffusion approximation approach using a so-called monotone gain of particle transverse energy $\varepsilon_\perp$. Further development of the dechanneling theory was done by Beloshitsky and Kumahov [27, 34] based on the Fokker–Planck equation. Later, the kinetic theory of dechanneling, which at the beginning was developed to describe the evolution of the channeled ion beams of relatively low energies in crystal, was used to describe the relativistic electron and positron beams passage through the oriented crystal [35, 36]. The need for a number of model assumptions in the derivation of equations and determination of diffusion coefficients makes it difficult to obtain accurate quantitative results for the dechanneling length in such approach (see analysis and comparison of theoretical and experimental results, e.g., in [37,38]).

2.2.3 Computer simulations based on Monte Carlo method

An alternative to the kinetic theory is a computer simulation based on the Monte-Carlo method, which takes into account the effect of incoherent scattering and the change of fast charged particles motion regime in a crystal. Depending on the problem under consideration, different algorithms for simulating the interaction of

charged particles with the crystal lattice field can be used for this purpose, i.e., with various degree of details of this interaction.

Note, that in the first theoretical works devoted to radiation at channeling of relativistic positrons and electrons, calculations were made exclusively with the use of the approximation of the continuous potential $U_{\mathrm{p}}(x)$ of crystalline planes (2.13) or axes (2.1) [39]. However, the comparison of the results of calculations with experimental data revealed that for an adequate description of these data it is important to take into account the evolution of the particle beam as it passes through a crystal, i.e. redistribution of energies of particle transverse movement $\varepsilon_{\perp}$ due to incoherent scattering.

One of the simplest computer models that was used to analyze the influence of incoherent scattering on the formation of the radiation spectra of a relativistic electron in plane channeling is the so-called "macro-collision" model. In this model the trajectory of particles in the interplanar space is described by the equations of motion in a continuous field $U_{\mathrm{p}}(x)$ of crystalline planes (2.13). Thus, $\varepsilon_{\perp\,\mathrm{p}}$ is conserved, as noted in section 2.1.2. Significant changes of $\varepsilon_{\perp\,\mathrm{p}}$ due to incoherent multiple scattering on crystal atoms occur when a channeled electron passes through a crystalline plane. The consideration of such changes in this model is done by adding the incoherent scattering angle $\Delta\theta$ to the angle θ, at which the electron crosses the crystal plane:

$$\varepsilon_{\perp\,\mathrm{p}} = \frac{\varepsilon(\theta + \Delta\theta)^2}{2}. \tag{2.24}$$

This added angle $\Delta\theta$ is played as a random variable in accordance with the distribution function of the multiple scattering angle in the conventional "layer of amorphous matter" along the particle trajectory of thickness $\Delta l = 2\,u_1/\,\theta$. To simplify the calculations it is assumed that the atom positions in this "u-layer" are chaotic and uniformly spread with the density $n_u = n\,d_{\mathrm{p}}/\,u_1$. In the case of the axial orientation of the crystal the "macro-collision" model is build in the similar way, but in this case the "elementary act" of incoherent scattering of the particle, when the changes of the energy of its transverse motion $\varepsilon_{\perp}$ occur, is the passage of a fast particle through a cylindrical "u-rod" of the radius u_1 along crystalline axis. Before and after passing the "u-rod", it is assumed that the particle moves in the continuous field of crystal atomic row (2.12), i.e, with a constant $\varepsilon_{\perp}$.

The relative simplicity and speed of this model allowed ones to investigate the incoherent scattering effect on the interference properties of gamma radiation of channeled electrons and to find out the basic mechanism of the so-called "quasi-reflection" effect of relativistic electron beam on a thin crystal [40, 41]. The phenomenon of anomalous diffusion of channeled charged particles in crystals [42–44]

was foreseen with its help. However, in order to obtain quantitative characteristics of scattering or gamma radiation, during the passage of charged particle beams through the crystal, it is necessary to use more precise approaches.

Another algorithm that is widely used for computer simulation of a charged particle passage through a crystal is the so-called "aggregate collisions method" [45, 46]. As in the previous model, in the first approximation the total particle trajectory is found by solving equations of motion in the average field of rows or planes of crystal atoms. To take into account the incoherent scattering effect, this trajectory is divided into $i_{\max}$ relatively small segments on which the transverse motion energy $\varepsilon_\perp$ is assumed to be constant with a predefined accuracy $\delta\varepsilon_\perp$. Further, the possible change in the energy of the transverse motion $\Delta\varepsilon_\perp$ is calculated, which is due to the influence of the thermal vibrations of atoms from the nearest row or plane of the crystal, as well as the scattering of the fast charged particle on the electronic subsystem of the crystal.

The calculation of $\Delta\varepsilon_\perp$ is carried out similarly to the previous model, i.e, the incoherent scattering angle of the particle $\Delta\theta_i$ is added to the current magnitude of the angle θ_i on the i segment of the trajectory:

$$\varepsilon_{\perp\,\mathrm{p}} = \frac{\varepsilon(\theta + \Delta\theta)^2}{2} + q\,U_{\mathrm{p}}(x_i), \tag{2.25}$$

where $U_{\mathrm{p}}(x_i)$ is the continuous potential of the nearest crystalline plane, taking into account the contribution of neighboring planes, x_i is the distance to this plane.

The random value of the angle $\Delta\theta_i$ is played in accordance with the function of angular distribution of the scattering of a fast particle on the i-th segment of the trajectory as in a layer of amorphous matter of corresponding thickness with a special density of atoms $n^*(x_i)$. This density is calculated according to the Gaussian distribution of the atoms positions of the nearest crystalline plane due to their thermal oscillations with the amplitude u_1:

$$n^*(x_i) = \frac{n_\perp}{\sqrt{2\,\pi\,u_1^2}}\,\exp\left(-\frac{x_i^2}{2u_1^2}\right), \tag{2.26}$$

where $n_\perp = n\,d_{\mathrm{p}}$ is the "two-dimensional density" of the atoms in the plane (y, z), d_{p} is the distance between the neighboring crystallographic planes.

In the case of the axial crystal orientation, instead of the continuous potential of the nearest crystalline plane $U_{\mathrm{p}}(x_i)$, the continuous potential of the nearest crystalline axis $U(\rho)$ is used and the corresponding two-dimensional Gaussian density distribution of atoms

$$n^*(\rho_i) = \frac{n_{\mathrm{r}}}{2\,\pi\,u_1^2}\,\exp\left(-\frac{\rho_i^2}{2u_1^2}\right), \tag{2.27}$$

where $n_{\mathrm{r}} = n\,S_{\perp}$ is the "one-dimensional density" of the atoms along the chosen crystallographic axis (z axis), $S_{\perp}$ is the area of the elementary cell of the crystalline lattice in the plane (x, y) (see Fig. 2.4).

If the change in the energy of the transverse motion $\Delta\varepsilon_{\perp}$ after passing the i-th segment of the particle trajectory in the crystal is more than $\delta\varepsilon_{\perp}$, then the length of the segment is divided in half and the calculation of $\Delta\varepsilon_{\perp}$ is repeated for this reduced length. This procedure is repeated until $\Delta\varepsilon_{\perp}$ becomes less than $\delta\varepsilon_{\perp}$. Then the next step in calculating the new $(i+1)$ segment of the particle trajectory is made with the new value $\varepsilon_{\perp}\prime = \varepsilon_{\perp} + \Delta\varepsilon_{\perp}$ and the corresponding value $\theta_{i+1} = \theta_i + \Delta\theta_i$.

Thus, it would seem that this algorithm allows to calculate the trajectory of a particle in a continuous crystal field with any predetermined accuracy. However, the question arises: whether the Bethe–Moliere theory [47] of multiple scattering of fast charged particles in an amorphous medium can be used to describe the incoherent scattering on extremely small segments of the particle trajectory, in addition, with a significantly reduced effective atomic density.

Such problems do not arise in the simulation of the motion of fast charged particles in the oriented crystal using a model of binary collisions, when a collision of a particle with each atom of a crystal lattice along its trajectory is played separately. At the same time, there is no artificial distribution on coherent scattering (due to a continuous potential approximation), and incoherent, which in a model way takes into account the fluctuation of thermal vibrations of atoms in lattice nodes. By using the binary collisions model, the fluctuations of atom positions in the crystal lattice are played in accordance with the Debye theory and are taken into account when calculating the impact parameter of the collision of a particle with each subsequent atom. Thus, the model of binary collisions naturally (model independently) takes into account not only a real discreteness of crystal rows or planes, but also the effect on the motion of a particle of thermal vibrations of atoms, depending on the temperature of the crystal. Moreover, it is possible to "turn on" and "turn off" the heat fluctuations of the atoms to determine their effect. It is also possible to take into account the correlation between fluctuations of neighboring atoms, to simulate the effect of phonons and other excitations of the crystalline lattice on the motion and radiation of particles in a crystal. Such a model is the most detailed in describing the interaction of a fast charged particle with crystalline lattice atoms. Therefore, it is the most resource-consuming in terms of computer calculations. On the other hand, the calculating power of modern computers is quite sufficient to obtain satisfactory statistics when conducting the simulation of the high energy charged particles beams passage through thick crystals based on the model of binary collisions.

Chapter 3

Computational model of particles passage through a crystal

3.1 Binary collision model

The main feature of crystals is the periodicity of its atomic structure that opens up unique possibilities for the fast charged particles beam manipulation. The motion of such particles in a periodical structure can be well described by continuous potential approach [15], in which the position and hence the potential of atoms is averaged over some geometrical clusters (e.g. rows, planes, one-dimensional slices "plane slices of finite thickness", etc.). This simplification gives the opportunity to obtain analytical assumptions for main parameters of particle beam in crystal, and also speeds up the simulation of particle propagation through a crystal.

However, with a constant growth of computational facilities the second factor is loosing its relevance, as well as a nicety of modern experiments claims higher accuracy from theoretical predictions. In this light, Monte-Carlo approach based on the binary collision model is in favor. As it was mentioned in the previous chapter, this approach has the most organic way of taking into account the thermal vibration of atoms at the crystal nodes.

For an atomic potential we use screen Coulomb potential $U(r)$ with the Moliere screening function $\Phi_{\mathrm{M}}(r/R_{\mathrm{TF}})$:

$$U(r) = \Phi_{\mathrm{M}}\left(\frac{r}{R_{\mathrm{TF}}}\right)\frac{Z\,e^2}{r}, \qquad \Phi_{\mathrm{M}}\left(\frac{r}{R_{\mathrm{TF}}}\right) = \sum_{i=1}^{3}\alpha_i\,e^{-\beta_i\,r/R_{\mathrm{TF}}} \tag{3.1}$$

where R_{TF} is the Thomas–Fermi radius: $R_{\mathrm{TF}} \approx 0.8853\,R_{\mathrm{B}}\,Z^{-1/3}$, $R_{\mathrm{B}} \approx 0.5292$ A is a Bohr radius; $\alpha_1 = 0.35$, $\alpha_2 = 0.55$, $\alpha_3 = 0.10$, $\beta_1 = 0.3$, $\beta_2 = 1.2$, $\beta_3 = 6.0$ are

Moliere parameters [48]. The plots of these functions are presented in Fig. 3.1 for the crystal materials (listed on the right), that are commonly used in the channeling and related experiments. To compare the atomic potentials of various crystal materials, the distance r is in units of distances between the neighboring planes $d_{\rm p}$ for the orientation (110).

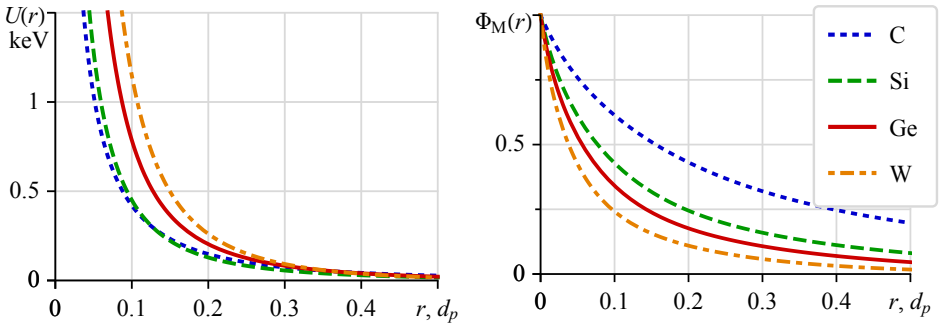

Figure 3.1: Coulomb potentials with screening by Moliere parameterization $U(r)$ of the crystals listed on the right (left plot). Screening functions $\Phi_{\rm M}(r)$ (right plot).

As the particle energy is much greater than the potential of one atom for almost all impact parameters, we calculate the deflection angle of particle on each consequent atom:

$$\Delta\vec{\vartheta}_{\rm a}(\vec{r}) = \frac{Z\,e^2\,\vec{r}}{\varepsilon\,r^2}\sum_{i=1}^{3}\alpha_i\,\beta_i^2\,K_0(\beta_i\,r), \tag{3.2}$$

where K_0 is a Bessel function.

The impact from neighboring atoms is taken into account in the same way:

$$\Delta\vec{\vartheta} = \Delta\vec{\vartheta}_{\rm a}(\vec{b}) + \Delta\vec{\vartheta}_n(\vec{r}_1, \vec{r}_2, \ldots \vec{r}_N), \qquad \Delta\vec{\vartheta}_n = \sum_{k=1}^{N}\Delta\vec{\vartheta}_a(\vec{r}_k), \tag{3.3}$$

where $\vec{b}$ is the impact parameter of the nearest atom taking into account the thermal vibration, $\Delta\vec{\vartheta}_n$ is the total increment of the angle gained by interaction with neighboring atoms, $\vec{r}_k$ is a vector from the neighboring crystal node position of number k to the position of moving particle, N is the number of neighboring atoms taken into account.

The displacement of nearest atom due to the thermal vibration (u_x, u_y) is drawn with a normal distribution probability:

$$P(u_x)\,du_x = \frac{1}{\sqrt{2\,\pi\,\overline{u_x^2}}}\exp(-\frac{u_x^2}{2\,\overline{u_x^2}})\,du_x, \tag{3.4}$$

and with the same formula for u_y. The displacement in z-direction is neglected. The mean-square displacement of atoms (i.e. the square of the amplitude of thermal vibrations) is calculated using the following formula (see, e.g., [49]):

$$\overline{u_x^2} = \frac{146.4(\mathrm{A}^2)}{M\,\theta_\mathrm{D}} \left(\frac{\Phi_\mathrm{D}(\varkappa)}{\varkappa} + \frac{1}{4} \right) \qquad \Phi_\mathrm{D}(\varkappa) = \frac{1}{\varkappa} \int_0^\varkappa \frac{\zeta\, d\zeta}{\exp(\zeta) - 1} \tag{3.5}$$

where M and θ_D are the atomic mass and the Debye temperature of the monocrystal, $\Phi_\mathrm{D}(\varkappa = \theta_\mathrm{D}/T)$ is the Debye function and T is the temperature of the crystal.

Table 3.1: Crystal parameters used in the simulations

	Z	M	a_el, A	n_el	d_p, A	θ_D, K
C	6	12.0	3.567	8	1.26	2000
Si	14	28.1	5.431	8	1.92	543
Ge	32	72.6	5.657	8	2.00	290
W	74	183.9	3.165	2	2.24	310

The main parameters of the crystals used in this simulations are listed in the Table 3.1. Here a_el is the linear size of crystal elementary cell, n_el is a number of atoms in a crystal elementary cell, d_p is the distance between crystallographic planes (110).

The amplitude of thermal vibrations for the crysrals listed in Table 3.1 is shown in Fig. 3.2.

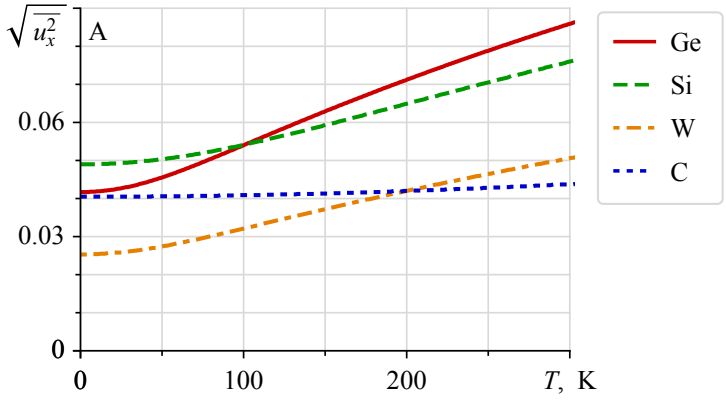

Figure 3.2: Amplitude of thermal vibrations of atoms as a function of temperature in the Debye approximation for different crystals, listed on the right.

The thermal vibrations of atoms lead to incoherent scattering and, hence,

dechanneling. Thus, the reduction of its amplitude would strengthen the channeling regime. From Fig. 3.2 one can see that cooling down the germanium crystal from ambiance (~ 300 K) to cryogenic (~ 80 K) temperatures can essentially reduce dechanneling, as the amplitude of thermal vibrations in this case falls by 41 %. For a silicon crystal this fall is about 29 %.

The simulation showed that it is essential to take into account the thermal vibrations only for the nearest atom, hence, to speed up the calculation $\Delta\vec{\vartheta}_n$ is tabulated in refer to a nearest crystal node position for current crystal orientation.

3.2 Scattering on the electron subsystem

The multiple scattering on the electron subsystem of crystal lattice is taken into account using the aggregate collisions model (see, e.g., [45]).

The multiple scattering angle of a particle from the path Δl in amorphous media has a normal distribution with the root-mean-square angle [1]:

$$\vartheta_x^{(\mathrm{rms})} = \sqrt{\overline{\vartheta_x^2}} = \frac{13.6\ \mathrm{MeV}}{\varepsilon}\ \sqrt{\frac{\Delta l}{X_0}}\left[1 + 0.038 \ln\left(\frac{\Delta l}{X_0}\right)\right], \tag{3.6}$$

where X_0 is the radiation length

$$X_0 = \left(\frac{4\,Z^2\,e^6\,n}{m^2}\ \ln(m\,R_{\mathrm{TF}})\right)^{-1}, \tag{3.7}$$

n is the density of atoms, m is the electron mass.

To describe scattering on the uniformly spread electron gas we use Eq. (3.6) with modified radiation length:

$$X_0' = \left(\frac{4\,e^6\,n_e}{m^2}\ \ln(m\,\omega_{\mathrm{p}}^{-1})\right)^{-1}. \tag{3.8}$$

where $n_e = Z \cdot n$ is the density of electrons and ω_{p} is the plasma frequency (see, e.g., [3, 4]):

$$\omega_{\mathrm{p}} = \sqrt{4\,\pi\,n\,Z\,e^2/m} \tag{3.9}$$

In the case of planar channeling, the density of electrons throughout the particle trajectory is not constant. From the Gauss theorem we can conclude that the averaged over z density of electrons $\bar{n}_e(x)$ has the same behavior as a continuous plane potential $U_{\mathrm{p}}(x)$ (2.13). It is important to take this into account for two reasons. Firstly, particles with different energies of transverse motion have different average

densities of electrons throughout their trajectories. The second reason is that the positively charged particle at the minimum of potential energy (see Fig. 2.7) has an equal probability to get or to loose a part of the energy of its transverse motion, whereas at the maximum of potential energy (when the component of velocity perpendicular to the crystal plane $v_\perp = 0$) it can only gain the energy. Note that the particle spends more time in the part of its trajectory at $v_\perp \sim 0$ ("hang effect"), thus, it is important in which part of the trajectory this incoherent scattering is taken into account.

Besides, in this approach there are two limitations on the trajectory step Δl: the number of electrons in one step Δl should not be small, so that the multiple scattering approach can be applied, and Δl itself should not be very large, so that $\vartheta_x \ll \theta_\mathrm{c}$.

To meet all these requirements in our simulation the additional scattering angle $\Delta\vartheta_x$ is drawn once the term $\Delta l/X_0$ corresponds to $\vartheta_x^{(\mathrm{rms})} \geq 0.05\,\psi_\mathrm{c}$. The angle of multiple scattering on the electron subsystem on the trajectory step Δl is calculated using Eq. (3.6) with the following expression for the term $\Delta l/X_0$:

$$\frac{\Delta l}{X_0} = \frac{4\,e^6}{m^2}\ \ln(m\,d_\mathrm{p}) \int\limits_0^{\Delta l} \bar{n}_e(l)\,dl. \tag{3.10}$$

The calculations show that scattering on the electron subsystem essentially effects the dechanneling rate in the thick (> 1 cm) crystals, but it can be neglected in the thin (< 1 mm) ones.

3.3 Continuous plane potential

In our model, scattering of charged particle on atoms of a crystal is described using binary collision model (see Section 3.1) and to take into account scattering on the electron subsystem we use aggregate collision model with modified radiation length and variable step on the trajectory (see Section 3.2). Nevertheless, to calculate the value of energy of the particle transverse motion and hence, distinguish between the channeling and over-barrier regimes of motion we use the distribution of continuous plane potential.

Substituting the expression of atom potential (3.1) in the formula for the continues plane potential (2.2), and integrating over y, z and thermal displacement of

atom in the x direction u_x, one can obtain the expression for the continues potential of one atomic plane:

$$U_{1\,\mathrm{p}}(x) = \frac{2\pi\, n_{\mathrm{el}}\, Z\, e^2\, R_{\mathrm{TF}}\, d_{\mathrm{p}}}{a_{\mathrm{el}}^2} \sum_{i=1}^{3} \frac{\alpha_i}{2\beta_i}\, e^{\beta_i^2\, \overline{u_x^2}^2/(\,2R_{\mathrm{TF}}^2)} \times$$
$$\times \left(e^{-\beta_i\, x\,/R_{\mathrm{TF}}}\ \mathrm{Erfc}\left(\frac{\beta_i\, \overline{u_x^2}/\,R_{\mathrm{TF}} - x/\,\overline{u_x^2}}{\sqrt{2}} \right) + \right.$$
$$\left. + e^{\ \beta_i\, x\,/R_{\mathrm{TF}}}\ \mathrm{Erfc}\left(\frac{\beta_i\, \overline{u_x^2}/\,R_{\mathrm{TF}} + x/\,\overline{u_x^2}}{\sqrt{2}} \right) \right) \qquad (3.11)$$

where $\mathrm{Erfc}(z)$ is a complementary error function[1]; n_{el} is a number of atoms in a crystal elementary cell: $n_{\mathrm{el}} = 8$ for face-centered cubic (fcc) "diamond" lattice, i.e. for C, Si, Ge, and $n_{\mathrm{el}} = 2$ for body-centered cubic (bcc) lattice, i.e. for tungsten; a_{el} is the linear size of elementary cell (see Table 3.1).

Neglecting thermal vibrations of atoms in the lattice nodes with respect to interplanar distance ($2\sqrt{\overline{u_x^2}}/d_{\mathrm{p}} \sim 0.07 \ll 1$) the Eq. (3.11) can be simplified to the following:

$$U_{1\,\mathrm{p}}(x) = \frac{2\pi\, n_{\mathrm{el}}\, Z\, e^2\, R_{\mathrm{TF}}\, d_{\mathrm{p}}}{a_{\mathrm{el}}^2} \sum_{i=1}^{3} \frac{\alpha_i}{\beta_i}\, e^{-\beta_i\, \sqrt{x^2}\,/R_{\mathrm{TF}}} \qquad (3.12)$$

Here one can see, that without screening effect ($R_{\mathrm{TF}} \gg d_{\mathrm{pl}}$) the plane potential would be constant.

Thus, it should be noted that, although the screening function decreases slower than Coulomb potential at the small distances (see Fig. 3.1), it plays an essential role at coherent scattering on crystal atoms. For instance, without screening effect there would be no planar channeling at all. This is, actually, the consequence of Gauss law.

Figure 3.3 presents the distribution of continuous potential of crystal planes calculated with Eqs. (2.14) and (3.11) for different crystals. In the left plot there is a comparison of (110) plane potential of different crystals.

From the left plot one can see that the crystals with greater atomic number Z has a deeper potential well and hence, more particles can be captured in the channeling regime in case of nonparallel beam and/or in case of channeling in a bent crystal. Thus, in these cases, tungsten and germanium crystals should be more efficient than silicon and diamond. The disadvantage of tungsten is in its mosaic structure, i.e. it is impossible to make rather thick monocrystal from it. However, to achieve

[1] $\mathrm{Erfc}(z) = 1 - \frac{2}{\sqrt{\pi}} \int_0^z e^{-t^2}\, dt$

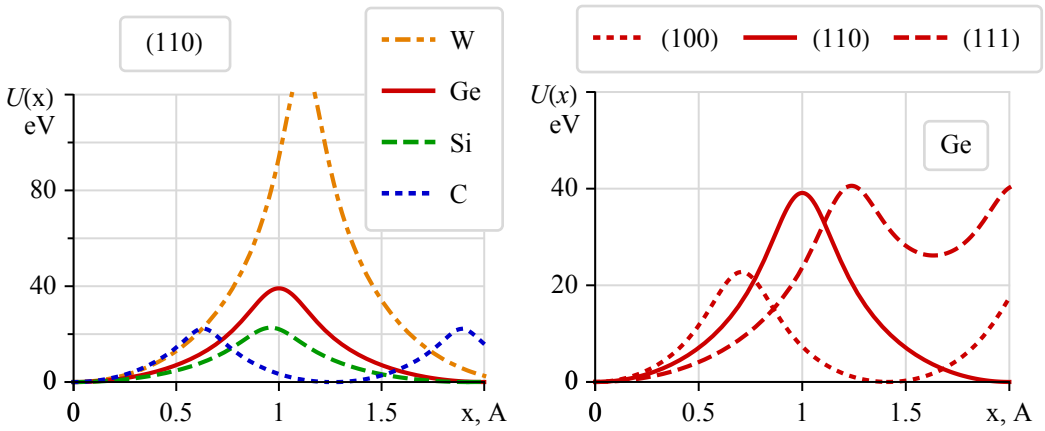

Figure 3.3: Crystal plane potentials $U_{\mathrm{p}}(x)$ using the Moliere approximation of single atom potential. On the left plot: comparison of (110) plane potentials of different crystals listed in the plot. On the right plot: comparison of potentials of different planes for germanium crystal.

maximal scattering on ultra-shot length (about 10 μm) tungsten would be the best material. The most commonly used crystals in channeling experiments is silicon, because it is much easier to produce a thick silicon monocrystal than germanium. Nevertheless, there is a growing interest in utilizing germanium crystals.

On the right plot in Fig. 3.3 there is a comparison of potentials of different planes of germanium crystal. We present the results only for germanium crystal, as diamond, silicon and germanium crystals have the same lattice structure ("fcc"-diamond) and these plots differ only by scale factors. The orientation (111) has a double plane structure, so there are two potential wells of different depths. Despite the fact that the first potential well of (111) plane is deeper than (110) plane, in case of thick crystal, particles captured in the second potential well of (111) plane leave the channeling regime with much faster rate due to a higher electron density in this interplanar space. Thus, after a certain thickness ($\sim$ 1 cm) the crystals with orientation (110) become more efficient than the ones with (111).

3.4 Parameterization of channeling efficiency in a bent crystal

The binary collision model is a powerful instrument that allows accurately describe different effects of particle interaction with crystal. The only downside of this model

is that it is quite time-consuming. The objective of our study is to find the phenomenological formula for the channeling efficiency as a function of particle energy and crystal bending radius.

Such a formula can be very useful for the calculation of channeling efficiency of the secondary particle beam produced in the fixed target as it has a huge energy spread (from almost zero to the value of incident particle beam).

The channeling efficiency or the efficiency of particle deflection η_{def} is the ratio of the number of particles which are captured in the channeling regime and deflected by the full angle of crystal curvature to the total number of particles impinging into the crystal. It can be expressed as:

$$\eta_{\text{def}} = \eta_{\text{acc}} \left(1 - \eta_{\text{dech}}\right), \tag{3.13}$$

where η_{acc} is the acceptance factor, i.e. the ratio of the number of particles which are captured into the channeling regime to the total number of incident particles, η_{dech} is the dechanneling probability. The acceptance factor in turn can be expressed as:

$$\eta_{\text{acc}} = \eta_{\text{ang}}\, \eta_{\text{ch}}, \tag{3.14}$$

where η_{ang} is the angular acceptance factor, i.e. the fraction of secondary particles produced in the narrow interval of angles $\theta_x \in (-\theta_{\text{acc}}, +\theta_{\text{acc}})$ that can be captured in the channeling regime, η_{ch} is the channeling acceptance factor. Further, we describe this terms in details.

3.4.1 Acceptance angle: θ_{acc}

The acceptance angle θ_{acc} is the maximal value of the angle between the particle momentum and the crystal plane, at which the particle can be captured into the channeling regime. This angle is analogous to the Lindhard angle (2.18) but with taking into account the crystal curvature. The value θ_{acc} is defined by the effective potential well of plane channel of bent crystal and it was calculated using continuous potential model. The dependence of acceptance angle on particle energy ε and crystal curvature radius R was fitted by the following expression:

$$\theta_{\text{acc}} = \sqrt{\frac{2\,U_{\text{eff}}}{\varepsilon}} \left(1 - \frac{\varepsilon}{R}\frac{1}{U'_x}\right) \tag{3.15}$$

where U_{eff} is a maximal value of plane potential taking into account thermal vibrations of atoms, U'_x is a gradient of the plane potential. The values of these parameters are listed in Table 3.2 and the dependence (3.15) is shown in Fig. 3.4.

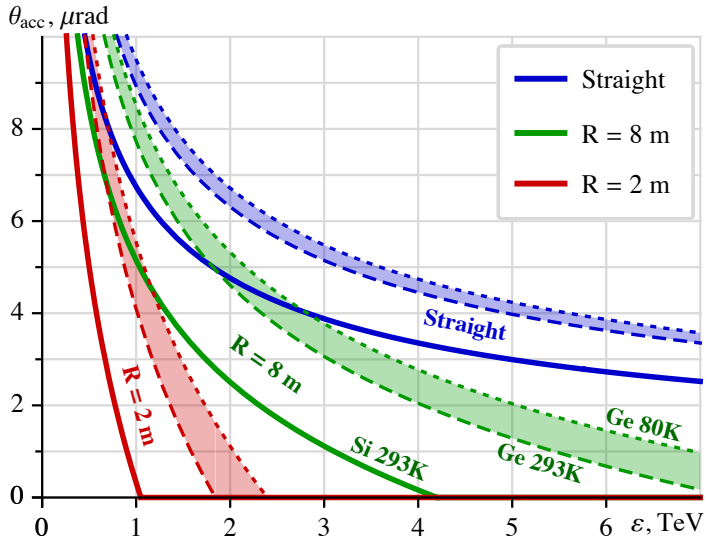

Figure 3.4: Acceptance angle as a function of energy of channeled particle in silicon crystals (solid curves) germanium crystals at room temperature (dashed curves) and cooled down to 80°K (dots). Blue curves are for straight crystals, green and red curves are for bent crystals with radii of curvature $R = 8$ m and 2 m, respectively.

As germanium has a rather small value of Debye temperature (see Table 3.1), cooling down the crystal leads to a significant decrease of amplitude of atom thermal oscillations in crystal nodes. Through this effect, cooling down the crystal to a liquid nitrogen temperature noticeably gains the deflection efficiency. For this reason, we also present the results for germanium crystal at 80°K (see upper margin of filled double curves in Figs. 3.4 and 3.5)

For a straight crystal ($R \to \infty$) the term in brackets is unity (see blue curves in Fig 3.4). For a bent crystal there is a critical value of the relation $\varepsilon/R = U_x'$, after which no particles can be captured in the channeling mode. This corresponds to a critical bending radius R_{cr} for a given energy. In the Figure 3.4 colors of the curves correspond to different curvature radii. These radii are critical for the energy values at which curves cross the abscissa axis. The negative values acceptance angle θ_{acc} (3.15) should be treated as zero.

Comparing the values of U_x' (see Table 3.2) one can see that the critical radius for the same energy for germanium crystal is about two times greater than for silicon. Hence, in terms of angular acceptance, it is of equal efficiency to use a twice thinner germanium crystal to deflect the particle on the same angle comparing to silicon one. And the efficiency would be even higher going further away from the R_{cr} to a soft part of the spectra (see Fig 3.4). Note that for the deflection of short-living particles this spatial benefit is essential.

Table 3.2: Parameters for the efficiency of channeling acceptance

Crystal	T, °K	$U_{\rm eff}$, eV	U'_x, TeV/m	$\eta_{\rm str}$	k_θ
Si	293	22.8	0.525	0.775	0.405
Ge	293	40.0	0.922	0.785	0.396
Ge	80	45.2	1.200	0.812	0.353

3.4.2 Channeling acceptance factor: $\eta_{\rm ch}$

In fact, the fulfillment of condition $|\theta_x| < \theta_{\rm acc}$ is not sufficient for particles to be captured into the channeling regime. It is also necessary for the channeled particle to have the negative energy of transverse motion with respect to the effective interplanar potential $U_{\rm eff}(x)$:

$$\varepsilon_{\perp\,\rm p}(\theta_x, x) = \frac{\varepsilon\,\theta_x^2}{2} + \; U_{\rm eff}(x) < 0, \tag{3.16}$$

where

$$U_{\rm eff}(x) = U^+(x) - U(d/2) - \frac{\varepsilon}{R}\;(x - d/2)\,, \quad \left(-\frac{d}{2} < x < \frac{d}{2}\right), \tag{3.17}$$

where x is the impact parameter with respect to the planar channel (see e.g., [50]). The centrifugal term $\varepsilon\, x/R$ in Eq. (3.17) describes the distortion of interplanar potential caused by the crystal curvature.

In addition to a wide energy range, the secondary particles produced in the fixed target usually have the Gaussian-like angular distribution with the width $\sim \gamma^{-1}$ corresponding to a particle energy. The ratio of acceptance angle $\theta_{\rm acc}$ to the width of angular distribution is quite small even for heavy baryons of high energies, e.g., for 7 TeV particle with mass ~ 5 GeV in a straight germanium crystal this ratio is

$$\gamma\,\theta_{\rm p} \sim \frac{\sqrt{2\,U_0\,\varepsilon}}{M} \approx 0.005. \tag{3.18}$$

For this reason, we consider the angular distribution of particles captured in the channeling regime as uniform. It is clear that the distribution over impact parameter x is uniform as well. Thus, the channeling acceptance factor can be written in the following form:

$$\eta_{\rm ch} = \frac{1}{2\,d_{\rm p}\,\Theta_{\rm acc}} \int\limits_{-\theta_{\rm acc}}^{\theta_{\rm acc}} \int\limits_{-d_{\rm p}/2}^{d_{\rm p}/2} \Theta_{\rm H}\left(-\varepsilon_{\perp\,\rm p}(\theta_x, x)\right)\; d\theta_x\, dx, \tag{3.19}$$

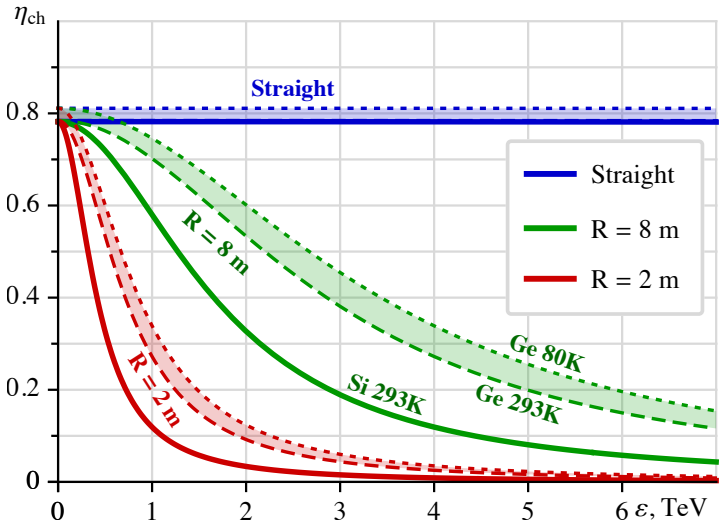

Figure 3.5: Channeling acceptance factor for uniform angular distribution over energy. Silicon crystals — solid curves, germanium crystals at room temperature — dashed curves and cooled down to 80°K — dots. Color represents the crystal curvature (listed on the right).

where Θ_{H} is the Heaviside function.

The value of channeling acceptance factor was calculated using the same approach as for the acceptance angle. Its dependence on particle energy ε and crystal curvature radius R was fitted by the following expression:

$$\eta_{\mathrm{ch}}(\varepsilon, R) = \frac{\eta_{\mathrm{str}}}{1 + \left(\dfrac{\varepsilon}{R}\,\dfrac{1}{U'_x\, k_\theta}\right)^2} \tag{3.20}$$

where η_{str} is the channeling acceptance factor for a straight crystal. For a parallel incident beam $\eta_{\mathrm{str}} = 1$, and in case of uniform angular distribution $\eta_{\mathrm{str}} \approx 0.77$–$0.82$; k_θ is a factor defined by plane potential and angular distribution of initial beam. The values of these parameters are listed in Table 3.2.

Figure 3.5 represents the dependence of channeling acceptance factor on particle energy ε and crystal curvature radius R. Note that for germanium crystal this factor is better than for silicon crystal, even for a crystal with twice smaller bending radius, what makes the germanium crystal preferable again.

3.4.3 Angular acceptance factor: η_{ang}

Angular acceptance factor η_{ang} is defined as the fraction of particles that are produced in the narrow interval of angles with respect to the crystal plane (zy):

$$\theta_x \in (-\theta_{\text{acc}}, +\theta_{\text{acc}}). \tag{3.21}$$

As the initial angular distribution of secondary particles produced in a fixed target is very close to the normal one with a standard deviation $1/2\,\gamma^{-1}$. If we align the crystal to a direction of primary particle beam the angular acceptance factor can be expressed as follows:

$$\eta_{\text{ang}} = \text{erf}\left(\sqrt{2}\ \theta_{\text{acc}}\,\gamma\right)\ \frac{\partial \text{N}_{\text{norm}}}{\partial\varepsilon} \tag{3.22}$$

where $\text{erf}(x)$ is the error function, $\partial N_{\text{norm}}/\partial\varepsilon$ is a normalized spectra of secondary particles.

3.4.4 Dechanneling probability: η_{dech}

At the motion of channeled particle through a crystal, there is an incoherent scattering on electron subsystem of a crystal and on thermal vibrations of the atoms at lattice nodes, that can lead to its dechanneling.

The dechanneling probability η_{dech} was calculated by means of Monte-Carlo simulation of particle passage through the crystal using a binary collision model of incident particle interaction with atoms of crystal lattice (see Section 3.1) and an aggregate collision model for taking into account scattering on electron subsystem of the atom (see Section 3.2).

The dechanneling probability is fitted by the following expression:

$$\eta_{\text{dech}}(\varepsilon, R, L) = 1 - e^{-\sqrt{\frac{L}{L_{\text{dech}}(\varepsilon,R)}}} \tag{3.23}$$

where L is a crystal length, $L_{\text{dech}}(\varepsilon, R)$ is a function of dechanneling length over particle energy and crystal bending radius; ε_{max} is a particle energy corresponding to maximal dechanneling length L_{max} for a given bending radius R:

$$L_{\text{dech}}(\varepsilon, R) = L_{\text{max}}\frac{\varepsilon}{\varepsilon_{\text{max}}}\ e^{1-\frac{\varepsilon}{\varepsilon_{\text{max}}}} \tag{3.24}$$

$$\varepsilon_{\text{max}} = R\ F_{\text{dech}},\ \ L_{\text{max}} = k_{\text{dech}} R \left(\frac{R_0}{R}\right)^{b_{\text{dech}}} \tag{3.25}$$

Table 3.3: Dechanneling parameters

Crystal	T,°K	k_{dech}	R_0, m	b_{dech}	F_{dech}, TeV/m
Si	293	0.0146	3.7	0.1	0.097
Ge	293	0.0130	3.3	0.2	0.137
Ge	80	0.0226	2.9	0.2	0.146

The parameters are obtained by fitting the results of computer simulations and indicated in the Table 3.3.

The germanium crystal at room temperature performs better than silicon, in terms of dechanneling length in the harder part of spectrum (see Fig 3.6). Additional benefit can be achieved by cooling down the germanium crystal.

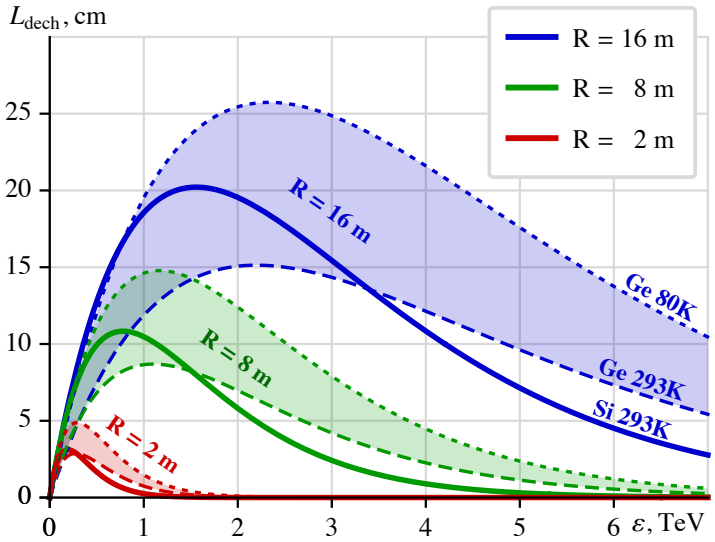

Figure 3.6: Dechanneling length over energy (for uniform angular distribution) for silicon and germanium crystals at room and cryogenic temperatures.

For Monte-Carlo approaches it is convenient to use the expression for the length at which a played particle leaves the channeling regime and starts to interact with a crystal like with an amorphous media,

$$L\left(L_{\text{dech}}, RND\right) = L_{\text{dech}} \ \ln^2\left(1 - RND\right) \tag{3.26}$$

where RND is a random value from 0 to 1.

The applicability of this parametrisation for massive particles (e.g. pions, protons, etc.) is in energy range from 80 GeV to 7 TeV, for electrons and positrons — from 400 MeV.

The model has been verified by comparing its results with the experimental data [51] (see Fig 3.7).

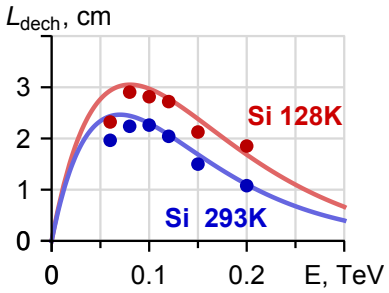

Figure 3.7: Dechanneling length over energy for silicon crystals at room temperature and 128°K. Curves — simulation results, circles — experimental data [51].

Chapter 4

Crystal parameters optimization for measuring Λ_c^+ MDM

4.1 Magnetic dipole moment of charmed baryons

The magnetic dipole moment (MDM) of a particle is its fundamental characteristic that determines the torque which particle experiences in an external magnetic field. The MDMs of many particles are presently known [1]. For electron the QED prediction agrees with experimentally measured value up to very high precision. For muon the measurement of the BNL E821 experiment [52] disagrees with the Standard Model prediction by 3–4 standard deviations, which may suggest physics beyond the Standard Model. The disagreement for the muon $g-2$ is the subject of many studies (see, *e.g.*, review [53]). The MDM of the τ-lepton has not been measured so far and is of great interest for testing calculations in the Standard Model [54].

For hadrons, the MDMs are measured for the baryon octet with $J^P = \frac{1}{2}^+$. Historically, reasonable agreement between the measured MDM and predictions of the quark model was important to substantiate the constituent quark models of the hadrons.

In general, the MDM of the spin-$\frac{1}{2}$ particle is expressed as

$$\vec{\mu} = \frac{2\mu}{\hbar}\vec{S}, \qquad \mu = \frac{q\hbar}{2mc}\frac{g}{2}, \tag{4.1}$$

where $\vec{S} = \frac{\hbar}{2}\vec{\sigma}$, m is the particle mass, q is the particle electric charge, g is the gyromagnetic factor. The value $g = 2$ corresponds to a Dirac particle without magnetic moment anomaly. Usually, the MDM of baryons is measured in units of

the nuclear magneton $\mu_N \equiv e\hbar/(2m_p c)$ [1], where m_p is the proton mass and e is the elementary charge.

It would be very important to measure the MDM of the charm baryons $\Lambda_c^+(udc)$ and $\Xi_c^+(usc)$, which have not been measured so far because of their very short lifetime of the order of 10^{-13} s.

There has been many calculations of the MDM of the charm baryons in various models of their structure [55–71]. As for the Λ_c^+ baryon, majority of the calculations predict the MDM and g-factor in the ranges

$$\frac{\mu(\Lambda_c^+)}{\mu_N} = 0.37\text{–}0.42, \qquad g(\Lambda_c^+) = 1.80\text{–}2.05. \tag{4.2}$$

Thus, an experimental study of the MDM of heavy baryons can be useful to distinguish between different theoretical approaches.

One of the motivations for measurement of the MDM of the heavy baryons is also studying the MDM of the charm quark. If this quark behaves as a point-like Dirac particle, then the corresponding gyromagnetic factor g_c is equal or close to 2, while if the charm quark has a composite structure we can expect a sizable deviation from this value.

In the quark model the MDM of the heavy baryon is expressed in terms of the MDMs of the heavy and light quarks. In particular, for the charm baryons, the spin and flavor structure of the ground-state baryons Λ_c^+ and Ξ_c^+ implies that (see, *e.g.*, Ref. [55])

$$\mu(\Lambda_c^+) = \mu_c, \qquad \mu(\Xi_c^+) = \frac{1}{3}\left(2\mu_u + 2\mu_s - \mu_c\right). \tag{4.3}$$

MDMs in Eqs. (4.3) depend on the MDM of the charm quark. Let us consider Λ_c^+ and take "effective" mass of the c-quark $m_c = 1.6$ GeV as suggested from the charmonia spectroscopy [55]. Keeping explicitly the g-factor of the charm quark we can write

$$\frac{\mu(\Lambda_c^+)}{\mu_N} = 0.39\frac{g_c}{2}, \qquad g(\Lambda_c^+) = 1.91\frac{g_c}{2}. \tag{4.4}$$

For $g_c = 2$ these values are consistent with Eqs. (4.2).

For Ξ_c^+ one needs to specify also the masses of the light constituent quarks. Choosing $m_u = 336$ MeV and $m_s = 509$ MeV, which reproduce MDMs of the baryon octet [72], one obtains from (4.3)

$$\frac{\mu(\Xi_c^+)}{\mu_N} = 0.83 - 0.13\frac{g_c}{2}, \quad g(\Xi_c^+) = 4.37 - 0.69\frac{g_c}{2}, \tag{4.5}$$

where the first numbers in each quantity in (4.5) come from the u and s quarks, and the second — from the c quark.

The combined measurements of MDMs of Λ_c^+ and Ξ_c^+ may help to obtain information on the g-factor of the charm quark.

In this chapter we discuss the feasibility of the MDM measurement for the positively charged charm baryons Λ_c^+ and Ξ_c^+ at the LHC. This extends the proposal of the UA9 collaboration [73].

4.2 Principle of measurement

The experimental results on MDM are all obtained by a well-assessed method that consists of measuring the polarization vector of the incoming particles and the precession angle when the particle is traveling through an intense magnetic field. The polarization is evaluated by analyzing the angular distribution of the decay products. No measurement of magnetic moments of charm or beauty baryons (and τ lepton) has been performed so far. The main reason is that the lifetimes of charm/beauty baryons are too short to measure the magnetic moment by standard techniques.

One proposal to meet the challenge of measuring the magnetic moments of baryons with heavy flavored quarks is to use the strong effective magnetic field inside the channels of a bent crystal instead of the conventional magnetic field to induce the precession of the polarization vector and measure the magnetic moment. Some theoretical aspects of this phenomenon with possible applications to the LHC have recently been discussed in [74], where the author carried out the preliminary estimations of the possibilities to measure MDMs of the short-lived particles, in particular, charmed baryons at the LHC energies. In Ref. [75] the authors suggested to use this method for studying the electric dipole moments (EDM) of the strange Λ baryon and the charm baryons.

The theoretical formalism of the precession of the polarization vector of spin-$\frac{1}{2}$ particle in external electric, $\vec{E}$, and magnetic, $\vec{H}$, fields has been known for a long time [**?**, 76–80]. In Refs. [50, 81–86] this formalism was applied to the case of the bent crystals.

In the planned fixed-target experiment at the LHC, the high-energy proton beam produces the polarized charm baryons by interacting with nuclei of a target-converter

$$p + A \to \Lambda_c^+(\Xi_c^+) + X, \tag{4.6}$$

which are directed into the bent crystal. The initial polarization vector $\vec{\xi}_i$ of the charm baryon is perpendicular to the reaction plane spanned by the proton and baryon momenta, $\vec{q}$ and $\vec{p}$, respectively, because of the space-inversion symmetry of the strong interaction.

When falling on a bent crystal, a small fraction of baryons gets in the regime of planar channeling (see, e.g., [50,84,87]). Note that only positively charged particles can be efficiently deflected by a bent crystal using planar channeling phenomenon. The planar channeling of negatively charged particles is very unstable due to the enhancement of their multiple scattering on lattice atoms (see, e.g., [88]). However, the negatively charged particle can be also deflected using the so-called stochastic mechanism of multiple scattering by atomic strings of a bent crystal. This mechanism was proposed in [85]. The possibility to use it for the MDM measurement was considered in [86].

The motion of channeled relativistic baryons in the interplanar electric field of a bent crystal imitates the particle motion in a strong magnetic field directed along the crystal bending axis (axis Oy in Fig. 4.1). The MDM vector of baryon rotates around this axis. The gradient of the interplanar electric field of a silicon crystal reaches the maximum value about 5 GeV/cm that corresponds to the value of the induction of effective magnetic field of thousands of tesla in the rest frame of a TeV baryon. The initial value of the 3D polarization vector can be determined using the non-channeled baryons. The absolute value of the polarization can be also measured as a by-product of this experiment. Various aspects of this analysis will be discussed later.

The first experimental realization of such method was carried out in Fermilab [2] at the 800 GeV proton beam. The strange $\Sigma^+(uus)$ baryons (with lifetime 0.8×10^{-10} s) produced on the Cu target had average momentum 375 GeV/c and the absolute value of polarization (12 $\pm$ 1) %. After passing 4.5 cm of the bent silicon single crystal the polarization vector precessed by about 60°. This new technique allowed to obtain the MDM of the Σ^+ hyperon $\mu = (2.40 \pm 0.46_{stat} \pm 0.40_{syst})\,\mu_N$ which was consistent with the world-average value.

The proposed experiment at the LHC is much more difficult because the lifetimes of the charm baryons Λ_c^+ and Ξ_c^+ are three orders of magnitude less than the lifetime of Σ^+. In order to measure the angle of MDM precession with sufficient accuracy and correspondingly extract the MDM at the LHC energies, it is necessary to carry out the optimization of target-converter and bent crystal parameters by means of detailed computer simulation as well as to study the properties of charm baryons as it is discussed in detail later.

4.3 Spin precession in a bent crystal. Master formulae

Because of the extremely short lifetime of charmed baryons in comparison with the Σ^+ hyperon, in our case it is not possible to prepare a beam of polarized baryons in advance and to measure the degree of their initial polarization, as was done in the Fermilab experiment [2]. In our case, as explained below, the crystal could be used as a beam collimator.

To be captured into the channeling regime, the incoming particle must have a very small angle θ_x between its momentum and the crystal plane of the chosen channel, namely, $|\theta_x| < \theta_{\rm acc}$, where $\theta_{\rm acc}$ is the acceptance angle (3.15). The axis Ox is perpendicular to the channel plane (see Fig. 4.1).

The Λ_c^+ baryons emitted from the amorphous target-converter are polarized and isotropically distributed over the azimuthal angle around the direction of the initial proton beam. The polar angle θ that determines the characteristic cone of the relativistic Λ_c^+ baryon emission in the laboratory frame has a value of the order of γ^{-1}, where $\gamma = \varepsilon/m$ is the Lorentz factor of the Λ_c^+, ε and m are its energy and mass, respectively. In the conditions of the LHC experiment $\theta \approx 10^{-3}$ rad.

The acceptance angle of planar channeling (3.15) for particles with the energy of several TeV in a silicon crystal is about several microradians, that is at least two orders of magnitude smaller than a characteristic angular width of the Λ_c^+ beam θ after the target–converter. Therefore, only a small part of this beam can be captured in the channeling regime when entering the crystal. For all channeled particles the angle θ_x is limited in the interval $(-\theta_{\rm acc}, +\theta_{\rm acc})$. At the same time, there are no limitations on the value of θ_y of the Λ_c^+ to be channeled.

Thus, the conditions for the particle capture into the planar channeling regime pick out by themselves the region in the phase space of the Λ_c^+ momentum with a certain direction of the polarization vector, namely, across the channeling plane (up or down in Fig. 4.1).

After passing the bent crystal the polarization vector rotates by the angle [82,83]

$$\Theta_\mu = \gamma \left(\frac{g}{2} - 1 - \frac{g}{2\gamma^2} + \frac{1}{\gamma} \right) \Theta \approx \gamma \left(\frac{g}{2} - 1 \right) \Theta, \tag{4.7}$$

with respect to the direction of the initial polarization vector. Here $\Theta = L/R$ is the deflection angle of the channeled baryon momentum after passing the bent crystal, L and R are the length and bending radius of the crystal.

In the conditions of the LHC the Lorentz factor γ can be quite big, of the order of 10^3. In this case the approximate equality in (4.7) holds (unless incidentally the relation $g = 2$ happens).

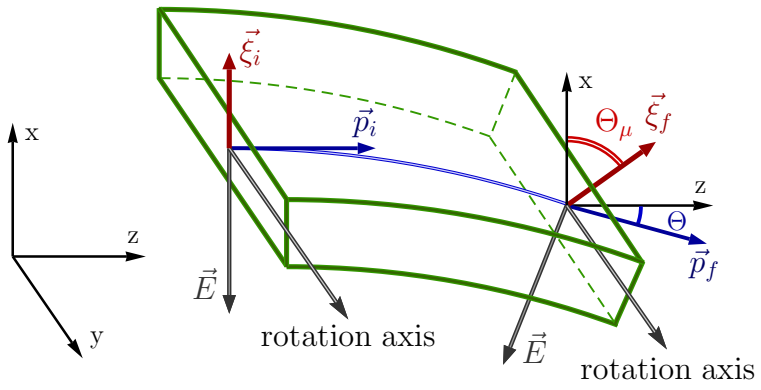

Figure 4.1: Schematic layout of experiment. Effective electric field $\vec{E}$ is orthogonal to the momentum $\vec{p}$. The figure shows the case $g > 2$.

The schematic layout of the experiment is shown in Fig. 4.1. To simplify the following formulae and for better understanding the experiment layout, here we consider Λ_c^+ baryons to be parallel to the z axis. In our further calculations we take into account the proper angular distribution of baryons at the entrance into the crystal.

In this frame the components of the proton momentum $\vec{q}$, baryon initial $\vec{p}_i$ and final $\vec{p}_f$ momenta, effective electric field $\vec{E}_i$ and $\vec{E}_f$ in the crystal, rotation axis along $\vec{E} \times \vec{p}$, and the initial $\vec{\xi}_i$ and final $\vec{\xi}_f$ polarization vectors are:

$$\begin{aligned}
\vec{q} &= (0,\, q_y,\, q_z), \\
\vec{p}_i &= p\,(0,\, 0,\, 1), \qquad \vec{p}_f = p\,(-\sin\Theta,\, 0,\, \cos\Theta), \\
\vec{E}_i &= E\,(-1,\, 0,\, 0), \quad \vec{E}_f = E\,(-\cos\Theta,\, 0,\, -\sin\Theta), \\
\vec{E} \times \vec{p} &= E\,p\,(0,\, 1,\, 0), \\
\vec{\xi}_i &= \xi\,(1,\, 0,\, 0), \qquad \vec{\xi}_f = \xi\,(\cos\Theta_\mu,\, 0,\, \sin\Theta_\mu).
\end{aligned} \tag{4.8}$$

The absolute value of polarization $\xi = |\vec{\xi}|$ stays constant and is determined by the process (4.6).

4.4 Possible experimental setup for performing this experiment

In the last decade the UA9 Collaboration has developed the technology and more recently used it to demonstrate that bent silicon crystals can efficiently steer the

diffusive halo surrounding the circulating beam in the LHC, up to 6.5 TeV energy [89].

A scenario to deflect the halo particles in the vicinity of an interaction region of LHC is currently under study. The deflected particles should be kept in the vacuum pipe and will follow trajectories well distinct from those of the circulating beam core. Inserting a target in the pipe, the deflected halo can be efficiently used for fixed-target physics. An additional absorber should intercept halo particles not interacting with the target, thereby allowing the possibility of fixed-target operation in parasitic mode. In particular, by directing the deflected halo into another bent crystal tightly packed with a short and dense target, located in the LHC pipe just before an existing detector, living baryons should be produced and their polarization may be measured from the analysis of the decay products. As an example, a preliminary optical layout compatible with the existing installations in IR8 is presented [90, 91] and it is suggested to use the interaction zone close to the LHCb detector. The LHCb detector will be particularly well suited to perform this experiment and preliminary discussions are undergoing.

In addition an Expression of Interest [73] has been presented in October 2016 at SPSC proposing to perform preliminary studies of the double crystal setup in SPS. In March 2017 this proposal has been accepted by SPSC for the next two years and the experiment will be performed in 2017 and 2018.

4.5 Absolute statistical error of measured g-factor

The orientation of the baryon polarization vector after the crystal can be determined from the angular distribution of its decay products. For the weak decays of the spin-$\frac{1}{2}$ baryon into the two-particle final states of baryon and meson ($\frac{1}{2} \to \frac{1}{2} + 0$, $\frac{1}{2} \to \frac{1}{2} + 1$, $\frac{1}{2} \to \frac{3}{2} + 0$) the following relation holds

$$\frac{1}{N}\frac{dN}{d\cos\vartheta} = \frac{1}{2}(1 + \alpha\,\xi\cos\vartheta), \tag{4.9}$$

in the rest frame of the baryon. Here N is the number of events, ϑ is the angle between the direction of final baryon (analyzer) and the polarization vector $\vec{\xi}_f$. The weak-decay parameter α characterizes parity violation in the decay.

From the angular analysis one can obtain the expression for the absolute statistical error of the measured g-factor:

$$\Delta g = \frac{1}{\alpha\,|\xi|\,\gamma\,\Theta}\,\sqrt{\frac{12}{N_{\Lambda_c}}}, \tag{4.10}$$

where N_{Λ_c} is the number of reconstructed Λ_c^+ deflected by a bent crystal. Note that Eq. (4.10) is obtained for a fixed value of boost γ.

For this analysis we decide to consider only the Λ_c^+ baryons which decayed after having passed the full length of the crystal. The number of reconstructed Λ_c^+ that were produced in the target and deflected by a bent crystal can be expressed as follows:

$$N_{\Lambda_c} = \Phi \; t \; \eta_{\text{det}} \; \frac{\Gamma_j}{\Gamma} \; N_{\text{tar+crys}}, \tag{4.11}$$

where $N_{\text{tar+crys}}$ is the number of deflected Λ_c^+ per one proton impinging the target:

$$N_{\text{tar+crys}} = \int \eta_{\text{def}} \; e^{-\frac{L_{\text{crys}}}{c\tau\gamma}} \; d\varepsilon. \tag{4.12}$$

Here η_{def} can be obtained using Eqs. (3.13), (3.14) and (3.22), in which instead of normalized spectra of secondary particles $\partial N_{\text{norm}}/\partial\varepsilon$ we use the Λ_c^+ energy distribution after the target $\partial N_{\text{tar}}/\partial\varepsilon$:

$$\frac{\partial N_{\text{tar}}}{\partial\varepsilon} = \rho \, N_{\text{A}} \, \sigma_{\Lambda_c} \, \frac{A_{\text{tar}}}{M_{\text{tar}}} \, \frac{\partial N}{\partial\varepsilon} \int\limits_0^{L_{\text{tar}}} e^{-\frac{L}{c\tau\gamma}} \; dL. \tag{4.13}$$

Then, taking into account the energy distribution of Λ_c^+, we obtain the expression

Table 4.1: List of notations in Eqs. (4.11)–(4.14).

Terms in Eqs. (4.11)–(4.14)	Values	Units
Proton flux, Φ	5×10^8	s^{-1}
Time of data taking, t	$\sim 10^6$	s
Detection efficiency, η_{det}	0.03	-
Deflection efficiency, η_{def}	(see Sec. 4.5.6)	-
Crystal length, L_{crys}	4–20	cm
Λ_c^+ decay length, $c\tau$	60.0	μm
Lorentz factor of Λ_c^+, γ	500–2000	-
Normalized production spectra, $\frac{\partial N}{\partial \mathcal{E}}$	(see Fig. 4.3)	TeV^{-1}
Cross section (p+N→Λ_c^++...), σ_{Λ_c}	13.6 ± 2.9	μb
Target density, ρ	19.25	gr/cm^3
Avogadro number, N_{A}	6.022×10^{23}	mol^{-1}
Nucleon number of target, A_{tar}	183.84	-
Molar mass of target, M_{tar}	183.84	gr/mol
Target thickness, L_{tar}	1	cm

for the absolute statistical error of measured g-factor:

$$\Delta g = \frac{1}{\alpha_j \, |\xi| \, \Theta} \sqrt{\frac{12}{\Phi \; t \; \eta_{\text{det}} \; \frac{\Gamma_j}{\Gamma} \; \int \frac{\partial N_{\text{tar+crys}}}{\partial \varepsilon} \, \gamma^2 \; d\varepsilon}}. \tag{4.14}$$

The definitions of different terms in Eqs. (4.11)–(4.14) and their values are given in Table 4.1 and discussed in the following sections. Here Γ_j/Γ and α_j are the branching fraction and weak-decay parameter for the j-decay mode of Λ_c^+, correspondingly.

4.5.1 Λ_c^+ initial polarization: ξ

The polarization of the Λ_c^+ baryons has been measured in the reaction of 230 GeV/c protons with a Copper target and gives $\mathrm{P}(\Lambda_c^+) = -0.65\,^{+0.22}_{-0.18}$ at transverse momentum $p_t > 1.2$ GeV/c [93] (the sign of the polarization is defined with respect to the normal to the production plane, $\vec{q}\times\vec{p}_i$). The E791 experiment [92] finds evidence for an increasingly negative polarization of Λ_c^+ as a function of p_t^2, in agreement with the model [94–96]. These data are shown in Fig. 4.2 together with fitted curves.

In the same plot we show the theoretical prediction in the so-called hybrid model [94] (for the process $\pi^- p \to \Lambda_c^+ X$) describing the Λ_c^+ polarization as a function of transverse momentum.

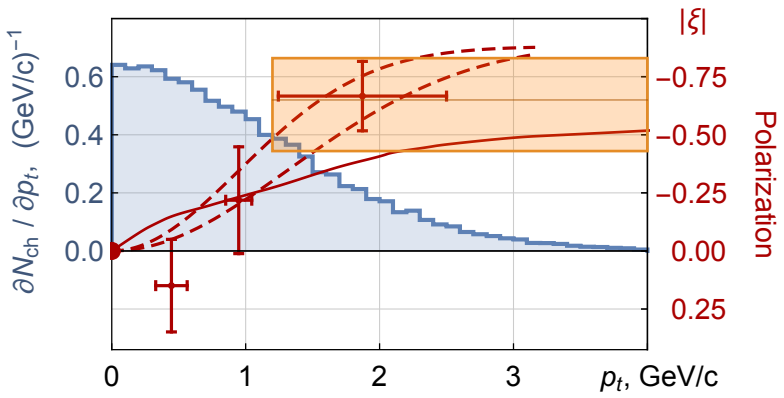

Figure 4.2: Polarization of Λ_c^+ as a function of its transverse momentum. Experimental data: red crosses [92], orange rectangular area [93]; dashed red curves — experimental data fit by the normal distribution; solid red curve — theoretical prediction by the so-called hybrid model [94] for the process $\pi^- p \to \Lambda_c^+ X$. Channeled baryons distribution over transverse momentum: blue histogram (simulation results obtained using Pythia8).

Using simulation code Pythia version 8.1 (Pythia8) [97] we show the transverse momentum distribution of channeled Λ_c^+ baryons (see blue histogram in Fig. 4.2).

By convolving the transverse momentum distribution and polarization curve as a function of transverse momentum we obtain the mean square value of Λ_c^+ polarization around -0.37 and -0.40 ± 0.05 for the theoretical prediction and experimental data, respectively.

No such measurements exist for the Ξ_c^+ baryons. It is also important to mention that the absolute polarizations of Λ_c^+ and of Ξ_c^+ as a function of transverse momentum could be measured by the proposed experiment.

In addition, they could also be measured by using the available data on beam gas interaction at the LHCb (SMOG data [98]).

4.5.2 Λ_c^+ weak-decay parameters: α_j

The weak-decay parameter α is the decay-channel-dependent quantity and it is compiled for various decay channels in case of the Λ_c^+ baryon in Table 4.2.

For the decay channels containing Λ or Σ^+ in the final states, the parameter α has been measured. The decay channel $\Lambda_c^+ \to p\,K^-\,\pi^+$ has a large branching fraction and it would be interesting to use this decay mode for the MDM measurement. The E791 experiment [92] reports measurements of the amplitudes for Λ_c^+ decay into nonresonant $p\,K^-\,\pi^+$ and to $p\,\overline{K}^*(890)^0$, $\Delta^{++}(1232)\,K^-$, and $\Lambda(1520)\,\pi^+$ modes. Using the measured amplitudes the values of the weak parameter α can be extracted with large errors as in [75]. It would be extremely important to perform this analysis using the LHCb data. On the other hand, no measurement of the α parameters exists in case of Ξ_c^+, and it would be important to measure these parameters in the LHCb experiments.

Table 4.2: Branching fractions Γ_j/Γ and weak-decay parameters α_j for different decay modes of Λ_c^+.

Channel	Fraction (Γ_j/Γ)	α_j	Source
$\Lambda_c^+ \to \Lambda(p\pi^-)\pi^+$	$1.07(28)\,\% \times 63.9(5)\,\%$	$-0.91(15)$	[1]
$\Lambda_c^+ \to \Lambda(p\pi^-)e^+(\mu^+)\nu_{e(\mu)}$	$2.0(6)\,\% \times 63.9(5)\,\%$	$-0.86(4)$	[1]
$\Lambda_c^+ \to pK^-\pi^+$	$(5.0 \pm 1.3)\,\%$	–	[1]
$\Lambda_c^+ \to \Delta(1232)^{++}(p\pi^+)K^-$	$0.86(30)\,\% \times 99.4\,\%$	$-0.67(30)$	[75]
$\Lambda_c^+ \to \overline{K}^*(892)^0(K^-\pi^+)\,p$	$1.6(5)\,\% \times 100\,\%$	–0.545(345)	[75]
$\Lambda_c^+ \to \Lambda(1520)(pK^-)\pi^+$	$1.8(6)\,\% \times 45(1)\,\%$	–0.105(604)	[75]

4.5.3 Λ_c^+ production cross section: σ_{Λ_c}

The center-of-mass energy for the fixed target experiment at the 7 TeV LHC proton beam is $\sqrt{s} = 115$ GeV and no measurements of the cross section of $p + A \to \Lambda_c^+ + X$ process (σ_{Λ_c} cross section) exist at this center-of-mass energy.

In [99] the Λ_c cross section has been estimated from the total charm production cross section or explicitly from the Λ_c cross section measured in three experiments at different center-of-mass energies: the PHENIX experiment in proton–proton collisions at $\sqrt{s} = 200$ GeV [100, 101], the LHCb Λ_c cross section measurement in pp collisions at $\sqrt{s} = 7$ TeV [102] and the measurements of the D mesons cross section performed in pA collisions at HeraB at a center-of-mass energy of $\sqrt{s} = 42$ GeV [103]. These three evaluations are compatible within less than 1.7 standard deviations. The spread of the values is explained by the poorly known total charm cross section, the poorly known Λ_c fragmentation function and the lack of experimental open charm data close to $\sqrt{s} = 115$ GeV.

For current analysis we took the weighted mean of the three values, $\sigma(\Lambda_c) = 13.6 \pm 2.9$ μb.

4.5.4 Λ_c^+ energy distribution: $\partial N_{\text{tar}}/\partial\varepsilon$

The Λ_c^+ produced in the target–converter will have a wide energy spectrum from zero to the energy of the incident proton. Low-energy Λ_c^+, constituting a majority of the produced particles, can not be deflected by a bent crystal at a sufficiently large

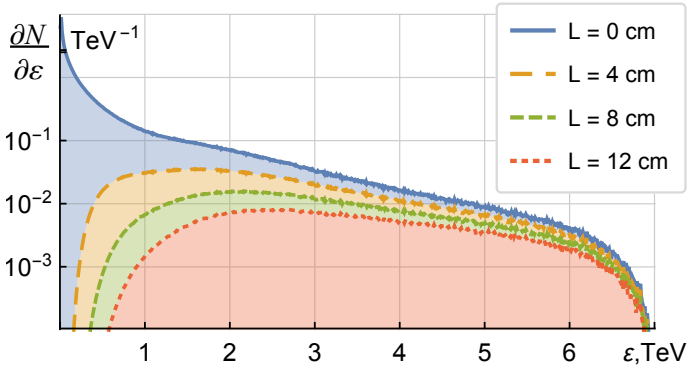

Figure 4.3: Energy distribution of Λ_c^+ baryons produced by 7 TeV protons in p-N collision in a fixed target normalized to one produced Λ_c^+ baryon. Solid blue curve is for the initial distribution ($L = 0$), dashed curves are for different distances from the production point (listed on the right).

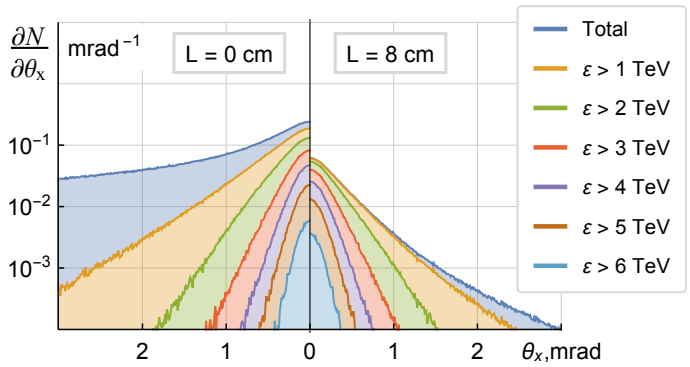

Figure 4.4: Angular distribution of Λ_c^+ baryons produced by 7 TeV protons in p-N collision in a fixed target normalized to one produced Λ_c^+ baryon. Solid blue curve is for the distribution integrated over the energy, other colors are for different regions of energy (listed on the right). On the left — at the production point ($L = 0$), on the right — at the distances ($L = 8$ cm).

angle to be used for measuring MDM, due to their rapid decay. The normalized energy distributions of baryons produced by a 7 TeV proton in a tungsten target of zero thickness are shown in Fig. 4.3. These results are obtained using Pythia8.

The simulation gives also the angular distribution of produced Λ_c^+ (see Fig. 4.4), which is important for the determination of the Λ_c^+ beam fraction that could be captured in the channeling regime in a bent crystal. For the energies higher than 0.5 GeV the distribution is very close to the normal one with a standard deviation $\approx \frac{1}{2}\,\gamma^{-1}$, that in the case of Λ_c^+ baryon energies of several TeV is of the order of milliradians.

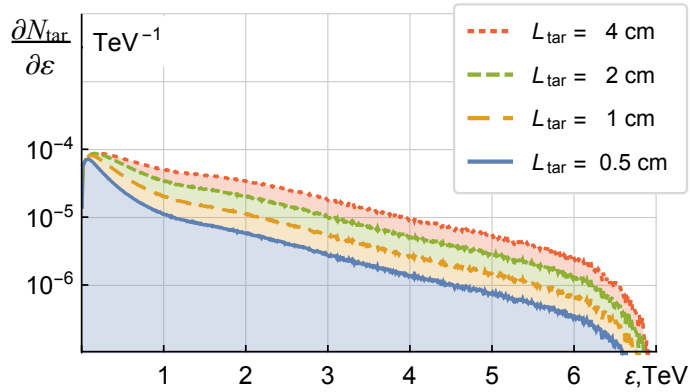

Figure 4.5: Spectra of Λ_c^+ baryons right after the tungsten targets of different thicknesses $L_{\rm tar}$ (listed on the right).

Figure 4.5 shows the Λ_c^+ differential energy distribution after the target (see Eq. (4.13)) for different target thicknesses with the parameters listed in Table 4.1 and the normalized spectra given in Fig. 4.3 for $L = 0$.

At high energies the number of Λ_c^+ is proportional to the target thickness. Furthermore, the specific ionization losses of TeV baryons in a tungsten target are about 40 MeV/cm and therefore can be neglected as well as the multiple scattering of the Λ_c^+ in the target, that gives a correction of the order of percent of the value of the characteristic angular width of Λ_c^+ production γ^{-1}. The main limitation would come from secondary particle production in the target. This should be carefully evaluated. For the present study we decide to use $L_{\rm tar} = 1$ cm.

4.5.5 Detector efficiency: $\eta_{\rm det}$

Many decay channels of the Λ_c^+ could be used: $\Lambda(p\pi^-)\,\pi^+$, $\Lambda\ell^+\nu_\ell$, $p\,\overline{K}^{*0}(890)$, or $\Delta^{++}(1232)\,K^-$. For the first two decay modes the weak-decay parameters α have been measured with a reasonable accuracy, while only preliminary measurement of the branching fractions and evaluations of the weak-decay parameter values are available for the other decay modes. A specific analysis should be performed for evaluating the detector efficiency for each of these channels. For the sensitivity studies we have decided to select two of these decay modes: $\Lambda(p\pi^-)\,\pi^+$ and $\Delta^{++}(1232)\,K^-$.

For a preliminary evaluation of the detector efficiency we take the LHCb as a reference detector, by considering typical trigger, acceptance, tracking and vertex reconstruction efficiency. In particular, due to the very energetic spectrum, the reconstruction of Λ baryon is rather complicated. In fact, the Λ present in the final states, can be very difficult to be detected since most of them could decay after passing the detector tracking volume. The efficiency of the $\Lambda(p\pi^-)\,\pi^+$ decay channel has been evaluated to be in the range $\eta_{\rm det}(\Lambda(p\pi^-)\,\pi^+) = (1\text{–}3)\times 10^{-3}$. On the other hand, the decay mode $\Delta^{++}(1232)\,K^-$ seems to be more promising and a preliminary evaluation of the efficiency gives $\eta_{\rm det}(\Delta^{++}(1232)\,K^-) = (2\text{–}4)\,\%$. The other channels could be also used and a more precise evaluation of the detector efficiency should be the object of dedicated studies.

4.5.6 Deflection efficiency: $\eta_{\rm def}$

The efficiency of particle deflection is calculated using the approach developed in Section 3.2. In Fig. 4.6 we present the energy dependence of the following parameters:

- The efficiency of Λ_c^+ deflection η_{def}, i.e. the ratio of the number of Λ_c^+ captured into the channeling regime and deflected by the full angle Θ (without taking into account the decay) to the total number of Λ_c^+ impinging into the crystal.
- The acceptance factor η_{acc}, i.e. the ratio of the number of Λ_c^+ captured in the channeling regime to the total number of Λ_c^+ impinging into the crystal.
- The angular acceptance factor η_{ang}, i.e. the fraction of Λ_c^+ produced in the target-converter in the narrow interval of angles $|\theta_x| < \theta_{\text{acc}}$ that can be captured into a channeling regime.

The results of calculations of the angular acceptance factor η_{ang} and acceptance factor η_{acc} as functions of Λ_c^+ energy are presented by the dotted blue and dashed red curves in Fig. 4.6, respectively. Note that these factors have a quite different dependence on particle energy.

Solid black curves represent the deflection efficiency η_{def} of the crystal of length $L_{\text{crys}} = 8$ cm. The difference between the solid black and dashed red curves in Fig. 4.6 is caused by the dechanneling effect.

Figure 4.6 shows that a germanium crystal has better efficiency with respect to a silicon one and allows to keep more energetic Λ_c^+ which, in addition, are more efficient for the MDM measurement, see Eq. (4.14).

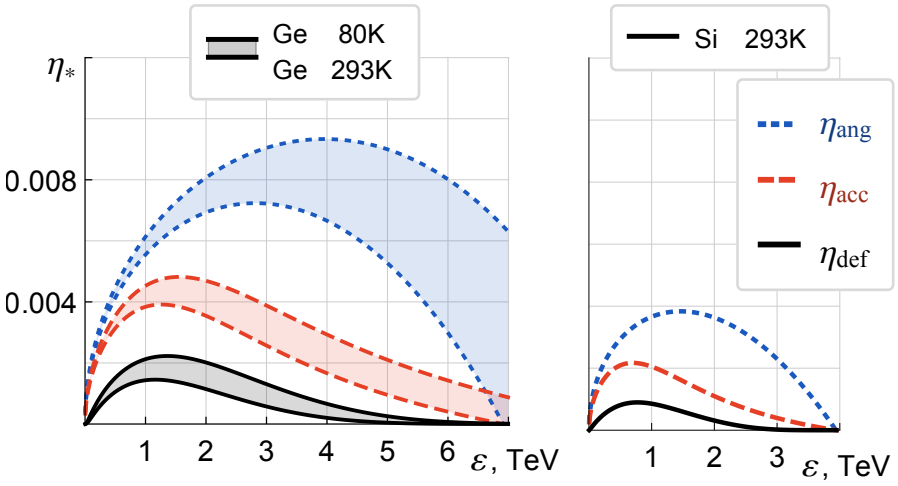

Figure 4.6: Angular acceptance factor η_{ang} (dotted blue curves), acceptance factor η_{acc} (dashed red curves), deflection efficiency of 8 cm bent crystal η_{def} (solid black curves) as functions of channeled particle energy in germanium (on the left) and silicon (on the right) crystals. Curvature radius is 7.5 m for all crystals.

4.5.7 Crystal parameters optimization

To obtain the optimal crystal parameters and to compare the efficiencies of silicon and germanium crystals we introduce the relative efficiency η_{rel} of the MDM precession measurement with respect to the efficiency of silicon crystal with $L_{crys} = 8$ cm and $R = 22$ m (further, the default crystal). This parameter corresponds to the ratio of data taking times needed to measure the g-factor with the same absolute error Δg (see Eq. (4.14)) for two different crystals:

$$\eta_{rel} = \frac{t_0}{t} = \frac{\Theta^2 \int \frac{\partial N_{\text{tar}}}{\partial \varepsilon} \eta_{\text{def}} \gamma^2 e^{-\frac{L_{\text{crys}}}{c\tau\gamma}} d\varepsilon}{\Theta_0^2 \int \frac{\partial N_{\text{tar}}}{\partial \varepsilon} \eta_{\text{def},0} \gamma^2 e^{-\frac{L_{\text{crys},0}}{c\tau\gamma}} d\varepsilon}. \tag{4.15}$$

Here, quantities with index "0" correspond to the default crystal.

In Fig. 4.7 the upper plot represents η_{rel} for silicon and germanium crystals at room temperature and for germanium cooled down to 80° K as a function of crystal

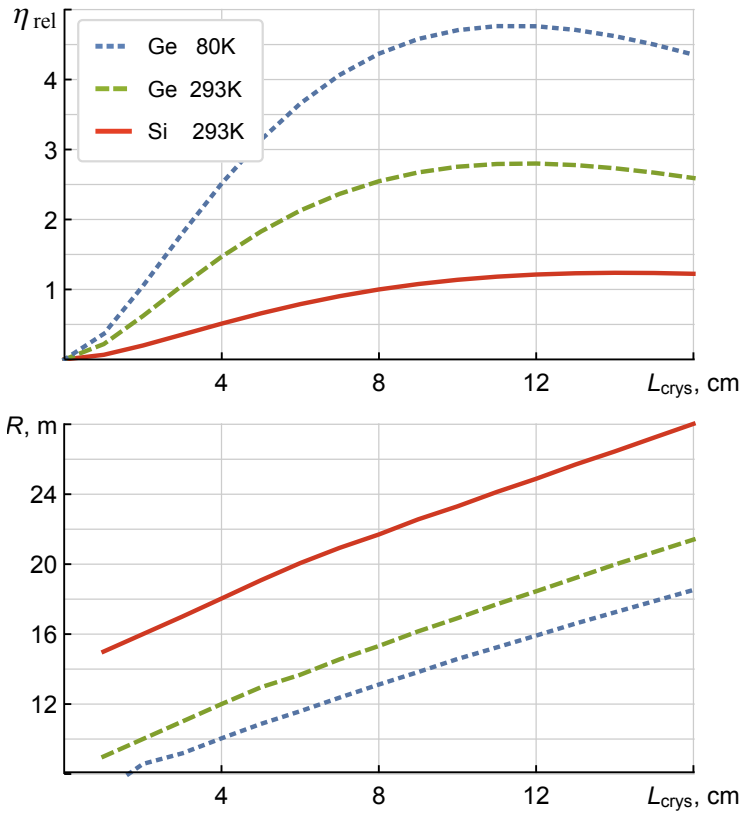

Figure 4.7: Relative efficiency of MDM precession measurement η_{rel} with respect to the efficiency of default crystal as a function of crystal length L_{crys} (upper plot). Optimal curvature radius R as a function of crystal length L_{crys} (bottom plot).

length L_{crys} calculated for the optimal curvature radius R (shown in the bottom plot).

The positions of maxima of curves in Fig. 4.7 (upper plot) correspond to the optimal crystal lengths. The bottom plot shows the optimal curvature radius R as a function of crystal length L_{crys}.

Note that η_{rel} depends only on target and crystal properties as well as the baryon energy distribution and decay time. Thus, the optimal crystal parameters can be found by maximizing this term for all decay channels at once. The applicability limit for this approach is that the detector efficiency η_{det} should not have a strong dependence on the Λ_c^+ baryon energy. In the opposite case decay parameters α and Γ_j and the detection efficiency η_{det} should be integrated together with the terms in Eq. (4.15) over the energy.

In Table 4.3 we give the results for the relative efficiency of the MDM precession measurement η_{rel} for three values of L_{crys}, both for silicon and germanium crystals.

In the table we also give the value for the number of deflected Λ_c^+ per incident proton $N_{\text{tar+crys}}$, which can be obtained by plugging η_{def}, $\partial N_{\text{tar}}/\partial\varepsilon$ and the decay factor in Eq. (4.12). Note that there is no direct relation between $N_{\text{tar+crys}}$ and η_{rel} as η_{rel} is also proportional to square of the deflection angle Θ^2 and square of Lorentz factor γ^2 of Λ_c^+. It is important to notice that the value $N_{\text{tar+crys}}$ is typically of the order of 10^{-8}.

For the sensitivity analysis we choose a silicon crystal at room temperature with $L_{\text{crys}} = 8$ cm and $R = 22$ m.

As follows from Table 4.3, the use of germanium crystal at room temperature increases the efficiency by a factor 2.5 (for a germanium crystal cooled down to 80° K this factor is 4.4).

To provide this measurement at the LHCb the deflection angle Θ should be at least 15 mrad. Thus, we performed the calculation to find how much the data taking time should be increased η_{rel}^{-1} with respect to the default crystal case ($\Theta \approx 0.0036$) to meet the same precision on g-factor.

In Table 4.4 we give the results for the relative efficiency of MDM measurement η_{rel}^{-1} for four values of L_{crys} both for silicon and germanium crystals. Curvature radii R are chosen to obtain the deflection angle $\Theta = 0.015$ (except for the first row that represents the default crystal with $\Theta \approx 0.0036$).

Table 4.3: Optimal crystal parameters: $L_{\rm crys}$ and R

	$L_{\rm crys}$, cm	R, m	Θ, mrad	$N_{\rm tar+crys}$	$\eta_{\rm rel}$
Si @ 293°K	4	18	2.2	3.2×10^{-8}	0.5
	8	22	3.6	1.6×10^{-8}	1.0
	12	25	4.8	0.9×10^{-8}	1.2
Ge @ 293°K	4	12	3.3	4.0×10^{-8}	1.5
	8	15	5.3	1.9×10^{-8}	2.5
	12	18	6.7	1.1×10^{-8}	2.8
Ge @ 80°K	4	10	4.0	4.8×10^{-8}	2.5
	8	13	6.2	2.5×10^{-8}	4.4
	12	16	7.5	1.5×10^{-8}	4.8

Table 4.4: Optimal crystal radius of curvature R for Θ =15 mrad

	$L_{\rm crys}$, cm	R, m	Θ, mrad	$N_{\rm tar+crys}$	$\eta_{\rm rel}^{-1}$
Si @ 293°K	8	22.0	3.6	1.5×10^{-8}	1
Si @ 293°K	8	5.3	15	4.1×10^{-10}	216
	12	8.0		5.1×10^{-10}	80
	16	10.7		5.4×10^{-10}	45
	20	13.3		5.3×10^{-10}	32
Ge @ 293°K	8	5.3	15	1.9×10^{-9}	22
	12	8.0		2.1×10^{-9}	11
	16	10.7		1.9×10^{-9}	7.6
	20	13.3		1.6×10^{-9}	6.6
Ge @ 80°K	8	5.3	15	4.2×10^{-9}	8.2
	12	8.0		4.3×10^{-9}	4.3
	16	10.7		3.8×10^{-9}	3.2
	20	13.3		3.1×10^{-9}	3.1

4.5.8 Estimation on data taking time

The absolute statistical error of g-factor was calculated using the formula (4.14) with the parameter values described above in this section and listed in Tables 4.1 and 4.2.

In Fig. 4.8 we show the evolution of the g-factor error using the most promising channel $\Delta^{++}(1232)\,K^-$ decay mode. The bands display different choice of absolute Λ_c^+ polarization, α parameters and Λ_c^+ cross section according to values and accuracy given in Tables 4.1 and 4.2. As it can be noted, the bands are quite large and depending on the values of several parameters entering this evaluation, the difference

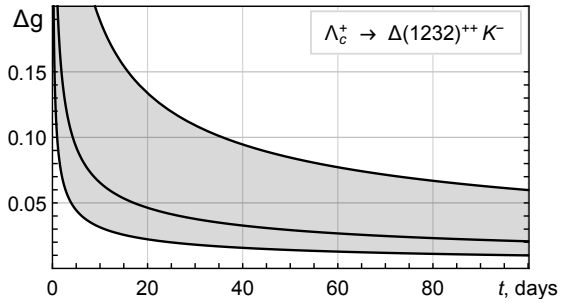

Figure 4.8: Error of the gyromagnetic factor g as a function of data taking time t for the $\Delta^{++}(1232)\,K^-$ decay mode using default crystal ($\Theta \approx 3.6$ mrad).

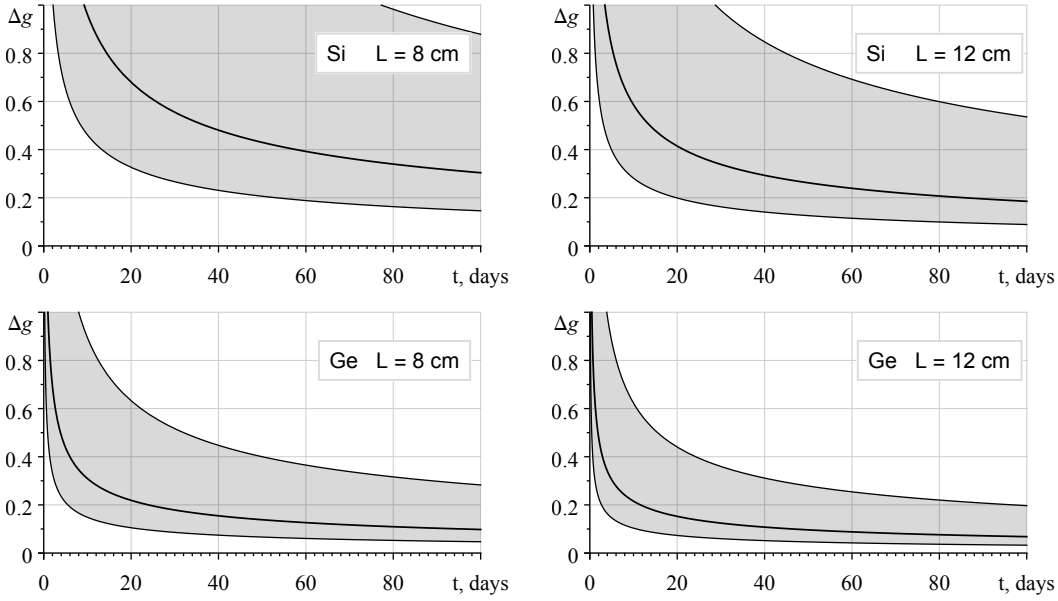

Figure 4.9: The same as in Fig. 4.8 but for various crystals with the deflection angle $\Theta = 15$ mrad. Note that the scale on Δg differs from the one in Fig. 4.8.

in terms of data taking time can be very significant. It is important to emphasize that the width of these bands is mainly coming from the uncertainty of the α parameter, Λ_c^+ initial polarization and Λ_c^+ cross section. Thus, it is extremely important to measure more accurately these parameters using, for instance, the existing LHCb data.

The results presented in Fig. 4.8 have been calculated for a default crystal, i.e. the silicon crystal at room temperature of length $L_{\text{crys}} = 8$ cm and radius of curvature $R = 22$ m. As explained in Section 4.5.7 and shown in Table 4.3, the data

taking time can be reduced by about a factor (2.5–4.8), if germanium crystal could be used.

On the other hand, to meet the requirements of LHCb the deflection angle have to be $\Theta = 15$ mrad, i.e. essentially greater than the optimal one (≈ 3.6 mrad).

The last column in the Table 4.4 $\eta_{\rm rel}^{-1}$ is a scaling factor of the time axis in Fig. 4.8 if we change the crystal. The time dependence of precision $\Delta g \sim 1/\sqrt{t}$ is the same for setups with different crystals. Nevertheless, as the scaling factor $\eta_{\rm rel}^{-1}$ is quite large we give the plots for $\Delta g(t)$ as a function of data taking time for various crystals in Fig. 4.9, to compare the efficiency of silicon and germanium crystals, with lengths of 8 and 12 cm.

Figure 4.9 shows that with $\Theta = 15\,$mrad a precision on g-factor of $\pm$ 0.1 could be reached within the time from ten days to about one year of data taking with the most probable time of about two months using germanium crystal with the length ($L_{\rm crys} = 12$ cm). Cooling down the germanium crystal (if possible) could reduce the time by a factor of two.

The use of a longer crystal (see the right plots in Fig. 4.9) reduces the data taking time needed to obtain the same Δg, due to the hardening of the deflected Λ_c^+ spectra (see Fig. 4.10).

Figure 4.10 shows the spectra of Λ_c^+ produced by the 7 TeV proton beam of a flux ($\Phi = 5{\times}10^8$ s^{-1}) during one day in 1 cm tungsten target and deflected by germanium and silicon crystals — dashed green and solid red curves, correspondingly. Thin and thick curves — for crystal lengths 8 and 12 cm.

Note that in current study so far we assume that the efficiency of the detector does not depend on the energy of decay products of Λ_c^+ ($\eta_{\rm det} = 0.03$). Figure 4.11 shows the spectra of decay products of Λ_c^+ statistics represented in Fig. 4.10, considering $\Delta^{++}(1232)\,K^-$ decay mode.

From the kinematics of decay process, the soft part of K^- spectra corresponds to a harder part of $\Delta(1232)^{++}$ (and hence p and π^+) spectra and vice versa. Thus, if there is a limit on detecting the energetic particles it will make the soft part of the spectra of the rest decay products unusable, hence, the useful part of the spectra would be in the middle.

From the figure 4.11 we make a conclusion that, if the detecting efficiency of particles with energies greater than 500 GeV (800 GeV) is much less than the efficiency of less energetic particles, it is better to use 8 cm instead of 12 cm long silicon (germanium) crystal. In any case, the use of germanium crystal should reduce the data taking time by a factor 3–10, depending on whether it is possible to detect energetic decay products.

The results obtained in this Chapter were published in [99]

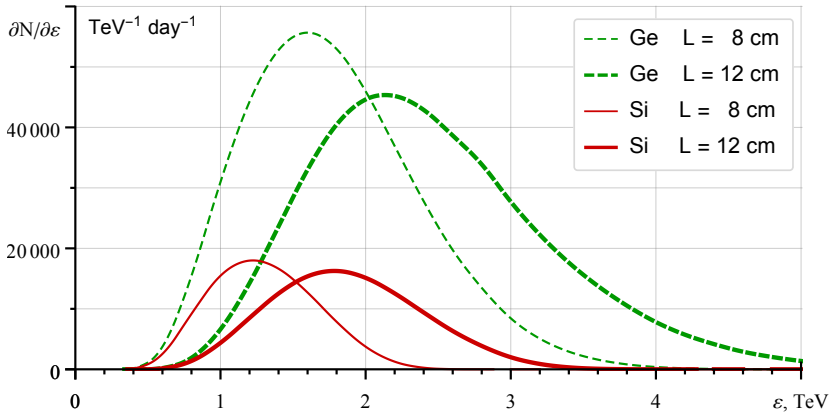

Figure 4.10: Spectra of Λ_c^+ deflected by various crystals (listed on the right).

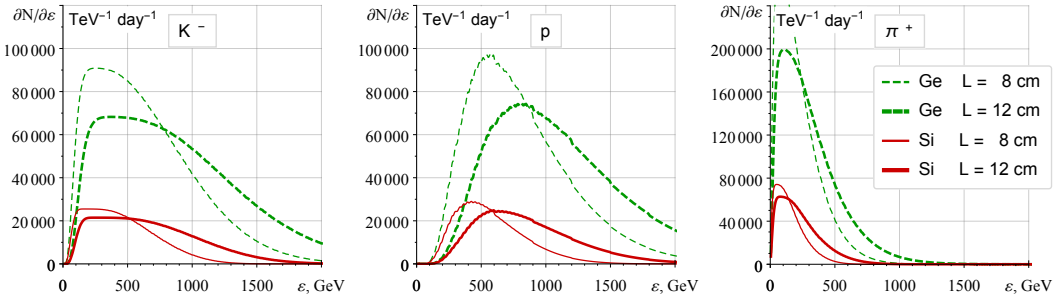

Figure 4.11: Spectra of decay products (K^-, p and π^+) of Λ_c^+ deflected by various crystals.

Chapter 5

Multiple scattering effects on radiation

5.1 Introduction

As it was shown in previous chapters, the correlations in consecutive collisions of fast charged particle with atoms of a crystal lattice can lead to a number of different effects in elastic scattering of the particle, among them the planar and axial channeling, the "doughnut scattering" effect and others. All these effects are the result of coherent effect at particle scattering on aggregate of atoms at consecutive multiple collisions at the particle motion close to a one of main crystallographic directions (plane or axis).

It is obvious that coherent effects in the scattering of relativistic electrons and positrons in crystals should be manifested in some form also in their bremsstrahlung, which is determined by the scattering features of charged particles. Indeed, in the early 1950s Ferretti [104], Ter-Mikaelian [105] and Uberall [106] showed that when relativistic electrons fall at small angles to the crystallographic axes or planes, coherent and interference effects take place in the radiation by these particles. At certain conditions, this can lead to a significant (tens of times) exceeding the radiation intensity in some regions of spectrum in comparison with bremsstrahlung of these particles in an amorphous target of the same thickness. In these works the foundations of the theory of coherent bremsstrahlung (CB) in crystals were laid, many predictions of which were soon confirmed experimentally (see, e.g., [107–109]).

Practically at the same time Landau and Pomeranchuk [11] showed that multiple scattering of ultra relativistic electrons on atoms in an amorphous matter leads to the suppression of the soft part of radiation spectrum in comparison with the

predictions of the Bethe-Heitler theory of bremsstrahlung [110]. Unfortunately, at that time there were no accelerators of sufficiently high energy to be convinced of the existence of this effect. Attempts to observe this effect in cosmic rays could not give a sufficient statistics for satisfactory quantitative confirmation [111, 112]. It should be noted that the conditions of manifestation of both these effects is determined by the same parameter, namely, the coherence length (or the formation zone) of bremsstrahlung process [105] (see also [3, 4]). The coherence length is a one of the most important parameters determining the radiation features not only in crystalline or amorphous matter, but also other external fields such as a field of an undulator, a wiggler, a synchrotron, etc.

5.2 Bremsstrahlung and coherence length concept

5.2.1 Bremsstrahlung cross section

Bremsstrahlung is a second order effect of perturbation theory. Two Feynman diagrams describing the radiation process of an electron in an external field in the first Born approximation are shown in Fig. 5.1

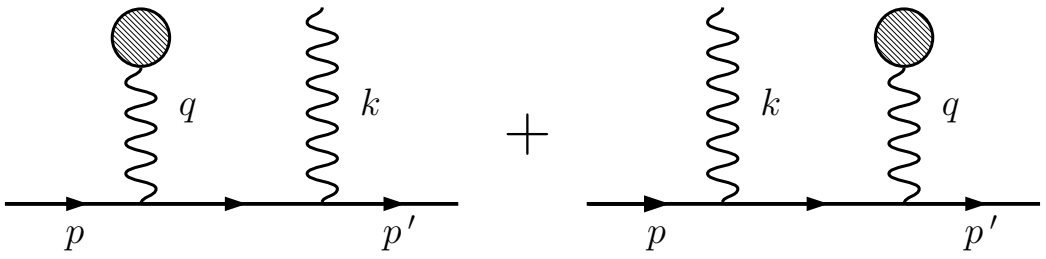

Figure 5.1: Feynman diagrams of radiation process of an electron in an external field.

Here p and p' are the 4-momenta of the initial and final electrons, k is the 4-momentum of the emitted photon and q is the 4-vector of the momentum transfer to the external field.

The corresponding differential cross section of the relativistic electron radiation in an external field $U(\vec{r})$ in the first Born approximation can be represented in the form [4, 113]

$$d\sigma^{(B)} = e^2\omega\, d\omega \frac{do\, do'}{4(2\pi)^4}\frac{p'}{p}|M_{\rm B}|^2|U_q|^2, \tag{5.1}$$

where ω is the energy of emitted photon, $\omega = |\vec{k}|$, $do = \sin\vartheta d\vartheta d\phi$ and $do' = \sin\vartheta' d\vartheta' d\phi'$ are elements of solid angles in the direction of the wave vector of the

radiated photon $\vec{k}$ and of the momentum of the particle in the final state $\vec{p}'$, $\vec{p}$ is the momentum of the initial electron. Here and below, we use the system of units, in which the velocity of light and the Planck constant are taken to be equal to one: $c = \hbar = 1$.

The matrix element of the electron transition from an initial state $\psi_i(\vec{r}, t)$ into a final state $\psi_f(\vec{r}, t)$ with the radiation of a photon, $M_{\rm B}$, according to the rules of the Feynman diagram technique can be written as [4, 113]

$$M_{\rm B} = \overline{u'} \left(\hat{e}^* \frac{\hat{f}' + m}{f'^2 - m^2} \gamma_0 + \gamma_0 \frac{\hat{f} + m}{f^2 - m^2} \hat{e}^* \right) u, \tag{5.2}$$

were $f' = p' + k$ and $f = p - k$ are intermediate 4-momenta, u and $\overline{u'}$ are bispinors of the radiating particle in the initial and final states defining by the corresponding Dirac equation.

U_q is the Fourier component of the potential energy of interaction of the electron with the external field $U(\vec{r})$

$$U_q = \int d^3r \, e^{i\vec{q}\vec{r}} U(\vec{r}), \tag{5.3}$$

If the potential energy of particle interaction with external field $U(\vec{r})$ does not depend on time, the corresponding 4-momentum conservation law for this process has the form

$$p = p' + k + q. \tag{5.4}$$

Taking into account the smallness of the typical values of the angles of scattering and radiation of a relativistic electron in the field of an atom, after the standard procedure of the averaging over the spins of initial particles and summing over the spins of final particles and over polarizations of photons in (5.1) (see, e.g., [113]), one can obtain the following expression for the bremsstrahlung cross section in the term of momentum transfer $\vec{q}$, which is very convenient for further analysis and calculations [3, 4]

$$d\sigma = \frac{e^2}{4\pi^3} \frac{d\omega}{\omega} \, dq_z \, d^2q_\perp \frac{\delta}{m^2} \frac{q_\perp^2}{q_z^2} \frac{\varepsilon'}{\varepsilon} \left[1 + \frac{(\omega)^2}{2\varepsilon\varepsilon'} - 2\frac{\delta}{q_z} \left(1 - \frac{\delta}{q_z} \right) \right] |U_q|^2, \tag{5.5}$$

where q_z and $\vec{q}_\perp$ are the components of the momentum transfer parallel and orthogonal to the momentum of the initial electron $\vec{p}$, ε and ε' are the energy of the initial and final electrons and $\delta = \omega m^2 / 2\varepsilon\varepsilon'$. The transition from the variables (ϑ'^2, φ) in (5.1) to the variables $(q_z, \vec{q}_\perp^2)$ in (5.5) including integration of the cross sections over the angles radiation ϑ is described in detail in the books [3, 4].

The expression (5.5) has been obtained under the assumption of the relative smallness of the characteristic values of the transverse component of the momentum transfer $\vec{q}_\perp \ll m$. Note, that this region make the main contribution to the bremsstrahlung cross section for most of usually considered type of external field including the Coulomb field of the atomic nucleus.

In the region of large values of the momentum transfer, where $p \gg q_\perp \gg \delta$, following [4], the Born cross section of radiation (5.1) can be represented as the product of the radiation probability $dW(q_\perp)$ and the Born cross section of scattering of the particle in an external field

$$d\sigma^{(\mathrm{B})}(q_\perp) = dW(q_\perp) \cdot d\sigma_e^{(\mathrm{B})}(q_\perp), \tag{5.6}$$

where $dW(q_\perp)$ and $d\sigma_e^{(\mathrm{B})}(q_\perp)$ are defined by the formulae

$$dW(q_\perp) = \frac{2e^2}{\pi}\frac{d\omega}{\omega}\frac{\varepsilon'}{\varepsilon}\left\{\frac{2\xi^2\left(1+\frac{\omega^2}{2\varepsilon\varepsilon'}\right)+1}{\xi\sqrt{\xi^2+1}}\ln\left(\xi+\sqrt{\xi^2+1}\right)-1\right\}, \tag{5.7}$$

$$d\sigma_e^{(\mathrm{B})}(q_\perp) = \frac{1}{4\pi^2\hbar^4 v^2}\,|U_{q_\perp}|^2\; d^2q_\perp. \tag{5.8}$$

Here $\xi = q_\perp/2m$ and $U_{q_\perp} = \int dz\, d\vec{\rho}\, e^{i\vec{q}_\perp\vec{\rho}}U(\vec{r})$.

The Fourier component of the potential energy (5.3) for the Coulomb potential of an atomic nucleus is

$$U_q = \int d^3r\, e^{i\vec{q}\vec{r}}\frac{Ze|e|}{r} = \frac{4\pi Ze|e|}{q^2}, \tag{5.9}$$

where $Z|e|$ is the charge of the atomic nucleus.

For the screened Coulomb potential (3.1) it is

$$U_q = \int d^3r\, e^{i\vec{q}\vec{r}}\frac{Ze|e|}{r}\exp(-r/R) = \frac{4\pi Ze|e|}{q^2+R^{-2}}, \tag{5.10}$$

where $R = 0.885\cdot R_\mathrm{B}\cdot Z^{-1/3}$ is the Thomas–Fermi screening radius, and $R_\mathrm{B} = 1/me^2$ is the Bohr radius.

For the Moliere potential (3.1) which was used in previous sections of this thesis for the fast charged particle scattering simulation in a crystal, the Fourier component is

$$U_q = \int d^3r\, e^{i\vec{q}\vec{r}}\frac{Ze|e|}{r}\sum_{i=1}^{3}\alpha_i\exp(-\beta_i r/R) = \sum_{i=1}^{3}\alpha_i\frac{4\pi Ze|e|}{q^2+\beta_i R^{-2}}, \tag{5.11}$$

where $\alpha_i = (0.1; 0.55; 0.35)$ and $\beta_i = (6.0; 1.2; 0.3)$.

After integration in (5.5) and (5.6) over q_z and $q_\perp$ covering both ranges (low and high) of the transverse component of the momentum transfer, following the procedure described in [12], one can obtain the final expression for the cross section of a relativistic electron radiation in the screening Coulomb field of an atom.

$$\omega \frac{d\sigma_{BH}}{d\omega} = \frac{16Z^2e^6}{3m^2}\frac{\varepsilon'}{\varepsilon}\left[\left(1+\frac{3}{4}\frac{\omega^2}{\varepsilon\varepsilon'}\right)\ln\left(183Z^{-1/3}\right)+\frac{1}{12}\right], \tag{5.12}$$

This formula is known as the Bethe–Heitler formula [110] for the cross section of the electron radiation in the field of atom. This formula is obtained taking account of the tabulated values of the Thomas–Fermi screening function.

5.2.2 Coherence length: quantum treatment

The concept of the coherence length of radiation process was introduced into the bremsstrahlung theory by Ter-Mikaelian [3, 105], when he study the coherent and interference effects in the radiation of ultra relativistic electrons on atoms of crystalline lattice. It was the result of analysis of the bremsstrahlung cross section dependence on the momentum transferred. The structure of this dependence is visible from expression (5.5) when integrating it over the longitudinal and transversal components of the momentum transfer

$$\frac{d\sigma}{d\omega} \sim \int d^2q_\perp \int_\delta^\infty \frac{dq_z}{q_z^2} q_\perp^2 \left|U_q\right|^2. \tag{5.13}$$

It is obvious that the main contribution to the integral (5.13), and therefore to the bremsstrahlung cross section, gives the region of small values of the longitudinal momentum transfer q_z.

The lower limit at the integration over q_z in (5.13), designated by δ, is minimal value of the longitudinal momentum transfer determined by the 4-momentum conservation law (5.4) which could be rewritten in the three-dimensional form as

$$\begin{aligned} \varepsilon &= \varepsilon' + \omega, \\ \vec{p} &= \vec{p}' + \vec{k} + \vec{q}. \end{aligned} \tag{5.14}$$

Using the relativistic relation between the electron mass, momentum and energy $\varepsilon^2 = p^2 + m^2$, and supposing for simplicity that all particle momenta is parallel to the direction of the motion of initial electron (axis z), we obtain

$$q_{z\,\min} = p - p' - k = \sqrt{\varepsilon^2 - m^2} - \sqrt{\varepsilon'^2 - m^2} - \omega. \tag{5.15}$$

If the electron energy is high enough, $\varepsilon \gg m$, after the expansion in powers of m/ε in (5.15), we have

$$q_{z\,\min} \approx \varepsilon\left(1-\frac{m^2}{2\varepsilon^2}\right)-\varepsilon'\left(1-\frac{m^2}{2\varepsilon'^2}\right)-\omega=\frac{\omega m^2}{2\varepsilon\varepsilon'}\equiv\delta. \tag{5.16}$$

It is easy to verify that rejection of the assumption of parallelism of all momenta leads only to increasing the value of δ. Indeed, taking into account the smallness, in comparison with unity, of characteristic values of the scattering angle of relativistic electron $\vartheta_{\rm s}$, which is the angle between the vectors $\vec{p}$ and $\vec{p}'$, and the characteristic angle of photon emission $\theta \approx \gamma^{-1} = \varepsilon/m$, and using the corresponding expansions, one can obtain

$$q_z = p - p'\cos\vartheta_{\rm s} - k\cos\theta \approx \delta + \varepsilon'\frac{\vartheta_{\rm s}^2}{2} + \omega\frac{\theta^2}{2}. \tag{5.17}$$

The expression for transversal component of the momentum transfer $q_\perp$ can be also obtained from the laws of conservation of energy and momentum (5.14) in the same manner

$$q_\perp^2 = (\vec{p}'_\perp + \vec{k}_\perp)^2 = (\varepsilon'\vartheta_{\rm s})^2 + (\omega\theta)^2 + 2\,\varepsilon'\,\vartheta_{\rm s}\,\omega\,\theta\cos\phi', \tag{5.18}$$

where φ' is the angle between the planes $(\vec{p},\vec{k})$ and $(\vec{p},\vec{p}')$.

From expressions (5.17) and (5.18) imply that

$$q_z \geq \delta + \frac{q_\perp^2}{2\varepsilon}. \tag{5.19}$$

In accordance with the Heisenberg uncertainty principle, the minimum value of the longitudinal component of the momentum transfer $q_z = \delta$ must correspond to a certain spatial region along the momentum of initial electron

$$l \sim \frac{\hbar}{q_z}, \tag{5.20}$$

which is responsible for the main contribution to the process considered, as it was noted above when discussing the structure of the expression (5.5).

This length determines the size of space domain along the particle momentum, in which the interference phenomena are essential in the interaction of a particle with atoms of a medium. Ter-Mikaelian called it the coherence length of bremsstrahlung processes (see [3, 105]):

$$l_c = \delta^{-1} = \frac{2\varepsilon\varepsilon'}{m^2\omega}. \tag{5.21}$$

The typical values of the transversal component of the momenta transfer $q_\perp$, which gave the main contribution to the bremsstrahlung cross section (5.13) in the case of a screened atomic potential (3.1), lie in the interval $\hbar/R \leq q_\perp \leq m$. These values $q_{\perp\,\mathrm{eff}}$ are associated with the transversal distances responsible for the radiation, namely, the screening radius of the Coulomb field of atomic nuclear

$$\rho_{\mathrm{eff}} \sim \hbar/q_{\perp\,\mathrm{eff}} \leq R. \tag{5.22}$$

As follows from (5.21), the coherence length l_c grows quickly with the growth of the electron energy and, for sufficiently high energies, this length can exceed the distance between atoms in a medium. Note that the coherence length l_c depends essentially from the energy of emitted photon as well: the smaller the photon energy, the greater the coherence length (see (5.21)).

In 1953, Ter-Mikaelian paid attention to the fact [105] that in the case of ultra relativistic electron passing though a crystal at a small angle relative to one of the crystallographic axis or plane, the bremsstrahlung of this electron on the atoms located within the coherence length will have a coherent character. It means, that the bremsstrahlung cross section in such a case will be proportional to the square of the number of atoms within the coherence length, in contrast to the bremsstrahlung cross section in an amorphous medium.

Note that for a long time, there was an opinion that since the atoms in the amorphous medium are located chaotically, then the correlations between collisions of a fast electron with different ones are absent, and radiation in an amorphous medium is a simple sum of radiation on individual atoms, which is described by the Bethe–Heitler formula (5.12). In this case, the spectral density of bremsstrahlung in the amorphous target of thickness T can be obtained by simple multiplication of the Bethe–Heitler cross section(5.12) by the density of atoms n and the target thickness T

$$\frac{dE_{BH}}{d\omega} = \omega \frac{d\sigma_{BH}}{d\omega}\, n\, T. \tag{5.23}$$

Reference literature usually uses a representation of the spectral density of radiation in an amorphous target in terms of the so-called radiation length (see, e.g., [3,4,114])

$$X_0 = \frac{m^2}{4\, Z^2\, e^6\, n\, \ln(183\, Z^{-1/3})}. \tag{5.24}$$

In this case, the Bethe–Heitler formula for the radiation spectral density has a form

$$\frac{dE_{BH}}{d\omega} = \frac{4}{3}\frac{t}{X_0}\frac{\varepsilon'}{\varepsilon}\left(1 + \frac{3}{4}\frac{\omega^2}{\varepsilon\varepsilon'}\right). \tag{5.25}$$

There are a number of coherent and interference effects in the radiation of relativistic electrons and positrons in oriented crystals, including channeling radiation (see, e.g., [3,4]). The basic characteristics of these effects, in particular, the positions of the corresponding maxima in the electron radiation spectrum, are determined by the ratio of the coherence length l_c and the spatial parameters of a crystal lattice in the direction of the particle momentum.

Under the influence of the results on coherent bremsstrahlung in a crystal obtained by Ter-Mikaelyan [105], Landau and Pomeranchuk showed, that not only in a crystal, but also in amorphous medium the multiple collisions of high energy electron with atoms can leads to essential discrepancy with the prediction of the Bethe–Heitler theory of bremsstrahlung [11]. More detailed analysis of this effect is presented below in section (LPM effect). The coherence length of radiation is the key parameter of the LPM effect, as well.

Because Ter-Mikaelyan introduced the concept of coherence length using the Heisenberg uncertainty principle, it is widely believed in the literature that the corresponding effects are of a quantum nature. Let's show that the analogous concept of the coherence length arises quite naturally within the framework of classical electrodynamic, as well.

5.2.3 Coherence length: classical interpretation

The spectral-angular density of radiation of a charged particle in an external field is defined in the classical electrodynamics by the expression (see, e.g., [4, 115])

$$\frac{d^2E}{d\omega do} = \frac{e^2}{4\pi^2}\left|\vec{k}\times\vec{I}\right|^2, \tag{5.26}$$

where $\vec{k} = \omega\,\vec{n}$ is the wave vector in the direction of radiation $\vec{n}$, $do = \sin\theta\, d\theta\, d\phi$ is the element of solid angle along the unit vector $\vec{n}$ and

$$\vec{I} = \int_{-\infty}^{\infty} dt\, \vec{v}(t) e^{i(\omega t - \vec{k}\cdot\vec{r}(t))}. \tag{5.27}$$

Here $\vec{r}(t)$ is the trajectory of a particle in an external field $U(\vec{r})$, $\vec{v}(t) = \dot{\vec{r}}(t)$ is the velocity of the particle. Both of them are defined from the equation of motion [4,115]

$$\frac{d}{dt}\frac{m\vec{v}(t)}{\sqrt{1-\vec{v}^2(t)}} = -\nabla U(\vec{r}). \tag{5.28}$$

Moving in the field of an atom, ultra relativistic electron ($\gamma \gg 1$) scatters by this field on relatively small angles, $\vartheta_s \ll 1$, so, its trajectory in an amorphous

matter is close to a rectilinear. Let's consider first the radiation of electromagnetic waves by such an electron radiates in the forward direction ($\theta = 0$). In this case, the difference of phases $\Delta\Phi$ of the waves radiated by the electron within the time interval $\Delta t = (t,\, t + \Delta l/v)$ is equal to

$$\Delta\Phi = \omega\Delta t - k\Delta r(\Delta t) \approx (\omega - kv)\Delta t = \omega(1 - v)\Delta t \approx \omega\Delta t/2\gamma^2, \tag{5.29}$$

where $\Delta r(\Delta t)$ is the distance passed by the particle in time $\Delta t = \Delta l/v$. Here, for simplification, we neglect the scattering angle within time interval Δt: $\vartheta_{\rm s}(\Delta t) = 0$.

If $\Delta\Phi \gg 1$, the exponent in (5.26) has fast oscillations which gives almost zero contribution into the integral defining the spectral density of radiation (see (5.26) and (5.27)). Thus, the main contribution to the radiation gives the spacial region of the particle trajectory, for which the phases difference $\Delta\Phi$ in order of magnitude is equal to one. This distance can be treated as the formation zone of radiation process or the coherence length of radiation. Defining the coherence length $l_{\rm c}$ as the length at which $\Delta\Phi = 1$ we obtain

$$l_{\rm c} = \frac{2\gamma^2}{\omega}. \tag{5.30}$$

This expression for the coherence length $l_{\rm c}$ coincides with the expression for the $l_{\rm c}$ obtained earlier on the basis of the quantum mechanical description of bremsstrahlung process (see (5.21)), if in the last one we neglect the quantum recoil effect at radiation, i.e. put $\varepsilon' = \varepsilon$.

It is known, that the formula for bremsstrahlung in Classical Electrodynamics does not take into account recoil effect in radiation directly, but using additional equation for radiation losses (see, e.g., [4,115]). That is why, the classical describing the radiation processes is valid only for the relatively soft part of radiation spectrum of relativistic particles, namely, $\omega \ll \varepsilon$.

Thus, the formulae for the coherent length of radiation obtained both in the framework of Quantum and Classical Electrodynamics coincide in the region of the validity of the last one, therefore, there is no reason to consider effects connected to the coherent length as a quantum mechanical effects.

Let's consider the corrections to the simplest expression for the coherence length (5.30), which connected with necessity accounting the different possible angles of observation of radiation θ, the scattering of relativistic electron in an external field (e.g., aggregates of atoms in amorphous matter), as well as the influence of the polarization effect when the radiation takes place in the medium.

All these effects on the coherence length can be taken in account by more exact counting of the phase difference (5.29), namely

$$\Delta\Phi = \omega\Delta t - \vec{k}\cdot\Delta\vec{r}(\Delta t) \approx \omega(1 - v\sqrt{\varepsilon_\omega}\cos\theta\cos\vartheta_s)\Delta t, \tag{5.31}$$

where ε_ω is the dielectric permittivity of medium, $k = \omega\sqrt{\varepsilon}_\omega$. For relatively high energy of emitted photons, $\omega \gg \omega_p$, where ω_p is the plasma frequency (3.9), the dependence of the dielectric permittivity on the photon energy determines by formula

$$\varepsilon_\omega \approx 1 - \frac{\omega_p^2}{\omega^2}, (\omega \gg \omega_p). \tag{5.32}$$

The typical values of the radiation angle of the relativistic electron θ, as well as its scattering angle in the field of atoms ϑ_s are small in comparison with one. Therefore, $\cos\theta$ and $\cos\vartheta_s$ in (5.31) can be expanded in small values of the corresponding angles. Keeping only the first two terms of these expansions, adding the corresponding expansion of $\sqrt{\varepsilon}_\omega$ in power of ω_p/ω, we obtain

$$\Delta\Phi \approx \omega\left(\frac{1}{2\gamma^2} + \frac{\theta^2}{2} + \frac{\vartheta_s^2}{2} + \frac{\omega_p^2}{2\omega^2}\right)\Delta t. \tag{5.33}$$

Putting the phase difference $\Delta\Phi$ (5.33) equal to one, we obtain the corrections to the expression for the coherence length l_c caused by nonzero angle of radiation observation, particle scattering effect and medium polarization

$$l_c^* \approx \frac{2\gamma^2/\omega}{1 + \gamma^2\theta^2 + \gamma^2\vartheta_s^2 + \gamma^2\omega_p^2/\omega^2}, \tag{5.34}$$

Comparing (5.34) with (5.30), one can conclude that each term in the denominator of expression (5.34), becoming appreciably larger than unity, leads to a substantial reduction in the coherent length.

Taking into account the fact that the coherence length was introduced as a spatial region making the main contribution to the radiation, it can be expected that its substantial reduction will also lead to a noticeable decrease in the radiation intensity.

In fact, if the term $\gamma^2\theta^2$ in (5.34) becomes greater than one (this means that the observation angle of the radiation θ exceeds the value γ^{-1}), the radiation intensity in this direction rapidly decreases. This is confirmed by direct calculations of angular distribution of bremsstrahlung (see, e.g., [3, 4]).

In the soft region of radiation spectrum, where the photon energy ω is less than value $\gamma\omega_{\rm p}$, the last term in the denominator in (5.34) becomes greater than one. This also leads to decreasing of the coherence length, as it follows from (5.34). The corresponding effect of suppression of radiation due to the medium polarization was predicted and first described by Ter-Mikaelian in 1954 [116] (see also [3, 4]). This effect is know in literature under the different names, such as "dielectric suppression", "density effect" or "Ter-Mikaelian effect" [3, 4, 117–119], and it was experimentally proofed in a number of measurements (see, e.g., [117–119]).

Not only the condition for the appearance of this effect, namely,

$$\omega < \omega_{\rm TM} \equiv \gamma\omega_{\rm p}, \tag{5.35}$$

but even the factor of the dielectric suppression of radiation (TM effect) are the exactly the same as the factor of decreasing the coherence length [3, 4]:

$$\frac{dE_{\rm TM}}{d\omega} = \frac{dE_{\rm BH}}{d\omega} \cdot \frac{1}{1+\gamma^2\omega_{\rm p}^2/\omega^2}. \tag{5.36}$$

In the classical limit ($\omega \ll \varepsilon$), the Bethe–Heitler formula (5.25) obtained in the framework of quantum approach transforms to

$$\frac{dE_{\rm BH}}{d\omega} = \frac{4}{3}\frac{t}{X_0}. \tag{5.37}$$

Much more complicated is the problem of accounting the scattering effect on radiation. The condition for the appearance of this effect, as it follows from the expression for the coherence length (5.34), is

$$\gamma\vartheta_{\rm s} > 1. \tag{5.38}$$

If $\gamma\,\vartheta_{\rm s} \leq 1$, we have so called dipole regime of radiation, which describes by the Bethe–Heitler formula (5.25) for the entire energy range of the emitted photons, excluding the the soft part of the spectrum (5.35), where Ter-Mikaelian effect takes place.

In the opposite case, defined by inequality (5.38) and called the non-dipole regime of radiation, one can expect the suppression of the radiation due to the scattering effect.

The coherence length (5.30) grows very quickly with the particle energy growth and with the decrease of energy of the radiated photon, and can exceed the mean

value of the distance between atoms in amorphous matter. In this case, the relativistic electron has a multiple collisions with atoms within the coherence length of radiation l_c, and, at certain conditions, the root-mean-square angle of such a multiple scattering $\sqrt{\overline{\theta_l^2}}$ can become greater than γ^{-1}.

In 1953, Landau and Pomeranchuk showed [11], that multiple scattering in amorphous medium can leads to suppression of radiation in comparison with the corresponding result giving by the Bethe–Heitler formula of bremsstrahlung (5.25). The quantitative theory of this effect was developed later by Migdal [120, 121] (see also [3, 4, 12]). Nevertheless, many questions, both from the point of view of theory and experiment, remained open. Consideration of some of these problems, in particular, the effect of multiple scattering of ultrarelativistic electrons on the spectral-angular and polarization characteristics of bremsstrahlung in a thin layer of amorphous and crystalline matter is the subject of study in the subsequent sections of this part of the thesis.

5.3 LPM effect: theory and experiment

5.3.1 The LPM effect

To describe the effect of multiple scattering on bremsstrahlung, Landau and Pomeranchuk [11] used the formulae of classical electrodynamics for the spectral radiation density of a relativistic electron moving in an amorphous medium along a certain trajectory. For this purpose, the formula (5.26) for spectral-angular distribution of radiation, first of all, must be integrated over the solid angle do.

Then, assuming that the scattering angles of the fast electron within small intervals of time are small, and carrying out the corresponding expansions, they presented the trajectory of a relativistic electron as slightly different from the straight line, with subsequent averaging over the scattering angles. Simplifying the averaging procedure, they made some of inaccuracies, that did not allow them to obtain the correct quantitative result for the spectral radiation density, which would give the correct asymptotic behavior with increasing energy of the emitted photon, namely, the transition to the Bethe-Heitler result.

The correction of the Landau–Pomeranchuk method of calculations was done later in the works of Laskin, Mazmanishvili, Nasonov, and Shul'ga, [122–124] on the basis of the method of functional integration. The detailed analysis of different methods of calculation used for describing the LPM effect is presented in the book [12].

The main quantitative result of Landau and Pomeranchuk theory is the specific dependence of the spectral radiation density on the energy of emitted photons ω. In contrast to the classical limit ($\omega \ll \varepsilon$) of the Bethe–Heitler radiation spectrum (5.37), which does not depend on ω, the Landau–Pomeranchuk final formula contains such a dependence in the form [11, 12]:

$$\frac{dE_{\rm LP}}{d\omega} = \frac{e^2}{2}\sqrt{\frac{3\omega q}{2\pi}}\,t, \quad q = \overline{\vartheta_{\rm s}^2}/l_{\rm c}. \tag{5.39}$$

The quantitative theory of the multiple scattering effect on an electron radiation in an amorphous medium was developed by Migdal on the basis of the kinetic equation method [120, 121]. That is why this effect in literature very often named as the Landau–Pomeranchk–Migdal (LPM) effect.

The result of Migdal's theory describing the multiple scattering effect in the soft part of electron radiative spectrum (i.e., neglecting the quantum recoil effect at $\omega \ll \varepsilon$) can be presented with logarithmic accuracy in the following form [12, 120]:

$$\frac{dE_{\rm LPM}}{d\omega} \approx \frac{dE_{\rm BH}}{d\omega} \cdot \Phi_{\rm M}(s), \tag{5.40}$$

where $\Phi_{\rm M}(s)$ is the Migdal's function

$$\Phi_{\rm M}(s) = 24s^2 \left\{ \int_0^\infty dt\, \coth t\, e^{-2\,s\,t} \sin 2st - \frac{\pi}{4} \right\}. \tag{5.41}$$

The argument of this function, s, can be presented in the form

$$s = \frac{1}{2\sqrt{2}}\sqrt{\frac{\omega}{\omega_{\rm LPM}}}, \tag{5.42}$$

where

$$\omega_{\rm LMP} = 16\,\pi\, Z^2 e^4\, n\, m^{-4}\, \varepsilon^2\, \ln(mR), \quad s\,(\omega = \omega_{LPM}) \approx 0.3536. \tag{5.43}$$

The dependence of the Migdal function on the parameter s is presented in Fig. 5.2

As it is clearly seen from the Fig. 5.2, the value of parameter $\omega_{\rm LPM}$ in (5.42) determines the photon energy region $\omega < \omega_{\rm LPM}$, in which the multiple scattering influences radiation spectrum essentially.

If $\omega > \omega_{\rm LMP}$, the Migdal function is close to unity, and the spectrum of radiation in this case tends to the corresponding result of the Bethe–Heitler theory (5.37).

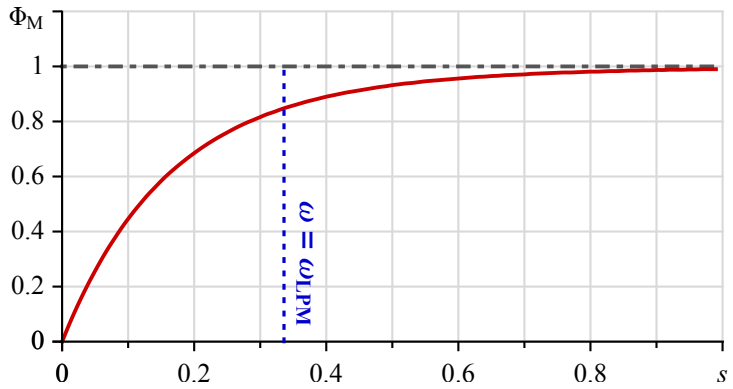

Figure 5.2: The Migdal function $\Phi_{\rm M}(s)$.

In the soft part of radiation spectrum, when $\omega \ll \omega_{\rm LMP}$, that means $s \ll 1$, the Migdal function (5.41) can be expanded in a series in powers of s, and the first term of this expansion is

$$\Phi_{\rm M}(s) \approx 6\, s. \tag{5.44}$$

This result is differ from formula (5.39) only by numerical coefficient.

The intensity of radiation in this case is much less, than the corresponding result given by the Bethe–Heitler formula (5.37)

$$\frac{dE_{\rm LP}}{d\omega} \ll \frac{dE_{\rm BH}}{d\omega} \tag{5.45}$$

5.3.2 SLAC experiment E-146

As it was already mentioned, in 1950s years, the accelerators of sufficiently high energy to verify the theoretical predictions concerning the LPM effect did not exist. The only possibility to observe this effect at that time was the cosmic rays detection. However, because of low statistics of such measurements, it was impossible to carry out the quantitative comparison of results of theoretical calculations with experimental data with a sufficient accuracy (see, e.g., [111,112]). The first attempt to make experiment using the secondary electron beam of 40 GeV proton accelerator was done at IHEP (Protvino, USSR) [125], but the statistic was also not enough for the quantitative verification of the theory.

The problem of experimental verification of the Migdal's theory becomes an actual again, when the energy of modern accelerators come up to the TeV range. It was not only the pure theoretical interest, but mainly the practical one. The

point is that at high energies, the LPM effect can substantially change not only the bremsstrahlung spectrum, but, as a consequence, the total radiation losses of ultra high energy particles in materials of detectors and radiation shielding for a new generation of accelerators and cosmic ray equipment. Such important concepts like the radiation length or the cascade length of electromagnetic showers in matter, begin to depend on the particle energy due to the LPM effect in contrast to their convenient treatment (see, e.g., [126, 127]).

To improve the exiting computer simulation codes like EGS 5, GEANT 3, GEANT 4 and others, which are widely used for such type of calculations, by including the LPM cross sections and other related parameters (see [128–130]), it was necessary first to verify the corresponding theoretical formulae. This was one of the main reasons of the special experimental investigation of bremsstrahlung process in different materials at the conditions of the LPM effect, which was carried out at SLAC in 1990s years.

The SLAC experiment E–146 was specially devoted to the verification of the Migdal quantitative theory of the LPM effect [120,121], which describes the suppression of radiation of relativistic electrons in an amorphous matter due to the multiple scattering on atoms. It was a big series of measurements using electron beam of SLAC Linac of two energies, 8 and 25 GeV [117–119,131–134]. The bremsstrahlung spectral density from the wide range of materials, starting from carbon and finishing by uranium, was measured in the diapason of gamma quanta energies from 200 keV up to 500 MeV. The targets of thicknesses from 0.1 % up to 6 % of radiation length was used for these measurements.

Generally, the analysis of the data obtained in SLAC experiment E–146 showed a good agreement between the results of calculations using the Migdal formula (5.40), which describe the LPM effect, and the experimental data for relatively thick (several % of the corresponding radiation length X_0 (5.24)) targets of heavy materials, from iron till uranium [117].

For the targets of rather light material, like carbon, the theoretical analysis of obtained results showed that the main mechanism of radiation suppression in the soft part of the spectrum (up to 75 % reduction) was the dielectric suppression (or "longitudinal density effect") [117–119], instead of the LPM effect (5.40). Thus, not only LPM effect, but also, predicted by Ter-Mikaelian [116], the dielectric suppression effect, described by formuls (5.36), was observed and studied in SLAC experiment E–146.

In the case of aluminum target both these effects, LPM and dielectric suppression, works together with comparable efficiency, as it follows from the comparison of

experimental data with results of calculations based on formulae of Migdal theory of the LPM effect (5.40) and (5.41), as well as Ter-Mikaelian's formula for the dielectric suppression effect (5.36). An analysis of the conditions for the manifestation of these effects, based on the previously discussed concepts of the coherence length (see the relations (5.34), (5.35) and (5.38)), confirms the "superposition" of these two effects in the considered region of the bremsstrahlung spectrum under the conditions of the E–146 experiment [117–119]. This again confirms the effectiveness of using the concept of coherence length for analyzing the influence of various factors on the bremsstrahlung process.

For the most soft part of the measured spectra (hundreds keV) there were observed the increasing of the spectral density of radiation, that caused by transition radiation contribution (see, e.g., [3, 135]). Because of the same physical nature of dielectric suppression effect and the transition radiation of relativistic electron crossing the vacuum-target boundary, namely, changing the own Coulomb field of the projectile particle in matter due to the polarization of the medium atoms (see, e.g., [136]), the threshold in emitted photon energy for both this effect is the same: $\omega < \gamma\,\omega_{\rm p}$.

For the target of more heavy materials, such as iron, lead, tungsten and uranium, the Migdal theory (5.40) gave rather good quantitative agreement with the experimental data (see [117, 119]). The reasons of such behavior of different mechanisms of the medium influence on radiation become clear below (in subsection 5.3.3) at the carrying out the comparative analyze of corresponding conditions for different target parameters and particle energies.

Thus, the main disagreements between the data obtained in SLAC experiment E–146 and the results of calculations in the framework of Migdal's theory of the LPM effect, which take place in the soft part of the measured gamma quanta spectrum, were eliminated by accounting "the contribution" of dielectric suppression effect and the transition radiation, and the experimental data for relatively thick (several % of the corresponding radiation length X_0 (5.24)) targets of heavy materials, from iron till uranium [117]. Some minor discrepancies remained even after these effects were taken into account.

However, in the case of golden target of 0.7 % of radiation length thickness X_0 there was a significant disagreement between theory and experiment for both 8 and 25 GeV electrons, which could not be explained by the effects mentioned above. In the first publications of the SLAC E–146 group, a special attention was devoted to this problem [132–134].

By analyzing all the parameters of these measurements, it was determined that in the case of golden target of 0.7 % X_0 thickness, there was realized the condition when

the coherence length of radiation exceeds the target thickness in the certain region of emitted gamma quanta energy. Such "unexpected" behavior of the radiation spectrum at low frequencies was named in [134] as "the edge effect" and firstly they tried to exclude it by subtraction procedure, because "no satisfactory theoretical treatment of this phenomenon" was found for that moment.

Actually, they found out the article of Ternovskii [137], in which the multiple scattering effect on bremsstrahlung in the finite thickness target was considered using the Migdal kinetic equation method. Remind, that this method was developed by Migdal for describing the bremsstrahlung in a boundless amorphous medium [120]. However, when the participants of the E–146 experiment group tried to use the Ternovskii formula to describe their "edge effect", they obtained the exceeding over the Bethe–Heitler result [110] instead of the expected suppression of radiation, and they wrote in [132] that this formula gives "unphysical result".

It should be noted, that the effect of the suppression of radiation in a thin layer of matter, exactly in the case $t \ll l_c$, was also considered earlier theoretically by Shul'ga and Fomin in [138] and [139] using very effective simplification of the formulae (5.26) and (5.27) for spectral-angular density of radiation (see for details section 5.4). In these works, the predicted effect of radiation suppression of in a thin layer of matter was discussed in details, including the specific behavior of the spectral density of radiation, namely, its strange logarithmic increase with increasing target thickness, and the possibility of physical interpretation of this effect on the basis of consideration of the space-time evolution of the radiation process by ultra relativistic electron in matter [139]. It was also stated there, that analogous effect of radiation suppression should take place in a thin aligned crystals.

In [140], it was shown, that "the unexpected" behavior of the radiation spectrum at low gamma quanta energies observed in SLAC experiment E–146 in the case of the golden target of $0.7\,\%\,X_0$ thickness, it was the direct confirmation of existence of predicted in [138] effect of the suppression of radiation in a thin layer of matter (see Fig. 5.3).

It was also shown in [140], that the so-called "unphysical result" obtained using the Ternovskii formula [137] is connected with the usage in this formula the asymptotic expression for a mean-square angle of multiple scattering, which is not applicable for the SLAC experiment E–146 conditions.

The observation of the above-mentioned discrepancy in SLAC experiment E–146 stimulated a new wave of theoretical investigations of the multiple scattering effect on radiation (see, e.g. [140–148]). The quantitative theory of the radiation suppression effect in a thin layer of matter was developed in these works using

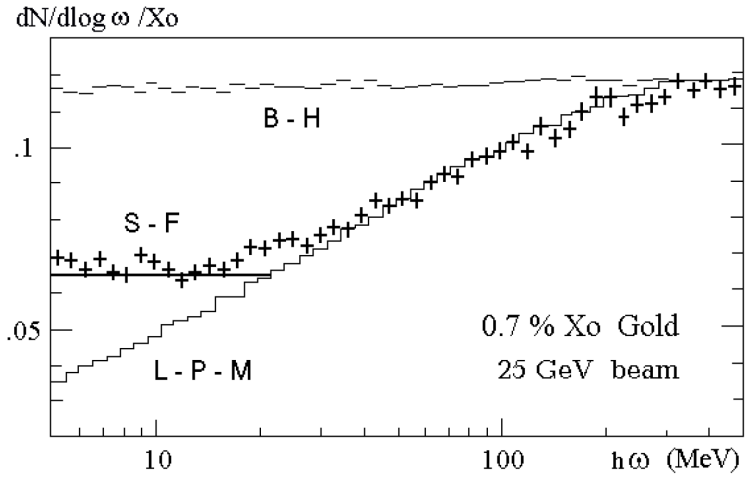

Figure 5.3: The spectral density of 25 GeV electrons radiation in the gold target of $0.7\,\%\,X_0$ thickness: crosses are the results of SLAC experiment E–146 [134], solid line is the result of calculations [140]

different approaches. The results obtained in these works are in a good agreement with the SLAC E–146 experimental data (see reviews [12, 117, 149]).

In fact, an apparent manifestation of the suppression of radiation in a thin layer of matter due to the multiple scattering effect in the SLAC experiment E–146 was observed only for the gold target of $0.7\,\%\ X_0$ thickness and 25 GeV electrons, and in a relatively narrow photon energy region: from 1 to 30 MeV. As it was already mentioned, there are two additional effects that have essential influence on radiation process in matter in the same photon energy region for 25 GeV electrons, namely, the dielectric suppression (or the Ter-Mikaelian effect) [3, 116] and the transition radiation from the target bounds [3, 135].

Thus, for the clear experimental observation and quantitative theoretical description of each effect it would be better to separate them in different spectrum regions of emitted photons, using for this purpose, different dependence of these effects on the main parameters of the task, and, first of all, their dependance on the particle initial energy.

Such experimental investigations were carried out at the SPS accelerator in CERN by international collaboration NA63 using the secondary electron and positron beams with the energy up to 300 GeV (see [127, 150–153] and others). Big part of these investigations was devoted especially to the detailed study of the suppression of radiation in a thin layer of substance [151–153]. In these papers, this effect was named as the Ternovskii–Shul'ga–Fomin (TSF) effect by the reason of

its theoretical prediction, physical interpretation and quantitative description in the works of these authors [137–140, 144, 145] (see also [12]).

Before the theoretical analysis of the experimental results obtained by CERN NA63 collaboration, let's first carry out the detailed comparative analysis of the conditions for the manifestation of different medium effects on radiation of ultra relativistic electrons in matter.

5.3.3 The LPM and TSF effects conditions

As follows from the analysis of expression for the coherence length (5.34) in Section 5.2.3, the condition for the suppression of radiation due to the multiple scattering effect (5.38), can be written as

$$\vartheta_{\rm s}(l_{\rm c}) > \gamma^{-1}. \tag{5.46}$$

This means that the particle scattering angle in the limits of the coherence length of radiation $\vartheta_{\rm s}(l_{\rm c})$ exceeds the characteristic angle of the relativistic particle radiation $\theta_k = \gamma^{-1}$. It is so-called non-dipole regime of radiation (see, e.g., [4]).

The root-mean-square angle of electron multiple scattering on atoms in an amorphous medium at the depth t can be defined using the formula (see, e.g., [114])

$$\overline{\vartheta}_{\rm ms}(t) \equiv \sqrt{\overline{\vartheta^2}_{\rm ms}(t)} = \frac{\varepsilon_{\rm s}}{\varepsilon}\sqrt{\frac{t}{X_0}}\left[1 + 0.038\ln\left(\frac{t}{X_0}\right)\right], \tag{5.47}$$

where $\varepsilon_{\rm s}^2 = 4\pi \cdot m^2/e^2$. Since both angles θ_k and $\overline{\vartheta}_{\rm ms}$ inversely proportional to the electron energy ε, the target thickness l_γ for which

$$\overline{\vartheta}_{\rm ms}(l_\gamma) = \gamma^{-1} \tag{5.48}$$

does not depend on the electron energy ε and is determined by the radiation length X_0 of the target material only

$$l_\gamma \approx 0.12\,\%\, X_0. \tag{5.49}$$

If the target thickness t is less than l_γ, the spectral density of radiation for all possible emitted photon energies is defined by the Bethe–Heitler formula (5.25).

If $t > l_\gamma$, there are three possible regimes of radiation in this case depending on the energy region of emitted photon.

For the relatively hard region of emitted photon spectrum, when $l_c < l_\gamma$, there is not enough multiple scattering to push significant part of the beam particles out of the radiative cone γ^{-1}, and we have a dipole regime of radiation, which is described by the Bethe–Hietler formula (5.25).

For the non-dipole regime of radiation, when

$$l_c > l_\gamma, \tag{5.50}$$

there are two different cases, defined by the ratio between the coherence length l_c and the target thickness t, with quite different behavior of radiation spectrum.

If the coherence length is less than the target thickness, but bigger than l_γ, i.e.,

$$t > l_c > l_\gamma, \tag{5.51}$$

the Migdal theory [120] of the LPM effect, which describes the suppression of radiation in a boundless amorphous medium, is quite applicable.

The condition (5.50) determines the characteristic energy of the photons $\omega_{\rm LPM}$, below which the multiple scattering effects the radiation spectrum essentially:

$$\omega < \omega_{\rm LPM} = \frac{\varepsilon}{1 + \varepsilon_{\rm LPM}/\varepsilon}, \tag{5.52}$$

where

$$\varepsilon_{\rm LPM} = \frac{e^2 m^2}{4\pi} X_0 \approx 7.7\,{\rm TeV} \times X_0\,({\rm cm}). \tag{5.53}$$

The expression (5.52) showed that for ultra high electron energy ($\varepsilon \gg \varepsilon_{\rm LPM}$) the whole spectrum of emitted gamma quanta is suppressed due to the LPM effect, because $\omega_{\rm LPM} \approx \varepsilon$.

If the initial energy of an electron ε is close to $\varepsilon_{\rm LPM}$ defined by (5.53), then $\omega_{\rm LPM} \approx \varepsilon/2 \approx 4\,{\rm TeV} \times X_0$ (cm), and the soft half part of the radiation spectrum of such electron will be suppressed by the multiple scattering effect.

If $\varepsilon \ll \varepsilon_{\rm LPM}$, then, as it follows from (5.52),

$$\omega_{\rm LPM} \approx \frac{\varepsilon^2}{\varepsilon_{\rm LPM}} = \frac{4\pi}{e^2}\frac{1}{X_0}\gamma^2 \approx \frac{1720}{X_0}\gamma^2. \tag{5.54}$$

Namely this case was realized at the conditions of the SLAC E–146 experiment. For the radiation of 25 GeV electrons in the golden target for which $X_0 \approx 0.33$ cm,

we obtain $\omega_{\rm LPM} \approx 250$ MeV, that is in a good agreement with corresponding experimental data presented in [133, 134] (see also Fig. 5.3). Note that the value of $\omega_{\rm LPM}$, given in [133, 134], is overestimated by a factor of 2, due to ignoring the logarithmic correction in calculating the rms angle of multiple scattering (5.47), which is inadmissible in the case of thin targets for which $t \ll X_0$.

For relatively thin target, when the target thickness is less than the coherence length of radiation $l_{\rm c}$, but still bigger than l_γ, i.e.,

$$l_{\rm c} > t > l_\gamma, \tag{5.55}$$

the radiation spectral density will be also suppressed in comparison with the Bethe–Hietler formula prediction due to the multiple scattering effect at $t > l_\gamma$. However, the Migdal formula is not applicable in this case, because it was obtained for boundless amorphous medium. At the conditions (5.55), we have the suppression of radiation in a thin layer of matter, or the co-called TSF effect [137–139]. The behavior of the radiation spectral density at the TSF effect condition is essentially different both from the results given by Bethe–Hietler or Migdal formulae (see Fig. 5.3).

The change of regime of the radiation suppression from LPM to TSF occurs when the coherence length of radiation becomes equal to the target thickness:

$$l_{\rm c} = t. \tag{5.56}$$

This condition defines the upper limit for the emitted photon energy ω_{TSF} for which the TSF regime of radiation takes place:

$$\omega_{\rm TSF} = \frac{\varepsilon}{1 + \varepsilon_{\rm TSF}/\varepsilon}, \tag{5.57}$$

where

$$\varepsilon_{\rm TSF} = \frac{m^2 t}{2} \approx 6.6\,{\rm PeV} \times t\,({\rm cm}). \tag{5.58}$$

If $\varepsilon \gg \varepsilon_{\rm TSF}$, then $\omega_{\rm TSF} \approx \varepsilon$. This means that whole radiation spectrum is suppressed due to the TSF effect. In this case, of course, it is meant that the radiation non-radiation condition (5.50) is satisfied.

In the opposite case, i.e., $\varepsilon \ll \varepsilon_{\rm TSF}$, the formula (5.55) which defined the value of the gamma quanta energy threshold of the TSF effect $\omega_{\rm TSF}$, that is also the

bound between to spectrum regions of TSF and LPM effects manifestation, can be rewritten in the following form:

$$\omega_{\mathrm{TSF}} \approx \frac{\varepsilon^2}{\varepsilon_{\mathrm{TSF}}} = \frac{2\gamma^2}{t} \approx \frac{3.9 \cdot 10^{-11}\ \mathrm{MeV}}{t\,(\mathrm{cm})}\gamma^2. \tag{5.59}$$

For the conditions of the SLAC E–146 measurements of the radiation of 25 GeV electrons in the golden target of 25 μm thickness ($t = 0.7\,\%X_0$), we obtain $\omega_{\mathrm{TSF}} \approx$ 39 MeV, that is exactly what they observed, when discovered "unexpected" behavior of the radiation spectrum [132–134] (see Fig. 5.3).

As it was already mentioned in section 5.2.3, in the soft part of relativistic electron radiation spectrum, namely,

$$\omega_{\mathrm{p}} < \omega < \gamma\,\omega_{\mathrm{p}}, \tag{5.60}$$

there is the "dielectric suppression" effect (or "Ter-Mikaelian effect") [3], as well as the transition radiation [135]. The essential difference in dependence on the particle energy ε of the conditions of the different effects manifestation gives the possibility to separate them in the different radiation spectrum regions.

Indeed, the characteristic energy thresholds of the emitted gamma quanta for the LPM and TSF effects depends on the initial electron energy (at least, if $\varepsilon < \varepsilon_{\mathrm{LPM}}$, $\varepsilon_{\mathrm{TSF}}$) as $\sim \varepsilon^2$, as it follows from (5.54) and (5.59), in contrast to the Ter-Mikaelian effect, for which the energy threshold (5.60) increases with the photon energy only as $\sim \varepsilon$. This gives an opportunity to study each of these effects more precisely by transition to higher particle energy diapason.

In addition to the separation of the regions of action of different mechanisms of suppression of the radiation of relativistic particles in matter, an increase of the primary electron energy leads to a substantial expansion of the spectral region of manifestation of each of these effects. This advantages became the incentive to carry out a new experimental studies of different kinds of the medium effects on radiation of ultra relativistic particles at essentially higher electron energies in comparison with SLAC experiment E–146.

The investigations started at SLAC experiment E–146 were continued and essentially expanded by the participants of international collaboration CERN NA63 using the secondary electron and positron beams of SPS accelerator with the particle energies up to 300 GeV. They performed the verification of the LPM effect for Ir, Ta and Cu targets of thicknesses about 4 % of radiation length, which showed a good agreement of measured data with the calculations based on the Migdal theory of the

LPM effect. Thus, these results could be treated as the firstly observed the effective expansion of electron radiation length due to the LPM effect [127, 150]. In [154], there was considered the possibility of the LPM effect observation for the low Z materials that was impossible at SLAC experiment E–146 due to the overlay with the dielectric suppression effect in the same region of the radiation spectrum [117, 119].

A special attention at CERN experiment NA63 (see [7, 151–153] was devoted to the detailed study of the suppression of radiation in a thin layer of matter, or the TSF effect, as well as to observation of the interference effect in the bremsstrahlung in thin structured targets, predicted in [155]. The first attempt of this study [151] was not successful, because the conditions for the TSF effect was not fulfilled quite satisfactory.

The analysis of the conditions of this experiment, which was performed in [156] on the basis of presented in this section formulae (5.55)–(5.59), showed the following.

At first, for the set of gold targets with the thickness $t = 2$ μm each, the multiple scattering is not enough to fulfill the condition of non-dipole radiation (5.46) because $t < l_\gamma \approx 4$ μm in this case. Thus, the total intensity of radiation by the set of 53 such targets, which is referred in [151] as Au2, is just a sum of bremsstrahlung by each ones described by Bethe–Heitler formula (5.25) (some deviation from the B–H result in the soft part of the measured spectrum [151] probably connected to the interference effect in transition radiation).

Secondly, the gamma quanta energy threshold for TSF effect for the Au10 case in [151] that corresponds to the each target thickness $t \approx 10$ μm, is about $\omega_{\rm TSF} \approx 5$ GeV following (5.59). However, the coherence length of radiation for such a gamma quanta energy (5.30) is about of $l_{\rm c} \approx 10$ μm that coincides with the target thickness. Therefore, the radiation spectrum region for the TSF effect for the Au10 case is quite narrow, 2–5 GeV, and also the effects of multiple scattering on radiation, i.e. the deviation from the Bethe–Heitler spectrum, is not expected to be significant, because $t \approx 2\, l_\gamma$. For most of the measured spectrum, 5–20 GeV, in the considered case Au10 is determined by the LPM effect.

And thirdly, in the case of the tungsten target of thickness $t = 20$ μm, referred as W20 in [151], the gamma quanta energy upper threshold for TSF effect is about $\omega_{\rm TSF} \approx 2.5$ GeV which is almost coincides with the lower limit of the photon energy measured in this experiment $\omega_{\rm min} = 2\,$GeV [151]. Thus, there was no opportunity to observe the TSF effect in this case.

The results of our comparative analysis of the conditions of manifestation of different mechanisms of the medium effects on radiation of relativistic electrons in matter presented in this section was published earlier in [156].

5.4 Radiation in a thin layer of matter

5.4.1 Spectral-angular distribution

Until now we have analyzed the effect of multiple scattering on the spectral density of radiation of relativistic electrons in matter. Since bremsstrahlung is determined precisely by the scattering of a particle, there is reason to expect that the effect of multiple scattering should manifest itself not only in the emission spectrum of electrons, but also in the angular distribution of radiation and its polarization characteristics. Therefore, we will conduct the analysis in terms of the spectral-angular density of radiation.

As it was shown in 5.2.3, the most important parameter determining such an influence is the coherence length (5.34). The larger this length, the stronger the influence of the medium on the radiation process can be expected.

The value of the coherence length (5.21) is determined primarily by the value of the electron energy and the energy of the emitted photon. The greater the energy of the electron and the lower the energy of the emitted photon, the greater the coherence length. For this reason, the multiple scattering effects on radiation, the LPM effect ((5.40)), as well as the dielectric suppression, the Ter-Mikaelian effect ((5.36)) is manifested primarily in the relatively soft part of the radiation spectrum.

In the soft part of the radiation spectrum, $\omega \ll \varepsilon$, we can neglect the quantum recoil effect on radiation, and consider the radiation process in the framework of classical electrodynamics.

The spectral-angular density of radiation in classical electrodynamics is determined by the expressions (5.26) and (5.27). Integrating by parts in (5.27), we obtain the following expression for the vector $\vec{I}$:

$$\vec{I} = i \int_0^T dt\, e^{i(\omega t - \vec{k}\cdot\vec{r}(t))} \frac{d}{dt} \frac{\vec{v}(t)}{\omega - \vec{k}\cdot\vec{v}(t)}. \tag{5.61}$$

This representation of $\vec{I}$ is rather convenient for the analysis and further calculations, since the integrand in (5.61) is different from zero only in the region of an external field action on the particle, i.e. within the target of thickness T, when the acceleration of the particle is nonzero. Thus, the limits of the integration over t in (5.61) can be reduced to the interval $(0,\, T)$, instead of the integration interval $(-\infty,\, +\infty)$ in (5.27).

If the coherence length of radiation is essentially bigger than the thickness of the target, i.e. $l_c \gg T$, this means that according to our previous consideration of the

classical interpretation of the coherent length (see section 5.2.3), the argument of the exponent in (5.61) is small in comparison with one: $\omega\, t - \vec{k}\cdot\vec{r}(t) \ll 1$. Replacing this exponent factor by unity, and performing the trivial integration over t in (5.61) we obtain

$$\vec{I} \approx i\left(\frac{\vec{v}'}{\omega - \vec{k}\cdot\vec{v}'} - \frac{\vec{v}}{\omega - \vec{k}\cdot\vec{v}}\right), \tag{5.62}$$

where $\vec{v}$ and $\vec{v}'$ are the velocities of the electron before and after its passing the target.

The expression (5.62) shows that if the condition $l_c \gg T$ is fulfilled, the radiation of an electron does not depend on the details of the particle trajectory within the target and is defined exclusively by the resulting angle of its scattering by the target $\vartheta_s = (\vec{v} \wedge \vec{v}')$.

The general expression for the polarization tensor of radiation is [157]

$$J_{ik} = \frac{e^2\omega^2}{4\pi^2}\left(\vec{e}_i\vec{I}\right)\left(\vec{e}_k\vec{I}^*\right), \tag{5.63}$$

where $\vec{e}_{i,k}$ are the polarization vectors which are the unit vectors orthogonal to the wave vector $\vec{k}$ and to each other: $\vec{e}_{i,k}\,\vec{k} = 0$, $\vec{e}_i\,\vec{e}_k = \delta_{ik}$.

The degree of the linear polarization of radiation is determined by expression

$$P = \frac{J_{11} - J_{22}}{J_{11} + J_{22}}. \tag{5.64}$$

The degree of the circular polarization of radiation is

$$P_{circular} = \frac{J_{12} - J_{21}}{J_{11} + J_{22}}. \tag{5.65}$$

In [158] there was proposed a method for producing high energy gamma quanta with circular polarization by coherent radiation of ultrarelativistic electrons passing through a crystal at a small angle to the crystal axis. This method is based on specific features of non-dipole regime of radiation that allows obtaining a high enough degree (about 50 %) of circular polarization of emitted gamma quanta using the special type of photon collimation. The natural limitation of efficiency of this method for hard part of the radiation spectrum is connected with rapid decreasing of the number of emitted gamma quanta with photon energy increasing $dN/d\omega \approx 1/\omega$.

However, there is one more effect that suppresses the emission of circular polarization photons in a soft part of the spectrum despite the increasing of the total

number of emitted photons. Really, if the energy of the emitted photon is small enough, so that the coherence length of radiation process is larger than crystal thickness ($l_c \gg T$) then the polarization matrix (5.63) in this approximation becomes symmetrical

$$J_{ik} = J_{ki}, \tag{5.66}$$

and the degree of circular polarization of emitted gamma quanta (5.65) is equal to zero.

This statement can be formulated as the following general theorem: if the coherence length of radiation process is much larger than the effective spatial region in which a relativistic electron interacts with an external field, then the circular polarization of the emitted photon tends to zero for any observation angle [159].

A possible physical interpretation of this statement is following. In order to obtain a circular polarization, a certain "history of scattering of the radiating particle" with the changes of directions of the particle acceleration vector is needed. Such a "scattering history" is absent in the case of radiation in a thin target ($T \ll l_c$), when the radiation process is described by the formula (5.62), that is, as radiation from the "angle type trajectory".

In contrast to circular polarization, linear polarization of radiation can occur in this case, and the degree of linear polarization for the non-dipole radiation regime ($\vartheta_s > \gamma^{-1}$) can reach quite large values due to the effective spatial separation of the characteristic radiation cones of the relativistic particle $\Delta\theta \approx \gamma^{-1}$ in this case (See Fig. 5.4).

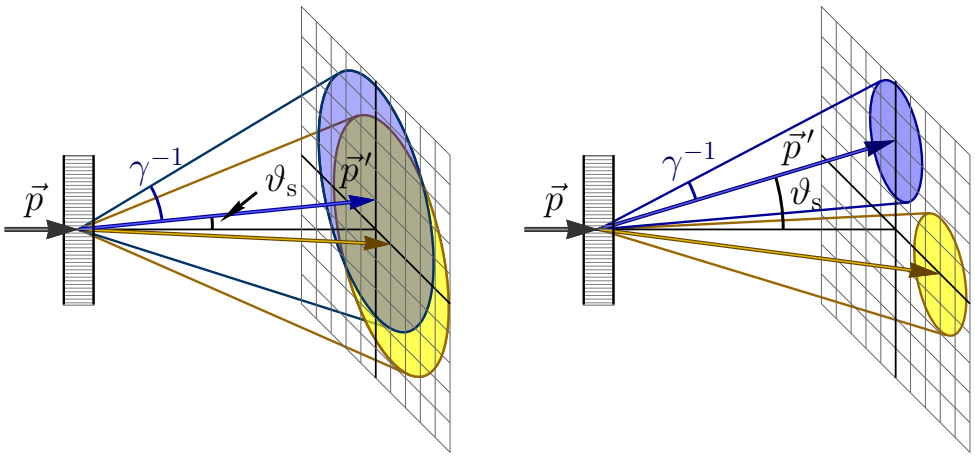

Figure 5.4: The spatial separation of the characteristic cones of the relativistic particle at the non-dipole regime of radiation.

The spectral-angular density of radiation can be written in terms of polarization matrix elements as

$$\frac{d^2E}{d\omega do} = J_{11} + J_{22}. \tag{5.67}$$

Substituting expression (5.62) into (5.63), and then into (5.67), and calculating the corresponding scalar products in the resulting expression, taking into account the smallness of the characteristic angles of fast electrons scattering $\vartheta_s \ll 1$ and the photon emission by relativistic particles $\theta \ll 1$, we obtain (see for the details Appendix A) the following expression for the spectral-angular density of radiation of ultra relativistic electrons in a thin layer of matter:

$$\frac{d^2E}{d\omega do} = \frac{e^2\gamma^2}{\pi^2} \frac{\beta^2}{\left(1+\alpha^2\right)^2} \frac{\left(\left(1-\alpha^2\right)\sin\phi + \alpha\beta\right)^2 + \left(1+\alpha^2\right)^2\cos^2\phi}{\left(1+\alpha^2+\beta^2-2\,\alpha\beta\sin\phi\right)^2}, \tag{5.68}$$

where $\alpha = \gamma\,\theta$, θ and φ are the polar and azimuthal angles which are defined by the wave vector of emitted photon $\vec{k}$, $do = \sin\theta\, d\theta\, d\phi$, $\beta = \gamma\,\vartheta_s$ is the polar angle of particle scattering by the target in the units of γ^{-1}.

It should be specially noted that the spectral-angular density of the radiation in a thin layer of matter does not depend on the energy of the emitted photon, as follows from (5.68). However, such a dependence is present in the definition of the applicability conditions of this approximation, namely $l_c > T$, that the corresponding photon energy region $\omega < \omega_{TSF}$, where ω_{TSF} is defined by inequality (5.57).

The expression for the angular distribution of radiation in a thin target (5.68) obtained in the thesis differs somewhat from the analogous expression obtained earlier in [160], although gives exactly the same numerical results. The structure of expression (5.68) seems more convenient for physical analysis, as well as for the subsequent use in computer simulation of the radiation process in a thin aligned crystals, since the particle scattering angle $\beta = \gamma\,\vartheta_s$ in (5.68) is presented as a separate factor. Namely this factor, as it was mentioned above, determines the regime of particle radiation: dipole, if $\beta < 1$, or non-dipole, if $\beta > 1$.

The formula (5.68) is defined the two-dimensional structure of the angular distributions of radiation by a single relativistic electron scattered at the certain angles $\vartheta_s = \gamma^{-1}, 2\,\gamma^{-1}, 4\,\gamma^{-1}$ and $8\,\gamma^{-1}$ presented in Fig. 5.5. These figures show a non-trivial evolution of the angular distribution of radiation intensity at the transition from quasi-dipole regime of radiation ($\gamma\,\vartheta_s = 1$) to the essentially non-dipole one ($\gamma\,\vartheta_s \gg 1$).

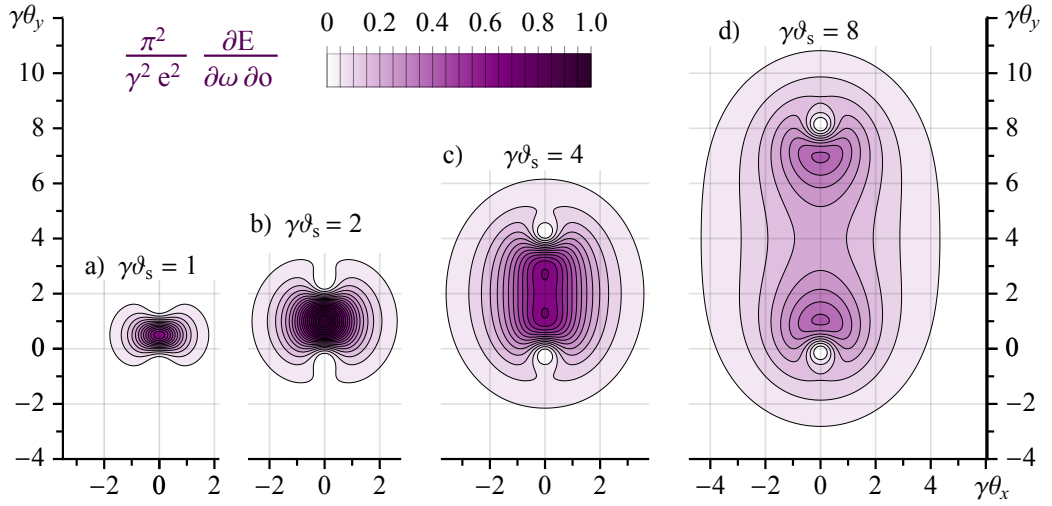

Figure 5.5: Angular distribution of radiation by a single electron scattered through the angle ϑ_s measured in the units of γ^{-1} : $1(a)$, $2(b)$, $4(c)$, $8(d)$. The initial direction of the electron motion is $\theta_x = \theta_y = 0$.

The maximum value of radiation intensity is reached at $\gamma\,\vartheta_s = 2$ (see Fig. 5.5 *b*). The form of the angular distribution of radiation in this case is not much different from the dipole or quasi-dipole radiation case (see Fig. 5.5 *a*). The picture of angular distribution of radiation changes remarkably at the transition to the essentially non-dipole region ($\gamma\,\vartheta_s \gg 1$) that demonstrates the Figure 5.5 *c* and, especially, Figure 5.5 *d*. The angular distribution splitting into two maximums, the first, in the direction of initial motion of the electron, and the second one, in the direction of the scattered electron motion. Closely to each of these maximums, there are two minimums of the radiation intensity with abrupt transition between these maxima and minima (see Fig. 5.5 *c*).

If we consider the radiation of the relativistic electron beam passing through a thin target, the formula (5.68) must be averaged over particle scattering angle behind the target ϑ_s with the corresponding distribution function $f(\vartheta_s)$. We recall that all the characteristics of the radiation of a relativistic electron in a thin target $T \ll l_c$ are determined exclusively by the angle of its scattering by this target. Thus, all the formulae obtained in this section can be used to describe radiation in both amorphous and crystalline targets using the corresponding distribution functions of the particles scattered by the target.

$$\left\langle \frac{d^2E}{d\omega do} \right\rangle = \int d^2\vartheta_s\, f(\vartheta_s)\, \frac{d^2E}{d\omega do}. \tag{5.69}$$

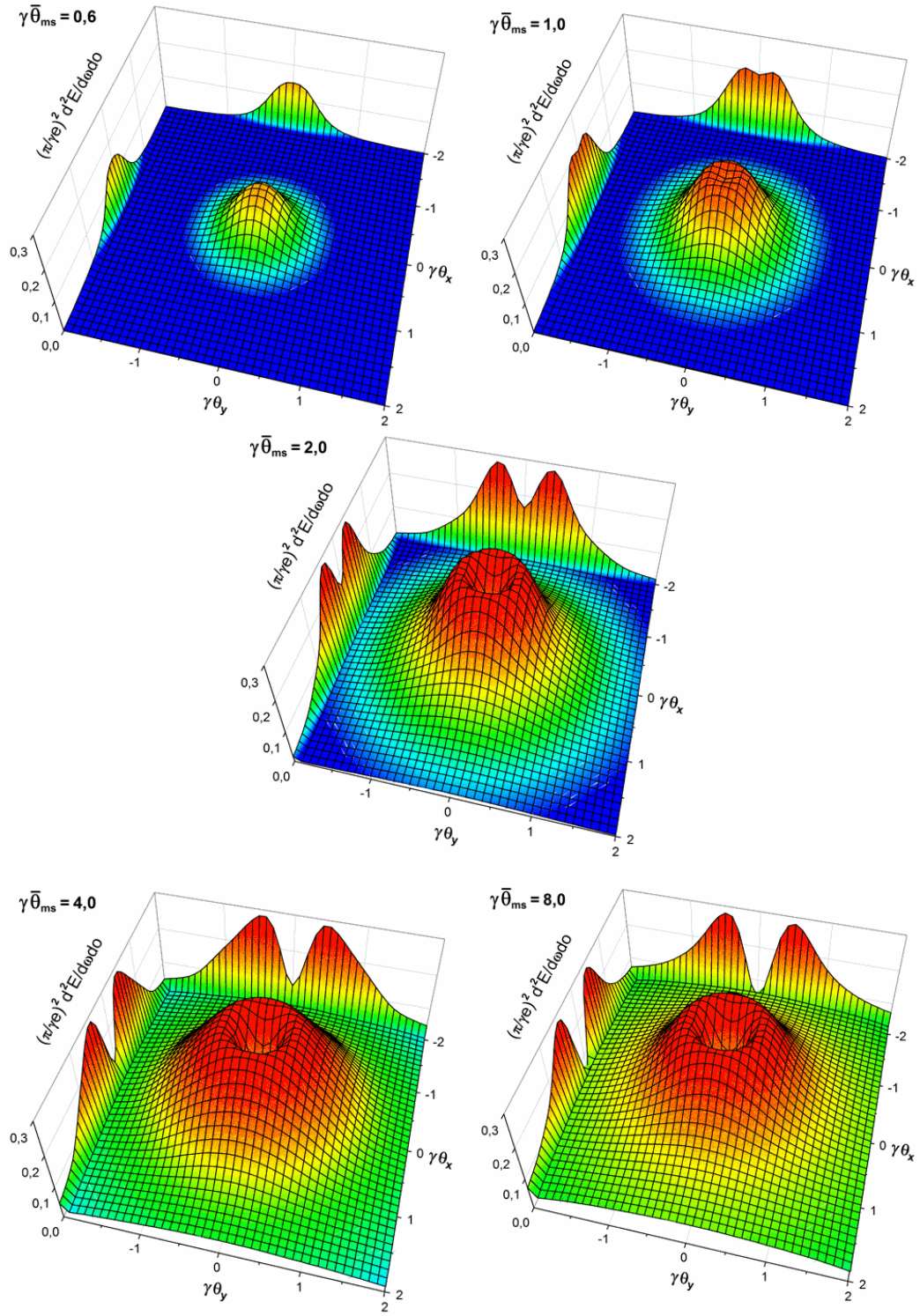

Figure 5.6: Angular distribution of radiation of an electron beam. The initial direction of the electron beam motion is $\theta_x = \theta_y = 0$

In the case of a thin amorphous plate, for the averaging the expression (5.68), one can use the Bethe–Moliere function [47, 161]

$$f_{\rm BM}(\vartheta_{\rm s}) = \frac{1}{2\pi}\int_0^T \eta\, d\eta\, J_0(\eta\,\vartheta_{\rm s}) \times \exp\left\{-n\,T\int \chi\, d\chi\, \sigma(\chi)[1 - J_0(\eta\,\chi)]\right\}, \quad (5.70)$$

where n is the density of atoms in a plate and $\sigma(\chi)$ is the cross section of electron scattering by a single atom at a small angle $\chi \ll 1$.

The results of numerical calculations of the angular distributions of relativistic electron radiation in a thin amorphous target, which obtained using formulae (5.68), (5.69) and (5.70) are presented in Fig. 5.6.

Fig. 5.6 demonstrates the evolution of the angular distribution of radiation at the transition from the dipole regime of radiation $\gamma\bar{\theta}_{ms} < 1$ to the non-dipole one $\gamma\bar{\theta}_{ms} > 1$. One can see as the angular distribution of dipole radiation, i.e. at $\gamma\bar{\theta}_{ms} = 0.6$ described by the Bethe–Heitler theory, with the typical maximum of radiation intensity that coincides with the electron beam direction, smoothly comes to a specific "volcano-like" distribution at the non-dipolity condition at $\gamma\bar{\theta}_{ms} = 8$ with a deep minimum of radiation intensity in the electron beam direction, in contrast to the dipole regime of radiation, and the maximum at the angle $\theta \approx \gamma^{-1}$ in this direction.

The next important difference from the dipole regime of radiation refers to the dependence of the radiation intensity on the electron scattering angle. Namely, the bremsstrahlung intensity at the dipole regime of radiation, as well-known, is proportional to the mean-square value of electron scattering angle. But, the radiation intensity at the non-dipole regime reaches its maximal value at $\gamma\bar{\theta}_{ms} = 2$ (at the angle $\theta \approx \gamma^{-1}$) and then still be practically a constant with $\bar{\theta}_{ms}$ increasing. The qualitative physical treatment of such unusual behavior of the radiation intensity is connected with the idea of a "half-bare electron", and will be discussed at the end of this Chapter.

5.4.2 Polarization of radiation in a thin crystal

If a beam of relativistic electrons passes through a crystal at a small angle ψ to one of crystallographic axes (axis z) there takes place a coherent effect in electron scattering, exhibited as a characteristic annular angular distributions of the particles outgoing from the crystal ("doughnut scattering" effect [4, 23]). This coherent effect takes place only for the scattering over azimuthal angle φ (see Fig. 2.3) as

a result of correlations in sequent scattering of a fast electron by atoms located along this crystal axis. In this case the magnitude of the root-mean-square angle of multiple scattering of electron can exceed substantially (by several times) the corresponding parameter for the electron scattering in an amorphous target of the same thickness [23], and the smaller is the target thickness, the greater is this difference.

Generally the dynamics of a relativistic particle beam in an aligned crystal is rather complicated, since various fractions of a beam are involved in various regimes of motion: finite and infinite, regular and chaotic, with transitions between them. The analytical description of the particle dynamics can be conducted only in some limiting cases. Thus, for example, the theory of multiple scattering of relativistic charged particles on atomic strings of a crystal, based on the continuous string approximation, describes the coherent azimuthal scattering of above-barrier electrons [23]. However, this theory does not describe transitions of particles between two different fractions of the electron beam in the crystal, since the continuous string approximation does not take into account incoherent scattering. It is possible to take incoherent scattering into account by analytical methods only in the case of rather large incident angles $\psi \gg \psi_c$, where ψ_c is the critical channeling angle (2.8) [15]. At the same time, as it was already mentioned, the orientation effects in scattering and radiation of a relativistic electron beam passing through a crystal are mostly manifest in the range of angles $\psi \approx \psi_c$. Therefore, for the quantitative description of these effects, a computer simulation of the passing of an electron beam through an aligned crystal appears to be the most adequate.

With the purpose of a quantitative analysis of the multiple scattering effect on coherent radiation of a relativistic electron in a thin crystal, we performed a computer simulation on the basis of the Monte–Carlo method and the binary collisions model of the electron interactions with the atoms of a crystalline lattice. This model is described in details in the Chapter 3 of this thesis. Such an approach allows taking into account both the coherent scattering of fast electrons on the atomic strings of a crystal and the incoherent scattering of the electrons connected with the thermal fluctuations of the atom positions in the lattice and with the electronic subsystem of the crystal. The angular distribution of radiation and polarization of the whole particle beam is presented as a sum of radiation and polarization of each electron calculated using the formulae (5.62), (5.63), (5.64) and (5.67) .

The results of the computer simulation of electron scattering, radiation and polarization are presented in Figs. 5.7 and 5.8.

The left part of Fig. 5.7 *a* represents the results of computer simulation of the angular distribution of 1 GeV electrons scattered by 10 μm silicon crystal when the

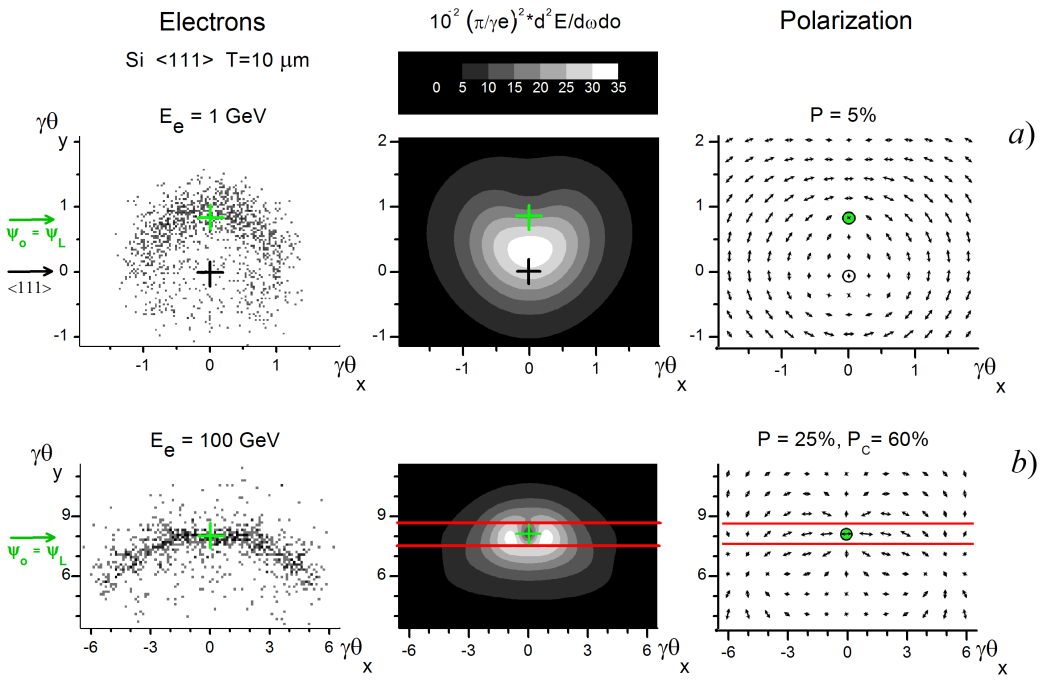

Figure 5.7: Angular distributions of scattered electrons (left) as a result of computer simulation of 1 GeV (a) and 100 GeV (b) electron beam passed through the 10 μm silicon crystal when the electron beam is directed to the crystal at the angle $\psi = \psi_{\rm L}$ to the axis <111>. Arrows show the direction of the crystal axis <111> and the initial electron beam direction. The angular distributions of intensity (middle) and linear polarization degree (right) of radiation by scattered electrons for 1 GeV (a) and 100 GeV (b) of the initial electron beam energy. Dashed lines shows the optimal position of the slit photon collimator with the angular width γ^{-1} to obtain the highest degree of linear polarization.

electron beam is incident at the angle $\psi = \psi_{\rm L}$ to the crystal axis <111>. The initial divergence of the electron beam was taken as 10 μrad that is equal to 0.02 in the units of γ^{-1}. Fig. 5.7 a (left) demonstrate the typical for the "doughnut scattering" effect annular angular distribution of scattered electron. The initial direction of the electron beam is shown in this figure by the arrow $\psi = \psi_{\rm L}$. The position of the crystal axis <111> is shown in Fig. 5.7 a by black (or white) crosses.

The coherent azimuthal electron scattering for these initial conditions (electron beam energy $\varepsilon = 1$ GeV, incident angle $\psi = \psi_{\rm L}$ and crystal thickness $T = 10$ μm) is strong enough to close the ring of the electron angular distribution around the crystal axis <111>. Incoherent scattering of the projectile relativistic electron on thermal vibrations of lattice atoms and on the electron subsystem of the crystal is isotropic in transverse plane (x, y) and it leads to the blooming of the coherent

scattering ring. So, we can say that due to the "doughnut scattering" effect the relativistic electron beam is turned as a whole from the initial incident direction (that was $\psi = \psi_c$) to the crystal axis <111> with essential expansion of its angular size.

The middle part of Figure 5.7 *a* represents the results of calculation of the angular distribution of radiation which is accompanied by the electron beam pass through the crystal. We use here the units γ^{-1} that is a natural scale for angular distributions of relativistic particle radiation. The calculation was carried out using formula (5.67) in which the integration over the scattering angle ϑ_s was replaced by direct summation of contribution from each electron, scattered by the crystal at the angle ϑ_s. The scattering angle ϑ_s was defined by the computer simulation of the electron pass through the crystal with statistics $N = 5000$. The angular distribution of an electron radiation was calculated by formula (5.67). The sum was normalized to one incident electron.

For electron energy $\varepsilon = 1$ GeV the value of the Lindhard angle for a silicon crystal oriented by <111> axis to the electron beam direction is $\psi_c = 0.41$ mrad that is very close to the character value of the photon emission angle $\gamma^{-1} \approx 0.51$ mrad. Taking into account that the character value of electron scattering angle is close to ψ_c (see Fig. 5.7 *a*, (left)) one can conclude that there is a dipole regime of radiation in this case.

In fact, the angular distribution of radiation in Fig. 5.7 *a* (middle) shows the angular distribution of emitted photons, which is characteristic for dipole regime of radiation with one maximum near the crystal axis. The integral degree of linear polarization of this radiation is about 5 % only, and the direction of polarization is vertical, i.e. along the y-axis (see Fig. 5.7 *a*, right).

The results of analogous calculations for 100 GeV electron beam in the silicon crystal of the same thickness and orientation are presented in Fig. 5.7 *b*. The initial beam divergence was taken as 1 μrad that is about five times less than γ^{-1}. One can see that the 10 μm crystal thickness is not enough to close the ring of coherent scattering for 100 GeV electrons (Fig. 5.7 *b* (left)). There is also markedly weaker influence of incoherent scattering to the formation of angular distribution of scattered electrons than in the previous case ($\varepsilon = 1$ GeV). However, the most significant changes occur in angular distributions of radiation and polarization (Fig. 5.7 *b*, middle and right). In particular, for 100 GeV electrons case there is a depletion of the photon angular distribution at $\gamma\theta_x \approx 0$ and ψ belonging to the interval $(\psi - 1/2\,\gamma^{-1}, \psi + 1/2\,\gamma^{-1})$. The reason of these transformations is the essentially non-dipole regime of radiation in crystal for 100 GeV electrons: $\vartheta_s \approx \psi_c = 41$ μrad and $\gamma^{-1} \approx 5.1$ μrad, so, the non-dipole parameter is $\gamma\vartheta_s \approx 8$.

The integral degree of linear polarization is about 25 %, and it is horizontal (along x-axis) in this case. Using the slit-type horizontal photon collimator with the angular width $\triangle\theta = \gamma^{-1}$ and putting them as it sowed in Fig. 5.7 *b* (right) by dashed lines it is possible to obtain linearly polarized photon beam with polarization degree about 60 %.

Note, that just the special type of coherent scattering in a crystal and the non-dipole regime of radiation allow us to obtain a high degree linearly polarized photon beams on the basis the angular separation of emitted gamma quanta. The condition for the non-dipole regime of radiation, namely $\gamma\,\vartheta_{\rm s} > 1$, can be fulfilled not only by increasing the electron energy but also using the crystals with higher atomic number.

The results of our calculations of scattering and radiation of 100 GeV electrons passed through the 10 μm tungsten crystal at the angle $\psi = \psi_{\rm c}$ to the crystal axis <111> are presented in Fig. 5.8. The Lindhard angle in this case is $\psi_{\rm c} = 125$ μrad that is equal to 24.4 in units of γ^{-1}, so there is the condition of a deep non-dipole effect at radiation $\gamma\,\vartheta_{\rm s} \gg 1$.

The "doughnut scattering" effect takes place in this case also, and the whole angular distribution of scattered electron looks very similar to the electron distribution in Fig. 5.7 *a* (left) but in corresponding scale. In Fig. 5.8 (left) we can see only a small part of the whole angular distribution which is located around the initial direction of the incident electron beam.

The angular distribution of emitted gamma quanta presented in Fig. 5.8 (middle) demonstrates that despite a relatively wide angular distribution of scattered electron ($\triangle\vartheta_{\rm s} \approx 2\psi_{\rm c} = 250$ μrad) the radiation is concentrated mainly in a small cone ($\triangle\theta \approx 4\gamma^{-1} = 20$ μrad) along the incident electron beam direction with a "black hole" of γ^{-1} in diameter in the middle of the cone.

The integral degree of linear polarization (horizontal) of radiation is about 5 %. For the horizontal slit-type photon collimator with the angular width $\triangle\theta = \gamma^{-1}$ marked in Fig. 5.8 (right) by dashed lines the degree of linear polarization (horizontal) of collimated photon beam comes up to 77 %. If we turn this collimator to the vertical position (in parallel to y-axis) we obtain the linearly (vertically) polarized photon beam with 70 % of polarization degree. Note, that such a behavior of polarization is very similar to the amorphous target case but for the same efficiency of radiation it is necessary to use significantly thicker amorphous target.

All these features of angular distributions of radiation and polarization are associated with the superposition of two different effects: coherent electron scattering by the crystal rows ("doughnut scattering" effect) and suppression of radiation due

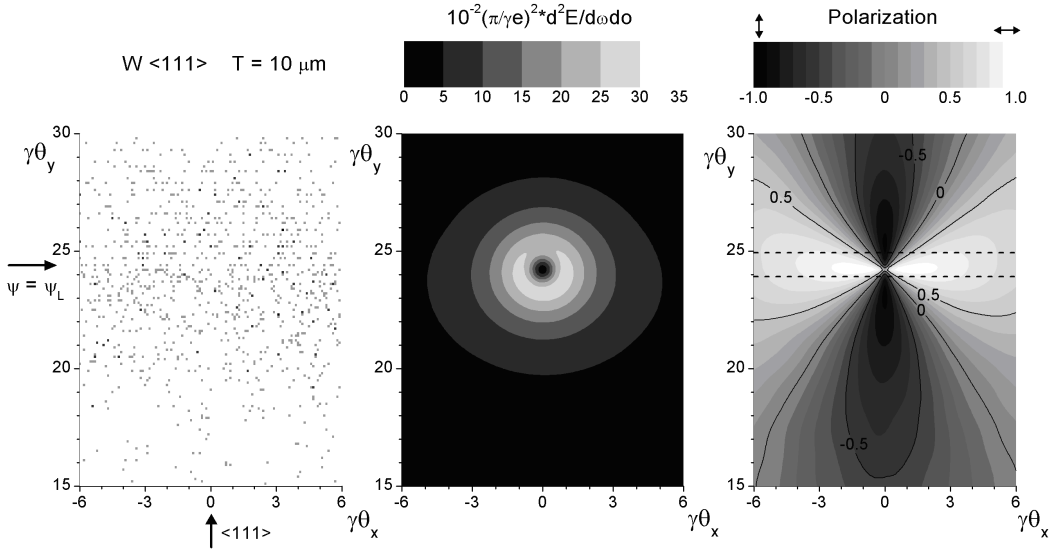

Figure 5.8: The same as in Fig. 5.7 but for the tungsten crystal and 100 GeV of initial energy of the electron beam.

to this coherent multiple scattering (analogous to the LPM effect in an amorphous target).

As it was discussed in Chapter 2 of this thesis, positively and negatively charged particles moving in aligned crystal along crystallographic planes or axises, can have different regimes of the motion: regular or chaotic, finite motion in transverse plane (the channeling) or the above-barrier motion. It is reasonable to expect that the difference in the scattering in the field of crystal lattice have to lead to differences in the radiation of particles with different signs of electric charge.

Note that the first experimental observation of the fundamental difference in orientation dependence of electron and positron radiation in a crystal took place at the linac LUE–2 GeV in Kharkiv Institute of Physics and Technology in 1968. Actually, it was the first observation of relativistic electron and positron radiation at the channeling regime. However, for that moment, this experimental result was in the direct contradiction with the predictions of the convenient theory of coherent bremsstrahlung which was developed in works of [104–106] in the framework of the first Born approximation of perturbation theory. Therefore, the first publication of the results of these experiments appeared only several years later [162], after a theoretical explanation of the principal possibility of the differences in the emission of electrons and positrons [163].

With the aim to study the difference between the radiation of ultra relativistic electrons and positrons in a thin crystal at the essentially non-dipole regime of radiation, in [164] such a situation was considered on the basis of computer simulation

of 200 GeV electron and positron beams which incident on the tungsten crystal of 20 μm thickness at the angle $\psi = \psi_c$ to the axis <111>. The results of the computer simulation of electron (positron) scattering, radiation and polarization are presented in Fig. 5.9.

The initial direction of the electron (positron) beam is in the center of black square on the figures 5.9 *a, b*. The black square also indicates the angular region where the gamma-radiation is mainly located. Namely, this region is represented in Figs. 5.9 *a, b* (middle) with corresponding zooming. The angular distributions of intensity (middle) and linear polarization degree (right) of radiation by scattered electrons for 200 GeV of the initial electron beam energy. Dashed lines shows the optimal position of the slit photon collimator with the angular width $\triangle\theta = \gamma^{-1}$ to obtain the highest degree of linear polarization.

Fig. 5.9 *a* (left) demonstrate the typical for the "doughnut scattering" effect annular angular distribution of scattered electrons when initial electron beam impinges on the crystal at the Lindhard angle $\psi = \psi_c$. The position of the crystal axis <111> is shown in Fig. 5.9 *a* (left) by black cross. The initial direction of the electron beam is in the center of black square on this figure. The black square is also indicates the angular region where the gamma-radiation is mainly located. Namely this region is represented in Fig. 5.9 *a* (middle) with corresponding zooming.

The results of analogous calculations for 200 GeV positron beam in the tungsten crystal of the same thickness and orientation are presented in Fig. 5.9 *b*. One can see that angular distribution of scattered electrons Fig. 5.9 *a* (left) and positrons Fig. 5.9 *b* (left) is rather different. This difference is connected with the character of the motion of positrons and electrons in a lattice field. As a result we have also different structure of angular distribution of radiation and its polarization, see Figs. 5.9 *a, b* (right).

The integral degree of linear polarization of electron radiation is about zero. However, using the slit-type horizontal photon collimator with the angular width $\triangle\theta = \gamma^{-1}$ and putting them as it sowed in Fig. 5.9 *a* (right) by dashed lines it is possible to obtain linearly polarized photon beam with polarization degree about 80 %.

The left part of Fig. 5.9 *c* represents the results of computer simulation of the angular distribution of 200 GeV electrons (positrons) scattered by 20 μm tungsten crystal at random orientation (like in amorphous target). The initial divergence of the electron beam was taken as 1μrad that is equal to 0.4 in the units of γ^{-1}. The root-mean-square angle of multiple scattering $\bar{\vartheta}_s$ for this case is about $3\,\gamma^{-1}$. It means that we have non-dipole regime of radiation even at random orientation

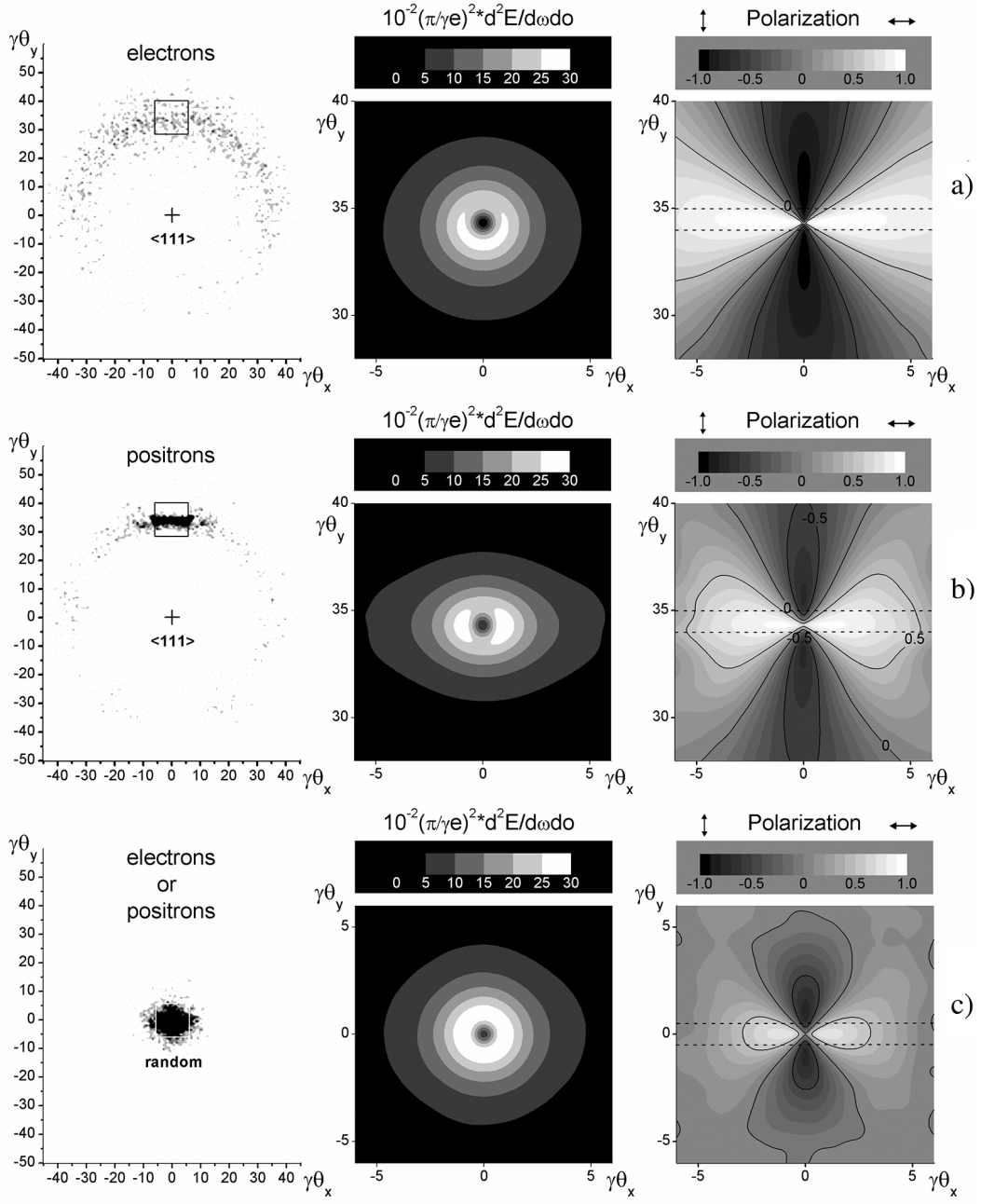

Figure 5.9: The angular distributions of scattered electrons (left) as a result of computer simulation of 200 GeV electron (a) and positron (b) beams propagation through a 20 μm tangsten crystal when the electron beam is directed to the crystal at the angle $\psi = \psi_c$ to the axis <111>. Black crosses show the direction of the crystal axis <111> and the initial electron beam direction.

of 20 μm tungsten crystal with the "non-dipole" parameter is $\gamma\,\bar{\vartheta}_{\rm s} \approx 3$. The Fig. 5.9 *c* (middle) shows the corresponding angular distribution of emitted gamma quanta. In contrast to the dipole radiation case there are the deep minimum along the initial electron beam direction. We use here the units γ^{-1} that is a natural scale for angular distributions of relativistic particle radiation.

Note that just the special type of coherent scattering in a crystal and the non-dipole regime of radiation allow us to obtain a high degree linearly polarized photon beams on the basis the angular separation of emitted gamma quanta.

If we turn this collimator to the vertical position (in parallel to y-axis) we obtain the linearly (vertically) polarized photon beam with about 80 % of polarization degree. Note, that such a behavior of polarization is very similar to the amorphous target case but for the same efficiency of radiation it is necessary to use significantly thicker amorphous target. Another situation for radiation of positron beam in crystal at the same condition. Horizontal collimation gives the result 75 % of linear polarization, but the vertical one gives only 50 %.

For the experimental observation of the effects described above a high angular resolution (better than γ^{-1}) of the gamma-detector is needed, as well as a small (less than γ^{-1}) divergence of the electron beam. For 200 GeV electrons the necessary angular resolution is about 2 μrad, that is quite small angle. It means that for the spatial resolution in order of 1 mm it is necessary to a base about 500 m long. It may be possible to realize at future linear electron-positron colliders, but it is too difficult to realized at modern accelerator.

In order to reduce such strong requirements to the angular resolution of the detecting system for experimental observation of discussed here effects, we consider the possibility of maximal decreasing the initial particle energy keeping in mind the necessity to fulfill the condition of non-dipole radiation and thereby to avoid a mixture of the radiation cones of particles scattered in different directions.

To minimize electron energy keeping the non-dipole regime of its radiation is possible by using the coherent effect at relativistic electron scattering on atomic chains along the crystallographic axis. As it was already mentioned, the root-mean-square angle of multiple scattering in this case can exceed essentially the analogous parameter for amorphous matter [23]. This effect is as strong, as high the charge of the atomic nuclear of a crystal is, so, a good candidate for the crystal converter would be a tungsten single crystal.

The results of our calculations of the angular distributions and polarization of radiation by 3.5 GeV electrons incident on the 10 μm thick tungsten crystal at the Lindhard angle $\psi = \psi_{\rm c}$ to the axis <111> are presented in Fig. 5.10. These

calculations are based on the computer simulation of electrons scattering by the tungsten crystal using binary collision model, as previously. In this case $\bar{\vartheta}_s \approx \psi_c \approx 0.7$ μrad and the parameter of non-dipolity is $\gamma\,\bar{\vartheta}_s \approx 5$.

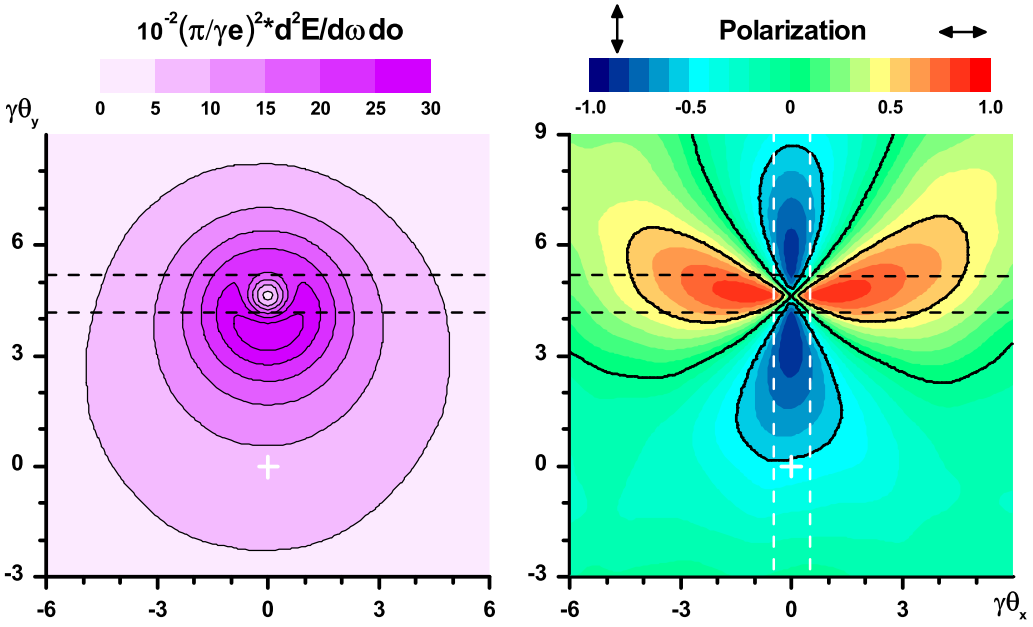

Figure 5.10: The angular distributions (in units of γ^{-1}) of radiation power spectrum emitted by 3.5 GeV electron beam incident on the tungsten single crystal of 10 μm thick at the angle ψ_c to the axis <111> (left) and the degree of linear polarization of this radiation (right).

The angular distribution of emitted photons is presented on the left part of the Fig. 5.10. The right part represents the angular distribution of the linear polarization degree of emitted photons from the 100 % vertically polarized photons ($P = -1$) to 100 % horizontal polarization ($P = 1$). All angles in Fig. 5.10 are measured in units γ^{-1}. The integral (over all angles) degree of linear polarization of radiation is close to zero. However, using the slit-type horizontal (or vertical) photon collimator with the angular width $\Delta\theta_\gamma = \gamma^{-1}$ and putting it as shown in Fig. 5.10 by dashed lines it is possible to obtain a linearly polarized (along the collimator plane) photon beam with polarization degree of about 60 %. Note that due to the higher value of the averaged row potential, the radiation intensity in the case of axially oriented crystal is much higher than at the planar orientation case, which is applied normally for production of polarized photon beams.

Unfortunately, decreasing the particle energy from hundreds to several GeV in order to decrease the characteristic cone of radiation $\triangle\theta_k \approx \gamma^{-1}$, we have substantially narrowed the range of applicability of the TSF effect: $\gamma\,\omega_p < \omega < \omega_{TSF}$, that

means 0.5 MeV $< \omega <$ 2 MeV for the case under consideration. This circumstance considerably complicates the possibility of experimental observation of the effect under consideration. Most likely, successful implementation of such an experiment will become possible only after the creation of linear electron-positron colliders of the TeV range of energies ILC or CLIC.

Without the possibility of direct experimental verification of theoretical calculations and modeling of the angular distributions of radiation intensity and its polarization characteristics in thin amorphous and crystalline targets under the TSF effect conditions (i.e. at substantial non-dipolity of radiation), we decided to conduct at least an indirect verification of the approach used here by comparison with the experimental data on the spectral density of ultra relativistic electron radiation under the conditions of the TSF effect recently obtained at the CERN SPS accelerator in the framework of the NA63 collaboration [152] and [153].

5.4.3 CERN experiment NA63

In our work [156], in addition to analysis of the conditions of the experiment [151] (see Section 5.3.3), the preliminary calculations of the radiation spectral density specially for the CERN SPS secondary beam energies were carried out. The main aim of these calculations was to indicate the optimal conditions for the TSF effect observation in future CERN experiments. Since the particle energy of the secondary electron and positrons beams was assumed to be of the order of hundreds of GeV, these calculations were performed in the framework of Quantum Electrodynamics on the basis of the approach developed earlier in [145] using formulae (5.6)–(5.8) with the Moliere potential of an atom (5.11) and the Bethe–Moliere distribution function (5.70) over the particle scattering angles ϑ_s [47].

The results of calculations of the radiation spectra of 250 GeV electron in tantalum target of different thicknesses: 0.1; 0.5; 1.5 and 5 % X_0 are presented in Fig. 5.11.

The dotted line BH in Fig. 5.11 is calculated using the Bethe–Heitler formula (5.25). This radiation spectrum depends on the emitted photon energy only due to the recoil effect at radiation, which is negligibly small, because for the photon energy region under our consideration here $\omega \ll \varepsilon$.

The solid curves TSF 1, TSF 2, TSF 3 and TSF 4 in Fig. 5.11 are calculated for the target thicknesses: $t = 0.15$; 0.5; 1.5 and 5 % X_0 respectively in the same approach. There is a significant suppression of radiation compared to the BH spectrum for gamma quanta energies $\omega < \omega_{\rm TSF}(t)$.

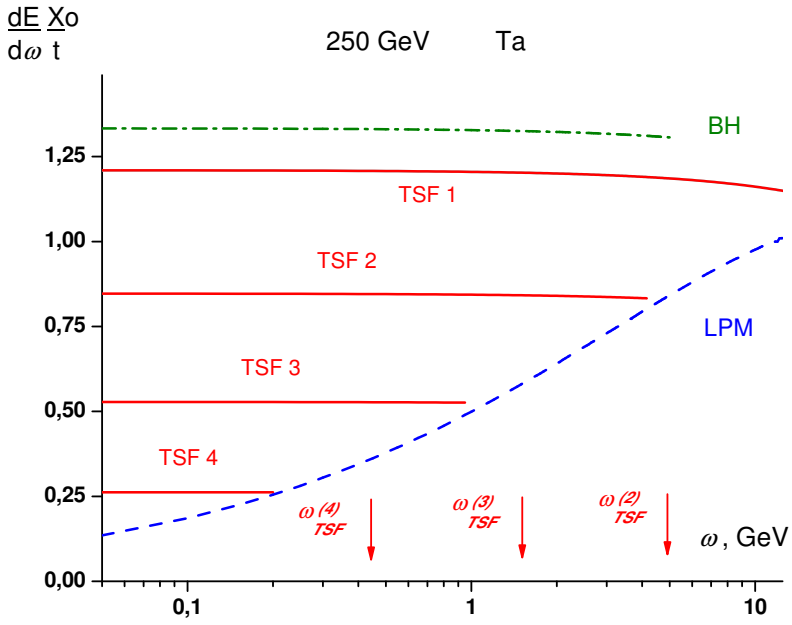

Figure 5.11: The radiation spectrum density per unit length for 250 GeV electrons in tantalum target of different thicknesses: 0.15; 0.5; 1.5 and 5% X_0. The solid lines TSF 1, TSF 2, TSF 3 and TSF 4 are calculated using formulae (5.57)–(5.59) for target thicknesses: 0.15; 0.5; 1.5 and 5 % X_0 respectively. The dotted line BH is calculated using the Bethe–Heitler formula (5.25). The dashed line LPM is calculated using the Migdal formula (5.40).

The degree of suppression and the photon energy threshold of the TSF effect $\omega_{\rm TSF}$ depends on the target thickness t as it follows from (5.57) and (5.58). The values of $\omega_{\rm TSF}(i) \approx 5$; 1.7 and 0.5 GeV for the corresponding target thicknesses: $t(i) = 0.5$, 1.5 and 5 % X_0 are marked in Fig. 5.11 by corresponding arrows. For the target thickness $t = 0.15$ % X_0, $\omega_{\rm TSF} \approx 20$ GeV, that is out of the figure area. Each of these arrows divides the radiation spectrum into two regions where different mechanisms of radiation suppression take place: in the left part (the lower photon energy) there is the TSF mechanizm, in the right part (the higher photon energy) there is the LPM effect (the dashed curve LPM calculated using the Migdal formula (5.40)–(5.43)).

In contrast to the TSF, the LPM radiation spectrum density per unit length presented in Fig. 5.11 does not depend on the target thickness, however, the low limit of applicability of the Migdal formula, which is $\omega_{\rm TSF}$, depends strongly on the target thickness (see (5.57)). Thus, tracing the gamma quanta spectrum curve for the fixed

target thickness starting from a low energy, namely from $\omega_{\rm TM}$ to avoid the overlap with dielectric suppression effect (see (5.60)) to the higher, one can observe the following behavior of the radiation spectrum: in the energy region $\omega_{\rm TM} < \omega < \omega_{\rm TSF}$ the spectrum follows one of the curves TSF depending on target thickesses, and then for $\omega_{\rm TSF} < \omega < \omega_{\rm LPM}$, it follows the LPM curve, and finally, for $\omega_{\rm LPM} < \omega < \varepsilon$, the radiation spectrum comes to the BH curve.

For example, the radiation intensity of 250 GeV electrons in the tantalum target of thickness $t = 1.5\,\%\,X_0$ (the curve TSF 3 in Fig. 5.11) in the spectrum region 200 MeV $< \omega <$ 1 GeV does not depend on the ω, and approximately two times lower compared to the BH theory prediction. This is the suppression of radiation in a thin layer of matter, or the TSF effect, the condition for which is $t < l_{\rm c}$, but $t > l_\gamma$ (see (5.48) and (5.49)). In the region 1 GeV $< \omega <$ 20 GeV, when $t > l_{\rm c} > l_\gamma$, one can expect the pure LPM behavior of the radiation spectrum with the characteristic square-root dependence on the gamma quanta energy ω. For harder gamma quanta, $\omega >$ 20 GeV, the BH spectrum should be observed.

The conditions of appearance of the LPM and TSF effects (5.52) and (5.57) show that for the CERN SPS accelerator energies, both these effects take place in a relatively soft part of radiation spectrum $\omega_{\rm TM} < \omega < \omega_{\rm TSF} < \omega_{\rm LPM} \ll \varepsilon$ (e.g., for $\varepsilon = 250$ GeV, $\omega_{\rm LPM} \approx 21$ GeV and $\omega_{\rm TM} = \gamma\,\omega_{\rm p} \approx 40$ MeV). In this case the quantum recoil effect is negligible and one can use the classical approach to describe these effects.

Summing up, it is possible to conclude that for a clear observation of the TSF effect, it would be advisable either to lower the energy threshold of the registered gamma quanta, in comparison with the measurements made in [151], i.e. below 2 GeV, or to reduce the thickness of the target (but not less than l_γ (5.49)), or to increase the energy of initial particles as much as possible. Of course, it is better to do all this together, if possible.

A new series of measurements of the radiation of 206 and 234 GeV electrons in tantalum targets of several microns thickness, was carried out later by CERN collaboration NA63 [152]. The results obtained in these measurements showed a good agreement with the results of calculation based on different theoretical approaches developed in [140,144,145] and [155]. One of most interesting results from the point of view of the comparing the different modes of the multiple scattering effects on radiation is represented in Fig. 5.12 which is taken from [152].

This figure represents the experimental data in the form of the ratio between the radiation power-spectra of 206 GeV electron in two different cases of the measurements.

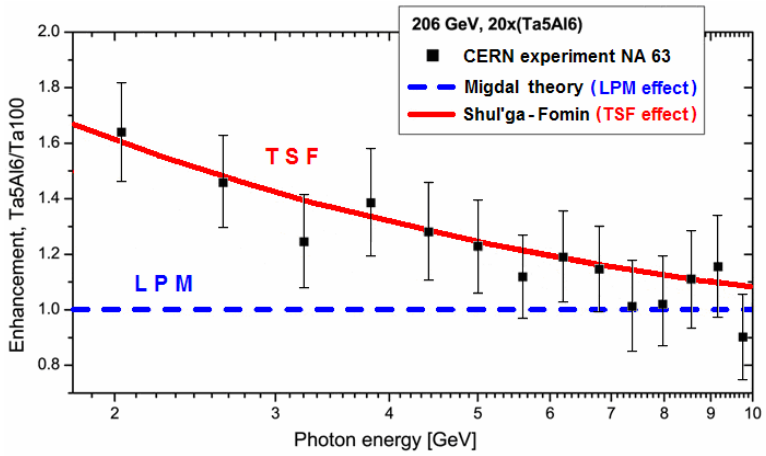

Figure 5.12: Enhancement of the normalized bremsstrahlung power-spectrum for the Ta5Al6 target compared to the Ta100 reference target for 206 GeV electrons. The experimental data taking from [152] is compared with the results of numerical calculations using formulae (5.40) and (5.72). More detailed description is in the text below.

The first one corresponds to the so-called "sandwich" target denoted in [152] as 20xTa5Al6, which consists from 20 tantalum foils of 5 microns thick separated by aluminum layers of 6 microns thick between them. The non-dipole regime of radiation for each of these tantalum foils is realized, $t > l_\gamma$ (5.49), because the parameter l_γ for the tantalum is equal to 4.4 microns. The minimal value of gamma quanta energy in this measurement was $\omega_{\rm min} = 2$ GeV that corresponds to the value of the coherence length of 200 GeV electron radiation $l_{\rm c} \approx 30$ μm (see (5.30)). Thus, the condition of the TSF effect $\omega < \omega_{\rm TSF}$ (5.57) for the each single tantalum layer of the target 20xTa5Al6 was fulfilled at least in the soft part of the measured radiation spectrum, namely, from $\omega = 2$ GeV till $\omega = \omega_{\rm TSF} \approx 12$ GeV. As it was shown in Section 5.3.3, at the gamma quanta energy $\omega_{\rm TSF}$, when the coherence length of radiation becomes equal to the target thickness, the TSF regime of radiation passes to the LPM effect.

The second type of the target, denoted in [152] as Ta100, was a single tantalum foil of 100 microns thick. For such a relatively thick target, the LPM regime of radiation takes place from $\omega = 2$ GeV till $\omega = \omega_{\rm LPM} \approx 14$ GeV, starting from which the LPM effect disappears and the radiation process is described by the Bethe–Heitler formula (5.37).

Thus, the ratio of the radiation powers in the targets 20xTa5Al6 and Ta200 in the gamma-ray energy range from 2 to 10 GeV, presented in Fig. 5.12, in fact, have to demonstrate the difference between two modes of the suppression of radiation due to the multiple scattering, namely, TSF and PLM effects.

The spectral density of radiation of ultra relativistic electron in a thin layer of matter for the considered here case of a soft part of the radiation spectrum, $\omega \ll \varepsilon$, can be obtained by the integration of the expression (5.68) for the spectral-angular distribution of radiation over the polar and azimuthal angles of emitted photons θ and φ. After carrying out such an integration, we arrive at the formula for the spectral density of radiation of the electron scattered at the angle $\vartheta_{\rm s}$ by the "zero-thickness target" (or at the "angle-type trajectory"), obtained, e.g., in [138] by means of analogous integration in (5.26), but at the earlier stage of calculations (see also [4, 12]):

$$\frac{dE_{\rm TSF}}{d\omega} = \frac{2e^2}{\pi}\left[\frac{2\xi^2+1}{\xi\sqrt{\xi^2+1}}\ln\left(\xi+\sqrt{\xi^2+1}\right)-1\right], \tag{5.71}$$

where $\xi = \gamma\,\vartheta_{\rm s}/2$.

For describing the radiation in a thin amorphous target it is necessary to average the expression (5.71) over electron multiple scattering on atoms of the target with the Bethe–Moliere distribution function $f_{\rm BM}(\vartheta_{\rm s})$ (5.70) [47]:

$$\left\langle\frac{dE_{\rm TSF}}{d\omega}\right\rangle = \int d^2\vartheta_{\rm s}\, f_{\rm BM}(\vartheta_{\rm s})\frac{dE_{\rm TSF}}{d\omega}. \tag{5.72}$$

The results of numerical calculations of the radiation spectral density per unit length of trajectory of the 206 GeV electron in a tantalum target, that was obtained using formulae (5.71) and (5.72), as well as using the Migdal formulae (5.40) presented in Fig. 5.13 by the curves TSF (dashed line) and LPM (dot-dashed line) correspondingly. All the curves in this figure are normalized on the Bethe–Heitler spectral density defined by (5.37).

The solid line TSF/LPM in Fig. 5.13 is the ratio of corresponding results for TSF and LPM curves. Applying this curve (the solid curve TSF) to the experimental results presented in Fig. 5.12, one can state an excellent agreement between theoretical predictions and measured data not only in the magnitude of the relationship between the TSF and LPM effects, but by the region of applicability of the corresponding theories as well.

The analysis of the results of other measurements presented in [152] for another thickness of the target or another energy of initial electron beam also showed a very good agreement with the theoretical predictions for the behavior of the TSF

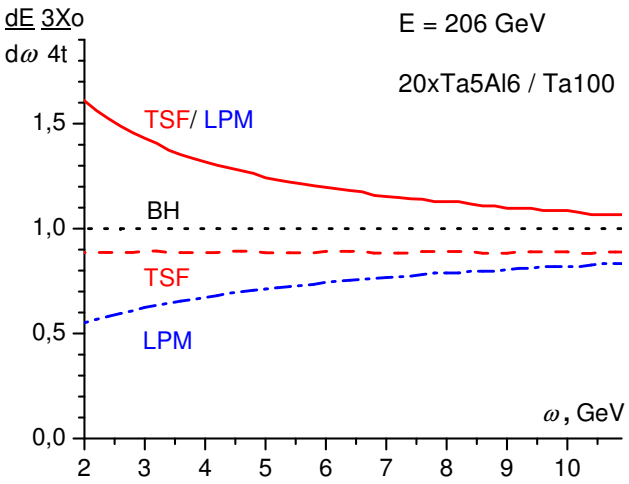

Figure 5.13: The radiation spectrum density per unit length for 206 GeV electrons in tantalum target normalized by the Bethe–Heitler spectral density (5.37) (doted line BH). The dot-dashed curve LPM is the result of calculation using the Migdal formula (5.40). The dashed curve TSF is calculated using formulae (5.71) and (5.72). The solid line TSF/LPM is the ratio of corresponding results for TSF and LPM curves.

effect. For example, for the "sandwich" target 10xTa10Al12.5, for which the thickness of each from 10 tantalum layers was chosen equal to 10 microns, the range of applicability of the TSF effect decreases in two times comparing with the case of the "sandwich" target 20xTa5Al6 in full accordance with the condition (5.59) of the TSF effect existance: $\omega < \omega_{\rm TSF} \approx 2\gamma^2/t$. According to this conditions, the increase of the initial energy of an electron from 206 to 234 GeV for the same tantalum target 20xTa5Al6, leads to 30 % expansion of the applicability range of the TSF effect in the gamma quanta spectrum, shifting its upper threshold from 12 to 16 GeV observed in the experiment [152].

The formula (5.71) has quite simple asymptotes at small and large values of a mean square angle of multiple scattering of particles by the target $\overline{\vartheta_{\rm s}^2}$:

$$\frac{dE}{d\omega} \approx \frac{2e^2}{3\pi}\gamma^2\overline{\vartheta_{\rm s}^2}, \qquad \gamma^2\overline{\vartheta_{\rm s}^2} \ll 1, \tag{5.73}$$

$$\frac{dE}{d\omega} \approx \frac{2e^2}{\pi}\ln(\gamma^2\overline{\vartheta_{\rm s}^2}), \quad \gamma^2\overline{\vartheta_{\rm s}^2} \gg 1. \tag{5.74}$$

As known, in an amorphous target, the value $\overline{\vartheta^2}_{\rm ms}$ is proportional to the target thickness t (see, (5.47) and [114]). Thus, if $\gamma^2\overline{\theta_l^2} \ll 1$, (that means $t \ll l_\gamma$) the

formula (5.71) gives the Bethe–Hietler result (5.37) with the conventional linear dependence from the target thickness.

In the opposite case, i.e., when $\gamma^2\overline{\theta_l^2} \gg 1$ at $t \gg l_\gamma$, the formula (5.71) shows only the logarithmic growth of radiation spectral density with the target thickness increasing. This means the suppression of the radiation from the unit pass in the target in comparison with the prediction of the Bethe–Heitler theory of bremsstrahlung [110].

It is really strange behavior of the radiation spectral density of relativistic electron: the number of the particle collisions with target atoms, as well as the corresponding root-mean-square angle of multiple scattering, increases linearly with the target thickness, but the bremsstrahlung intensity almost doesn't increase (only logarithmical growth). Roughly speaking, the fast electron scatteres on atoms without radiation!

In [138,139], special attention was stressed to this feature of radiation in a thin layer of matter. In order to find a physical explanation of this effect, an approach based on the description of the space-time evolution of the Coulomb field of a fast charged particle at its multiple scattering was developed in [12,139,165,166]. Within the framework of such an analysis, the concept of a "semi-bare electron", i.e., an electron with a non-equilibrium own Coulomb field, naturally arises. The physical essence of the suppression effect in a thin layer of matter, as well as the LPM effect in an infinite amorphous medium, is the relativistic retardation effect at the electron own Coulomb field restoration after the scattering at a relatively large angle $\vartheta_s > \gamma^{-1}$, ie, the non-dipole radiation mode. The most obvious effect of a "semi-bare electron" manifestation is the logarithmic thickness dependence of the intensity of radiation in a thin layer of matter.

The results of theoretical calculations of the thickness dependence of the radiation spectrum density of 150 GeV electrons passing though tantalum target demonstrate clearly the qualitative difference between the different regimes of radiation in amorphous matter, namely the BH, LPM and TSF regimes and their consequent replacements. Such dependences are represented in Fig. 5.14.

For $t < l_\gamma$, i.e., when the target thickness t is too small that the multiple scattering of relativistic electrons in the target is not enough to fulfill the condition $\gamma^2\overline{\theta_l^2} > 1$, the radiation process has a dipole character and the radiation power spectrum is described by the Bethe–Hietler formula (5.25). The soft part of the spectrum ($\omega \ll \varepsilon$) does not depend on ω and describes by more simple formula (5.37). The corresponding curve is presented in Fig. 5.14 by doted straight line BH.

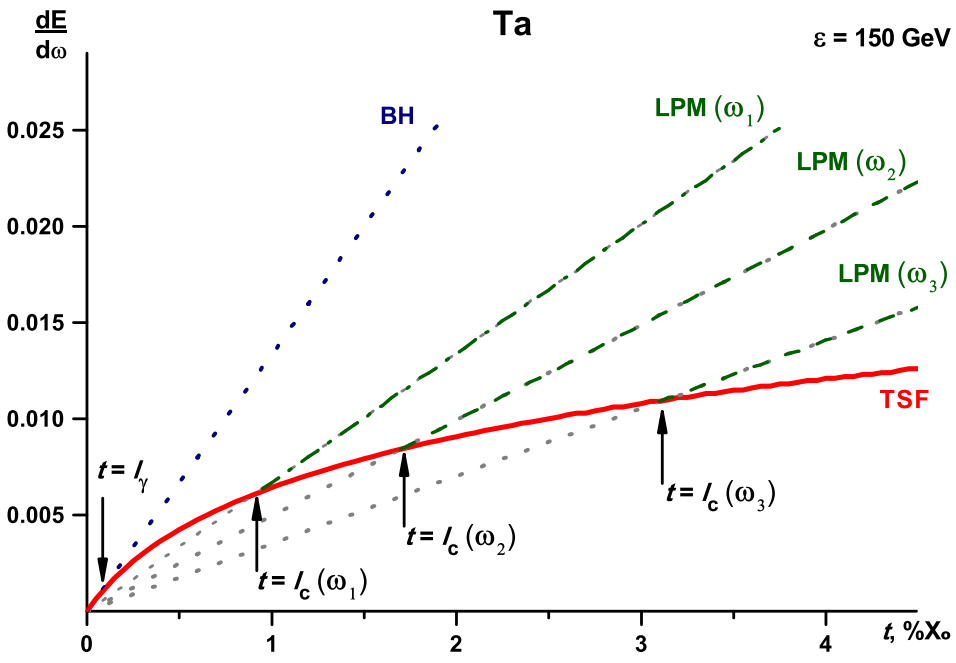

Figure 5.14: The radiation power spectrum of 150 GeV electrons in tantalum target via target thickness t ($\% X_0$). The detailed description of curves is given in text.

At the target thickness increasing the condition $t = l_\gamma$ could be fulfilled, and at this point the dipole regime of radiation is changed for the non-dipole that leads to suppression of radiation comparing with the Bethe–Hietler formula predictions.

For relatively soft photons, for which $l_c \gg t$, the radiation power for this part of radiation spectrum is determined by the formula (5.72), that means the TSF regime of radiation with the logarithmic dependence of radiation intensity on the target thickness t: the solid line TSF in Fig. 5.14. As it follows from (5.72), $\langle dE_{\rm TSF}/d\omega \rangle$ does not depend on the emitted photon energy ω, however, the validity condition of the TSF regime (5.55) does. This means that for different ω_n the transition from the TSF to LPM regime of radiation takes place at different values of target thickness $t_n = l_c(w_n)$. In Fig. 5.14 there are three such points marked by arrows for different photon energies ω_n, namely $\omega_1 = 150$, $\omega_2 = 350$ and $\omega_3 = 800$ MeV. There are also three different dot-dashed lines LPM in this figure, which are calculated using the Migdal formula (5.40) for these values of photon energy respectively. Thus, changing the target thickness one can consequently observe three different mechanisms of radiation of relativistic electron in amorphous target such as the BH, TSF and LPM.

The first, and unique for the moment, experimental investigation of the thickness dependence of the radiation spectrum density of ultra relativistic electrons in an

amorphous matter, in which the predicted earlier a special feature of the radiation of so-called "semi-bare" particles, was finally carried out at CERN by the collaboration NA63 [153].

In spite of all difficulties connected with a very complicate experimental setup and operating with a set of thinnest targets of several microns thickness, this experiment gave an opportunity to retrace the gradual transition from the Bethe–Heitler regime of radiation, with the linear dependence of bremsstrahlung intensity on the target thickness [110], through the Ternovskii–Shul'ga–Fomin mode of radiation, with the logarithmic dependence [137,138], to the Landau–Pomeranchk–Migdal regime, with the linear dependence of the radiation intensity again, but suppressed comparing with the Bethe–Heitler theory predictions [11, 120].

At the end of this section, in Figs. 5.15 we present the comparison of the results of our calculations of the thickness dependence of the spectral density of radiation with the experimental data obtained by the NA63 CERN collaboration [153]. For numerical calculations we used the original Fortran code based on the formulae (5.72) and (5.40).

The results of our calculations are presented in Figs. 5.15 as the radiation power spectrum per unit length, i.e. $dE/d\omega$ multiplied by X_0/t, as it was done in [153]. In these units the linear dependence of the radiation power spectrum for the BH (dot-dashed line) and LPM (dashed line) regimes of radiation are the constants, in contrast to the corresponding curves presented in 5.14, where usual $dE/d\omega$ is presented. Following [153], we took into account the multiphoton effect by corresponding normalization on the BH radiation spectrum.

The results of our calculations give a little excess (about 10 %) over the results presented in [153] by TSF curves in all figures, that may be connected with a different procedures of numerical calculations. This gives even slightly better agreement of our results with experimental data in average.

The TSF curves in Figs. 5.15 show the logarithmic behavior of the radiation power spectrum exactly in the intermediate region $l_c > t > l_\gamma$ for the given ω, as it follows from the theoretical analysis given in Section 5.3.3.

The essential discrepancy observing around the point $t = l_c$ is easily explainable by the fact that the Migdal theory of the LPM effect is applicable at $t \gg l_c$ while the (5.72) for the TSF regime of radiation is derived for $t \gg l_c$. In the intermediate region ($2\,l_c > t > l_c/2$) we have a smooth transition between these two regimes.

Finally, we have to conclude, that in fact, in [153] there was realized the first experimental study of the space-time evolution of the radiation process of ultra relativistic electron in matter, that demonstrated a non-trivial behavior of the charged

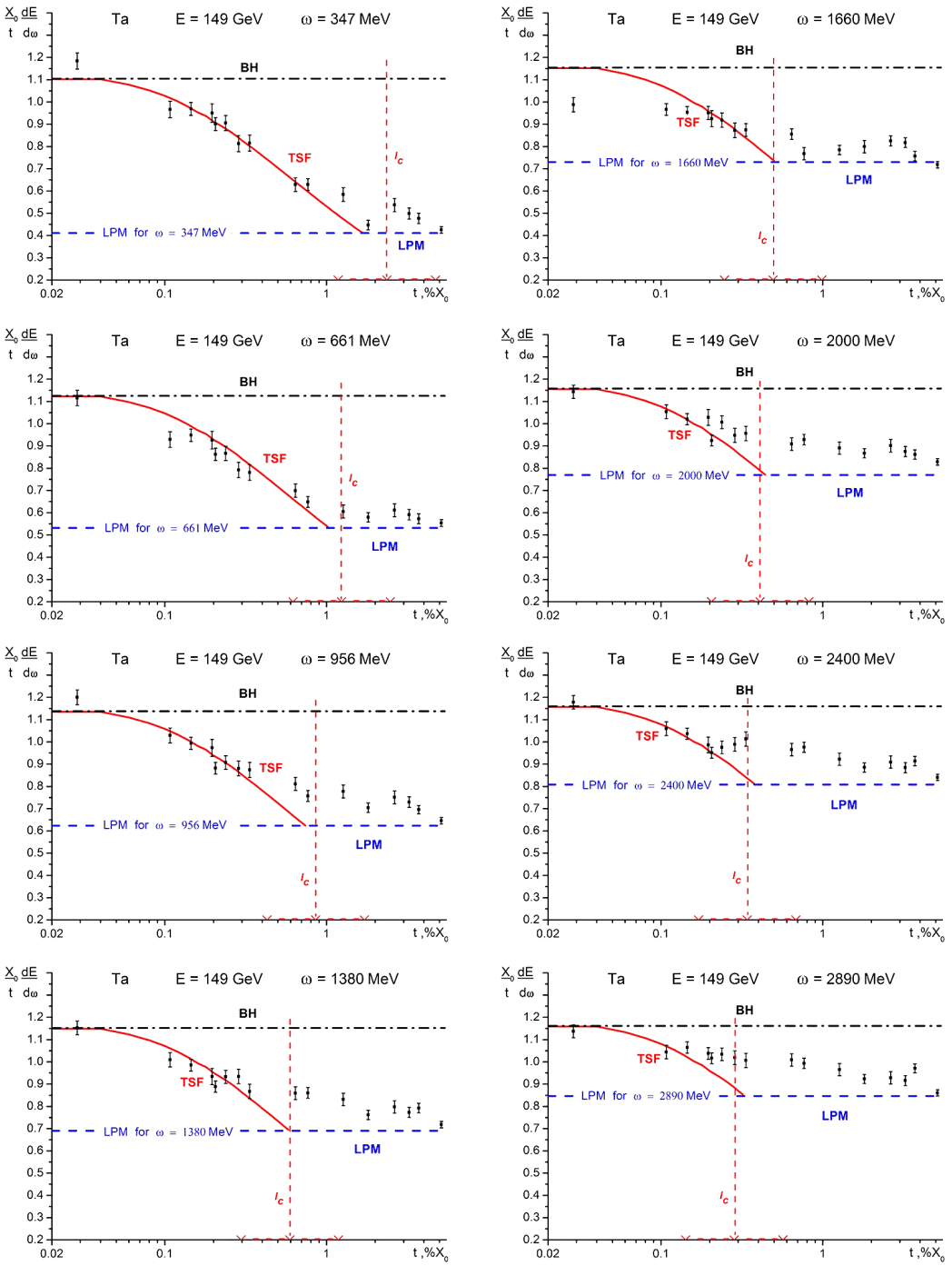

Figure 5.15: The radiation power per unit length for 149 GeV electron radiation in tantalum target as a function of the target thickness t in the units of the radiation length ($\%\, X_0$). The detailed description of curves is given in text.

particle with non-equilibrium own Coulomb field at the interaction with medium atoms in the framework of in QED [12, 139, 165, 166]. Note that this effect should have its analog also in QCD at quark–gluon interaction (see, e.g., [167–170] and references therein).

Our results represented in this Section, including preliminary analysis of the conditions of applicability of different approaches and effects in radiation for the optimization of their further experimental study, a new theoretical results on the features of spectral-angular and polarization characteristic of the radiation in a thin target at non-dipole regime of radiation, as well as comparison of obtained results with available experimental data, were published in [156, 159, 164, 171] and presented at a number of international conferences: Channeling 2004, QEDSP 2006, Channeling 2006, MGU 2007, RREPS 2009, Channeling 2010.

Finally, we have to conclude, that in fact, in [153] there was realized the first experimental study of the space-time evolution of the radiation process of ultra relativistic electron in matter, that demonstrated a non-trivial behavior of the charged particle with non-equilibrium own Coulomb field at the interaction with medium atoms in the framework of in QED.

Chapter 6

Conclusion to Part I

The theoretical study of the multiple scattering effect on the dynamics and radiation of high energy charged particles in an amorphous and crystalline media performed in the first part of the thesis by means of both analytical and numerical calculations, as well as with the help of computer simulation, showed the essential changing in electrodynamics processes at high energies caused by this effect. There is not only a fundamental aspect of the correct description of these processes at transition to the ultra high (TeV and higher) energy diapason of accelerated particles, but also an opportunity for practical use of new specific possibilities connected with coherent effects in scattering and radiation of fast charged particles in aligned crystals or non-dipole regime of radiation.

One of such possibilities, namely, to use the coherent effect in scattering of fast charged particles in aligned crystals for the measurement of the anomalous magnetic moment of short-living particle has been considered in the first part of this thesis in order to find the optimal conditions to carry out the measurement of the anomalous magnetic moment of the baryon Λ_c^+ at the LHC.

The optimization of the parameters for an experimental setup was carried out on the basis of Monte–Carlo simulation of the Λ_c^+ passage through a bent crystal in the planar channeling regime using the original computer code based on the binary collisions model. This model besides the coherent scattering of fast charged particle on crystal lattice atoms takes into account in the most natural way incoherent scattering on thermal vibrations of atoms at lattice nodes, and scattering on an electronic subsystem of a crystal.

The results of the research conducted in the thesis give an optimistic forecast for the possibility of carrying out such an experiment at the LHC and became the basis of the corresponding proposal. Our analysis shows that a precision of $\pm$ 0.1

on the g-factor could be reached within data taking time from a few days to about one month in case of using the crystal with optimal length and curvature.

The fulfillment of the LHCb detector requirement of deflecting the Λ_c^+ on the angle $\Theta = 15$ mrad reduces the efficiency of measuring the magnetic dipole moment of Λ_c^+ with respect to the case of optimal crystal parameters. The use of germanium crystal instead of silicon enhances the efficiency by a factor 3–10. In this case a precision on g-factor of ± 0.1 could be reached within the time from ten days to about one year of data taking with the most probable time of about two months. The uncertainty on the needed data taking time could be significantly reduced by measuring more precisely the α parameters and the absolute value of Λ_c^+ polarization.

For a greater efficiency of the experiment it is essential to be able to register energetic decay products of Λ_c^+. In case the detecting efficiency of particles with energies above 500 GeV (800 GeV) is very low, the silicon (germanium) crystal with a length ($L_{\text{crys}} = 8$ cm) is enough, otherwise there is a benefit of using longer ($L_{\text{crys}} = 12$ cm) crystals.

These results were published recently in [99].

The multiple scattering effects of ultra relativistic electrons and positrons radiation in aligned crystals are also considered in the first part of the thesis. This study is performed in the framework of both quantum and classical electrodynamics approach for describing the relativistic particle radiation and the computer simulation of fast charged particles passing though a crystal using the above-mentioned model.

The results of this investigation show a strong multiple scattering effects on relativistic electron and positron radiation in a thin crystal, as well as in a thin amorphous target. The non-dipole regime of particle radiation, which takes place due to multiple scattering at a certain conditions, leads not only to the suppression of the radiation spectrum in a soft part of emitted gamma quanta spectrum (the so-called TSF effect), but also to the essential changes in angular distributions of relativistic particle radiation and their polarization characteristics. It is shown in the thesis, that at the non-dipole regime of radiation of a high energy electrons the spectral-angular distribution and the polarization characteristics of radiation are essentially differ from the results of the Bethe–Heitler theory that are commonly used now. In particular, it is shown that in the contrast to the Bethe–Heitler theory predictions, instead of the maximum, there is a local minimum in the angular distribution of emitted gamma quanta in the initial direction of the electron beam motion. The maximum in the angular distribution of radiation is at the angle $\theta = \gamma^{-1}$ to the electron beam direction.

It is also shown, that using the natural separation of the characteristic cones of radiation of a relativistic particle $\triangle\theta = \gamma^{-1}$ at the condition of the non-dipole regime of radiation ($\gamma\vartheta_s > 1$), gives a new opportunity for obtaining a high degree of linear polarization by collimating the emitted photon beam by the slit collimator with the angular width $\triangle\theta = \gamma^{-1}$. The degree of linear polarization in this case comes up to 80 % for 200 GeV electrons passed through the 20 μm tungsten crystal, for example. One more result of this consideration is the general statement that the circular polarization of a photon emitted in a thin crystal ($T \ll l_c$) can not be essentially differ from zero. This statement is based on the fact of the symmetry of the polarization tensor at the condition $T \ll l_c$.

For the experimental observation of the effects described above a high angular resolution (better than γ^{-1}) of the gamma-detector is needed, as well as a small (less than γ^{-1}) divergence of the electron beam. This makes observing these effects on existing electron accelerators quite problematic. However, the currently designed future linear electron-positron colliders of the TeV range of energies like ILC and CLIC will be a very suitable tool for this. Moreover, when designing them, as well as developing corresponding detectors, it is necessary to take into account the effects considered in the present thesis.

Without the possibility of direct experimental verification of theoretical predictions for the angular distributions of radiation intensity and its polarization characteristics in thin amorphous and crystalline targets under the non-dipolity conditions, the indirect verification of the approach used in the thesis was conducted by comparison with the experimental data on the spectral density of ultra relativistic electron radiation under the conditions of the TSF effect obtained at the CERN SPS accelerator in the framework of the NA63 collaboration [152] and [153]. This comparison showed a good agreement with the results of the corresponding calculations. As the result of the theoretical analysis of the experimental data [153], we can conclude that the logarithmic dependence of radiation yield from the target thickness, which was confidently observed in this experiment, in fact, is the first direct demonstration of the radiation of a relativistic electron with non-equilibrium own Coulomb field (TSF effect) predicted and theoretically studied before in the works [137–139]. Note that this effect should have its analog also in QCD at quark-gluon interaction.

The results obtained in the Part I of this thesis were published in [99, 156, 159, 164, 171].

Part II

Transients in the nuclear burning wave reactor

Chapter 7

Introduction

7.1 Main problems of nuclear power

After the Chernobyl accident, the ensuring of safety of the operation of nuclear reactors has become the main requirement at designing a new generation of reactors. The fulfilment of this requirement implies the use of special physical principles and mechanisms that provide the reactor with the property of so-called "intrinsic safety", which excludes the possibility of uncontrolled reactor runaway under any circumstances.

Another problem of the long-term sustainable development of a nuclear power is a limited Earth's resources of ^{235}U isotope which is the main fuel component of nowadays nuclear reactors working on thermalized neutrons. This problem can be solved in principle by the transition from thermal neutron reactors to fast reactors (FR) that gives an opportunity to involve in the energy production not only ^{235}U, but also ^{238}U and ^{232}Th. As known, using fast reactor-breeders it is possible to organize an expanded reproduction of artificial fissile isotopes of ^{239}Pu (from ^{238}U) and ^{233}U (from ^{232}Th), which can be subsequently used as a fuel both for fast reactors and thermal reactors. This means the organizing the so-called closed fuel cycle which includes the creation of a number of fast reactor-breeders (hundreds in the global scale) as well as an appropriate industry for chemical reprocessing of spent fuel, extracting fissile isotopes, and fabricating a new nuclear fuel for further usage. In addition to the appreciable rise in the cost of nuclear energy production, this also leads to additional environmental and other risks associated with the need for transportation of fissile materials and their reliable protection from falling into the hands of terrorists.

One more crucial problem of large-scale production of nuclear energy is the treatment of long-lived radioactive waste. Some of minor actinides (MA), i.e. heavy

transuranic elements produced by neutron irradiation of fuel isotopes, have half-lives of tens and hundreds of thousands of years. These elements are one of the main environmental hazards of nuclear power in the long term.

There are different approaches and concepts developing now for the solving each of these problems (see, e.g., [172] and references therein). One of the most attractive concepts, which in the case of its realization can solve or at least mitigate all these problems simultaneously, is the fast reactor-breeder working in self-organizing regime of the nuclear burning wave (NBW). The intrinsic safety of such fast reactors (FR) consists in the fact that self-sustained non-linear process of production and burning of plutonium implements a special kind of negative reactivity feedback that ensures stability of the reactor operation. This prevents the appearance of reactivity-initiated accidents in FR without any reactivity control. In FR of this type natural or depleted uranium can be used as its main fuel, except for the ignition zone of the initial critical assembly. It is expected that in such a reactor it will be possible to use also spent fuel from conventional reactors, thus producing the post-combustion of the radioactive waste contained in it, including MA. The level of fuel burn-up can be very high that means very effective utilization of the nuclear fuel (which consists mainly from ^{238}U and ^{232}Th) and thereby gives the possibility to realize the so-called "one-through" open fuel cycle instead of the close one, thereby significantly reducing the cost of nuclear power.

The Part II of this thesis is devoted to development of the physical basis of the NBW reactor and, in particular, the theoretical investigation of transient processes in such a reactor and the stability of the NBW regime.

7.2 Basic principles of the NBW concept

The idea of organizing the breeding (production) of fissile nuclides and its burning (fission) in the same so-called Breed-and-Burn (B&B) reactor without refuelling and chemical fuel reprocessing was first announced by the Soviet academician S.M. Feinberg [173] in 1958 during the discussion of FR technology at the 2nd U.N. Int. Conf. Peaceful Uses of Atomic Energy (Geneva, Switzerland). He stated there that the difficulties of calculations and the considerable uncertainties in nuclear data, as well as the lack of fuel cells capable of providing a significant fuel burn-up do not allow to draw a definite conclusion about the feasibility of implementing this concept at that time.

There were also several attempts of theoretical consideration of the B&B reactor concept undertaken later by different research groups using different approaches and

schemes. Among them: the scheme of continuously adding the natural uranium to the active zone of reactor with simultaneous removing of spent fuel was considered on the basis of solving the set of burn-up equations studied by K. Fuchs and H. Hessel [174]; feasibility analysis of fuel self-provision fast reactor with deep fuel burn-up done by J.S. Slesarev, V.A. Stukalov and S.A. Subbotin [175]; the optimizing fuel rod reshuffling strategy in B&B reactor developed by M.J. Driscoll et al. [176]; and some others.

A fundamentally new concept of B&B fast reactor was proposed by Lev Feoktistov in 1988 [177,178]. This concept is based on the phenomenon of self-sustained non-linear nuclear burning regime in the form of traveling wave which propagates in fertile uranium or thorium medium. This phenomenon is analogous to well known example of the formation of stable propagation of the flame front at combustion process when a small region, where the reaction of oxidation takes place, moves at a constant velocity relative to the combustible. Depending on the condition of the combustible medium, the flame front propagation can be realised in two essentially different regimes. If the combustible material is "ready" for the oxidation process, then propagation of flame front takes place in the shock-wave regime, and such behaviour is called — detonation. If the medium is "not ready" and needs a certain preparation (for example, additional heating of cold combustible material near the flame front due to a thermo-conductivity process), this regime is called deflagration (or slow burning).

In the case of nuclear burning process, instead of thermo-conductivity, the breeding of fissile nuclides due to the neutron irradiation of a nearest layer of fertile fuel material takes place: $^{238}\mathrm{U}(n,\,\gamma) \rightarrow\ ^{239}\mathrm{U}(\beta) \rightarrow\ ^{239}\mathrm{Np}(\beta) \rightarrow\ ^{239}\mathrm{Pu}(n,\,\mathrm{fission})$.

The possibility of realization of essentially non-linear process of self-sustained slow nuclear burning in the form of running wave that propagate inside the fertile material ^{238}U (see Fig. 7.1) was first demonstrated by Feoktistov [177,178]. It was done on the basis of solution of the set of non-linear diffusion equations describing the neutron transport in multiplicative medium, properties of which are continuously changed due to the neutron irradiation. These changes were described by the set of corresponding burn-up equations.

Trying to find an analytical solution, Feoktistov maximally simplified the problem formulation. He considered a schematic one-dimensional linear model of FR with the U–Pu fuel cycle limiting the chain of nuclear transformations by only three main nuclides of this cycle: ^{238}U, ^{239}Np and ^{239}Pu.

Initiated in any way the nuclear chain reaction ("nuclear burning") will shift to the breeding zone, adjacent to the first one, due to the plutonium production there.

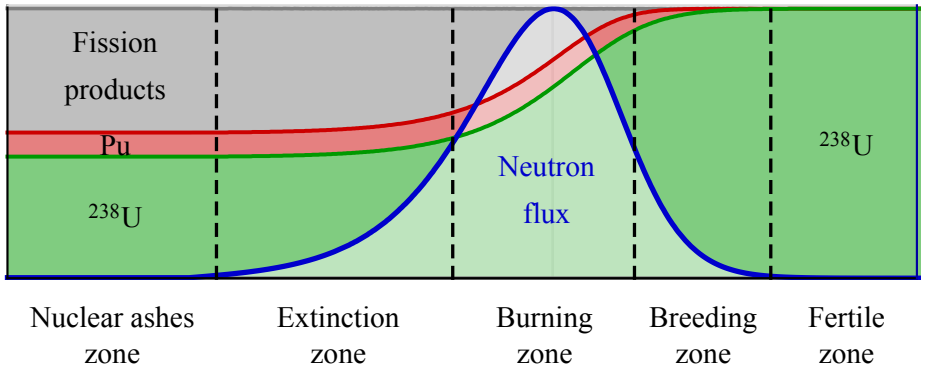

Figure 7.1: Propagation of nuclear burning wave inside the fertile material ^{238}U.

In such a way the nuclear burning wave can slowly propagate inside the breeding zone. After the front of this wave the chain reaction is dying down gradually due to the fuel burn-up and accumulation of a large amount of fission products, which absorb neutrons efficiently.

In the approach of self-similar solutions of abovementioned set of neutron diffusion and burn-up equations Feoktistov proved the existence of self-sustained regime of nuclear burning wave (he called it a "neutron-fission wave") which propagate into fertile zone, and estimated the velocity of the burning front propagation. Note that critical state in this simple model of FR was supported automatically without any external control. Feoktistov also find out the criterion of existence of a nuclear burning wave regime, namely, the equilibrium concentration of ^{239}Pu in the active zone of such a system must be slightly higher than critical one [177, 178]. The equilibrium concentration of plutonium is defined by a set of burn-up equations, while its critical concentration is defined by zeroing the time derivative of the neutron concentration in the corresponding non-stationary diffusion equation. As followed from the Feoktistov criterion, a self-sustained NBW regime is impossible in a reactor on thermal neutrons since a low conversion ratio from fertile to fissile materials in such a reactor [177, 178].

One of the main advantages of the proposed by Feoktistov concept of the B&B reactor is that it does not need a reactivity control and therefore the initial fuel composition of the reactor will evolve according to neutron-nucleus processes without an external intervention and any refuelling or fuel shuffling during the full reactor campaign. It is also necessary to remind, that such a reactor can use natural or depleted uranium (and, probably, thorium) as a fuel, excluding a start-up stage only.

The further development of Feoktistov's ideas was obtained in the works of Goldin et al. [179, 180]. In these papers the self-organizing B&B processes in FR, which the authors have called as a self-adjusting neutron-nuclide regime, was studied by means of numerical solution of the set of equations including the non-stationary quasi-diffusion equation, the fuel burn-up equations and the equations of reactor kinetics. The calculations were carried out using one-group approximation and one-dimensional models of FR consisting of two zones: the ignition zone, containing the uranium fuel enriched by plutonium up to a certain concentration providing the criticality of the FR at the initial stage, and the breeding zone filled with natural or depleted uranium.

The results of investigation [179, 180] have shown that in critical assemblies of FR a self-sustained nuclear burning regime can evolve without control for a long time reaching a high level of fuel burn-up (up to 30 %). However, as it follows from the results obtained in [179], the NBW is not observed in their model. The reactor starts to damp earlier than the wave regime is formed. The detailed analysis of the reasons, why the NBW regime was not observed in [179] was performs later in [181]. The possibility of the NBW regime in a linear one-dimentional FR was shown in [181] by some improving and modifying the calculation approach used in [179]. The existence of the NBW regime in a linear FR was also confirmed in [182] by numerical calculations carried out for the simple Feoktistov's model both in the self-similar solution approach and in the corresponding non-stationary one.

Attempts to study the NBW phenomenon by means of analytical methods for solving this essentially nonlinear, non-stationary problem were pursued, following Feoktistov [177, 178], in the works of a number of other authors [183–189] and others. Taking into account the complexity of the problem, for this purpose one has to resort to a number of rather strong simplifications, such as one-dimensional geometry; one-group approximation; a self-similar solution of the non-stationary equation. The last one means finding an asymptotic stationary solution of the problem, but losing an opportunity of the study of transient processes, as well as the stability study of the NBW regime. The majority of such approaches are based on the artificial introducing of "phenomenological" parameter of reactivity feedback, which is in fact the most important internal coupling factor of the self-organizing NBW regime. Undoubted value of analytical methods lies in the establishment of direct relations between different parameters in the system. However, the use of significant simplifications of the problem, which are inevitable in the considered case, makes it difficult to establish the correctness of obtained analytical (or semi-analytical) solutions to the real physical system.

In [190–192] a some combination of the NBW reactor with accelerator driven system (ADS), called as "Soliton Hybrid Reactor", in which the NBW parameters would be controlled by means of an external neutron source on the basis on a proton accelerator have been considered on the basis of both analytical approach and computer simulation using GEANT3 and ANET codes.

The concept of the fast reactor working in self-sustained NBW regime was also considered by many other research groups using different approaches for its study and different names, such as, the "Nuclear Deflagration Wave" [193], the "Criticality Wave" [183], CANDLE burn-up strategy [194], and others. The ambitious plan for the construction of so-called "Traveling Wave Reactor" in the near future was announced recently by the firm TerraPower created with financial support from Bill Gates [195].

In [193] the concept of a "Completely automated nuclear reactors for long-term operation" was considered by Edward Teller with co-authors on the basis of numerical solution of the corresponding non-stationary problem using the Monte–Carlo simulation of the "Deflagration Wave" propagation in FR of prolate form with a fuel of the U–Th cycle. The results of the simulations showed a possibility of the NBW regime realization in thorium fuel, and in this case the wave has traveled a distance of 5 m over 30 years. Due to the fact that this FR does not need a human access during its operation time, in [193] it was proposed to place it underground under a depth of 100 m in order to increase its safety.

Many aspects of the NBW concept were intensively studied by Hiroshi Sekimoto with co-authors (see, e.g., [194, 196–198]. In these works the nuclear burning regime (named CANDLE as the acronym stands for "Constant Axial shape of Neutron flux, nuclide densities and power shape During Life of Energy production") has been studied in the self-similar solution approach, i.e., in the same way as Feoktistov did [177, 178]. The value of the works of Sekimoto and his group is that the calculations were carried out using multigroup diffusion approximation in two dimensional cylindrical FR model employing a long nuclide chain in the burn-up equations, much larger than Feoktistov did. However, the consideration based on the self-similar solution of the neutron transport equation does not allow to describe a transient processes in such a system, as well as to carry out its stability study.

A significant contribution to development of the physical basis of the NBW reactor concept was done in works of the investigator group from NSC KIPT starting from 1999 [182, 199, 200]. The most important progress in the development of the deterministic approach which allows describing the space-time evolution of NBW, including the stage of its initiation, evalution and fading out, as well as the NBW

regime reaction to various external influences [181, 201–205]. This approach is based on numerical solving the non-stationary diffusion equation for neutron transport together with the set of burn-up equations for fuel components and the equations of nuclear kinetics for precursor nuclei of delayed neutrons. This computational model has undergone significant development, beginning with the consideration of the problem using a simplified model of one-dimensional planar geometry of a fast reactor in the single-group approximation [181], and ending with the solution of the evolutionary problem in the two-dimensional cylindrical geometry of the reactor using the multigroup approach [205].

The presented in this thesis results of studies of transient processes in the NBW reactor was obtained on the basis of the "intermediate" calculation scheme which describes the non-stationary processes in cylindrical FR using the radial buckling concept and effective multigroup approach developed in [203, 204]. This gives the possibility of significant (an order of magnitude) economy of the computing time at the simulation of non-stationary processes in the NBW reactor, while not missing the main factors determining the global behavior of the physical system. Among these factors there are the transverse leakage of neutrons, taking into account using the buckling approximation [206], and the space-time evolution of the neutron spectrum using the effective multigroup approach [204]. The direct comparison of the results of the calculations obtained using the above-mentioned model with those from the true two-dimensional model using a true multigroup calculation, carried out in [205], showed that the radial buckling approximation ensures a satisfactory description of the FR parameters with the only difference that neglecting the radial non-uniformity of the fuel burn-up leads to the fact that the same NBW behavior is observed at a slightly smaller reactor radius.

Chapter 8

The calculation scheme

The study of the nuclear burning wave phenomenon we perform by means of calculations of the space-time evolution of the neutron flux and fuel composition in fast reactor (FR) using the deterministic approach developed in [181, 201–204]. This approach is based on the numerical solution of the non-stationary diffusion equation of neutron transport in a multiplying medium together with the nuclear kinetics equations for delayed neutron precursors and the set of burn-up equations for the main nuclides of the fuel transformation chain. In [181, 201–204] this method was used for investigation of initiation and propagation of NBW in FR with the U-Pu fuel. Now we apply this method for analyzing the possibility of the NBW regime realization and its stability not only for FR with U–Pu, but also with Th–U and mixed Th–U–Pu fuel cycles.

8.1 Geometrical setup

We consider a cylindrical two-zone homogeneous FR (see Fig. 8.1). In the ignition zone near the left edge of the reactor the fuel is enriched with fissile nuclides (^{235}U, ^{233}U or ^{239}Pu) of about 10 % that is close to its equilibrium concentration at the NBW stationary stage [181, 201–204]. The second zone (the breeding zone), adjacent to the ignition one, is filled with fertile materials such as ^{238}U, ^{232}Th or their mixture. We chose a metal fuel to have as more hard neutron spectrum as possible in the assembly, and correspondingly higher breeding ratio. To compensate the swelling effect which is connected with production of a big amount of fission products, and which is noticeable enough for metal fuel, we put in our calculations a certain value of fuel porosity $p = 0.2$–0.3. Both zones also include the constructional material Fe and coolant of different types, such as liquid metal Na, Pb–Bi eutectic or He. The

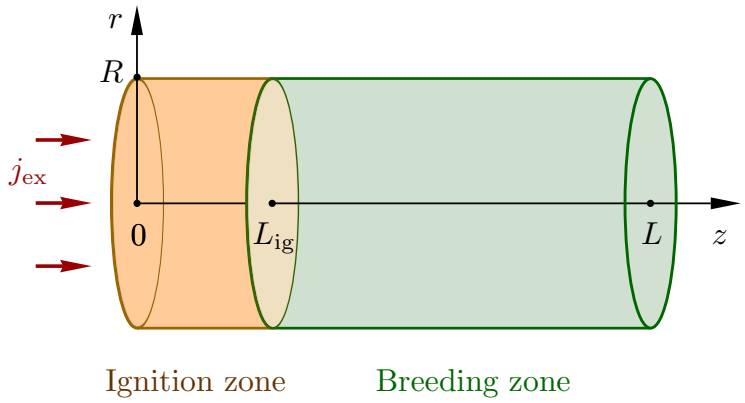

Figure 8.1: The initial critical assembly of FR

volume fractions of all these components were chosen to be close to the composition of actual fast reactors.

Parameters of the initial critical assembly, including the composition of the reactor core, its radius R and the length of the ignition zone L_{ig} (see Fig. 8.1), were determined by the numerical solution of the multi-group criticality problem [206]:

$$-\frac{\partial}{\partial z} D^{g} \frac{\partial \Phi^{g}}{\partial z} - \frac{1}{r}\frac{\partial}{\partial r} r\, D^{g} \frac{\partial \Phi^{g}}{\partial r} + \left(\Sigma_{a}^{g} + \Sigma_{in}^{g} + \Sigma_{mod}^{g} - \Sigma_{in}^{g\to g}\right)\Phi^{g} = \\ = \frac{1}{k_{eff}} \chi_{f}^{g} \sum_{g'=1}^{G} (\nu_{f}\,\Sigma_{f})^{g'}\,\Phi^{g'} + \Sigma_{mod}^{g-1}\Phi^{g-1} + \sum_{g'=1}^{g-1} \Sigma_{in}^{g'\to g}\,\Phi^{g'}, \qquad (8.1)$$

where, Φ^{g} is the scalar neutron fluxes in the energetic group g; $D^{g} = 1/(3\Sigma_{tr}^{g})$ is the group diffusion coefficient; $\Sigma_{a}^{g} = \Sigma_{f}^{g} + \Sigma_{c}^{g}$, Σ_{f}^{g}, Σ_{c}^{g}, Σ_{in}^{g}, Σ_{mod}^{g}, and Σ_{tr}^{g} are the group macroscopic cross-sections of absorption, fission, radiative capture, inelastic scattering, moderation and transport of neutrons; $\Sigma_{in}^{g'\to g}$ is the macroscopic cross-sections of neutron inelastic scattering for the transition from group g′ to g; χ_{f}^{g} is the neutron fission spectrum in group g; ν_{f} is the mean value of the neutron number in group g per one nuclear fission event; k_{eff} is the effective neutron multiplication factor. By varying the length of the ignition zone L_{ig} with the rest of the assembly parameters set (reactor radius and composition), we achieve the value of k_{eff} sufficiently close to unity, leaving it slightly larger than one to startup the reactor.

To generate a neutron field in the system and initiate the nuclear burning process we suppose that the left boundary of FR is irradiated by an external neutron flux j_{ex} during a certain time interval. The intensity of the external neutron flux has been chosen to be $j_{ex} = 6 \times 10^{11}\,\mathrm{cm}^{-2}\,\mathrm{s}^{-1}$ for all variants of calculations. This external neutron flux does not irradiate the ignition zone permanently but it is turned off

at an early enough stage of the FR operation. The turn-off moment $t_{\rm off}$ is chosen empirically to ensure a sufficient level of the neutron flux in the system for the further development of NBW process. In the calculation presented below the value $t_{\rm off}$ from 10 to 100 days was used depending on the FR composition. The initial space distribution of the neutron field Φ_0 corresponds to the neutron flux in the critical FR normalized to the averaged energy production of $10^{-8}\,\mathrm{kW\,cm^{-3}}$.

8.2 Neutron diffusion equation

Our study of initialization and propagation of NBW in the above mentioned FR is based on numerical solution of the non-stationary neutron diffusion equation. The calculations are carried out using the effective multi-group approach [201, 202] where the effective one-group cross sections are determined by means of averaging the group cross sections over the local neutron spectra found from solving the corresponding critical multi-group problem for the given time moment. These effective cross sections are used for solving the non-stationary problem under consideration in the one-group approximation.

A one-group non-stationary neutron diffusion equation with taking into account delayed neutrons can be written for the cylindrical model of FR in the form [206]:

$$\frac{1}{\nu}\frac{\partial\Phi}{\partial t} - \frac{\partial}{\partial z}\,D\,\frac{\partial\Phi}{\partial z} - \frac{1}{r}\frac{\partial}{\partial r}\,r\,D\,\frac{\partial\Phi}{\partial r} + \Sigma_{\rm a}\,\Phi - (1-\overline{\beta})(\nu_{\rm f}\,\Sigma_{\rm f})\,\Phi = \sum_j \sum_i \lambda_j^i\,C_j^i. \quad (8.2)$$

Here Φ is the scalar neutron flux, $\Sigma_\alpha = \Sigma_j\,\sigma_\alpha^j\,N_j$ is the macroscopic cross section of the neutron reaction (the index α corresponds to the reactions of neutron absorption (a) and fission (f)), N_j is the concentration of j'th nuclide; σ_α^j is the corresponding effective one-group microscopic cross section; $\nu_{\rm f}\,\Sigma_{\rm f} = \Sigma_j\,\nu_j^i\,\sigma_j^i\,N_j$, ν_j^i is the mean number of neutrons produced at a single nuclear fission event for the j'th fissile nuclide; $\overline{\beta} = \Sigma_j\,\beta_j\,(\nu_{\rm f}\,\Sigma_{\rm f})_j/\,\nu_{\rm f}\,\Sigma_{\rm f}$ is the effective fraction of delayed neutrons, $\beta_j = \Sigma_i\,\beta_j^i$ and β_j^i, C_j^i and λ_j^i are the portion of delayed neutrons, the concentration and decay constant of the precursor nuclei in the i'th group of the j'th fissile nuclide, correspondingly; $D = 1/(3\,\Sigma_{\rm tr})$ is the diffusion coefficient, $\Sigma_{\rm tr}$ is the macroscopic transport cross section, ν is the one-group neutron velocity.

The boundary conditions for the neutron flux Φ are written in the form

$$\left(\Phi - 2\,D\,\frac{\partial\Phi}{\partial z}\right)\Big|_{z=0} = 2\,j_{\rm ex}, \qquad \left(\Phi + 2\,D\,\frac{\partial\Phi}{\partial z}\right)\Big|_{z=L} = 0. \quad (8.3)$$

where j_{ex} is the external neutron flux falling onto the left boundary of FR ($z = 0$) while the right boundary ($z = L$) is free.

The conditions at the central axis and at the lateral surface of FR are:

$$\left.\frac{\partial \Phi}{\partial r}\right|_{r=0} = 0, \qquad \Phi|_{r=R+\delta_{\text{extr}}} = 0. \tag{8.4}$$

where R is the FR radius and $\delta_{\text{extr}} = 0.71\,\Sigma_{\text{tr}}$ is the extrapolation length.

These conditions are valid for any moment of time within the considered time interval $0 \le t \le T$. Besides, the scalar neutron flux in the corresponding critical assembly Φ_0 is chosen as the initial condition for Φ at the moment $t = 0$. We consider the nuclear burning wave propagation in the axial direction and reduce the problem to a one-dimensional case using the concept of radial buckling that takes an approximate account of the neutron leakage in the transversal direction (see, for example [206]). Then the equation (8.10) takes the form

$$\frac{1}{\nu}\frac{\partial \Phi}{\partial t} + \frac{\partial V}{\partial z} + D\,B_r^2 \Phi + \Sigma_{\text{a}}\,\Phi - (1-\overline{\beta})(\nu_{\text{f}}\,\Sigma_{\text{f}})\,\Phi = \sum_j \sum_i \lambda_j^i\, C_j^i, \quad V = -D\,\frac{\partial \Phi}{\partial z} \tag{8.5}$$

where $B_r = 2.405/(R + \delta_{extr})$ is the radial buckling parameter. It should be noted, that by using the radial buckling conception we neglect the effects of the fuel nuclide burn-up non-uniformity in the radial direction.

The boundary conditions (8.3) can be rewritten as

$$(\Phi + 2\,V)|_{z=0} = 2\,j_{\text{ex}}, \qquad (\Phi - 2\,V)|_{z=L} = 0. \tag{8.6}$$

At all values of z from the interval $0 \le z \le L$, an initial distribution of the neutron flux at $t = 0$ is taken in the form of the initial critical assembly eigenfunction normalized to a small magnitude.

8.3 Burn-up equations

During the FR campaign, its fuel composition changes according to the nuclear transformation chains characteristic of the chosen fuel cycle. In general case, for calculations of FR with different fuel cycles, such as U-Pu, Th-U or mixed Th-U-Pu, it is necessary to consider two main nuclear transformation chains (see Fig. 8.2) that start from the corresponding basic nuclides ^{238}U and ^{232}Th [206].

When writing down the burn-up equations, we use the following numbering of the nuclides entering into the U-Pu transformation chain: 1 — ^{238}U, 2 — ^{239}U,

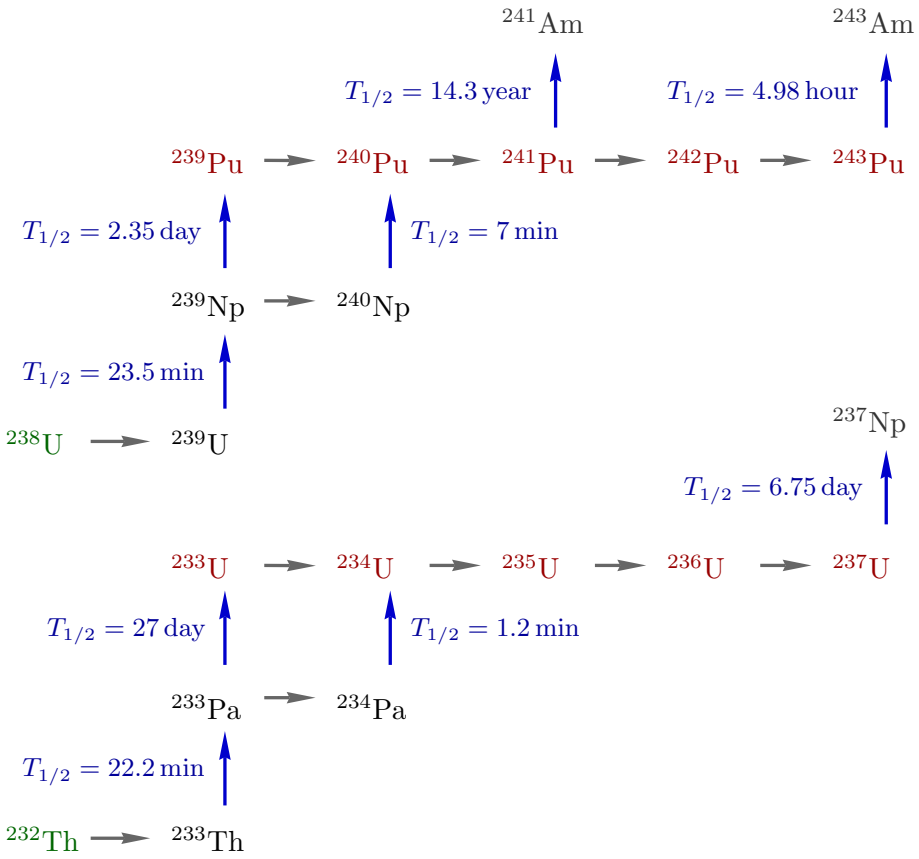

Figure 8.2: Scheme of the nuclear transformations starting from the basic isotope ^{238}U (on top) and ^{232}Th (at the bottom) under neutron irradiation. The horizontal arrows correspond to the (n, γ) reaction, and the vertical arrow corresponds to the β-decay of the nuclide with the half-period $T_{1/2}$.

3 — ^{239}Np, 4 — ^{239}Pu, 5 — ^{240}Pu, 6 — ^{241}Pu, 7 — ^{242}Pu, 8 — ^{243}Am, 9 — ^{241}Am, 10 — fission products (FP) that are considered as a single nuclide. In the calculations, the fission process by neutrons was taken into account for the nuclei with numbers 1, 4, 5, 6, 7. We omit the nuclide ^{243}Pu from the consideration in view of its fast decay. The concentrations of nuclei for this transformation chain

obey the following burn-up equations:

$$\begin{aligned}
\frac{\partial N_1}{\partial t} &= -\sigma_{\mathrm{a}1}\,\Phi\,N_1,\\
\frac{\partial N_l}{\partial t} &= -(\sigma_{\mathrm{a}\,l}\,\Phi+\Lambda_l)\,N_l+(\sigma_{\mathrm{c}\,(l-1)}\,\Phi+\Lambda_{(l-1)})\,N_{(l-1)},\quad (l=2{-}8),\\
\frac{\partial N_9}{\partial t} &= \Lambda_6\,N_6,\\
\frac{\partial N_{10}}{\partial t} &= \sum_{l=1,4,5,6,7}\sigma_{\mathrm{f}\,l}\,N_l\,\Phi. \qquad (8.7)
\end{aligned}$$

where $\sigma_{\mathrm{a}\,l}=\sigma_{\mathrm{c}\,l}+\sigma_{\mathrm{f}\,l}$, $\sigma_{\mathrm{c}\,l}$ and $\sigma_{\mathrm{f}\,l}$ are the effective one-group microscopic cross sections of absorption, radiation neutron capture and fission of the l-th nucleus; $\Lambda_l=\ln 2/\,T^l_{1/2}$ and $T^l_{1/2}$ are the decay constant and half life period of the l-th nucleus. At the initial time moment, certain initial concentrations of these nuclei are chosen: $N_l\,(t=0)=N_0\,l$.

We neglect the burn-up of nuclei ^{239}U, ^{241}Am, ^{243}Am ($\sigma_{\mathrm{a}\,2}=\sigma_{\mathrm{a}\,8}=\sigma_{\mathrm{a}\,9}=0$) since the decrease of their concentrations due to the absorption reactions is small as compared with effects of the processes that are taken into account. The changes of FP due to the neutron absorption also are not considered.

$$\begin{aligned}
\frac{\partial \bar N_1}{\partial t} &= -\bar\sigma_{\mathrm{a}1}\,\Phi\,\bar N_1,\\
\frac{\partial \bar N_l}{\partial t} &= -(\bar\sigma_{\mathrm{a}\,l}\,\Phi+\bar\Lambda_l)\,\bar N_l+(\bar\sigma_{\mathrm{c}\,(l-1)}\,\Phi+\bar\Lambda_{(l-1)})\,\bar N_{(l-1)},\quad (l=2{-}8),\\
\frac{\partial \bar N_{10}}{\partial t} &= \sum_{l=1,4,5,6,7}\bar\sigma_{\mathrm{f}\,l}\,\bar N_l\,\Phi. \qquad (8.8)
\end{aligned}$$

Here, we have designated the corresponding concentrations, microscopic cross sections and decay constants as $\bar N_l$, $\bar\sigma_{\alpha\,l}$ and $\bar\Lambda_l$ using the tilde, in order to distinguish them from analogous quantities for the U-Pu chain. We neglect here the burn-up of nuclei ^{233}Th and ^{237}U ($\bar\sigma_{\mathrm{a}\,2}=\bar\sigma_{\mathrm{a}\,8}=0$) for the same reason as it is mentioned before for the U-Pu fuel cycle.

For the fissionable nuclei from both transformation chains, we have to write down the nuclear kinetics equations for the concentrations of precursors of delayed neutrons. Since the flux Φ changes weakly during the decay time of the precursors of delayed neutrons [181], the number of nuclear kinetics equations may be essentially reduced by using the approximation of one equivalent group of delayed neutrons. In this case, these equations can be written in the following form:

$$\frac{\partial C_l}{\partial t}=-\lambda_l C_l+\beta_l(\nu\mathrm{f}\,\Sigma_{\mathrm{f}})_l\,\Phi,\qquad C_l(t=0)=C^0_l,\qquad \lambda_l=\beta_l/\sum_i\beta^i_l\lambda^i_l. \qquad (8.9)$$

In reactor calculations, the number of groups of delayed neutrons is taken equal to six [206]]. In the one equivalent group approximation, the term $\Sigma_l \Sigma_i \lambda_l^i C_l^i$ in Eq. (8.5) is replaced by $\Sigma_l \lambda_l C_l$ where index l runs over the number of fissionable nuclei in both transformation chains.

For the numerical solution of the diffusion equation (8.5), we use the conservative finite difference method [Pot'73] with a computational mesh with the step h in the variable z ($0 \leq z \leq L$). The time step τ is automatically chosen to ensure a specified accuracy of the neutron flux calculation and its value depends on the flux variation rate at the current time moment. The non-stationary diffusion problem is solved using the implicit difference scheme by Crank-Nicolson [207], as it was done in works [181,201–204]. In our numerical calculations, we use the analytical expressions for the concentrations of nuclei at the next time layer at each space node, which were obtained from the sets of equations (8.7) and (8.8) (see, for example, [181]). These expressions are valid if the neutron flux changes negligibly during the time step. As it is done for the burn-up equations, we also use certain analytical solutions of equations (8.9) for the concentrations of precursors at the next time layer at each space node (see [181]).

During the calculations we take into consideration the variation of neutron flux and the effective one-group cross sections in the FR with time. Therefore, at each time layer we solve the stationary multi-group problem for fluxes in the corresponding critical FR assembly whose composition changes according to the burn-up equations. The group neutron fluxes $\Phi^g(x)$ (where g is the number of neutron energy group) found using this procedure are used to obtain the effective one group cross sections.

The calculations were performed in the 26-group approximation using the group neutron constants from [208]. The method of averaging the group cross sections when passing from a greater number of energy groups to a smaller one is well known (see, for example, [206]). We have used the approach that takes into account the requirement of conservation of rates of corresponding reactions during this procedure.

The scheme of passing from the group microscopic cross sections to the effective one-group cross sections is defined by the relations

$$\sigma_\alpha^l = \sum_{g=1}^{26} \frac{\sigma_\alpha^{g\,l}\,\Phi^g}{\Phi_\mathrm{S}}, \qquad \Phi_\mathrm{S} = \sum_{g=1}^{26} \Phi^g, \tag{8.10}$$

where Φ_S is the neutron flux summed over 26 groups, the index α corresponds to the reactions of neutron capture (c), fission (f) and scattering (s).

The one-group neutron velocity is given by

$$\frac{1}{\nu} = \frac{1}{\Phi_{\mathrm{S}}} \sum_{g=1}^{26} \frac{\Phi^g}{\nu^g}, \tag{8.11}$$

where ν^g is the neutron velocity for the group g.

When averaging the transport cross section σ_{tr}, the requirement of conservation of the neutron leakage value was taken into account, which leads to the following expression

$$\sigma_{\mathrm{tr}}^l = \frac{\sum_{g=1}^{26} \sigma_{\mathrm{tr}}^{g\,l}\, D^g\, \Phi^g}{\sum_{g=1}^{26} D^g\, \Phi^g}. \tag{8.12}$$

Thus, during the whole lifetime of FR the cross sections are averaged in the correspondence to the neutron spectrum alteration that occurs. In this case, the values of effective one-group cross sections at each space point are corrected at each time layer according to the fuel composition changing with time.

As it was shown in [203,204], the results of calculations of the total neutron flux in the multi-group approximation agree well enough with the neutron flux calculated in the one-group approximation with the effective microscopic cross sections found by the aforementioned averaging procedure with the multi-group neutron spectrum for each node of the space mesh. For this reason, we shall search for an approximate solution of the non-stationary problem under consideration using the effective multi-group approach, in which the problem is reduced to solving the non-stationary one-group diffusion equation. In this case, at each time layer we solve a multi-group problem to calculate the group neutron fluxes in the corresponding critical assembly, whose composition changes according to the burn-up equations. The effective one-group cross sections are recalculated at each time step according to the found neutron spectrum at each space node. The solution of the non-stationary problem in this approximation with allowance for the mentioned alteration of the neutron spectrum allows a sufficiently exact description of the evolution of the total neutron flux and the nuclear burning process in the FR. This is the essence of our effective multi-group approach.

Chapter 9

Different compositions of NBW reactor

9.1 Fuel–coolant ratio in U–Pu fuel cycle

Basing on the above-described procedure of solving the set of non-linear equations under consideration, we have carried out a series of calculations of the NBW regime in the critical FR with the metal fuel of the U–Pu cycle with sodium coolant. In these calculations we do not consider any specific characteristics of the FR construction, fuel elements and coolant channels etc. and describe the FR using homogeneous approach, specifying certain realistic values of volume fractions of the constructional material $F_{\mathrm{Fe}} = 20\,\%$, sodium coolant F_{cool} and fuel F_{fuel} with the fuel porosity $p = 0.2$.

This study is aimed to find the optimal ratio between the fuel F_{fuel} and coolant F_{cool} volume fractions. To obtain the dependency of NBW parameters on the composition of the FR a series of calculation was performed for various radii R and various volume fractions of the fuel and coolant. Here we do not study the initiation of the NBW and start each new calculation using the distribution of fuel isotopes obtained in a previous calculation at a steady state regime of NBW propagation, i.e. far from the edges (the initiation of the NBW will be considered in details in the following sections). For each new calculation we reduce the radius R of the FR until we find the critical value R_{cr} at which the NBW regime disappears.

Figure 9.1 presents the total power production P_{tot} and density of power production W as a function of cylinder radius R of FR. Here R is in units of critical radius R_{cr}. The decrease of power production at the radii close to the critical ones is due to the increase of relative neutron leakage (increase of surface-volume ratio of

the active zone). Note that for more fuel concentrated composition (solid red curve) this dependence is stronger which is a negative factor. Besides, a greater issue is connected with a huge power production density in this case. On the other hand a less dense fuel composition (dotted blue curve) require a greater volume and hence is possible only at an extremely high-power FR.

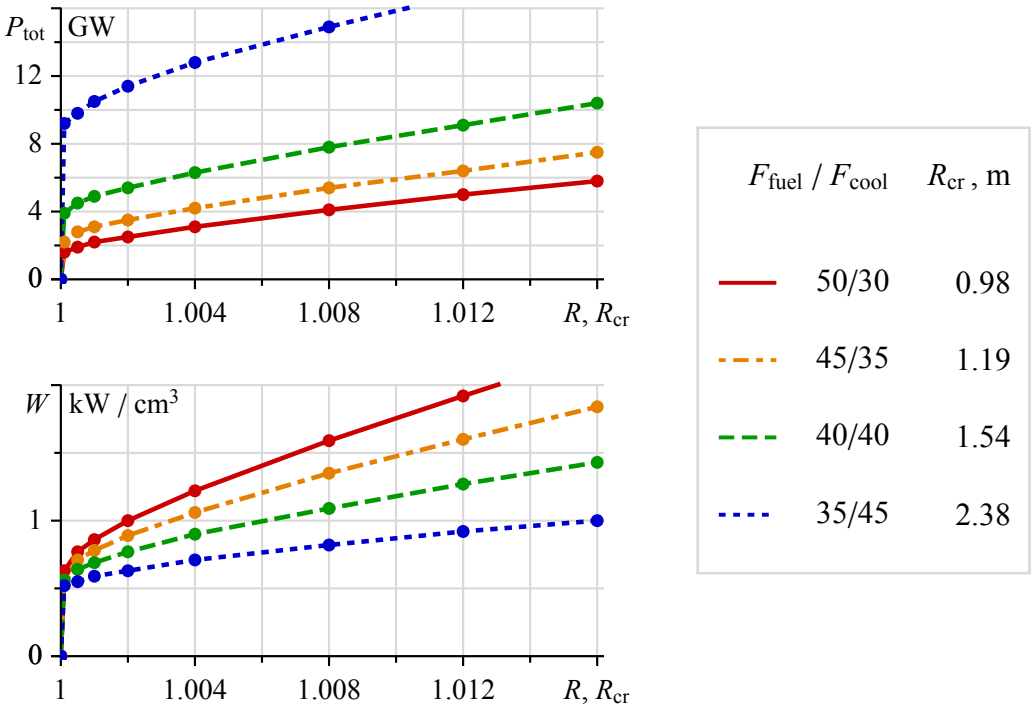

Figure 9.1: Total power production P_{tot} (upper plot) and density of power production W (bottom plot) as a function of cylinder radius R of FR for four variants of reactor composition F_{fuel} / F_{cool}, listed on the right together with the values of corresponding critical radii R_{cr}.

As can be seen from Fig. 9.1, the optimal volume fraction of the fuel is about 40–45 %. The NBW regime in U–Pu fuel starts with the value of power production density $W \approx 500$ W/cm^3, but in the region close to R_{cr} power production strongly depends on the radius. In this light, more stable regime is expected at a higher power production density which might be unrealistic. One of the possible solutions of this problem is to switch to a Th–U fuel.

9.2 Th–U fuel cycle

In this section we would like to clarify the possibility of the NBW regime realization in FR with Th–U fuel cycle. In [193,209] such a possibility was demonstrated on the

basis of the corresponding Monte-Carlo simulations, but in [210] it has been stated that CANDLE burn-up (that is the analogous of NBW regime and TWR concept) "cannot be achieved in the truest sense when thorium is used". Therefore, we decide to check the possibility of the NBW phenomenon in FR with Th–U fuel cycle on the basis of the calculation scheme described in Chapter 8 of this thesis. This approach was successfully applied before for FR with U–Pu fuel cycle in [181, 201–204].

A critical fast reactor of cylindrical shape with two homogeneous zones filled with metallic thorium-uranium fuel is considered (see Fig. 8.1). In the "Ignition zone" the fuel consists of ^{232}Th enriched with ^{235}U. "Breeding zone", adjacent to the "Ignition zone", is filled with ^{232}Th only. The calculations are performed in two cases: taking into account the presence in the reactor of the nuclei of the structural material (Fe) and the coolant (eutectic lead–bismuth alloy or helium), and in the case of a reactor medium consisting only of metallic thorium–uranium fuel, i.e. without structural material and coolant.

The results of our calculations for a hypothetical critical reactor of cylindrical form of the length $L = 5$ m and radius $R = 3.5$ m, which consisted only of ^{232}Th metal fuel with 10 % enrichment of ^{235}U in the fuse zone with a length $L_{\text{ig}} \approx 1.3$ m without taking into account the construction materials and coolant are presented in Fig. 9.2.

The length of the ignition zone was selected to ensure criticality of the reactor for a given cylinder radius and fuel enrichment level. The intensity of the external neutron flux was chosen equal to $j_{\text{ex}} = 6 \times 10^{11}$ cm^{-2} s^{-1}. The external neutron flux was turned off at the time moment $t_{\text{off}} = 100$ days, which provided a sufficient level of neutron flux in the system to realize a self-sustaining nuclear burning regime.

Figures 9.2 shows that the axial distribution of the neutron flux $\Phi(z)$ at the initial stage of burning process is concentrated mainly in the ignition zone. Its absolute value, despite the turning off the external neutron source, increases strongly and reaches a maximum $\Phi \sim 10^{16}$ cm^{-2} s^{-1} approximately at 3 years after the start of the reactor, and then gradually decreases and reaches a stationary value $\Phi \approx 0.25 \times 10^{16}$ cm^{-2} s^{-1}. This value of the neutron flux corresponds to the energy production density of approximately 400 W/cm^3. The total thermal power of the reactor is approximately 6 GW.

The shape of the axial distribution of the neutron flux $\Phi(z)$ after going to steady state remains almost unchanged throughout the whole campaign of the reactor, which lasts about 130 years, while the active nuclear fission region is gradually shifted to the reproduction zone in the form of a slow wave of nuclear burning.

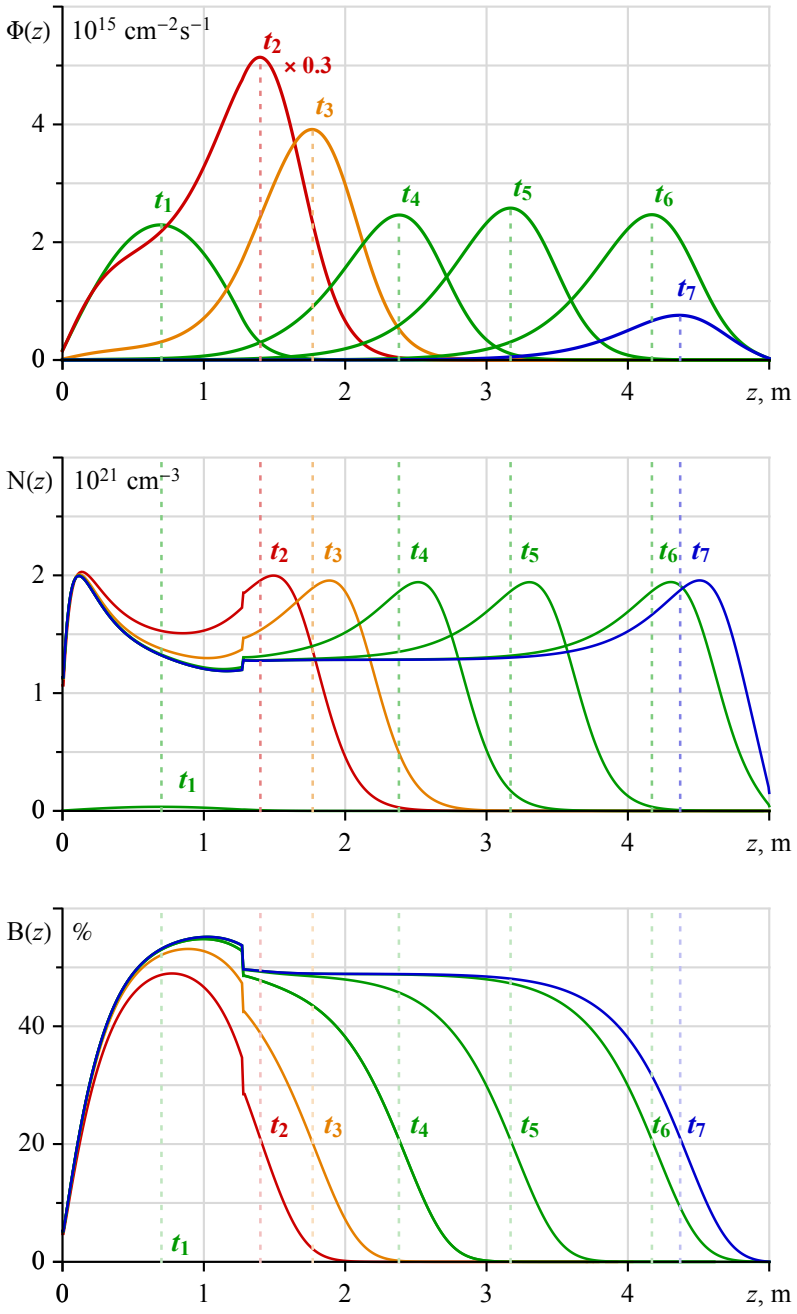

t_1 = 100 days, t_2 = 3, t_3 = 10, t_4 = 40, t_5 = 80, t_6 = 130, t_7 = 145 years

Figure 9.2: The NBW profiles in a hypothetical FR consisting only of metallic Th–U fuel: a scalar neutron flux $\Phi(z)$, concentration $N(z)$ of ^{233}U and the fuel burn-up depth $B(z)$, along the longitudinal coordinate of the reactor for different time moments listed at the bottom.

When the NBW reaches the right edge of the reactor, the stage of its attenuation begins.

The NBW velocity V, defined as the velocity of the moving position of the maximum of the neutron flux $\Phi(z)$ along the axis of the reactor (axis z), under the steady-state NBW conditions, is $V \approx 2$ cm/year. The value of the wave velocity V essentially depends on the radius of the reactor, since an increase in the radius reduces the effect of transverse leakage of neutrons and, as a consequence, leads to a higher level of neutron flux in the wave and, correspondingly, to a higher velocity of its propagation. Similar calculations for a reactor of radius $R = 4$ m give the value of the NBW velocity $V \approx 3.2$ cm/year.

The increase in the neutron flux in the reactor at the initial stage of its operation is due to the gradual production of ^{233}U in the ignition zone and near its right-hand boundary (see plot $N(z)$ in Fig. 9.2) in accordance with the axial distribution of the neutron flux in the system and a relatively small concentration of fission products, effectively absorbing neutrons, at this stage of the NBW evolution.

A superfluous increase in the neutron flux at the initial stage of the reactor operation can be avoided by using a neutron absorber simulating the distribution of fission products similar to the steady state of the NBW propagation, as well as a special initial distribution of fuel enrichment in the ignition zone. One of the possible scenario of solving this problem will be considered in Section 11.1.

Due to the fuel burn-up $B(z)$ (see Fig. 9.2) and the accumulation of a large amount of fission products in the ignition zone, the growth of the scalar neutron flux in the system is replaced by its decrease, and finally the neutron flux reaches a constant value corresponding to the steady-state regime of the NBW. The maximum concentration of ^{233}U, equal to about 2×10^{21} cm^{-3}, is observed near the NBW front moving along the reactor axis, as well as near the open (without reflector) reactor edge (see plot $N(z)$ in Fig. 9.2). Behind the wave there is a residual concentration level of ^{233}U along the entire reactor $N \approx 1.3\times10^{21}$ cm^{-3}. At the reactor attenuation moment, the burn-up depth of the fuel $B(z)$ reaches a high level of about 50 % over the entire length of the reactor except for regions close to its boundaries (see Fig. 9.2).

Fig. 9.3 shows the initial stage of the time evolution of the integral neutron flux Φ_{tot} over the volume of the reactor. The solid line illustrates the disturbance that arises in the system as a result of switching off the external neutron flux at a time point of $t_{\text{off}} = 100$ days. For comparison, the behavior of the integral neutron flux in FR in the case, when the external neutron source is not turned off, is presented by the dashed line.

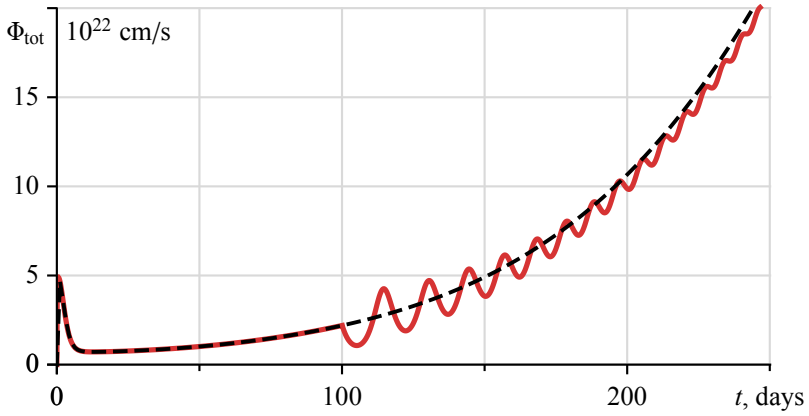

Figure 9.3: The integral neutron flux as a function of time $\Phi_{\text{tot}}(t)$ at the initial stage of FR operation when the external neutron flux is turned off at $t_{\text{off}} = 100$ days (solid red curve) and without switching off the external flux (dashed black curve).

The perturbation manifests itself in the form of a neutron flux oscillations with a period of about 10 days. The amplitude of these oscillations gradually damps, so that the system returns to a smooth increase in flux after about 200 days. This phenomenon demonstrates the self-regulating nature of the nuclear burning process in the reactor under consideration, which is stable to perturbations of the neutron flux. This stability is due to the presence of a negative reactivity feedback, which ensures the safe operation of the reactor without operational external control (the so-called "intrinsic safety") and is an important feature of the fast reactor operating in the NBW regime. A detailed analysis of the negative reactivity feedback mechanism for a reactor of this type is given below in Chapter 10.

The considered version of the calculations of a hypothetical fast reactor based on the Th–U cycle, although of physical interest, is however unrealistic due to the lack of structural materials and coolant in the reactor composition. Therefore, we also considered more realistic models of the reactor, taking into account the presence of a structural material (Fe) and a coolant (eutectic Pb-Bi alloy or helium) in the reactor composition, uniformly distributed throughout the reactor volume. However, all our calculations of the evolution of the burning process in such a reactor model which takes in account the presence of these necessary components, did not allow finding a solution in the form of NBW. And this was not only for the composition of the reactor with realistic volume fractions of fuel, structural material and coolant, but even with the inclusion of relatively small amounts of Fe, Pb-Bi or He.

As an example, the results of such calculations for a helium cooled critical FR of radius $R = 4$ m and length $L = 5$ m with an ignition zone of length $L_{\text{ig}} \approx 2.5$ m

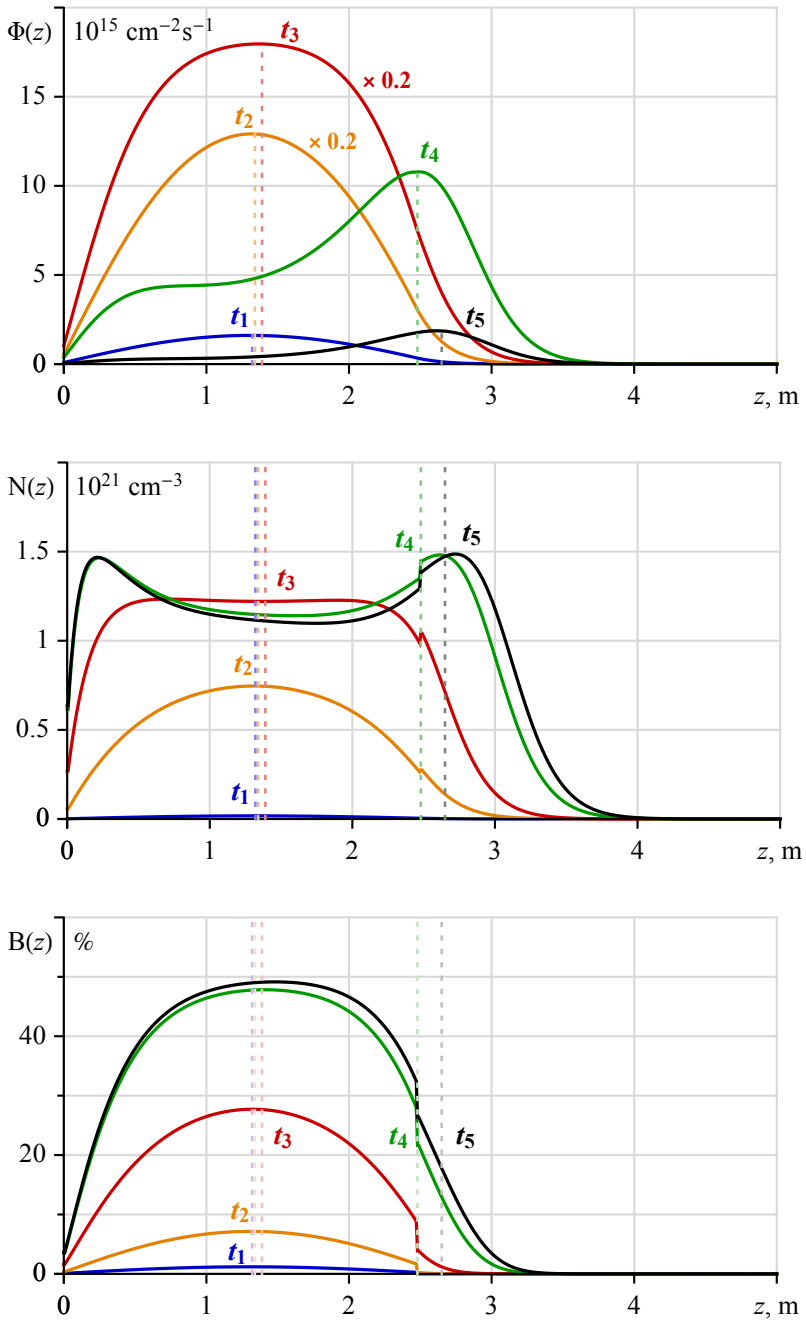

Figure 9.4: The same as in Fig. 9.2, for a reactor with 20 % volume fraction of the coolant (He) and 10 % of the volume fraction of the structural material (Fe) at time moments listed at the bottom.

enriched with 10 % of ^{235}U is presented in Fig. 9.4. In these calculations, the fuel volume fraction is 70 %, the helium coolant is 20 %, the structural material (Fe) is 10 %. It should be noted that the volume fractions of the coolant and the structural material used in this calculation are more than 2 times less than those commonly used in gas-cooled reactors.

Figure 9.4 shows that in this case there is also a strong increase in the scalar neutron flux $\Phi(z)$ at the initial stage of the nuclear burning process, despite the turning off the external neutron source at $t_{\text{off}} = 100$ days. There is also a high level of fuel burn-up in the combustion area (see plot $B(z)$ in Fig. 9.4). It can be said that in the case under consideration, a self-sustained nuclear burning regime is also established for a long time ($\sim$ 5 years), however, the system does not go into the NBW mode running along the reactor axis. After reaching the maximum value, the neutron flux slowly decreases during quite a long period of time. The active nuclear burning zone shifting somewhat to the breeding zone, due to the ^{233}U production in this zone (see plot $N(z)$ in Fig. 9.4).

Thus, the calculations show that in a hypothetical FR consisting only of metallic Th–U fuel, NBW can propagate, but adding even relatively small amounts of structural material and coolant leads to the impossibility of realizing the NBW mode. This qualitative difference in the results for the Th–U fuel cycle from the U–Pu cycle is due, primarily, to the low breeding rate of the fissile ^{233}U, which is about 1.5 times lower than the corresponding coefficient for the ^{239}Pu isotope in the case of metallic U–Pu fuel (see, e.g. [206]). The production periods of ^{233}U ($\approx$ 27 days) and ^{239}Pu ($\approx$ 2.5 days) are also significantly different.

The obtained result agrees with the conclusions of [210] on the impossibility of realizing the NBW regime in a FR with a Th–U fuel cycle and at the same time contradicts the results of [193], which admits such a possibility. For a final answer to this question, it is necessary to agree on the conditions under which calculations were made by different groups and refinement of mathematical models, which are used in this case.

9.3 Mixed Th–U–Pu fuel cycle

Basing on the above-described procedure of solving the set of non-linear equations under consideration, we have carried out a series of calculations of the NBW regime in the critical FR with the metal fuel of the mixed Th–U–Pu cycle. We emphasize that in the calculations we do not consider any specific characteristics of the FR

construction, fuel elements and coolant channels etc. and describe the two homogeneous zones of the FR in a simplified way by specifying certain realistic values of volume fractions of the constructional material $F_{\mathrm{Fe}} = 15\,\%$, coolant (Pb–Bi) $F_{\mathrm{cool}} = 30\,\%$ and fuel $F_{\mathrm{fuel}} = 55\,\%$ with the fuel porosity $p = 0.2$. First of all, we search for the initial critical FR configurations by means of solving the stationary critical parameter problem in the "true multi-group" and "effective multi-group" approximations. In our calculations, we use the 26-groups approximation with the BNAB group neutron constants [211]. In the initial critical FR assembly, we assume that the uranium fuel in the ignition zone is enriched with 10 % of plutonium (here, plutonium isotope content is $^{239}\mathrm{Pu} : {}^{240}\mathrm{Pu} : {}^{241}\mathrm{Pu} : {}^{242}\mathrm{Pu} = 0.70 : 0.22 : 0.05 : 0.03$). The reactor length is $L = 5$ m, and the ignition zone size $L_{\mathrm{ig}} \approx 0.5$ m. For the found initial critical assemblies of FR, we have performed calculations of the time evolution of space distributions of neutron flux and of the processes of burn-up and production of the fuel components during the reactor campaign.

The neutron field in the system and the process of nuclear burning are initiated by the external neutron flux of intensity $j_{\mathrm{ex}} \sim 10^{13}\ \mathrm{cm}^{-2}\,\mathrm{s}^{-1}$ that is turned off at a certain time moment t_{off} when the self-sustained regime has already been settled and is steady enough.

Here, we present the results of calculations for some of the most interesting variants of the FR composition for the mixed Th–U–Pu fuel cycle.

Figure 9.5 presents the time evolution of axial profiles of the main characteristics (the neutron flux $\Phi(z)$, the concentrations $N(z)$ of the produced main fissile isotopes ^{239}Pu and ^{233}U, and the fuel burn-up depth $B(z)$) that describe the process of initiation and propagation of the NBW for one of the FR compositions.

In this case the cylinder radius $R = 2.3$ m and the volume fraction of ^{232}Th in the fuel of the breeding zone $F_{\mathrm{Th}} = 62\,\%$. Note that this value of F_{Th} corresponds to nearly equal concentrations of ^{238}U and ^{232}Th nuclides in the fuel. The initial external flux is turned off at $t_{\mathrm{off}} = 100$ days.

This variant is characterized by a long-term reactor campaign ($t \sim 50$ years) and the stable NBW regime with values of energy production, NBW velocity, and energy production density at the NBW front, that are acceptable for the practical realization.

In Fig. 9.6 we present the most important integral characteristics of the FR operation regime: the time dependences of the NBW velocity $V(t)$ (we define it as the velocity of axial motion of the scalar neutron flux maximum) and the total reactor power $P_{\mathrm{tot}}(t)$, as well as the axial distribution of the neutron fluence $F(z)$ over the whole reactor campaign.

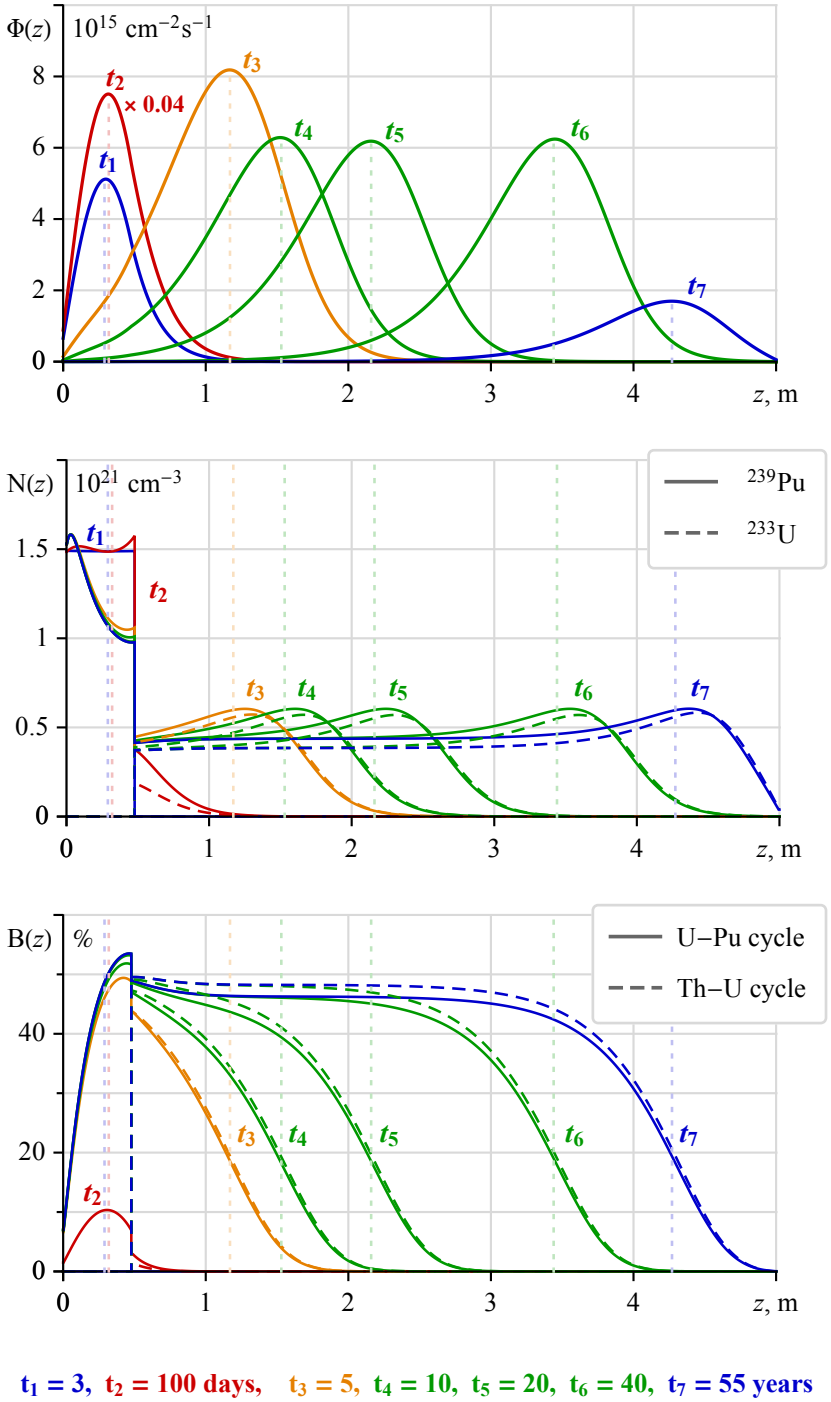

Figure 9.5: The axial distributions of the NBW characteristics: the scalar neutron flux $\Phi(z)$; the concentration of main fissile isotope $N(z)$; the fuel burn-up depth of the fuel components $B(z)$, at different time moments listed at the bottom.
Here $F_{\mathrm{Th}} = 62\,\%$ and $R = 2.3$ m.

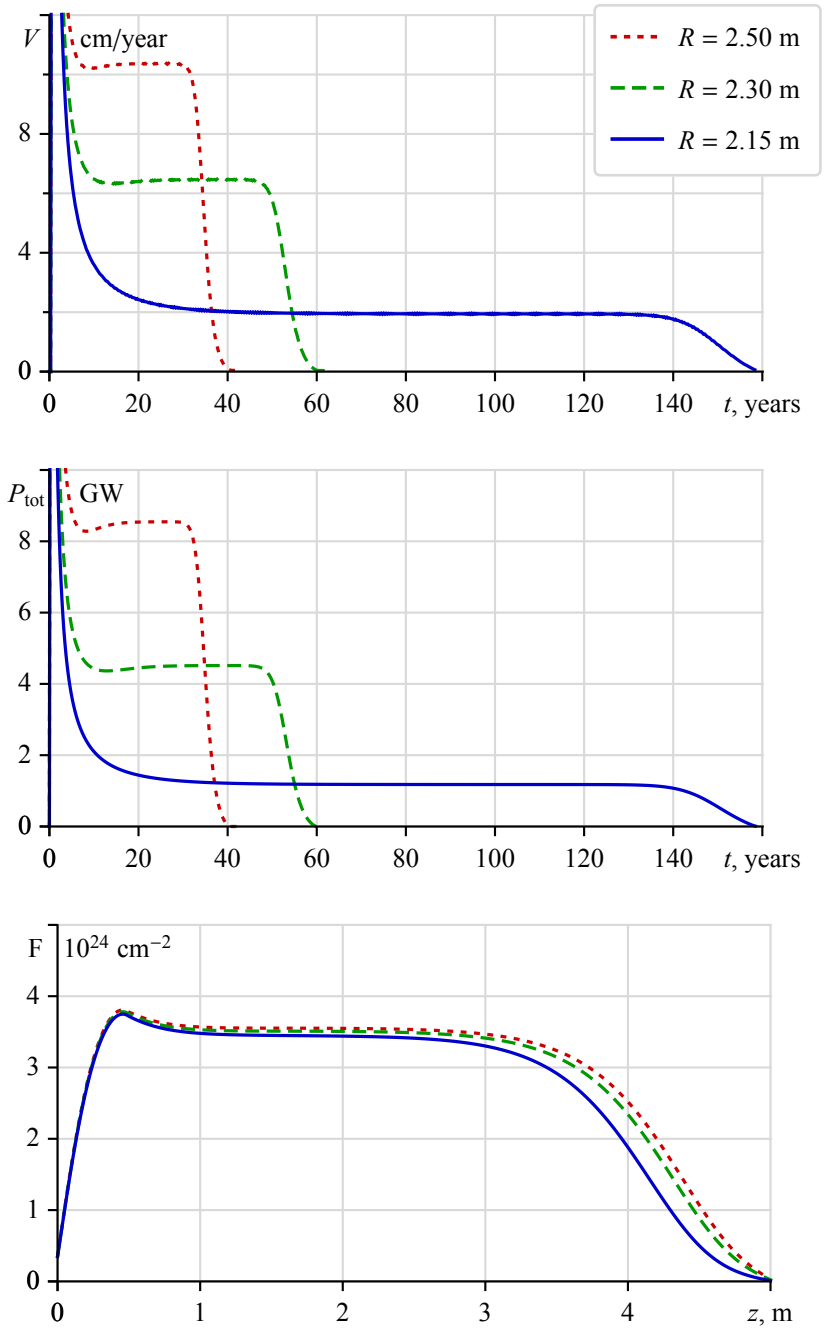

Figure 9.6: The NBW velocity $V(t)$ and the total FR power $P_{\text{tot}}(t)$ as a function of time; the axial distributions of the neutron fluence $F(z)$ for the whole reactor campaign for different reactor radii listed on the right. Here $F_{\text{Th}} = 62\,\%$.

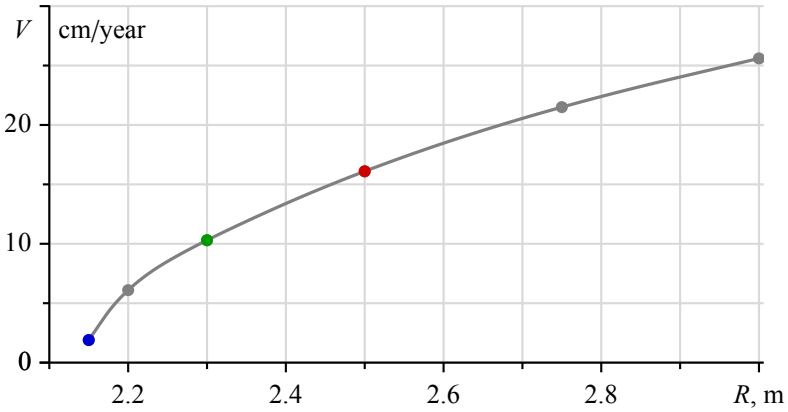

Figure 9.7: The NBW velocity as a function of the reactor radius $V(R)$.

Here we compare these dependences for three options of the FR geometry with different radii: $R = 2.5$ m, $R = 2.3$ m and $R = 2.15$ m. At the stationary stage of NBW its velocity values for these variants are 10.4, 6.5 and 1.9 cm/year, the total FR power is 8.5, 4.5 and 1.2 GW and the energy production density at the NBW front are 890, 440 and 160 W/cm^3, respectively.

As can be seen from Fig. 9.5, the neutron flux Φ increases strongly at the initial stage of the burning process, reaching its maximum magnitude during the first year. Then its magnitude gradually decreases and the flux distribution maximum shifts in the axial direction forming the NBW front. Simultaneously, corresponding changes occur in the concentration distributions of the produced isotopes ^{239}Pu and ^{233}U when the NBW front is formed. After about ten years of the reactor campaign, the system reaches the regime of the stationary NBW motion that is characterized by an approximately constant level of the neutron flux, whose maximum moves along the reactor axis with a constant velocity. At any time moment, the maxima of the concentration distributions of the produced isotopes ^{239}Pu and ^{233}U are situated near the wave front. The neutron flux falls down and the burning process gradually dies when the wave reaches the right edge of the reactor. During the wave propagation in the FR under consideration, the fuel burn-up achieves a high level (about 50 %).

It should be stressed that, at the same material composition of the FR, the NBW velocity and, as a result, the energy production density strongly depend on the radius of the reactor. The dependence of the NBW velocity on the reactor radius is shown in Fig. 9.7.

Figure 9.8 demonstrates the stability of the self-sustained nuclear burning regime relative to a perturbation of the neutron flux in FR at the initial stage of the reactor

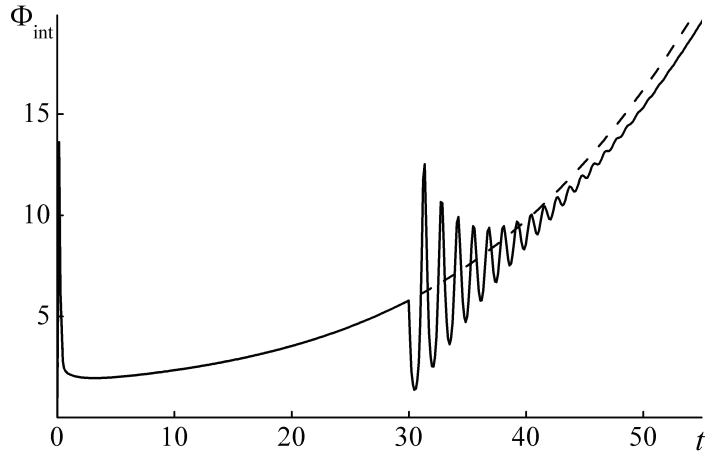

Figure 9.8: The integral neutron flux $\Phi_{\rm int}$ (10^{22} cm/s) as a function of time t (days) at the initial stage of the reactor campaign for $t_{\rm off} = 30$ days (solid line) and $t_{\rm off} = 100$ days (dashed line). Here $F_{\rm Th} = 62\,\%$ and $R = 2.3$ m.

campaign. Here, we present the variation of the integral (over the reactor volume) neutron flux $\Phi_{\rm int}$ caused by turning the external neutron flux $j_{\rm ex}$ off at $t_{\rm off} = 30$ days. It is seen that after the moment $t_{\rm off}$ the magnitude of $\Phi_{\rm int}$ at first sharply decreases and then flux oscillations arise that are gradually damped. This perturbation of neutron flux is damped by the reactor itself during approximately 20 days. This behavior of the reactor is a manifestation of the negative reactivity feedback, which is a characteristic of the NBW regime.

We also study the sensitivity of NWB main characteristics to a composition of the fuel of the breeding zone. In Fig. 9.9 we compare two variants of fuel composition with the volume fraction of ^{232}Th in the fuel $F_{\rm Th} = 62\,\%$ and $55\,\%$. To obtain the same maximum energy production density at the NBW front (about 500 W/cm^3) for both cases, the reactor radii are chosen $R = 2.2$ m and $R = 1.7$ m, correspondingly.

It is seen from Fig. 9.9 that at the stage of NBW stationary propagation, its characteristic velocity values are very close to each other: 6.3 and 5.9 cm/year for $F_{\rm Th} = 62\,\%$ and $55\,\%$, correspondingly. At the same time, mainly due to the difference of density between ^{238}U and ^{232}Th, the total reactor power differs more significantly: $P_{\rm tot} = 3.9$ GW and 2.3 GW, correspondingly.

The burn-up depths B for both fuel components (^{238}U and ^{232}Th) in the breeding zone are close to each other; moreover, the thorium component is characterized by a somewhat greater burn-up depth (see Fig. 9.5). The results of calculations for other FR variants show that this fact is independent of the ratio of the ^{238}U and ^{232}Th fractions and other reactor parameters.

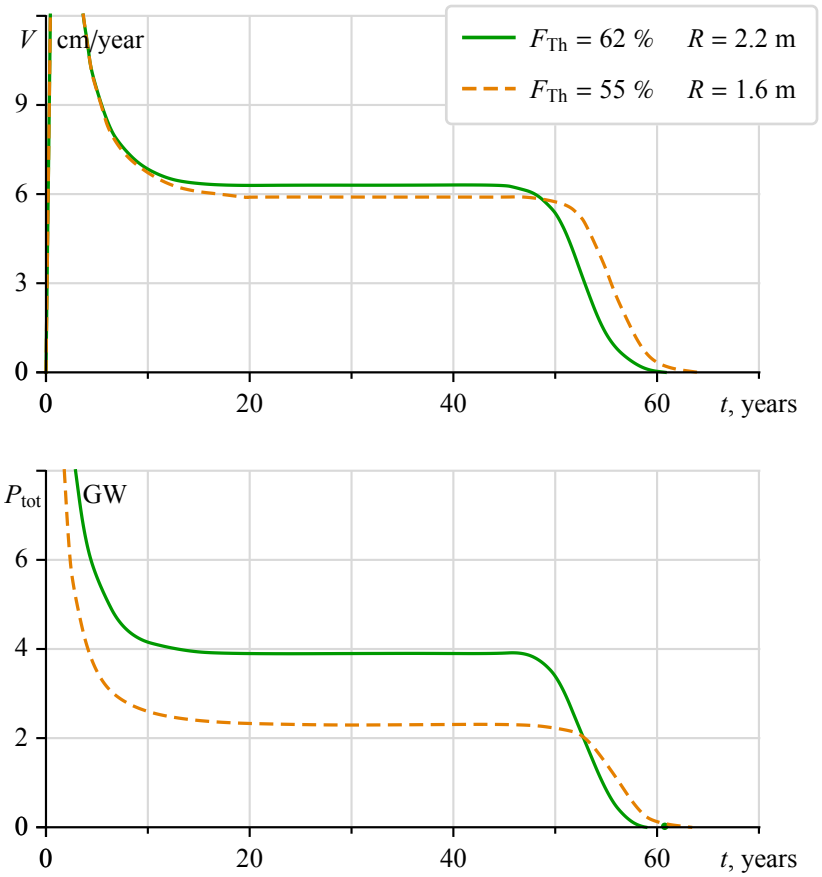

Figure 9.9: The NBW velocity $V(t)$ and the total FR power $P_{\text{tot}}(t)$ as a function of time; the axial distributions of the neutron fluence $F(z)$ for the whole reactor campaign for two different fuel compositions: volume fraction of Th in the fuel $F_{\text{Th}} = 62\,\%$ ($R = 2.2$ m) and $F_{\text{Th}} = 55\,\%$ ($R = 1.7$ m).

As for the neutron fluence for the whole reactor campaign, it only slightly differs for these calculation variants, and its value at the reactor center equals about 3.5×10^{24} cm^{-2}.

The results presented at this Chapter were published in [212–214].

Chapter 10

Negative reactivity feedback of the NBW regime

In the previous chapter, the stability of the NBW regime has been demonstrated in the perturbation of the neutron flux in the system resulting from turning off the external neutron source at the early stages of the NBW initialization. At this stage, the reactor has not yet reached a steady-state mode and has small positive reactivity. So, the damped oscillations of the neutron flux, which are the result of such a perturbation, occur against a background of a slowly increasing neutron flux in this case (see Figs. 9.3 and 9.8).

Now we consider the stability of the NBW regime at the stage, when the NBW reactor already reaches its steady state with a constant value of the neutron flux in the system and constant value of the NBW propagation velocity. We study the behavior of the NBW reactor in the event of certain external perturbations in the reactor neutron fields and in the event of fuel inhomogeneity in the form of its local initial enrichment by fissile isotopes in the way of the NBW propagation.

10.1 Fuel inhomogeneity

On basis of the above-outlined approach to the simulation of the processes in the FR with a fuel of the mixed Th–U–Pu cycle, We start the study of stability of the NBW regime by simulation of the reactor behavior in the case when the breeding zone contains the axial area, in which the fuel is enriched by isotope ^{235}U. As an example, Fig. 10.1 shows the results of such calculations for the FR with $F_{\mathrm{Th}} = 62\,\%$ (this corresponds to nearly equal concentrations of ^{238}U and ^{232}Th nuclides in the

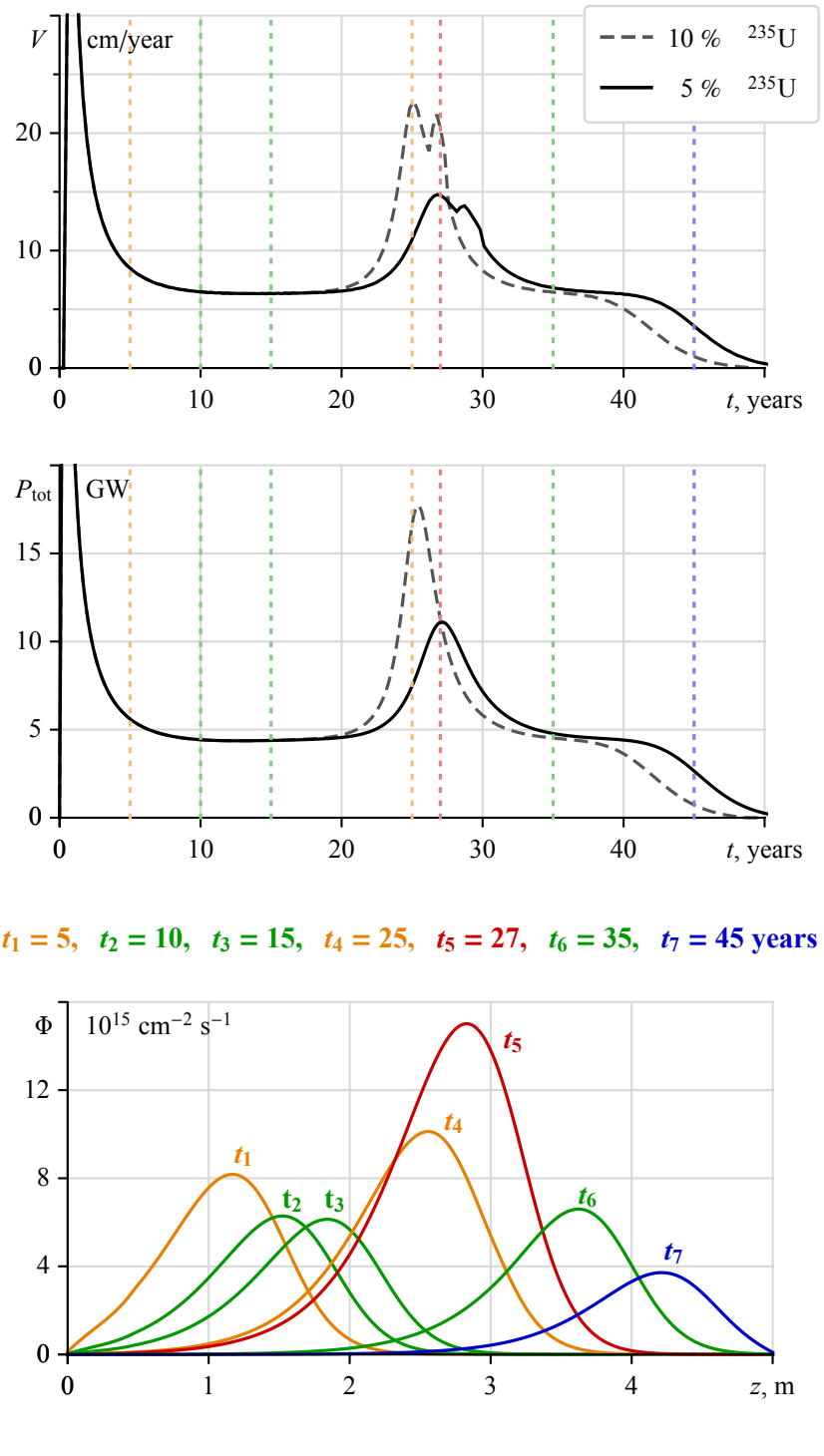

Figure 10.1: The NBW FR behavior in the case of presence of a uranium layer enriched with 5 % (solid curves) and 10 % (dashed curves) ^{235}U at $z = 3.0$–3.2 m: the axial distributions of the scalar neutron flux $\Phi(z)$ for different time moments t_i; the NBW velocity $V(t)$ and the total FR power $P_{\text{tot}}(t)$ as a functions of time.

fuel of the breeding zone), $R = 2.3$ m, when the enriched zone is located at $z = 3.0$–3.2 m, and for two cases of uranium enrichment: 5 % and 10 %.

These results show that at the NBW approaching the area with enriched uranium, the neutron flux and the wave velocity are gradually increased. Accordingly, the reactor power increases significantly too. Irregularity in velocity V behavior near its peak is apparently due to the fact that at the passage of enriched area, there is distortion of the axial shape of the neutron flux. This means that the definition of the NBW velocity using the position of the neutron flux maximum is not quite accurate. The value of the observed disturbance of the NBW regime strongly depends on the degree of the uranium enrichment. After passing the enriched area, the reactor returns to the previous regime of the NBW propagation with the same parameters as before passing.

For a more convincing demonstration of the stability of the wave regime with respect to the inhomogeneity of fuel enrichment, we considered hypothetical examples with very high parameters of such heterogeneity, which led to an unacceptably strong (albeit slow) increase in the neutron flux in the system. But even in such cases the NBW reactor "coped with the problem" and returned to its former steady state without any external interference. In a real reactor, of course, such a significant variation in the inhomogeneity of the fuel is not possible, and therefore there will not be such a large increase in the neutron flux.

10.2 Neutron flux perturbations

Then we carried out a study of the NBW stability relative to the disturbance of the neutron field in the reactor at the stationary stage of the NBW propagation, for example, after ten years from its start. For this purpose, we calculated the behavior of FR in the case of NBW reactor core irradiation by a volumetric neutron source, which operates at a constant intensity during short time (about one hour), and then turns off.

Consideration was given to different cases with varying intensity of such an "external" neutron sources Q_{ex} and its various axial position relative to the NBW front, located at $z = 1.6$ m at the moment when the external neutron flux was turned on ($t_0 = 10$ years). We do not explain the physical nature of the neutron source, and just use such a simple model for simulation of a very powerful sudden external disturbance of the neutron flux in FR. The behavior of the volume-averaged neutron flux in FR with respect to such perturbations in different cases is shown in Fig. 10.2. This figure shows that the effect of this perturbation depends on the

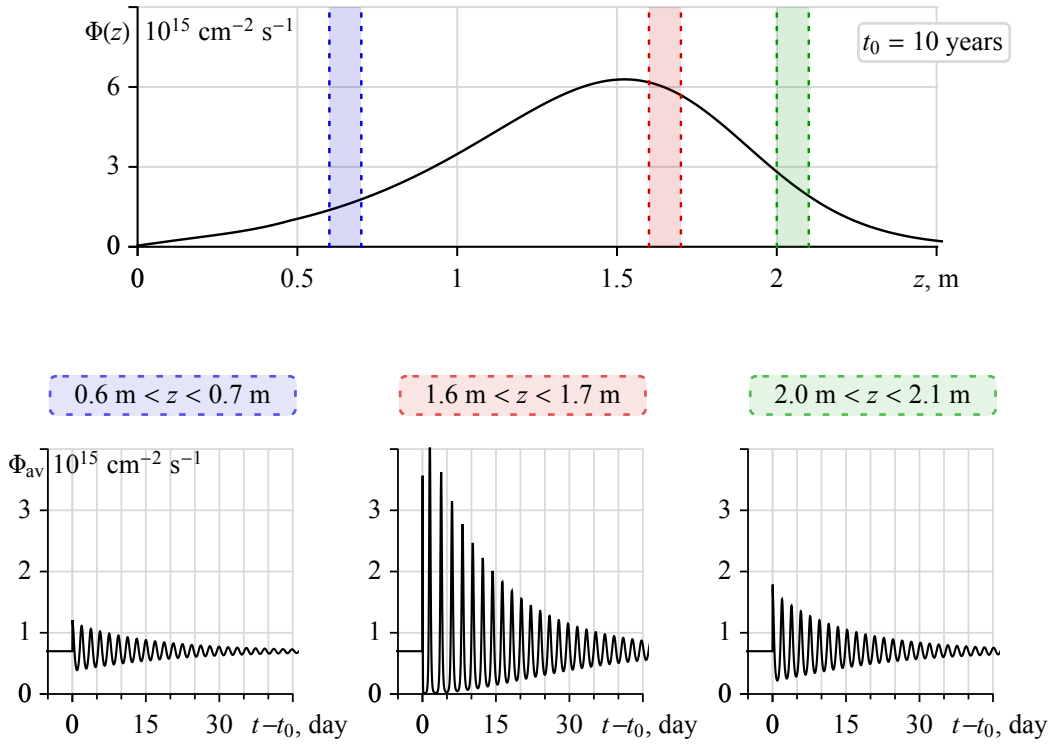

Figure 10.2: The perturbation of volume-average neutron flux $\Phi_{\rm av}(t)$ in the NBW FR caused by an external neutron source versus time. The source with intensity $Q_{\rm ex} = 2 \times 10^{11}$ cm^{-3} s^{-1} starts at $t_0 = 10$ years, lasts for one hour and is situated at (0.6 m $< z <$ 0.7 m) or (1.6 m $< z <$ 1.7 m) or (2.0 m $< z <$ 2.1 m).

intensity of the source and its axial location. In most cases, as shown in Fig. 10.2, this perturbation causes severe neutron flux oscillations in FR, which are quickly extinguished by the NBW reactor itself. Increasing the intensity of the neutron source and its approach to the wave front position increases the amplitude of these oscillations, although their period remains unchanged and roughly corresponds to the period of ^{239}Pu production in the fuel U-Pu cycle (about 2 days).

In Fig. 10.3 we analyze the initial stage of the neutron flux perturbation shown in Fig. 10.2 (central plot) in more detail. In order to clarify the mechanism of the negative reactivity feedback, besides the behavior of the neutron flux $\Phi_{\rm av}(t)$ averaged over the FR volume, we also present the accompanying variations of the volume-averaged concentrations $N_{\rm av}(t)$ of the main fissile nuclides ^{239}Pu ($N_{\rm Pu}$) and ^{233}U ($N_{\rm U}$) and main intermediate nuclides ^{239}Np ($N_{\rm Np}$) and ^{233}Pa ($N_{\rm Pa}$). For convenience of comparing variations of the volume-averaged concentrations of these nuclides, we have subtracted the difference $N_{\rm Pa} - N_{\rm Np} = 53.1 \times 10^{17}$ cm^{-3} in the stationary-wave

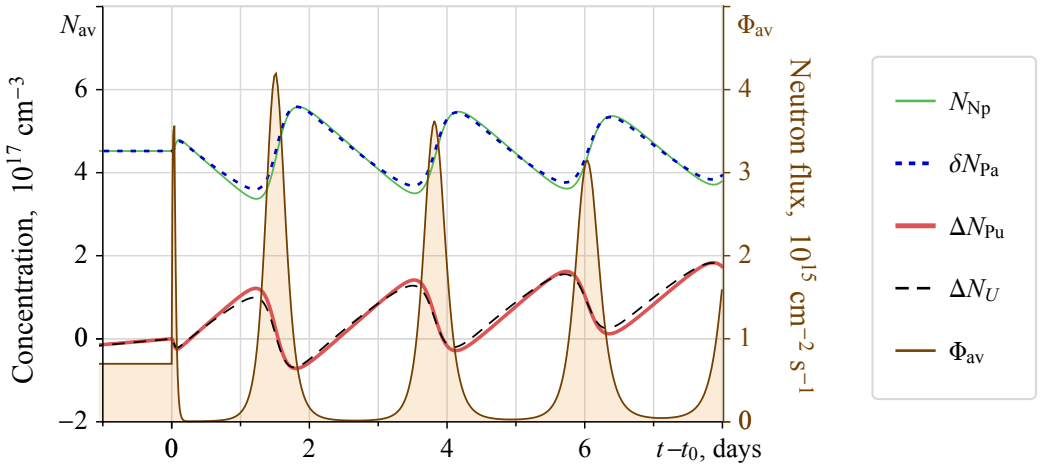

Figure 10.3: Evolution of the volume-averaged neutron flux $\Phi_{av}(t)$ and concentrations $N_{av}(t)$ of the main fissile and intermediate nuclides in the fuel of mixed Th–U–Pu cycle with time. First three oscillations from Fig 10.2 for the case ($1.6\,\text{m} < z < 1.7\,\text{m}$).

state ($t = t_0$) from the current ^{233}Pa concentration $\delta N_{Pa} = N_{Pa} - 53.1 \times 10^{17}$ cm^{-3}. This makes it evident that the variations of the concentrations of two intermediate nuclides during the perturbation practically coincide. One can see that the curves for the concentrations of main fissile nuclides ^{239}Pu and ^{233}U also are very close to each other (from N_{Pu} and N_U, we subtract their values at the time of the neutron source turning on $\Delta N_{Pu}(t) = N_{Pu}(t) - N_{Pu}(t_0)$ and $\Delta N_U(t) = N_U(t) - N_U(t_0)$).

Fig. 10.3 shows that the oscillations of the quantities under consideration are completely correlated. The oscillations of concentrations of the fissile nuclides ^{239}Pu and ^{233}U are governed by the variation of the neutron flux with the same period $\tau \approx 2$ days. When the flux increases (first, due to the action of the external neutron source), their concentrations fall down because of the intensive burning out by neutrons, which brings the FR to a sub-critical state and subsequently leads to a quickly decreasing neutron flux. On the contrary, the concentrations of intermediate nuclides ^{239}Np and ^{233}Pa increase with the neutron flux, but when the flux strongly decreases, their concentrations begin to fall down due to the β-decay. This β-decay, in its turn, increases the concentrations of the fissile nuclides ^{239}Pu and ^{233}U, which brings the FR to a supercritical state together with the subsequent increase of the neutron flux in the system. Due to the above-considered processes, the concentrations of the intermediate and fissile nuclides oscillate in antiphase with each other.

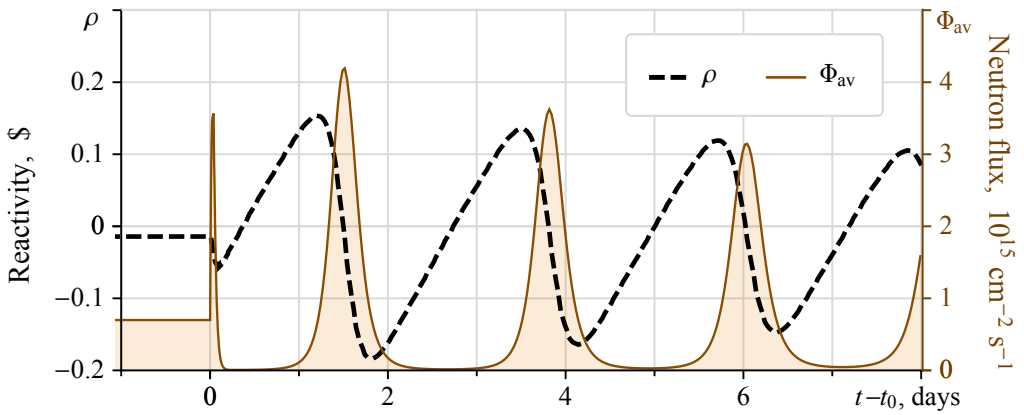

Figure 10.4: Variation with time of the reactivity $\rho(t)$ and volume-averaged neutron flux $\Phi_{\text{av}}(t)$ for the same condition as in Fig. 10.3.

This value of τ is close to the half-life of ^{239}Np ($\approx$ 2.34 days), which is an intermediate nuclides in the U–Pu cycle, and an order of magnitude different from the half-life of ^{233}Pa ($\approx$ 27 days), which is an intermediate nuclides in the Th–U cycle. While it may give the impression that ^{239}Np is responsible for the neutron flux oscillations and the stabilization of the NBW regime in the reactor with mixed thorium-uranium fuel, it is not true. ^{233}Pa actually has a greater half-life period than ^{239}Np, however due to this fact, its concentration in the core is about ten times higher than ^{239}Np at the equal value of initial concentrations of the corresponding fertile material. As a result we get approximately equal amounts of the fissile nuclides, ^{239}Pu and ^{233}U (see Fig. 10.3). So, both intermediate nuclides, ^{239}Np and ^{233}Pa, plays the equivalent role in the NBW stabilizing process.

The described correlated processes are repeated many times with gradually decreasing amplitude of oscillations until the FR damps these oscillations by itself and finally reaches the critical state. The above-discussed alternation of the sub-critical and supercritical states of the FR is also illustrated in Fig. 10.4 which shows the self-consistent variation of the reactivity and the volume-averaged neutron flux caused by the negative reactivity feedback.

The variation in time of the reactivity $\rho(t)$ caused by perturbation of the neutron flux in the reactor core by an external neutron source, shown in Fig. 10.4 by dashed line, was calculated according to the general definition of reactivity as

$$\rho = \frac{k_{\text{eff}} - 1}{k_{\text{eff}}} \tag{10.1}$$

where k_{eff} was determined by solving the criticality problem (see equation (8.1)) at each time step when solving the evolutionary problem by means of equation (8.5) and set of burn-up equations (8.7) and (8.8).

Thus, here we have considered different types of distortions of the self-sustained regime in the NBW reactor and showed its outstanding stability. We deliberately used an unrealistically powerful external perturbation of the neutron flux to demonstrate high efficiency of the negative reactivity feedback mechanism, which ensures stability of the NBW regime.

The results presented at this Chapter were published in [215].

Chapter 11

Transients in the NBW reactor

11.1 Smooth start-up

In Sections 9.2 and 9.3, we have studied the process of initiation of the NBW regime in FR with different fuel compositions including pure Th and mixed Th-U fuel. For this study we have used the deterministic approach which is based on solving the non-stationary diffusion equation for neutron transport together with the burn-up equations for fuel components and the equations of nuclear kinetics for precursor nuclei of delayed neutrons (see Sections 8.2 and 8.3). This approach gives us a possibility to describe a space-time evolution of the neutron field and fuel nuclide concentrations in the NBW reactor and to simulate the initiation and propagation of NBW in the axial direction of the cylindrical FR.

In these studies, we used a rather simplified FR start-up scenario in which the NBW propagation in the breeding zone filled with the fertile material is initiated by an external neutron flux that irradiates a homogeneous "Ignition zone" enriched with fissile isotopes (see Fig. 8.1). Our calculations showed, in particular for the FR with metal fuel of mixed Th–U–Pu cycle with taking into account of typical volume fractions of fuel, constructional material (Fe) and coolants (Pb–Bi eutectic), a principal possibility of initiating the NBW which then steadily propagates in the "Breeding zone" during a long time period (decades). For the FR with metal fuel of U–Pu cycle, such a possibility was demonstrated earlier in [203, 204].

However, the use of this simplified start-up scheme leads to an essential initial increase of the neutron flux in the ignition zone up to very high values that are unacceptable from the practical point of view and can even destroy the reactor. This initial neutron-flux increase develops slowly enough so that it could be prevented by means of conventional mechanisms of the reactor control in the ignition zone,

but it is also interesting to elaborate a method of smooth start-up of this FR, which would include choosing a proper composition of the ignition zone that could ensure acceptable neutron flux values and moderate power production. The aim of investigations of present section is searching for such a method of smooth start-up of the NBW reactor with using the fuel of U–Pu cycle.

The FR under consideration consists of the ignition zone, that contains ^{238}U enriched with plutonium (the isotope composition of plutonium is ^{239}Pu : ^{240}Pu : ^{241}Pu : ^{242}Pu = 0.70 : 0.22 : 0.05 : 0.03) and the breeding zone adjacent to the ignition one, that is filled with the fertile ^{238}U isotope (see Fig. 8.1). The both zones also contain the constructional material Fe and the Pb–Bi eutectic coolant. In the simplified start-up scheme used in [203,204], both these zones are homogeneous with the sharp boundary between them. The initiation of the nuclear burning process in the system is done by an external neutron flux j_{ex}, that irradiates the left side of the ignition zone. The initial configuration of the FR is chosen to be very close to the critical state by solving the corresponding criticality problem on reactor parameters that determine the variants of the size and the initial composition of the FR.

We have carried out a series of calculations of the space-time evolution of the NBW regime for different variants of the reactor parameters, which correspond to different compositions and geometrical dimensions of the initial critical FR assembly with using different variants of the ignition zone design. Below, we present the calculation results obtained for a variant of the NBW reactor with the simplified start-up scheme and, beside it, for the analogous FR with using the improved ignition zone design we found for a smooth start-up.

First, let us discuss the results obtained for the simplified scheme. In Fig. 11.1 we present the axial distributions of some constituents of the composition of such a critical FR assembly and corresponding scalar neutron fluxes (normalized to the average energy release 20 W/cm^3). Calculations were performed in the 26-group and effective multigroup approximations for such geometrical dimensions of the reactor: the FR length $L = 5$ m, the cylinder radius $R = 1.05$ m, the axial size of the ignition zone $L_{\rm ig} = 0.73$ m.

We have chosen the following values of the volume fractions of fuel, $F_{\rm fuel} = 44\,\%$, the constructional material Fe, $F_{\rm Fe} = 20\,\%$, and the Pb–Bi coolant $F_{\rm cool} = 36\,\%$. The value of the fuel void fraction $p = 0.2$. The concentration of plutonium in the ignition zone was chosen at 10 %.

The comparison of calculations of the neutron flux summed over 26 groups with the flux calculated in the effective multigroup approximation shows that the latter

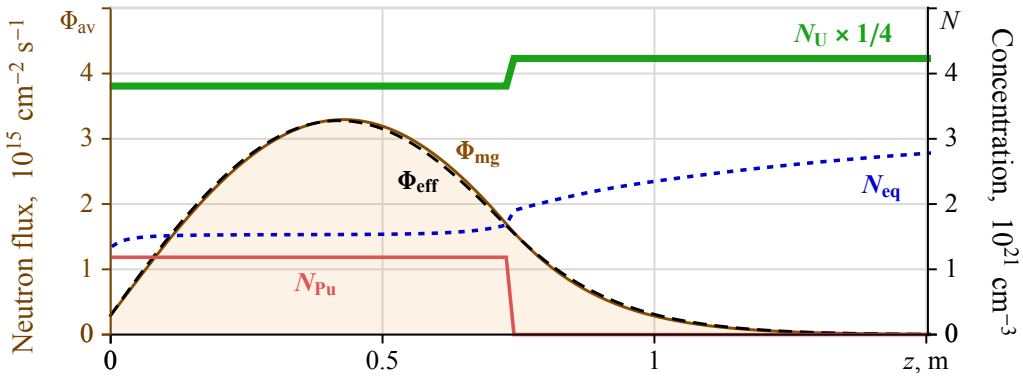

Figure 11.1: Axial profiles for the initial critical FR compositions with the simplified start-up schemes: the concentrations of the actual N_{Pu} (solid red curve) and equilibrium N_{eq} (shot-dashed blue curve) values for ^{239}Pu; and other values divided by 8: N_{U} (thick solid green curve) for ^{238}U; the neutron flux in the effective multigroup approximation Φ_{eff} (black dashes) and 26-group calculation Φ_{mg} (solid brown curve).

calculation reproduces the exact result in the multigroup approximation quite accurately. From Fig. 11.1, it follows that in the simplified scheme the maximum neutron flux is reached approximately in the ignition zone center. The neutron flux on "the tail" of its axial distribution, which illuminates the breeding zone and determines the speed of isotope ^{239}Pu production near the border of the ignition and breeding zones, is not large enough. From Fig. 11.1, one can see the ratio between the actual initial ^{239}Pu concentration and its equilibrium value, which is able to ensure, according to [177, 178], the self-sustained burning process and the NBW formation in this FR. The equilibrium value, $N_{\mathrm{eq}} = \sigma_{\mathrm{c,\,U}}\, N_{\mathrm{U}}/(\sigma_{\mathrm{f,\,Pu}} + \sigma_{\mathrm{c,\,Pu}})$, is determined as the value of ^{239}Pu concentration to which it tends asymptotically with the time course under a constant irradiation of the fuel by a neutron flux [177, 178].

The chain reaction in this FR with the simplified start-up scheme is initiated by an external neutron flux with intensity $j_{\mathrm{ex}} = 10^{13}$ cm^{-2} s^{-1} which is turned off at $t = 30$ days. As a result, after the initial period of approximately 2 years a stationary wave regime of nuclear burning is set in the FR under consideration.

Figure 11.2 presents the corresponding time dependence for the total power of energy production P_{tot}. Note that for the chosen FR radius and the breeding zone composition, the steady NBW regime is characterized by a realistic reactor power value ($\sim$ 3 GW). However, at the very beginning of the campaign, when the wave front is formed near the ignition zone border, there is a huge increase in the neutron flux in the ignition zone to value ($\sim$ 30 GW) that is more than an order of magnitude

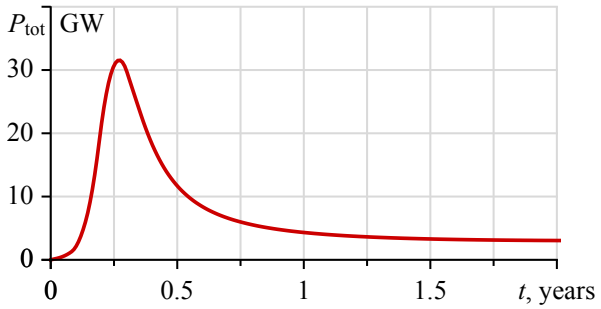

Figure 11.2: Total energy production power $P_{\text{tot}}(t)$ as a function of time for the FR variant with a simplified start-up critical configurations (see Fig. 11.1).

higher than the flux value at the steady NBW stage, which is unacceptable from a practical point of view.

For a better understanding of the process of forming the NBW front and the origin of the above-described unacceptable phenomena, in the Fig. 11.3 we consider the space evolution of the axial distributions of the neutron flux and main fuel components at the initial stage of the nuclear burning in the FR with the simplified start-up at several time moments at regular intervals (40 days) during the first year of the FR operation. It is seen from Fig. 11.3 *a*, that at $t < 150$ days (the moments: t_1–t_3) a large increase of the flux Φ occurs, while the position of its maximum is almost the same. Then (the moments: t_4–t_8), the Φ value gradually decreases to a level close to its value in the NBW and the position of the flux maximum gradually moves to the breeding zone, i.e. the wave starts to move. Figure 11.3 *b* shows that the time interval t_1–t_4, during which the flux Φ has the largest values, corresponds to the most radical changes of the axial profile of the ^{239}Pu concentration, which consist in its rapid production in the breeding zone near the ignition zone. This leads to creating its distribution form characteristic of the wave front. Then, with a decrease of the flux Φ during the time interval t_4–t_8, slower changes of the ^{239}Pu profile and the final formation of the wave front occur. From Fig. 11.3 *c*, it is seen that during the time interval t_1–t_4, the most rapid transformation and burning of the fertile ^{238}U isotope are observed, and at the interval t_4–t_8 these processes are slower but the NBW front moves further into the breeding zone.

From the above-mentioned facts, we can draw the following conclusions. For the simplified type of the ignition zone, a too radical rearrangement of the axial distribution profiles of the main fuel components is necessary to form the NBW front. However, the neutron flux fraction that irradiates the most important region of the ^{239}Pu production at the breeding zone border is rather small (see Figs. 11.1

and 11.3 *a*). A characteristic feature of the self-organizing process of nuclear burning in FR of this type is that the system itself adjusts in such a way that provides the neutron flux sufficient for the formation of NBW, which leads to its excessive growth.

The observed excessive increase of the neutron flux and energy production is rather slow, and it could be suppressed by a conventional system of external reactor control. However, this method would deprive this FR of its attractive features of self-regulation at the early stage of the NBW initiation which would be prolonged for many years. Therefore, here we set the task to provide an acceptable passage of the initial stage of the FR operation without violating the self-regulating nature of the burning regime by choosing an optimal composition of the enriched ignition zone itself. When choosing the ignition zone structure, we aim, firstly, to provide the displacement of a large part of the neutron flux distribution to the breeding zone, and secondly, to facilitate the necessary rearrangement of the initial composition of the ignition zone during the NBW front formation.

It should be noted that in [216], to solve the problem of the smooth start-up of the CANDLE reactor, the authors tried to bring the initial reactor composition maximally close (in terms of k_∞) to the composition characteristic of the steady NBW stage. The calculation method, used in [216], is based on the self-similar solution of diffusion equation for neutron transport [194,210]. This approach is quite sufficient for description of the steady NBW stage; however, it is unable to describe the non-stationary processes at the initiation of the NBW regime adequately. In this section, we have considered a number of possible variants for the ignition zone structure to optimize the regime start-up stage. On the basis of this analysis, we have proposed an improved ignition zone configuration for this FR, the use of which we consider below.

Figure 11.4 presents the characteristics of the initial critical FR assembly with the improved ignition zone of this type. The main parameters of the considered FR are the same as presented above, except the ignition zone. Now the plutonium content in the ignition zone is not constant, but varies by the linear law: $N_{\mathrm{Pu}} = N_{\mathrm{f}}[e_1 + z(e_2 - e_1)/L_{\mathrm{ig}}]$, where N_{f} is the concentration of the fuel nuclides in the breeding zone, and the coefficients e_1 and e_2 characterize the fuel enrichment in the ignition zone. In the breeding zone, in the layer adjacent to the ignition zone, $L_{\mathrm{ig}} < z < L_{\mathrm{ig}} + 4\Delta$, we add an exponential "tail" enriched with plutonium: $N_{\mathrm{Pu}} = N_{\mathrm{f}}\ e_2\ \exp[-(z - L_{\mathrm{ig}})/\Delta]$. This "tail" essentially facilitates forming the NBW front. The fuel volume fraction in the ignition zone varies linearly: $F_{\mathrm{f}}^{(\mathrm{ig})}(z) = F_{\mathrm{f}}\,[u_1 + (1 - u_1)z/L_{\mathrm{ig}}]$. The decrease of the fuel fraction in the ignition zone is chosen in such a way that the corresponding content of ^{238}U would ensure the equilibrium values N_{eq} being nearly at the level of the actual ^{239}Pu concentration (see Fig. 11.4).

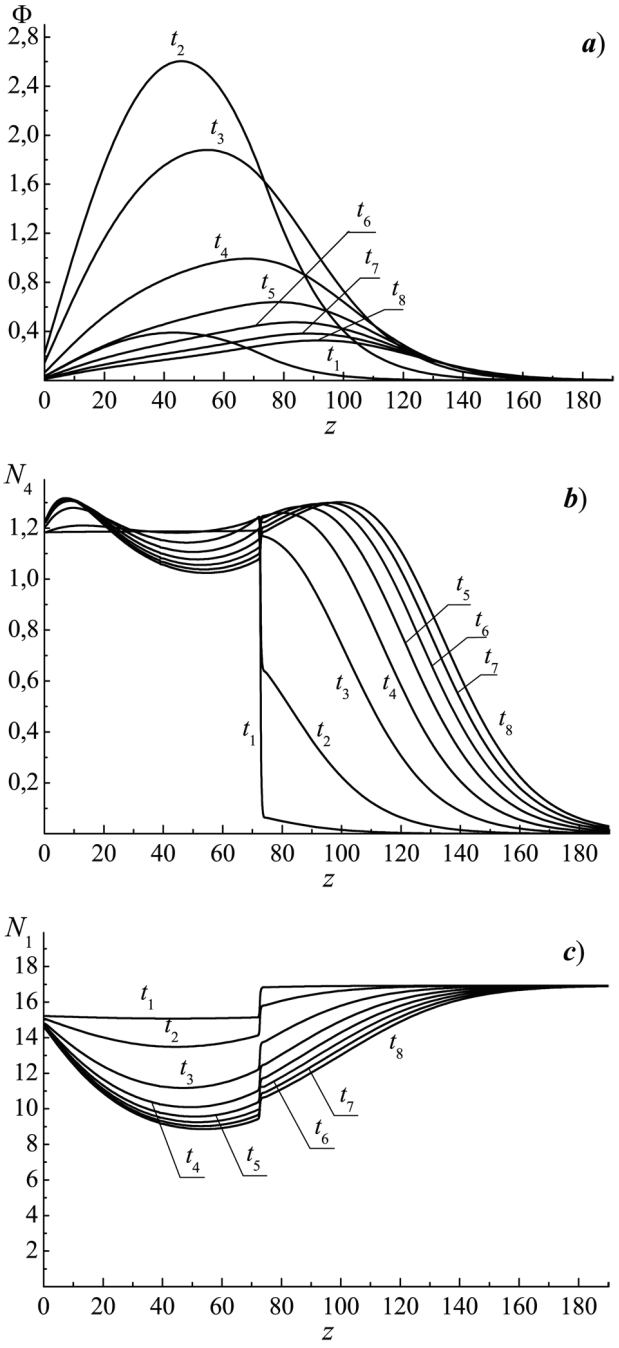

Figure 11.3: Initial evolution of axial profiles (z in cm) near the ignition zone (a) for the neutron flux Φ ($\times 10^{17}$ cm^{-2} s^{-1}) and the (b) ^{239}Pu and (c) ^{238}U concentrations N_4 and N_1 (10^{21} cm^{-3}) for the FR with simplified start-up scheme at the time moments $t_1 = 40$, $t_2 = 80$, $t_3 = 120$, $t_4 = 160$, $t_5 = 200$, $t_6 = 240$, $t_7 = 280$ and $t_8 = 320$ days.

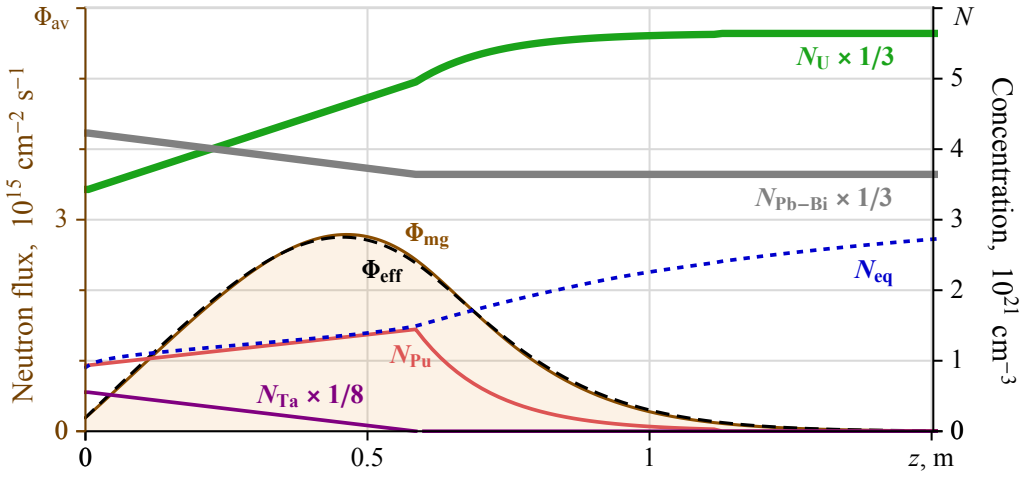

Figure 11.4: Axial profiles for the initial critical FR compositions with the improved smooth start-up scheme:
N_{Pu}, N_{eq} – the actual and equilibrium concentrations of ^{239}Pu;
N_{U}, $N_{\mathrm{Pb-Bi}}$ – the concentrations of ^{238}U and Pb–Bi (values divided by 3);
N_{Ta} – the concentration of ^{181}Ta (values divided by 8);
Φ_{eff} – the neutron flux in the effective multigroup approximation (dashes);
Φ_{mg} – the neutron flux obtained using 26-group calculation (solid line).

The volume freed from the fuel is filled up with a mixture of the Pb–Bi alloy, which weakly absorbs neutrons, and ^{181}Ta that is used as an absorbing material in fast reactors [206]. The relative volume fraction of ^{181}Ta, $F_{\mathrm{Ta}} = 0.58$, is chosen so that this mixture, in its absorption properties, could imitate the presence of fission products on the back side of the wave. An important effect of introducing this absorber in the ignition zone is shifting the maximum of the initial distribution of the neutron flux (see Fig. 11.4) in the direction of the breeding zone. Thus, an essential fraction of the flux falls on the region of forming the NBW front in the breeding zone. The values of the above-mentioned parameters of the ignition zone used in the case under consideration are as follows: $L_{\mathrm{ig}} = 0.585$ m, $e_1 = 0.079$, $e_2 = 0.122$, $\Delta = 0.135$ m, $u_1 = 0.687$.

Here, we also use a more effective scheme of bringing the initial neutron field in the FR to a chosen optimal level by using an additional absorbing ^{181}Ta regulator in the ignition zone. The initial configuration of FR is chosen with a little reactivity excess, $\rho \sim 10^{-4}$. The system is brought to a sub-critical state by the additional tantalum absorber which is gradually withdrawn from the system after turning the external neutron flux ($j_{\mathrm{ex}} \approx 10^{11}$ cm^{-2} s^{-1}), until the neutron field in the FR reaches the chosen level. Note that in this case we can use a significantly lower

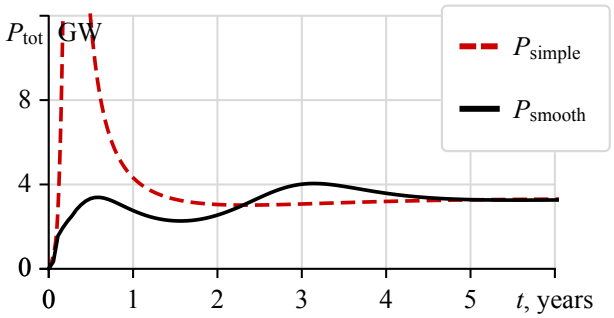

Figure 11.5: Total energy production power as a function of time for the FR variants with the simplified $P_{\text{simple}}(t)$ (dashes) and the improved smooth $P_{\text{smooth}}(t)$ (solid lines) start-up schemes, whose critical configurations are shown in Fig. 11.1 and in Fig. 11.4 correspondingly.

value of j_{ex}. According to this, the additional concentration of ^{181}Ta varies with time as: $N_{\text{Ta}}(t) = N_{\text{Ta}}(0)(t_{\text{ig}} - t)/t_{\text{ig}}$. In the presented calculation we put $N_{\text{Ta}}(0) = 0.25 \times 10^{21}$ cm^{-3}, $t_{\text{ig}} = 40$ days, and the neutron flux was brought to $\sim 80\,\%$ of its level in the NBW regime, after which the regulator withdrawal was stopped and j_{ex} was turned off.

In Fig. 11.5 we present the time dependencies of the total energy production power P_{tot} during the reactor campaign for the FR with the above-described improved ignition zone. The employing the improved start-up scheme allows us to prevent the exorbitant increase of the reactor power.

The NBW regime is formed slightly slower (for about 2.5 years) than in the case presented in Fig. 11.1. Note that the wave moves, at first, with a less velocity and a less power P_{tot} than at the stage of the steady NBW regime, which, probably, is due to the influence of edge effects from the ignition zone residuals. Finally, the NBW reaches the steady regime in several years, which is not an essential disadvantage of the considered scheme, because at this stage the FR power should be adjusted according to current demands by some proper methods (e.g., by changing the radial reflector efficiency), which are not considered here.

In Fig. 11.6, we consider the space-time evolution of the distributions of neutron flux and main fuel components at the beginning of this FR campaign. We present the axial profiles of these quantities for several initial moments of time t_1–t_8 of the reactor operation at regular intervals (100 days) and for the moment t_9, when the NBW has reached the steady regime. Unlike in Fig. 11.3 *a*, here there is no excessive increase of the neutron flux, and the rearrangement of the system components and the formation of the wave front occur smoothly. During the interval t_1–t_8, the

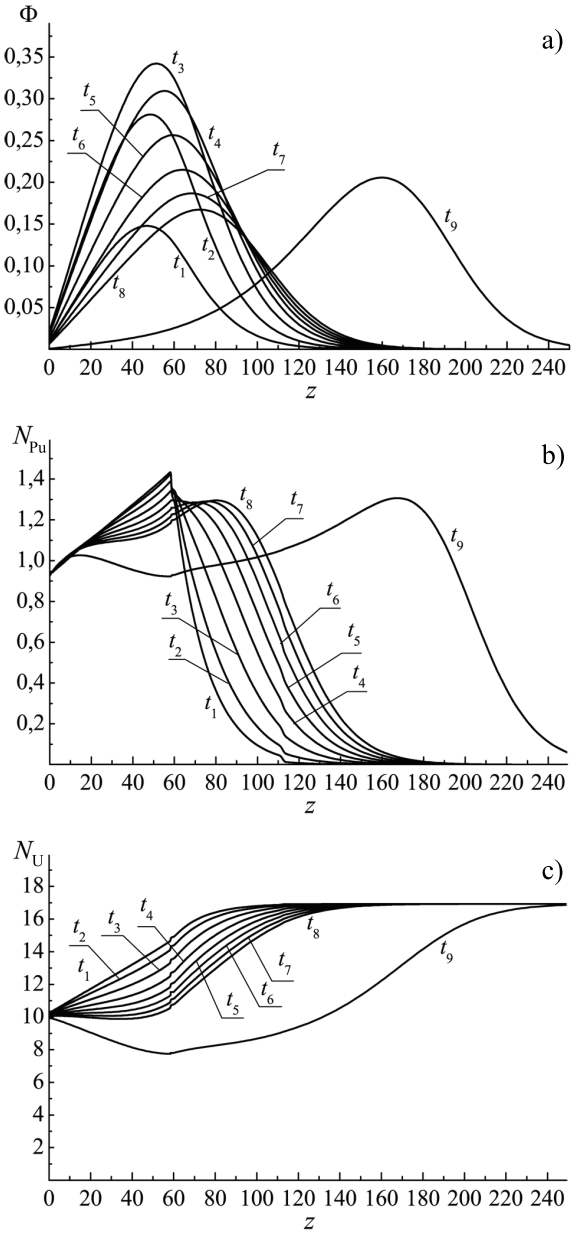

Figure 11.6: Initial evolution of axial profiles (z in cm) near the ignition zone (a) for the neutron flux Φ ($\times 10^{17}$ cm^{-2} s^{-1}) and the (b) ^{239}Pu and (c) ^{238}U concentrations $N_{\rm Pu}$ and $N_{\rm U}$ (10^{21} cm^{-3}) for the FR with the improved smooth start-up at the moments $t_1 = 100$, $t_2 = 200$, $t_3 = 300$, $t_4 = 400$, $t_5 = 500$, $t_6 = 600$, $t_7 = 700$, $t_8 = 800$ and $t_9 = 3000$ days.

maximum of the neutron flux gradually shifts toward the breeding zone. Note also that Figs. 11.6 *b* and *c* show that the initial profile of the ignition zone, in fact, imitates roughly the form of NBW front. It is interesting that, for the moment t_8, the ^{239}Pu and ^{238}U distributions in the wave front coincide with those for the moment t_9 in the steady regime, but the level of the neutron flux at t_8 is slightly lower, which corresponds to the initial slowdown of the burning wave mentioned above.

11.2 Forced shutdown

Despite the self-regulating nature of the NBW regime, it is necessary to provide a possibility of forced shutdown of such a reactor, as well as its further restart. The specifics of transient processes in the NBW reactor need a special detailed analysis because of essential nonlinearity of the NBW regime, which results in a nontrivial behavior of the reactor at external interventions. Such an analysis has not been yet performed.

To avoid the influence of any additional disturbing factors, such as external neutron flux at the initiation of the NBW regime, the essential changes of the fuel components in the active zone of the reactor and corresponding reactivity changes at the NBW start-up and transition to the steady state of NBW propagation, the neutron leakage through the open axial boundaries of the FR, etc., we will consider the forced shutdown of the NBW reactor at the moment, when it stays in the exactly steady state regime with a constant neutron flux, power production and velocity of the NBW propagation, and when its active zone is far enough from the axial ends of FR.

Fig. 11.7 shows the space-time evolution of the distributions of the neutron flux and the main fuel isotope ^{239}Pu concentration during the development of the NBW regime in the FR with the metal fuel of U–Pu cycle and optimized ignition zone considered in Section 11.1. Here we chose the FR radius is equal to $R = 1.04$ m. The axial profiles of the neutron flux and ^{239}Pu concentration are presented for several initial time moments (t_1–t_6) of the reactor operation at regular intervals (350 days), as well for the time moment $t_7 = 4000$ days, when the NBW has already reached its steady regime (see also Fig. 11.5).

Further we shall use the results of simulation of operation of the FR under consideration that are shown in Fig. 11.7, as a basic variant for investigating the transient processes during a forced shutdown of the FR at a certain moment at the

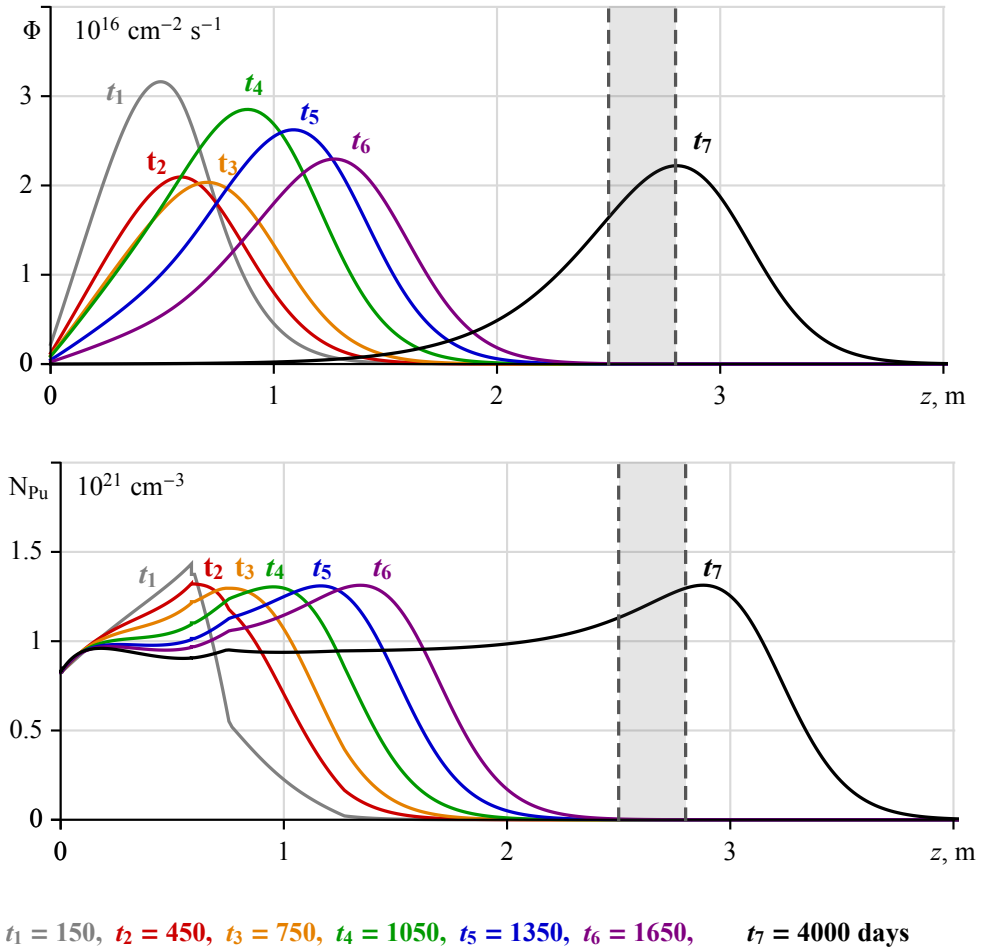

Figure 11.7: Evolution of axial profiles in the FR with the optimized ignition zone shown in Fig. 11.4 for the neutron flux $\Phi(z)$ and the ^{239}Pu concentration $N_{\rm Pu}$ at different time moments t_i.

stage of the steady propagation of NBW, which we shall choose shortly after the time moment t_1 in Fig. 11.7, and during the subsequent restarting of the FR.

We shall first consider the transient processes occurring at a forced shutdown of this FR, which we realize at the time moment $t_0 = 4015$ days by means of introducing a tantalum absorber into a certain zone near the current position of the neutron-flux maximum ($2.5 < z < 2.8$ m), which is shown by vertical dashed lines in Fig. 11.7. This process is simulated by increasing the ^{181}Ta concentration in zone according the linear law $N_{\rm Ta}(t) = N_{\rm Ta}^{(\max)}\,(t - t_0)/\Delta t_{\rm abs}$, where we have chosen the value $N_{\rm Ta}^{(\max)} = 4.5 \times 10^{20}$ cm^{-3}, and $\Delta t_{\rm abs}$ is the duration absorber introduction.

In Figs. 11.8 and 11.9 we present the time variation of the main characteristic

of the FR operation, which occur in the reactor during the mentioned introduction of tantalum absorber of neutrons ($0 < t - t_0 < \Delta\, t_{\rm abs}$).

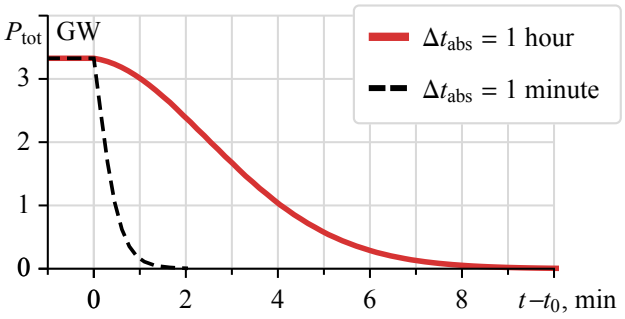

Figure 11.8: Evolution of the FR total power $P_{\rm tot}(t)$ at its shutdown ($t = t_0$): for two durations of Ta absorber introduction.

Figure 11.8 shows the behavior of the reactor power for two different durations of the absorber introduction: 1 hour and 1 minute. From the figure is seen, that at the both rates of introducing the considered absorber a smooth and reliable shutdown of the NBW regime and suppressing the chain reaction are ensured. It is interesting that in the case of the slow introduction of the absorber ($\Delta\, t_{\rm abs} = 60$ minutes) the reactor shutdown occurs even significantly earlier (approximately for 10 minutes) than the complete introduction of the absorber. At the quick absorber introduction ($\Delta\, t_{\rm abs} = 1$ minute), the FR extinction occurs much faster than in the first case, but it lasts longer (about two minutes) than the process of absorber introduction.

The behavior of corresponding quantities shown in Fig. 11.9 at the chosen time scale of these figures (days) is practically the same for both rates of introducing the absorber. It is seen from Fig. 11.9 that before its shutting down the reactor is in the self-sustaining critical state (with a great accuracy the reactivity is $\rho = 0$), and when the tantalum absorber is introduced, a rapid fall of the reactivity into the region of significantly negative values $\rho \approx -6.5 \times 10^{-3}$ (a sub-critical state) occurs, then there is a gradual increase in reactivity, which for the time period $t \approx 20$ days reaches a constant sub-critical value of $\rho \approx -1.25 \times 10^{-3}$. This behavior of the reactor reactivity (10.1) is caused by the processes shown in Fig. 11.9. Firstly, this figure presents the variation of the content of the intermediate isotope ^{239}Np in the FR volume, which has a certain constant value in the steady NBW regime, and after the reactor having been shut down, it gradually decreases owing to β-decay of ^{239}Np ($T_{1/2} \approx 2.35$ days) into the isotope ^{239}Pu.

Figure 11.9 also shows the corresponding variation of the difference of the ^{239}Pu content relative to its value at the moment $t = t_0$. At the stage of steady NBW

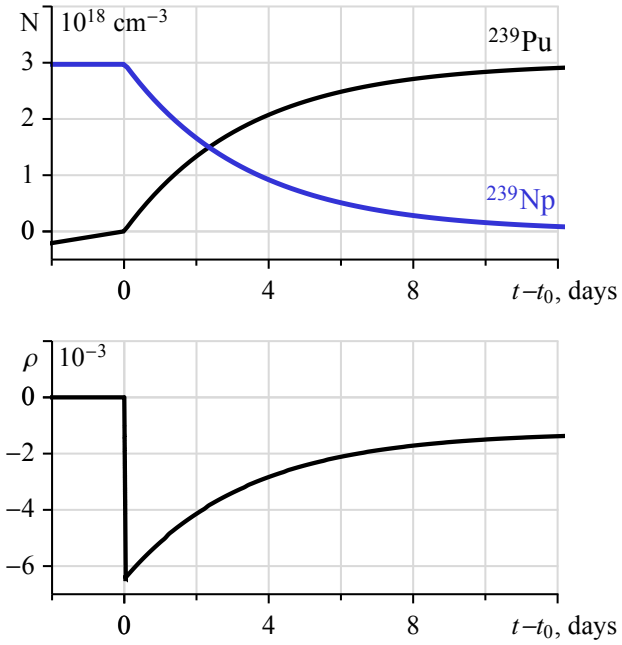

Figure 11.9: Evolution of the average over FR volume concentrations N(t) for ^{239}Np and ^{239}Pu isotope and the FR reactivity $\rho(t)$ at its shutdown ($t = t_0$). Concentration of ^{239}Pu is relative to $t = t_0$: $N_{\mathrm{Pu}}(t) - N_{\mathrm{Pu}}(t_0)$.

regime, an accumulation of ^{239}Pu occurs with a constant rate owing to the axial advance of the burning wave. After the reactor shutting down, owing to the decay of accumulated reserve of ^{239}Np in the absence of plutonium burning, at first a more rapid increase of the ^{239}Pu content is observed, which gradually slows down, and over the time period of $\Delta t \approx 20$ days the ^{239}Pu content reaches a certain constant value. It is just this accumulation of ^{239}Pu which leads to the reactivity growth observed in Fig. 11.9, although the chosen value $N_{\mathrm{Ta}}^{(\mathrm{max})}$ of the introduced absorber content is enough in order that the reactor remained in a sub-critical state.

However the described processes lead to creation of essential surplus of ^{239}Pu in the region of the stopped wave front as compared with the fuel composition in the regime of steady NBW propagation. Because of this, in the case of the complete withdrawal of the introduced absorber from the active zone this reactor would come to an essentially supercritical state.

11.3 Restart after shutdown

In view of the above-discussed points, the problem of restarting the NBW regime in the considered FR consists in the resumption of chain reaction in such a way

that would ensure a gradual burning out of the mentioned plutonium surplus and establishing the self-consistent fuel-component and neutron-flux distributions that correspond to the NBW regime.

When simulating the restarting of the considered FR, we realized this process by means of a gradual withdrawal of the above-described tantalum absorber with a simultaneous creation of neutron field inside the reactor by an external neutron source situated in the zone of active nuclear burning. We have considered a lot of variants of such a restart, which differed in the intensity value of the external neutron source, in its location and duration of its action, as well as in the rate of the tantalum absorber withdrawal. In these calculations, it has been revealed that the system behavior is rather sensitive to the rate of the occurring change of the FR parameters. In order to perform a steady and smooth process of renewing the NBW regime, it is necessary to carry out a sufficiently slow withdrawal of the tantalum absorber and increasing of the neutron-flux level in the reactor, so that the component content of the fuel in the system had time for self-consistently adjusting to these changes. At a too rapid absorber withdrawal and reactivity growth, we observed an onset of instabilities in the form of significant oscillations of the neutron flux as well as of the ^{239}Np and ^{239}Pu concentrations, which is an undesirable phenomenon.

On the basis of considering various variants of restarting the FR, we have succeeded to find some its scenarios that allowed us to ensure an acceptable course of resuming the NBW regime in this FR. Below we present results of the calculations for one of these scenarios. In this variant of the FR restart, the external neutron source with a constant intensity of $Q_{\rm ex} = 10^{10}$ cm^{-3} s^{-1} irradiates the FR region at the interval 2.9 m $< z <$ 3.0 m near the maximum of the axial distribution of ^{239}Pu. Note that locating this source in a different place at 2.4 m $< z <$ 2.5 m behind the tantalum absorber zone did not lead to a considerable change of the simulation results.

To provide a smooth going to the steady NBW regime, we have chosen the tantalum absorber withdrawing that is described by the following law of variation of the ^{181}Ta concentration: $N_{\rm Ta} = N_{\rm Ta}^{(\max)}[(t_{\rm R} + \Delta t_{\rm R} - t) \,/\, \Delta t_{\rm R}]^2$, where $t_{\rm R}$ is the moment of beginning the FR restart and $\Delta t_{\rm R}$ is the duration of the absorber withdrawal process. This law of withdrawal provides, at first, a more rapid increase of the reactor reactivity and then, as the neutron flux grows, the withdrawal rate slows down, which ensures a smooth going to the critical state $\rho = 0$ and allows avoiding undesirable oscillation of the neutron flux.

Figures 11.10 presents the time behavior of the reactor power, its reactivity and the content of fuel components ^{239}Np and ^{239}Pu for two cases, which are distinguished by the moment $t_{\rm R}$ of beginning the restart: in 20 days and in one day after

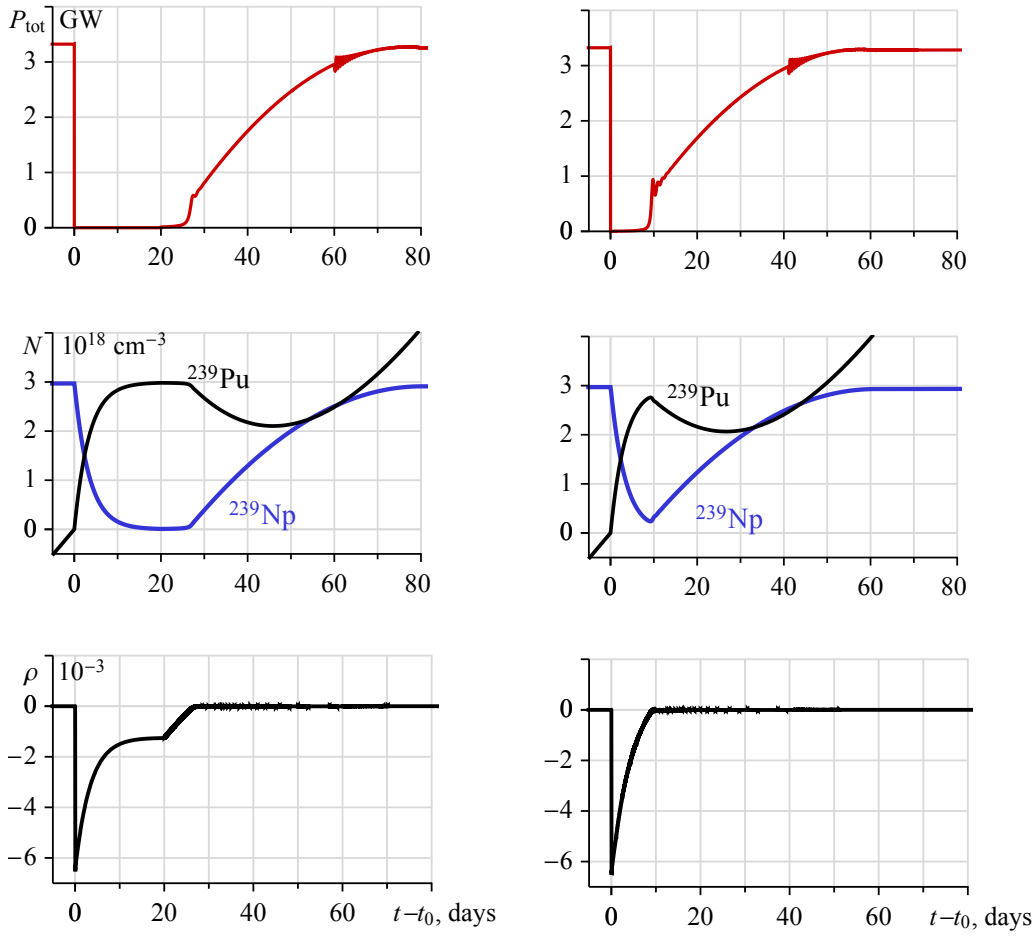

Figure 11.10: Evolution of the reactor power $P_{\text{tot}}(t)$, average over the FR volume concentrations N of ^{239}Np and ^{239}Pu and reactivity $\rho(t)$ at restarting of the FR after its shutdown ($t = t_0$) in 20 days (left plots) and in one day (right plots). Concentration of ^{239}Pu is relative to $t = t_0$: $N_{\text{Pu}}(t) - N_{\text{Pu}}(t_0)$.

the reactor shutdown, correspondingly. The duration of the absorber withdrawal for both these cases was the same, $\Delta t_{\text{R}} = 60$ days, and the external neutron source was turned of in 40 days after the restart beginning. As seen from the Fig. 11.10, in the both presented cases a sufficiently smooth and stable process of resuming the steady regime of NBW propagation occurs. Insignificant oscillations of the reactor power are observed because of sharply turning off the external neutron source, but they are not very essential and are rapidly damped.

An essential difference of the two considered cases consists in the fact, that over 20 days after shutting the FR down the whole accumulated reserve of ^{239}Np had enough time to completely turn into ^{239}Pu, but over one day this process has

only begun. This leads to considerable differences in the behavior of ^{239}Np and ^{239}Pu content and of the reactivity during the restarting (compare the behavior of corresponding curves in Fig. 11.10. In the first case, the observed reactivity growth consists of two stages: first due to the decay of ^{239}Np, and then due to the absorber withdrawal. In the second case, during the restart these two processes occur simultaneously (see Fig. 11.10 right plots). However, these differences do not essentially affect the reactor behavior during the restart.

The results presented in this Chapter were published in [217, 218].

Chapter 12

Conclusion to Part II

In the second part of the thesis, the study of transient processes in advanced fast reactor working in the nuclear burning wave (NBW) regime was performed using the deterministic approach based on numerical solving the non-stationary non-linear diffusion equation of neutron transport together with a set of the burn-up equations for fuel components and the equations of nuclear kinetics for precursor nuclei of delayed neutrons in the effective multi-group approximation. The model of cylindrical homogeneous reactor with metallic fuel of U–Pu, Th–U and mixed Th–U–Pu fuel cycles is considered in the framework of the buckling concept. The presence in the reactor core of constructional material (Fe) as well as the coolant of different types (Na, Pb–Bi eutectic or He) was taken into account by adding the corresponding macroscopic cross sections to the calculation scheme. The temperature effects and heat sink was not taken into account at this stage of calculations.

The performed calculations show that in the reactor with the breeding zone containing the metallic fuel in the form of a mixture of ^{238}U and ^{232}Th, in contrast to the case of using only ^{232}Th, the steady state regime of the NBW can be realized at realistic volume fractions of fuel, constructional material and coolant. It has been shown that such a reactor can be automatically sustained in a state close to the critical one during a long time period (tens of years) without external operational control and refueling.

The detailed analysis of a special kind of the negative reactivity feedback that is inherent to the NBW regime and underlies the "intrinsic safety" of such a reactor has been performed. This analysis showed a notable stability of the NBW regime relative to disturbances of the neutron flux in the system and to irregularities of the fuel composition.

The performed calculations also show that the characteristics of the nuclear burning process essentially depend on the reactor radius. An increase of the FR

radius leads to a rapid increase of the neutron flux in the system and, correspondingly, of the NBW propagation velocity. The decrease of the radius below a certain critical value makes the initiation of the NBW regime impossible.

The features of the initial stage of establishing the NBW regime have been studied in detail by means of consideration of various compositions of the reactor ignition zone. The special method of a smooth start-up of the NBW reactor preventing the excessive increase of neutron flux and power production at the initial stage is proposed.

A numerical simulation has been carried out for the forced shutdown of this FR by means of introducing the neutron absorber ^{181}Ta into a certain axial zone of active nuclear burning. The influence of the absorber introduction rate on the NBW regime extinction has been considered. Detailed studies have been performed concerning the transient physical processes in the FR after its shutdown and the evolution of the system reactivity owing to the ^{239}Np decay and corresponding production of ^{239}Pu, and the minimum amount of introduced tantalum, which is necessary for a reliable shutdown of reactor, has been estimated.

The problem of subsequently restarting the NBW regime in the considered FR consists in providing a gradual burn-out of the plutonium surplus, which was produced after the FR shutdown, and in establishing the self-consistent fuel-component and neutron-flux distributions that correspond to the NBW regime. This process is realized by a gradual withdrawal of the tantalum absorber with a simultaneous creation of the neutron field in the FR using an external neutron source located in the active burning zone. Basing on consideration of various variants of the FR restart certain restart scenario have been found that allow providing a stable and smooth process of resumption of the NBW regime in this FR. The transient physical processes accompanying the NBW restarting have been analyzed in detail.

In the case of the mixed Th–U–Pu fuel, it is possible to achieve values of the main operation parameters of the reactor that look to be acceptable for a practical use. For example, the neutron flux is about 6×10^{15} cm^{-2} s^{-1}, the energy production density is about 500 W/cm^3, the reactor campaign duration equals to approximately 60 years for the reactor length of 5 m, the NBW velocity is about 6 cm/year, the fuel burn-up depth both for ^{238}U and ^{232}Th reaches 45–50 %. The considered scheme makes it possible to involve a large amount of ^{232}Th (50–70 % of the fuel volume fraction) into the nuclear burning process. After the final extinction of the reactor, the concentrations of the produced fissile isotopes of plutonium and uranium, which could serve as a fuel for other reactors after a proper processing, reach a significant level (6–7 %) in the whole volume of the reactor.

Appendix A

Spectral-angular density of radiation in a thin target

The spectral-angular density of radiation $d^2E/d\omega\, do$ and the degree of linear polarization P can be determined in terms of polarization matrix elements as

$$\frac{d^2E}{d\omega do} = J_{11} + J_{22}, \qquad P = \frac{J_{11} - J_{22}}{J_{11} + J_{22}}. \tag{A.1}$$

The general expression for the polarization tensor of radiation is [157]

$$J_{ik} = \frac{e^2\omega^2}{4\pi^2}\left(\vec{e}_i\vec{I}\right)\left(\vec{e}_k\vec{I}^*\right), \tag{A.2}$$

where $\vec{e}_{i,k}$ are the polarization vectors which are the unit vectors orthogonal to the wave vector $\vec{k}$ and to each other: $\vec{e}_{i,k}\,\vec{k} = 0$, $\vec{e}_i\,\vec{e}_k = \delta_{ik}$.

In case of thin target, i.e. when the coherence length of radiation is essentially bigger than the thickness of the target $l_c \gg T$, we obtain (5.62)

$$\vec{I} \approx i\left(\frac{\vec{v}\,'}{\omega - \vec{k}\cdot\vec{v}\,'} - \frac{\vec{v}}{\omega - \vec{k}\cdot\vec{v}}\right), \tag{A.3}$$

where $\vec{v}$ and $\vec{v}\,'$ are the velocities of the electron before and after its passing the target. The expression (A.3) shows that if the condition $l_c \gg T$ is fulfilled, the radiation of an electron does not depend on the details of the particle trajectory within the target and is defined exclusively by the resulting angle of its scattering by the target $\vartheta_s = (\vec{v}\,\wedge\,\vec{v}\,')$.

To obtain the expressions for the spectral-angular density of radiation $d^2E/d\omega\, do$ and the degree of linear polarization P in case of an ultra relativistic electron in a thin layer of matter, we substitute the expression (A.3) into (A.2).

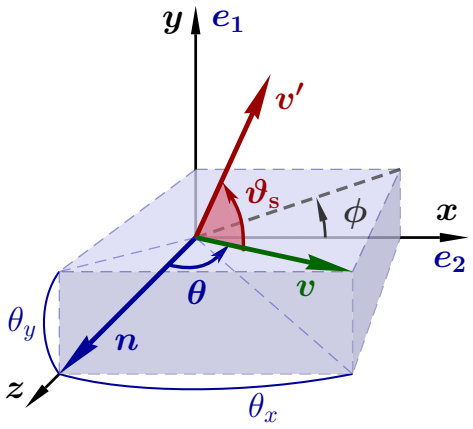

Figure A.1: Reference frame for calculation of intensity and polarization of radiation.

Thus, we can write the following expression for the linear combination of symmetrical elements of polarization matrix

$$J_{11} \pm J_{22} = \frac{e^2}{4\pi^2}\left(\left(\frac{\vec{e}_1\,\vec{v}\,'}{1-\vec{n}\,\vec{v}\,'} - \frac{\vec{e}_1\,\vec{v}}{1-\vec{n}\,\vec{v}}\right)^2 \pm \left(\frac{\vec{e}_2\,\vec{v}\,'}{1-\vec{n}\,\vec{v}\,'} - \frac{\vec{e}_2\,\vec{v}}{1-\vec{n}\,\vec{v}}\right)^2\right) \tag{A.4}$$

where $\vec{n} = \vec{k}/\omega$ is the unit vector in the direction of the wave vector $\vec{k}$.

Lets choose of the coordinate frame (see Fig. A.1) in which axis Oz is parallel to the wave vector of emitted photon $\vec{k}$ and the velocity of the electron after its passing the target $\vec{v}\,'$ lies in the plane $(Oy,\,\vec{v})$:

$$\begin{aligned} \vec{n} &= (0,0,1), & \vec{v} &= |\vec{v}|\,(\sin\theta\,\cos\phi,\ \sin\theta\,\sin\phi,\ \cos\theta), \\ \vec{e}_1 &= (0,1,0), & \vec{v}\,' &\in (Oy,\,\vec{v}), \\ \vec{e}_2 &= (1,0,0), & |\vec{v}| &= \sqrt{1-\gamma^{-2}}. \end{aligned} \tag{A.5}$$

where, θ and ϕ are the polar and azimuthal angles of electron velocities before its passing the target in the reference frame (A.5). In this frame the expression (A.4) can be written in the following way:

$$J_{11} \pm J_{22} = \frac{e^2}{4\pi^2}\frac{\left(\vec{v}\,'_x\,(1-\vec{v}_z) - \vec{v}_x\,(1-\vec{v}\,'_z)\right)^2 \pm \left(\vec{v}\,'_y\,(1-\vec{v}_z) - \vec{v}_y\,(1-\vec{v}\,'_z)\right)^2}{(1-\vec{v}_z)^2\,(1-\vec{v}\,'_z)^2} \tag{A.6}$$

As the characteristic angles of fast electrons scattering ϑ_s and the photon emission by relativistic particles θ are very small ($\sim \gamma^{-1}$), it is convenient to use the following notation:

$$\begin{aligned} &\alpha \equiv \gamma\,\theta, \qquad \alpha_x \equiv \gamma\,\theta_x \equiv \gamma\,\theta\cos\phi, \qquad \alpha_y \equiv \gamma\,\theta_y \equiv \gamma\,\theta\sin\phi, \\ &\beta \equiv \gamma\,\vartheta_{\rm s}. \end{aligned} \tag{A.7}$$

The expressions of the velocity components at $\gamma \gg 1$ can be simplified in the following way:

$$\begin{aligned} v_x &= \frac{\alpha_x}{\gamma}, \qquad v_y = \frac{\alpha_y}{\gamma}, \qquad 1 - v_z = \frac{1+\alpha^2}{2\,\gamma^2}, \\ v'_x &= \frac{\alpha_x}{\gamma}, \qquad v'_y = \frac{\alpha_y - \beta}{\gamma}, \qquad 1 - v'_z = \frac{1+\alpha_x^2+(\alpha_y-\beta)^2}{2\,\gamma^2}. \end{aligned} \tag{A.8}$$

Substituting the expression (A.8) into (A.6) we get

$$J_{11} \pm J_{22} = \frac{e^2\gamma^2\beta^2}{\pi^2}\,\frac{\left(\alpha_y^2 \pm \alpha_x^2\right)(\beta - 2\,\alpha_y)^2 + \left(1+\alpha^2\right)\left(1+\alpha^2+2\,\alpha_y(\beta-2\,\alpha_y)\right)}{\left(1+\alpha^2\right)^2\,\left(1+\alpha^2+\beta\,(\beta-2\,\alpha_y)\right)^2}. \tag{A.9}$$

The expressions for the spectral-angular density of radiation $d^2E/d\omega\,do$ and the degree of linear polarization P in case of an ultra relativistic electron scattering in a thin layer of matter can be simplified to the following:

$$\frac{d^2E}{d\omega do} = \frac{e^2\gamma^2}{\pi^2}\,\frac{\beta^2}{\left(1+\alpha^2\right)^2}\,\frac{\left(1+\alpha^2\right)^2 + \left(\alpha^2\beta + 2\alpha_y\right)(\beta - 2\alpha_y)}{\left(1+\alpha^2+\beta\,(\beta-2\alpha_y)\right)^2}, \tag{A.10}$$

$$P = 1 - \frac{2\alpha_x^2\,(\beta-2\alpha_y)^2}{\left(1+\alpha^2\right)^2 + \left(\alpha^2\beta+2\alpha_y\right)(\beta-2\alpha_y)}, \tag{A.11}$$

or in terms of polar angle ϕ:

$$\frac{d^2E}{d\omega do} = \frac{e^2\gamma^2}{\pi^2}\,\frac{\beta^2}{\left(1+\alpha^2\right)^2}\,\frac{\left(\left(1-\alpha^2\right)\sin\phi + \alpha\beta\right)^2 + \left(1+\alpha^2\right)^2\cos^2\phi}{\left(1+\alpha^2+\beta^2-2\alpha\beta\sin\phi\right)^2}, \tag{A.12}$$

$$P = 1 - \frac{2\,\alpha^2\cos^2\phi\;\;(\beta - 2\,\alpha\,\sin\phi)^2}{\left(\left(1-\alpha^2\right)\sin\phi + \alpha\beta\right)^2 + \left(1+\alpha^2\right)^2\cos^2\phi}. \tag{A.13}$$

Bibliography

[1] C. Patrignani et al. Review of Particle Physics. *Chin. Phys.*, C40(10):100001, 2016. (Cited on pages 4, 30, 41, 42 and 50.)

[2] D. Chen et al. First observation of magnetic moment precession of channeled particles in bent crystals. *Phys. Rev. Lett.*, 69:3286–3289, 1992. (Cited on pages 4, 44 and 45.)

[3] M.L. Ter-Mikaelian. *High-energy electromagnetic processes in condensed matter*. Wiley Interscience, New York, 1972. (Cited on pages 4, 20, 30, 62, 63, 65, 66, 67, 68, 70, 71, 72, 76, 78 and 82.)

[4] A.I. Akhiezer and N.F. Shul'ga. High-energy electrodynamics in matter. *Gordon and Breach, Amsterdam*, page 388, 1996. (Cited on pages 4, 5, 11, 30, 62, 63, 64, 67, 68, 69, 70, 71, 72, 79, 90 and 104.)

[5] A.W. Sáenz and H. Überall. *Coherent radiation sources*. Springer-Verlag, Berlin, 1985. (Cited on page 4.)

[6] A.P. Potylitsyn. Polarized photon beams of high energy, 1987. (Cited on page 4.)

[7] U.I. Uggerhoj. The interaction of relativistic particles with strong crystalline fields. *Rev. Mod. Phys.*, 77:1131–1171, 2005. (Cited on pages 4 and 83.)

[8] A. Potylitsyn. *Electromagnetic radiation of electrons in periodic structures*. Springer-Verlag Berlin and Heidelberg GmbH & Co. KG, 2013. (Cited on page 4.)

[9] X. Artru, R. Chehab, M. Chevallier, et al. Polarized and unpolarized positron sources for electron–positron colliders. *Nuclear Instruments and Methods in Physics Research Section B: Beam Interactions with Materials and Atoms*, 266(17):3868–3875, 2008. (Cited on page 5.)

[10] X. Artru, I. Chaikovska, R. Chehab, et al. Investigations on a hybrid positron source with a granular converter. *Nuclear Instruments and Methods in Physics Research Section B: Beam Interactions with Materials and Atoms*, 355:60–64, 2015. (Cited on page 5.)

[11] L.D. Landau and I.Yu. Pomeranchuk. Electron-cascade processes at ultra-high energies. *Dokl. Akad. Nauk SSSR*, 92:735–740, 1953. (Cited on pages 5, 61, 68, 72, 73 and 108.)

[12] A.I. Akhiezer, N.F. Shul'ga, and S.P. Fomin. *Landau–Pomeranchuk–Migdal Effect*. Cambridge Scientific Publishers, UK, 2005. (Cited on pages 5, 65, 72, 73, 78, 79, 104, 106 and 110.)

[13] J. Stark. Bemerkung über zerstreuung und absorption von β-stahken und röntgenstrahlen in kristallen. *Phys. Zs.*, 973(13), 1912. (Cited on page 8.)

[14] M.T. Robinson and O.S. Oen. Computer studies of the slowing down of energetic atoms in crystals. *Phys. Rev.*, 132:2385–2398, 1963. (Cited on pages 8 and 14.)

[15] J. Lindhard. Influence of crystal lattice on motion of energetic charged particles. *Mat. Fys. Medd. Dan. Vid. Selsk.*, 34(14):1–64, 1965. (Cited on pages 8, 9, 11, 16, 21, 23, 27 and 91.)

[16] D.S. Gemmell. Channeling and related effects in the motion of charged particles through crystals. *Rev. Mod. Phys.*, 46:129–227, 1974. (Cited on pages 9 and 13.)

[17] S.P. Fomin and N.F. Shul'ga. Rainbow scattering and orbiting of fast particles in crystals. *Physics Letters A*, 73(2):131–133, 1979. (Cited on pages 11 and 20.)

[18] S.K. Andersen, O. Fich, H. Nielsen, et al. Influence of channeling on scattering of 2–15 GeV/c protons, π^+, and π^- incident on Si and Ge crystals. *Nucl. Phys. B*, 167:1, 1980. (Cited on pages 11 and 20.)

[19] V.L. Morokhovsky and B.I. Shramenko. Orientation effects in scattering of high energy positrons and electrons in single crystals. *Proceedings of 7th All-Union Workshop on Physics of charged particle interaction with single crystals, Moscow, MGU*, page 173, 1976. (Cited on pages 11 and 20.)

[20] V.V. Beloshitsky and M.A. Kumakhov. *Phys. Tverd. Tela*, 15:1588, 1973. (Cited on pages 11 and 20.)

[21] Golovchenko J.A. *Phys. Rev. Ser. B*, 13:4672, 1976. (Cited on pages 11 and 20.)

[22] S.P. Fomin and N.F. Shul'ga. On theory of scattering of fast particles in a crystal. *Preprint KPTI, Kharkov*, 42:1–34, 1979. (Cited on pages 11, 12 and 20.)

[23] N.F. Shul'ga, Truten' V.I., and S.P. Fomin. On multiple scattering of relativistic particles in crystals. *Sov. Phys. – Techn. Phys.*, 27:1399–1400, 1982. (Cited on pages 11, 12, 90, 91 and 98.)

[24] A.I. Akhiezer, N.F. Shul'ga, V.I. Truten, et al. Dynamics of high-energy charged particles in straight and bent crystals. *Phys. Usp.*, 38(10):1119–1145, 1995. [Usp. Fiz. Nauk165,1165(1995)]. (Cited on pages 11, 12, 18, 20 and 21.)

[25] N.F. Shul'ga, Truten' V.I., and S.P. Fomin. Orientation effects in relativistic particle scattering in single crystals. *Preprint KPTI, Kharkov*, 11:1–27, 1982. (Cited on page 12.)

[26] A.I. Akhiezer, I.A. Akhiezer, and N.F. Shul'ga. *Zh. Eksp. Teor. Fiz.*, 76(10):1244, 1979. [Sov. Phys. JETP 49 625 (1979)]. (Cited on page 16.)

[27] M.A. Kumakhov. Spatial redistribution of a flux of charged particles in a crystal lattice. *Sov. Phys. Uspekhi*, 18(3):203, 1975. (Cited on pages 16 and 23.)

[28] A. Baurichter et al. Channeling of high-energy particles in bent crystals: Experiments at the CERN SPS. B164-165:27–43, 2000. (Cited on pages 17 and 19.)

[29] A.M. Taratin. Channeling of particles in a bent crystal. *Particles and Nuclei*, 29(5):1063–1118, 1998. (Cited on page 18.)

[30] V.M. Biryukov, V.I. Kotov, and Yu.A. Chesnokov. Steering of high-energy charged particle beams by bent single crystals. *Phys. Usp.*, 37:937–960, 1994. [Usp. Fiz. Nauk **164**, 1017 (1994)]. (Cited on page 18.)

[31] E.N. Tsyganov. Some aspects of the mechanism of a charge particle penetration through a monocrystal. 1976. (Cited on page 18.)

[32] A.A. Greenenko and N.F. Shul'ga. Turning a beam of high-energy charged particles by means of scattering by atomic rows of a curved crystal. *JETP Lett.*, 54(9):524–528, 1991. (Cited on page 20.)

[33] N.F. Shul'ga and A.A. Greenenko. Multiple scattering of ultrahigh-energy charged particles on atomic strings of a bent crystal. *Phys. Lett.*, B353(2–3):373–377, 1995. (Cited on page 20.)

[34] M.A. Kumakhov. A theory of flux peaking effect in channeling. *Rad. Eff.*, 15:85–96, 1972. (Cited on page 23.)

[35] V.V. Beloshitsky, F.F. Komarov, and M.A. Kumakhov. Dechanneling, flux peaking and energy losses of fast charged particles penetrating through thick crystals. *Phys. Rept.*, 139:293–364, 1986. (Cited on page 23.)

[36] S.V. Beslaneeva and V.I. Telegin. Angular distribution of the radiative energy losses of axially channeled ultrarelativistic electrons in single crystals. *Sov. Phys.*, JETP:671–678, 1987. [Zh. Eksp. Teor. Fiz.92,1201(1987)]. (Cited on page 23.)

[37] Y.H. Ohtsuki. Charged beam interaction with solids. In *Taylor & Frencis Ltd, London and New York*, 1983. (Cited on page 23.)

[38] Y.H. Ohtsuki and H. Nitta. Theory of dechanneling. In *Maratea 1986, proceedings, relativistic channeling*, pages 59–67, 1986. (Cited on page 23.)

[39] M.A. Kumakhov. On the theory of electromagnetic radiation of charged particles in a crystal. *Phys. Lett.*, A57:17–18, 1976. (Cited on page 24.)

[40] S.P. Fomin. Angular distributions of relativistic electrons passing through a thin plane oriented crystal. In *Abstracts of XX Workshop on Physics of Charged Particle Interaction with Crystals, MGU, Moscow*, page 34, 1990. (Cited on page 24.)

[41] V.P. Ermak et al. Angular distributions of planar multiscattering of electrons by silicon single crystals. In *Abstracts of XX Workshop on Physics of Charged Particle Interaction with Crystals, MGU, Moscow*, page 18, 1990. (Cited on page 24.)

[42] N.V. Laskin, N.F. Shul'ga, and S.P. Fomin. Dechanneling as diffusion in a random medium. *Dokl. Akad. Nauk SSSR*, 301:855–858, 1988. (Cited on page 24.)

[43] N.V. Laskin, S.P. Fomin, and N.F. Shul'ga. Dechanneling kinetics under dynamic chaos conditions. *Physics Letters A*, 138(6–7):309–312, 1989. (Cited on page 24.)

[44] Greenenko A.A., A.V. Chechkin, and N.F. Shul'ga. Anomalous diffusion and Levy flights in channeling. *Phys. Letters A*, 324:82–85, 2004. (Cited on page 24.)

[45] V.I. Glebov, V.V. Goloviznin, and A.M. Kanloev. Energy dependence of spectral-angular characteristics of channeling radiation. *Radiation Effects and Defects in Solids*, 82(3-4):189–198, 1984. (Cited on pages 25 and 30.)

[46] V.A. Bazylev, V.I. Glebov, and V.V. Goloviznin. Quantum theory of inelastic scattering of negatively charged particles by oriented crystals. *Sov. Phys. JETP*, 64:14–20, 1986. [Zh. Eksp. Teor. Fiz.91,25(1986)]. (Cited on page 25.)

[47] H. Bethe. Moliere's theory of multiple scattering. *Phys. Rev.*, 89:1256–1266, 1953. (Cited on pages 26, 90, 100 and 104.)

[48] G. Moliere. Theorie der Streuung schneller geladener Teilchen I. Einzelstreuung am abgeschirmten Coulomb-Feld. *Z. Naturforsch.*, A2:133, 1947. (Cited on page 28.)

[49] L.C. Feldman and J.W. Mayer. *Fundamentals of surface and thin film analysis*. North Holland, Elsevier Science Publishers, P. O. Box 211, 1000 AE Amsterdam, The Netherlands, 1986. (Cited on page 29.)

[50] V.M. Biryukov, V.I. Kotov, and Yu.A. Chesnokov. Steering of high-energy charged particle beams by bent single crystals. *Phys. Usp.*, 37:937–960, 1994. [Usp. Fiz. Nauk **164**, 1017 (1994)]. (Cited on pages 36, 43 and 44.)

[51] J.S. Forster et al. Deflection of GeV particle beams by channeling in bent crystal planes of constant curvature. *Nucl. Phys.*, B318:301, 1989. (Cited on page 40.)

[52] G.W. Bennett et al. Final report of the Muon E821 anomalous magnetic moment measurement at BNL. *Phys. Rev.*, D73:072003, 2006. (Cited on page 41.)

[53] F. Jegerlehner and A. Nyffeler. The Muon g-2. *Phys. Rept.*, 477:1–110, 2009. (Cited on page 41.)

[54] S. Eidelman and M. Passera. Theory of the tau lepton anomalous magnetic moment. *Mod. Phys. Lett.*, A22:159–179, 2007. (Cited on page 41.)

[55] J. Franklin, D.B. Lichtenberg, W. Namgung, et al. Wave function mixing of flavor degenerate baryons. *Phys. Rev.*, D24:2910, 1981. (Cited on page 42.)

[56] N. Barik and M. Das. Magnetic moments of confined quarks and baryons in an independent quark model based on Dirac equation with power law potential. *Phys. Rev.*, D28:2823–2829, 1983. (Cited on page 42.)

[57] M.J. Savage. Magnetic moment of the Lambda(c), Xi(c1)+ and Xi(c1)0. *Phys. Lett.*, B326:303–306, 1994. (Cited on page 42.)

[58] B. Silvestre-Brac. Spectrum and static properties of heavy baryons. *Few Body Syst.*, 20:1–25, 1996. (Cited on page 42.)

[59] S.-L. Zhu, W.-Y.P. Hwang, and Z.-S. Yang. The Sigma(c) and Lambda(c) magnetic moments from QCD spectral sum rules. *Phys. Rev.*, D56:7273–7275, 1997. (Cited on page 42.)

[60] T.M. Aliev, A. Ozpineci, and M. Savci. The magnetic moments of Lambda(b) and Lambda(c) baryons in light cone QCD sum rules. *Phys. Rev.*, D65:056008, 2002. (Cited on page 42.)

[61] B. Julia-Diaz and D.O. Riska. Baryon magnetic moments in relativistic quark models. *Nucl. Phys.*, A739:69–88, 2004. (Cited on page 42.)

[62] C. Albertus, E. Hernandez, J. Nieves, et al. Static properties and semileptonic decays of doubly heavy baryons in a nonrelativistic quark model. *Eur. Phys. J.*, A32:183–199, 2007. [Erratum: Eur. Phys. J.A36,119(2008)]. (Cited on page 42.)

[63] S. Kumar, R. Dhir, and R.C. Verma. Magnetic moments of charm baryons using effective mass and screened charge of quarks. *J. Phys.*, G31(2):141–147, 2005. (Cited on page 42.)

[64] A. Faessler, Th. Gutsche, M.A. Ivanov, et al. Magnetic moments of heavy baryons in the relativistic three-quark model. *Phys. Rev.*, D73:094013, 2006. (Cited on page 42.)

[65] M. Karliner and H.J. Lipkin. The new Σ_b multiplet and magnetic moments of Λ_c and Λ_b. *Phys. Lett.*, B660:539–544, 2008. (Cited on page 42.)

[66] Bh. Patel, A.K. Rai, and P.C. Vinodkumar. Heavy flavour baryons in hyper central model. *Pramana*, 70:797–804, 2008. (Cited on page 42.)

[67] A. Majethiya, Bh. Patel, and P.C. Vinodkumar. Single heavy flavour baryons using coulomb plus power law interquark potential. *Eur. Phys. J.*, A38:307–315, 2008. (Cited on page 42.)

[68] T.M. Aliev, K. Azizi, and A. Ozpineci. Magnetic moments of heavy Ξ_Q baryons in light cone QCD sum rules. *Phys. Rev.*, D77:114006, 2008. (Cited on page 42.)

[69] T.M. Aliev, K. Azizi, and A. Ozpineci. Mass and magnetic moments of the heavy flavored baryons with J=3/2 in light cone QCD sum rules. *Nucl. Phys.*, B808:137–154, 2009. (Cited on page 42.)

[70] N. Sharma, H. Dahiya, P.K. Chatley, et al. Spin $1/2^+$, spin $3/2^+$ and transition magnetic moments of low lying and charmed baryons. *Phys. Rev.*, D81:073001, 2010. (Cited on page 42.)

[71] A. Bernotas and V. Simonis. Magnetic moments of heavy baryons in the bag model reexamined. *Lith. J. Phys.*, 53:84, 2013. (Cited on page 42.)

[72] D.H. Perkins. *Introduction to high-energy physics, 4th ed.* Cambridge University Press, Cambridge U.K., 2000. (Cited on page 42.)

[73] L. Burmistrov, G. Calderini, Yu. Ivanov, et al. Measurement of short living baryon magnetic moment using bent crystals at SPS and LHC. Technical Report CERN-SPSC-2016-030. SPSC-EOI-012, CERN, Geneva, Jun 2016. (Cited on pages 43 and 47.)

[74] V.G. Baryshevsky. The possibility to measure the magnetic moments of short-lived particles (charm and beauty baryons) at LHC and FCC energies using the phenomenon of spin rotation in crystals. *Phys. Lett.*, B757:426–429, 2016. (Cited on page 43.)

[75] F.J. Botella, L.M. Garcia Martin, D. Marangotto, et al. On the search for the electric dipole moment of strange and charm baryons at LHC. *Eur. Phys. J.*, C77(3):181, 2017. (Cited on pages 43 and 50.)

[76] L.H. Thomas. The motion of a spinning electron. *Nature*, 117:514, 1926. (Cited on page 43.)

[77] L.H. Thomas. The kinematics of an electron with an axis. *Phil. Mag. Ser.7*, 3:1–21, 1927. (Cited on page 43.)

[78] V. Bargmann, L. Michel, and V.L. Telegdi. Precession of the polarization of particles moving in a homogeneous electromagnetic field. *Phys. Rev. Lett.*, 2:435–436, 1959. [,92(1959)]. (Cited on page 43.)

[79] R. Hagedorn. *Relativistic Kinematics*. Benjamin, New York, NY, 1963. (Cited on page 43.)

[80] V.B. Berestetskii, E.M. Lifshitz, and L.P. Pitaevskii. *Quantum Electrodynamics*, volume 4 of *Course of Theoretical Physics*. Pergamon Press, Oxford, 1982. (Cited on page 43.)

[81] V.G. Baryshevsky. Spin rotation of ultrarelativistic particles passing through a crystal. *Sov. Tech. Phys. Lett.*, 5:73, 1979. [Pis'ma. Zh. Tekh. Fiz. 5 (1979) 182]. (Cited on page 43.)

[82] V.L. Lyuboshits. The spin rotation at deflection of relativistic charged particle in electric field. *Sov. J. Nucl. Phys.*, 31:509, 1980. [Yad. Fiz.31,986(1980)]. (Cited on pages 43 and 45.)

[83] I.J. Kim. Magnetic moment measurement of baryons with heavy flavored quarks by planar channeling through bent crystal. *Nucl. Phys.*, B229:251–268, 1983. (Cited on pages 43 and 45.)

[84] A.I. Akhiezer, N.F. Shul'ga, V.I. Truten, et al. Dynamics of high-energy charged particles in straight and bent crystals. *Phys. Usp.*, 38:1119–1145, 1995. [Usp. Fiz. Nauk165,1165(1995)]. (Cited on pages 43 and 44.)

[85] A.A. Grinenko and N.F. Shul'ga. Turning a beam of high-energy charged particles by means of scattering by atomic rows of a curved crystal. *JETP Lett.*, 54:524–528, 1991. [Pisma Zh. Eksp. Teor. Fiz.54,520(1991)]. (Cited on pages 43 and 44.)

[86] A.A. Greenenko and N.F. Shul'ga. Spin rotation and deflection of high-energy charged particles in a bent crystal due to multiple scattering by atomic strings. *Nucl. Instrum. Meth.*, B67:212–216, 1992. (Cited on pages 43 and 44.)

[87] E.N. Tsyganov. Some aspects of the mechanism of a charge particle penetration through a monocrystal. preprint Fermilab TM-682, Batavia U.S.A., 1976. (Cited on page 44.)

[88] S.P. Fomin et al. Investigation of the electron channeling by means of induced electronuclear reactions. *Nucl. Instrum. Meth. B*, 129:29–34, 1997. (Cited on page 44.)

[89] W. Scandale et al. Observation of channeling for 6500 GeV/c protons in the crystal assisted collimation setup for LHC. *Phys. Lett.*, B758:129–133, 2016. (Cited on page 47.)

[90] W. Scandale et al. Optical layout for the measurement of short living baryon magnetic moment using bent crystals at lhc. In *Physics Beyond Colliders Kick-off Workshop*, Geneva, Switzerland, 6-7 September 2016. (Cited on page 47.)

[91] A. Stocchi et al. Measuring magnetic moments with bended crystal. In *Physics Beyond Colliders Kickoff Workshop*, Geneva, Switzerland, 6-7 September 2016. (Cited on page 47.)

[92] E.M. Aitala et al. Multidimensional resonance analysis of Lambda+(c) —> p K- pi+. *Phys. Lett.*, B471:449–459, 2000. (Cited on pages 49 and 50.)

[93] J.G. Korner, G. Kramer, and J. Willrodt. Weak decays of charmed baryons. *Z. Phys.*, C2:117, 1979. (Cited on page 49.)

[94] G.R. Goldstein. Polarization of inclusive Lambda(c)'s in a hybrid model. In *Hyperon physics symposium : Hyperon 99, September 27-29, 1999, Fermi National Accelerator Laboratory, Batavia, Illinois*, pages 132–136, 1999. (Cited on page 49.)

[95] W.G.D. Dharmaratna and G.R. Goldstein. Single quark polarization in quantum chromodynamics subprocesses. *Phys. Rev.*, D53:1073–1086, 1996. (Cited on page 49.)

[96] G.R. Goldstein. Polarization of inclusively produced Lambda(c) in a QCD based hybrid model. 1999. (Cited on page 49.)

[97] T. Sjöstrand, S. Mrenna, and P.Z. Skands. A brief introduction to PYTHIA 8.1. *Comput. Phys. Commun.*, 178:852–867, 2008. (Cited on page 50.)

[98] Maurice E. et al. Measurement of J/ψ and D^0 production in pAr collisions at $\sqrt{s_{NN}} = 110$ GeV. 2017. (Cited on page 50.)

[99] A.S. Fomin, A.Yu. Korchin, A. Stocchi, et al. Feasibility of measuring the magnetic dipole moments of the charm baryons at the LHC using bent crystals. *Journal of High Energy Physics*, 2017(8):120, Aug 2017. https://doi.org/10.1007/JHEP08(2017)120. (Cited on pages 51, 59, 112 and 113.)

[100] A. Adare et al. Measurement of high-p(T) single electrons from heavy-flavor decays in p+p collisions at $\sqrt{s} = 200\,\text{GeV}$. *Phys. Rev. Lett.*, 97:252002, 2006. (Cited on page 51.)

[101] S.S. Adler et al. Single electrons from heavy flavor decays in p+p collisions at $\sqrt{s} = 200\,\text{GeV}$. *Phys. Rev. Lett.*, 96:032001, 2006. (Cited on page 51.)

[102] R. Aaij et al. Prompt charm production in pp collisions at $\sqrt{s} = 7\,\text{TeV}$. *Nucl. Phys.*, B871:1–20, 2013. (Cited on page 51.)

[103] I. Abt et al. Measurement of D0, D+, D+(s) and D*+ production in fixed target 920-GeV proton-nucleus collisions. *Eur. Phys. J.*, C52:531–542, 2007. (Cited on page 51.)

[104] B. Ferretti. Sulla bremsstahlung nei cristalii. *Nuovo Cimento*, 7:118–134, 1950. (Cited on pages 61 and 95.)

[105] M.L. Ter-Mikaelian. Interference radiation of ultra fast electrons. *Zh. Exp. Teor. Fiz.*, 25:296–306, 1953. (Cited on pages 61, 62, 65, 66, 67, 68 and 95.)

[106] H. Uberall. High-energy interference effect of bremsstrahlung and pair production. *Phys. Rev.*, 103:1055–1067, 1956. (Cited on pages 61 and 95.)

[107] O.R. Frich and D.N. Olson. . *Phys. Rev. Lett.*, 3:141, 1959. (Cited on page 61.)

[108] G. Bologna, G. Diambrini, and G.P. Murtas. . *Phys. Rev. Lett.*, 4:134, 1960. (Cited on page 61.)

[109] W.K.H. Panofsky and A.N. Saxena. . *Phys. Rev. Lett.*, 2:219, 1959. (Cited on page 61.)

[110] H. Bethe and W. Heitler. On the stopping of fast particles and on the creation of passive electrons. *Proc. Roy. Soc. (London) A*, 146:83–125, 1934. (Cited on pages 62, 65, 77, 106 and 108.)

[111] M. Miesowicz, O. Stanisz, and W. Wolther. Investigation of an electromagnetic cascade of very high energy in the first stage of its development. *Nuovo Cimento*, 5(2):513–516, 1957. (Cited on pages 62 and 74.)

[112] A. Varfolomeev, R.R. Gerasimova, I.I. Gurevitch, et al. Influence of the medium density on bremsstrahlung in electron-photon showers in the energy range $10^1 1 - 10^1 3$ eV. *Sov. Phys. JETP*, 11:23–25, 1960. (Cited on pages 62 and 74.)

[113] A.I. Akhiezer and V.B. Berestetskii. *Quantum Electrodynamics*. New York: Interscience, 1965. (Cited on pages 62 and 63.)

[114] K.A. Olive and others (Particle Data Group). . *Chin. Phys. C*, 38:090001, 2014. (Cited on pages 67, 79 and 105.)

[115] J.D. Jackson. *Classical Electrodynamics, 3rd edition*. John Wiley and Sons, 1998. (Cited on pages 68 and 69.)

[116] M.L. Ter-Mikaelian. . *Dokl. Akad. Nauk SSSR*, 94:1033, 1954. (Cited on pages 71, 75 and 78.)

[117] S. Klein. Suppression of bremsstrahlung and pair production due to environmental factors. *Rev. Mod. Phys.*, 71:1501–1538, 1999. (Cited on pages 71, 75, 76, 78 and 83.)

[118] P.L. Anthony, R. Becker-Szendy, P. Bosted, et al. Measurement of dielectric suppression of bremsstrahlung. *Phys. Rev. Lett.*, 76:3550–3553, 1996. (Cited on pages 71, 75 and 76.)

[119] P.L. Anthony, R. Becker-Szendy, P. Bosted, et al. Bremsstrahlung suppression due to the Landau–Pomeranchuk–Migdal and dielectric effects in a variety of materials. *Phys. Rev., D*, 56:1373–1390, 1997. (Cited on pages 71, 75, 76 and 83.)

[120] A.B. Migdal. The influence of the multiple scattering on the bremsstrahlung at high energies. *Dokl. Akad. Nauk SSSR*, 96:49–52, 1954. (Cited on pages 72, 73, 75, 77, 80 and 108.)

[121] A.B. Migdal. . *Phys. Rev. Nauk SSSR*, 103:1811, 1956. (Cited on pages 72, 73 and 75.)

[122] N.V. Laskin, A.S. Mazmanishvili, and N.F. Shul'ga. . *Dokl. Akad. Nauk SSSR*, 277:850, 1984. (Cited on page 72.)

[123] N.V. Laskin, A.S. Mazmanishvili, and N.F. Shul'ga. . *Phys. Lett., A*, 112:240, 1985. (Cited on page 72.)

[124] N.V. Laskin, A.S. Mazmanishvili, N.N. Nasonov, et al. . *JETP*, 62:438, 1985. (Cited on page 72.)

[125] A. Varfolomeev et al. Effect of the medium on the bremsstrahlung spectra of 40 GeV electrons . *Sov. Phys. JETP*, 42:218–227, 1976. (Cited on page 74.)

[126] V.N. Baier and V.M. Katkov. Variation of radiation length due to LPM effect. *Phys. Lett.*, A327:202–209, 2004. (Cited on page 75.)

[127] H.D. Hansen, U.I. Uggerhoj, C. Biino, et al. Landau–Pomeranchuk–Migdal effect for multihundred GeV electrons. *Phys.Rev. D*, 69:032001–11, 2004. (Cited on pages 75, 78 and 83.)

[128] A. Mangiarotti, S. Ballestrero, P. Sona, et al. Implementation of the LPM effect in the discrete-bremsstrahlung simulation of GEANT3 and GEANT4. *Nucl. Instrum. Meth.*, B266(23):5013–5019, 2008. (Cited on page 75.)

[129] A. Schalike, V. Ivanchenko, M. Maire, et al. Improved description of Bremsstrahlung for high-energy electrons in GEANT 4. *Nucl. Sci. Symp. Conf. Rec.*, 266:5013, 2008. (Cited on page 75.)

[130] Y. Kirihara, Y. Namito, and H. Hirayama. Incorporation of Landau–Pomeranchuk–Migdal effect and dielectric suppression effect in EGS5 code. *Nucl. Instrum. Meth.*, B268(15):2426–2432, 2010. (Cited on page 75.)

[131] S.R. Klein, P.L. Anthony, R. Backe-Szendy, et al. A measurement of the LPM effect. *Preprint SLAC-PUB-6378*, pages 1–13, 1993. (Cited on page 75.)

[132] R. Becker-Szendy, P.L. Anthony, P. Bosted, et al. Quantum-mechanical suppression of bremsstrahlung. *Preprint SLAC-PUB-6400*, pages 1–15, 1993. (Cited on pages 75, 76, 77 and 82.)

[133] M.L. Perl. Notes on Landau–Pomeranchuk–Migdal effect: theory and experiment. *Preprint SLAC-PUB-6514*, pages 1–15, 1994. (Cited on pages 75, 76, 81 and 82.)

[134] P.L. Anthony, R. Becker-Szendy, P. Bosted, et al. An accurate measurement of the Landau–Pomeranchuk–Migdal effect. *Phys. Rev. Lett.*, 75:1949–1952, 1995. (Cited on pages 75, 76, 77, 78, 81 and 82.)

[135] G.M. Garibyan and Y. Shi. *Transition X-radiation (in Russian)*. Izdat. Akad. Nauk Arm. SSR, Erevan, 1983. (Cited on pages 76, 78 and 82.)

[136] S.V. Trofymenko and N.F. Shul'ga. Formation region effects in transition radiation, bremsstrahlung, and ionization loss of ultrarelativistic electrons. *Phys. Rev. Accel. Beams*, 19(11):112801, 2016. (Cited on page 76.)

[137] F.F. Ternovskii. On the theory of radiative processes in piecewise homogeneous media. *Sov. Phys. JETP*, 12:123–130, 1961. (Cited on pages 77, 79, 81, 108 and 113.)

[138] N.F. Shul'ga and S.P. Fomin. On suppression radiation effect in amorphous media and crystals. *JETP Lett.*, 27:117–120, 1978. (Cited on pages 77, 79, 81, 104, 106, 108 and 113.)

[139] S.P. Fomin and N.F. Shul'ga. On the space-time evolution of the process of ultra relativistic electron radiation in a thin layer of substance. *Phys. Lett. A*, 114:148–152, 1986. (Cited on pages 77, 79, 81, 106, 110 and 113.)

[140] N.F. Shul'ga and S.P. Fomin. On experimental verification of the Landau–Pomeranchuk–Migdal effect. *JETP Lett.*, 63:873–877, 1996. (Cited on pages 77, 78, 79 and 102.)

[141] R. Blankenbacler and S.D. Drell. The Landau–Pomeranchuk–Migdal effect for finite targets. *Phys. Rev. D*, 53:6265–6281, 1996. (Cited on page 77.)

[142] B.G. Zakharov. Structured targets and Landau–Pomeranchuk–Migdal effect for finite-size targets. *JETP Lett.*, 64:781–787, 1996. (Cited on page 77.)

[143] R. Baier, Yu.L. Dokshitser, A.H. Mueller, et al. The Landau–Pomeranchuk–Migdal effect in QED. *Nucl. Phys. B*, 478:577–597, 1996. (Cited on page 77.)

[144] N.F. Shul'ga and S.P. Fomin. Effect of multiple scattering on the emission of ultrarelativistic electrons in a thin layer of matter. *JETP*, 86(1):32–38, 1998. (Cited on pages 77, 79 and 102.)

[145] N.F. Shul'ga and S.P. Fomin. Bremsstrahlung of ultra relativistic electrons in a thin layer of mater. *Nucl. Instr. Meth. B*, 145:180–184, 1998. (Cited on pages 77, 79, 100 and 102.)

[146] V.N. Baier and V.M. Katkov. Theory of the Landau–Pomeranchuk–Migdal effect. *Phys. Rev. D*, 57(5):3146–3162, 1998. (Cited on page 77.)

[147] V.N. Baier and V.M. Katkov. Landau–Pomeranchuk–Migdal effect and transition radiation in structured targets. *Phys. Rev. D*, 60:076001–12, 1999. (Cited on page 77.)

[148] V.N. Baier and V.M. Katkov. Influence of a medium on pair photoproduction and bremsstrahlung. *Phys. Rev. D*, 62(3):1–13, 2000. (Cited on page 77.)

[149] V.N. Baier and V.M. Katkov. Concept of formation length in radiation theory. *Physics Reports*, 409(5):261–359, 2005. (Cited on page 78.)

[150] H.D. Hansen, U.I. Uggerhj, C. Biino, et al. Is the electron radiation length constant at high energies? *Phys. Rev. Lett.*, 91:014801, 2003. (Cited on pages 78 and 83.)

[151] U.I. Uggerhoj, H. Knudsen, S. Ballestrero, et al. Formation length effects in very thin targets. *Phys. Rev. D*, 72:112001–6, 2005. (Cited on pages 78, 83, 100 and 102.)

[152] H.D. Thomsen, J. Esberg, K. Kirsebom, et al. On the macroscopic formation length for GeV photons. *Phys. Lett. B.*, 672:323–327, 2009. (Cited on pages 78, 83, 100, 102, 103, 104, 105 and 113.)

[153] H.D. Thomsen, J. Esberg, K.K. Andersen, et al. Distorted Coulomb field of the scattered electron. *Phys. Rev. D.*, 81:052003, 2010. (Cited on pages 78, 83, 100, 108, 110 and 113.)

[154] S. Birol, O.B. Kolcu, and A. Dizdar. How to measure LPM effect in low Z materials? *Nucl. Instrum. Meth.*, B309:83–87, 2013. (Cited on page 83.)

[155] R. Blankenbecler. Structured targets and the Landau–Pomeranchuk–Migdal effect. *Phys. Rev.*, D55(1):190–195, 1997. (Cited on pages 83 and 102.)

[156] A.S. Fomin, S.P. Fomin, and N.F. Shul'ga. Multiple scattering effect on spectral, angular and polarization characteristics of bremsstrahlung in a thin amorphous target. *Proc. SPIE*, 6634:663406, 2007. (Cited on pages 83, 100, 110 and 113.)

[157] L.D. Landau and E.M. Lifshiz. *Course of Theoretical Physics, Vol 2: The Classical Theory of Field*. Pergamon Press, 1988. (Cited on pages 85 and 173.)

[158] V.P. Lapko and N.N. Nasonov. A new method for producing high energy gamma-quanta. *Nucl. Instr. Meth. B*, 84:48–50, 1994. (Cited on page 85.)

[159] A.S. Fomin, S.P. Fomin, and N.F. Shul'ga. Multiple scattering effect on angular distribution and polarization of radiation by relativistic electrons in a thin crystal. *Proc. SPIE*, 5974:177–184, 2005. (Cited on pages 86, 110 and 113.)

[160] S.P. Fomin, N.F. Shul'ga, and S.N. Shul'ga. Spectral-angular distribution of relativistic electron radiation in a thin layer of matter. *Phys. Atomic Nuclei*, 66(4):396–399, 2003. (Cited on page 87.)

[161] G. Moliere. Theory of the scattering of fast charged particles. 2. Repeated and multiple scattering. *Z. Naturforsch.*, A3:78–97, 1948. (Cited on page 90.)

[162] V.L. Morokhovsky, G.D. Kovalenko, I.A. Grishaev, et al. Channeling of positrons of 1 GeV energy. *Lett. Zh. Eksp. Teor. Fiz.*, 16:162–164, 1972. (Cited on page 95.)

[163] A.I. Akhiezer, P.I. Fomin, and N.F. Shul'ga. Coherent bremsstrahlung of ultrahigh-energy electrons and positrons in crystals. *Pisma Zh. Eksp. Teor. Fiz.*, 13:713–715, 1971. (Cited on page 95.)

[164] A.S. Fomin, S.P. Fomin, and N.F. Shul'ga. Fine structure of angular distributions and polarization of radiation by relativistic electrons and positrons in a thin crystal. *Journal of Kharkiv National University (Physical series "Nuclei, Particles, Fields")*, 721(1):39–44, 2006. (Cited on pages 95, 110 and 113.)

[165] E.L. Feinberg. . *Sov. Phys. JETP*, 23:132, 1966. (Cited on pages 106 and 110.)

[166] A.I. Akhiezer and N.F. Shul'ga. Influence of multiple scattering on the radiation of relativistic particles in amorphous and crystalline media. *Sov. Phys. Uspekhi*, 30:1972, 1987. (Cited on pages 106 and 110.)

[167] B.G. Zakharov. Fully quantum treatment of the Landau–Pomeranchuk–Migdal effect in QED and QCD. *JETP Lett.*, 63:952–957, 1996. (Cited on page 110.)

[168] B.G. Zakharov. Radiative energy loss of high-energy quarks in finite size nuclear matter and quark-gluon plasma. *JETP Lett.*, 65:615–620, 1997. (Cited on page 110.)

[169] R. Baier, Y.L. Dokshitzer, A.H. Mueller, et al. Radiative energy loss and p(T) broadening of high-energy partons in nuclei. *Nucl. Phys.*, B484:265–282, 1997. (Cited on page 110.)

[170] K. Aamodt et al. Suppression of charged particle production at large transverse momentum in central Pb-Pb collisions at $\sqrt{s_{NN}} = 2.76$ TeV. *Phys. Lett.*, B696:30–39, 2011. (Cited on page 110.)

[171] A.S. Fomin, S.P. Fomin, and N.F. Shul'ga. Radiation of a relativistic electron with non-equilibrium own Coulomb field. *Nuovo Cim.*, C034N4:45–53, 2011. (Cited on pages 110 and 113.)

[172] A.E. Waltar, D.R. Todd, and P.V. Tsvetkov. *Fast spectrum reactors*. Springer, 2012. (Cited on page 118.)

[173] S.M. Feinberg and E.P. Kunegin. Nuclear Power Plants, part 2, discussion. In *Proceedings of the 2nd UN International Conference on Peaceful Uses of Atomic Energy*, 1958. (Cited on page 118.)

[174] K Fuchs and H Hessel. The possibilities for the operation of a natural uranium breeder reactor without fuel element preparation. *Kernenergie (East Germany)*, 4, 1961. (Cited on page 119.)

[175] J.S. Slesarev, V.A. Stukalov, and S.A. Subbotin. Problems of development of fast reactors self-fuel-provision without fuel reprocessing. *Atomkernenergie Kerntechnik*, 45(1):58–60, 1984. (Cited on page 119.)

[176] B. Atefi, M.J. Driscoll, and D.D. Lanning. Evaluation of the breed/burn fast reactor concept. Technical Report COO-2250-40; MITNE-229 TRN: 81-000917, Massachusetts Inst. of Tech., Cambridge, USA, December 1979. http://www.osti.gov/scitech/servlets/purl/6772419. (Cited on page 119.)

[177] L.P. Feoktistov. An analysis of a concept of a physically safe reactor. Preprint IAE-4605/4, (in Russian), 1988. (Cited on pages 119, 120, 121, 122 and 157.)

[178] L.P. Feoktistov. Neutron-fissioning wave (in Russian). *Dokl. Akad. Nauk SSSR*, 309:864–867, 1989. (Cited on pages 119, 120, 121, 122 and 157.)

[179] V.Ya. Goldin and D.Yu. Anistratov. Fast neutron reactor in a self-adjusting neutron–nuclide regime. *Mathematical Modelling*, 7:12–32, 1995. (in Russian). (Cited on page 121.)

[180] V.Ya. Goldin, N.V. Sosnin, and Yu.V. Troshchiev. Fast neutron reactor in a self-controlled regime of 2d type. *Dokl. Ros. Acad. Nauk*, 358:747–748, 1998. (Cited on page 121.)

[181] S.P. Fomin, Yu.P. Mel'nik, V.V. Pilipenko, et al. Investigation of self-organization of the non-linear nuclear burning regime in fast neutron reactors. *Annals of Nuclear Energy*, 32:1435–1456, 2005. (Cited on pages 121, 123, 125, 130, 131 and 135.)

[182] V. Pilipenko, D. Belozorov, L. Davydov, et al. Some aspects of slow nuclear burning. In *Proceedings of ICAPP03*, Cordoba, Spain, May 4–7 2003. CD Paper 3169. (Cited on pages 121 and 122.)

[183] H. van Dam. Self-stabilizing criticality waves. *Annals of Nuclear Energy*, 27(16):1505–1521, November 2000. (Cited on pages 121 and 122.)

[184] W. Seifritz. Solitary burn-up waves in a multiplying medium. *Kerntechnik*, 65(5–6):261–264, 2000. (Cited on page 121.)

[185] H. van Dam. Flux distributions in stable criticality waves. *Annals of Nuclear Energy*, 30:1495–1504, 2003. (Cited on page 121.)

[186] X.-N. Chen and W. Maschek. Transverse buckling effects on solitary burn-up waves. *Annals of Nuclear Energy*, 32:1377–1390, 2005. (Cited on page 121.)

[187] X.-N. Chen, E. Kiefhaber, and W. Maschek. Fundamental burn-up mode in a pebble-bed type reactor. *Progress in Nuclear Energy*, 50:219–224, 2008. (Cited on page 121.)

[188] X.-N. Chen, E. Kiefhaber, D. Zhang, et al. Fundamental solution of nuclear solitary wave. *Energy Conversion and Management*, 59:40–49, 2012. (Cited on page 121.)

[189] V.M. Khotyayintsev et al. *Annals of Nuclear Energy*, 85:337–345, 2015. (Cited on page 121.)

[190] B. Gaveau, J. Maillard, G. Maurel, et al. Hybrid soliton nuclear reactors: a model and simulation (encapsulated long living accelerator driven system). *Nuclear Engineering and Design*, 235(15):1665–1674, 2005. (Cited on page 122.)

[191] B. Gaveau, J. Maillard, G. Maurel, et al. Equations of evolution of a hybrid soliton nuclear reactor. *J. Math. Pures Appl.*, 85:633–670, 2006. (Cited on page 122.)

[192] N. Catsaros et al. Investigating the breeding capabilities of hybrid soliton reactors. *Nuclear Engineering and Design*, 261:251–259, 2013. (Cited on page 122.)

[193] E. Teller, M. Ishikawa, L. Wood, et al. Completely automated nuclear reactors for long-term operation. In *International Conference on Emerging Nuclear Energy Systems*, pages 1–45, Obninsk, Russia, June, 24–28 1996. Preprint UCRL-JC-122708 Pt 2, LLNL. (Cited on pages 122, 134 and 140.)

[194] H. Sekimoto, K. Ryu, and Y. Yoshimura. CANDLE: the new burnup strategy. *Nuclear Science and Engineering*, 139(3):306–317, 2001. (Cited on pages 122 and 159.)

[195] T. Ellis, R. Petroski, P. Hejzlar, et al. Traveling-wave reactors: a truly sustainable and full-scale resource for global energy needs. In *Proc. of ICAPP 2010*, San Diego, CA, USA, June 13–17 2010. Paper 10189. (Cited on page 122.)

[196] H. Sekimoto and K. Tanaka. Candle Burnup for Different Cores. In *Proc. of PHYSOR*, 2002. (Cited on page 122.)

[197] Y. Ohoka and H. Sekimoto. Application of CANDLE burnup to block-type high temperature gas cooled reactor for incinerating weapon grade plutonium. *Proc. of GENES*, 4:15–19, 2003. (Cited on page 122.)

[198] H. Sekimoto. *Light a CANDLE. An Innovative burnup strategy of nuclear reactors. Second edition.* CRINES, Tokyo Institute of Technology, Tokyo, 2010. 102 p. (Cited on page 122.)

[199] A.I. Akhiezer, D.P. Belozorov, F.S. Rofe-Beketov, et al. On the theory of propagation of chain nuclear reaction. *Physica A.*, 273:272–285, 1999. (Cited on page 122.)

[200] A.I. Akhiezer, N.A. Khizhnyak, N.F. Shul'ga., et al. Slow nuclear burning. *Problems of Atomic Science and Technology*, 6:272–275, 2001. (Cited on page 122.)

[201] S.P. Fomin, Yu.P. Mel'nik, V.V. Pilipenko, et al. Study of self-organizing regime of nuclear burning wave in fast reactor. *Problems of Atomic Science and Technology, Series: Nuclear Physics Investigations*, 45(6):106–113, 2005. (Cited on pages 123, 125, 127, 131 and 135.)

[202] S.P. Fomin, Yu.P. Mel'nik, V.V. Pilipenko, et al. Fast reactor based on the self sustained regime of nuclear burning wave. In Čechák T. et al., editor, *Nuclear Science and Safety in Europe*, pages 239–251, Netherlands, 2006. Springer. (Cited on pages 123, 125, 127, 131 and 135.)

[203] S.P. Fomin, Yu.P. Mel'nik, V.V. Pilipenko, et al. Self-sustained regime of nuclear burning wave in U–Pu fast reactor with Pb–Bi coolant. *Problems of Atomic Science and Technology*, 3:156–163, 2007. (Cited on pages 123, 125, 131, 132, 135, 155 and 156.)

[204] S.P. Fomin, Yu.P. Mel'nik, V.V. Pilipenko, et al. Initiation and propagation of nuclear burning wave in fast reactor. *Progress in Nuclear Energy*, 50:163–169, 2008. (Cited on pages 123, 125, 131, 132, 135, 155 and 156.)

[205] S.P. Fomin, Yu.P. Mel'nik, V.V. Pilipenko, et al. Safe fast reactor based on the self-sustained regime of nuclear burning wave. In *Proc. IC "Global 2009"*, Paris, France, September 6–11 2009. Paper 94562009. (Cited on page 123.)

[206] A.E. Waltar and A.B. Reynolds. *Fast Breeder Reactors*. Pergamon Press, New York, 1981. (Cited on pages 123, 126, 127, 128, 131, 140 and 161.)

[207] J. Crank and P. Nicolson. A practical method for numerical evaluation of solutions of partial differential equations of the heat-conduction type. *Proc. Camb. Phil. Soc.*, 43:50–67, 1947. (Cited on page 131.)

[208] L.P. Abagyan et al. *Group constants for calculations of reactor and shielding*. Energoizdat, Moscow, 1981. (in Russian). (Cited on page 131.)

[209] E. Teller. Nuclear energy for the third millennium. Preprint UCRL-JC-129547, LLNL, 1997. (Cited on page 134.)

[210] H. Sekimoto. *Light a CANDLE. An innovative burnup strategy of nuclear reactors.* Tokyo Institute of Technology (INIS-JP–119), Tokyo, Japan, 2005. 47 p. (Cited on pages 135, 140 and 159.)

[211] I.I. Bondarenko et al. *Group Constants for Nuclear Reactor Calculations*. Consultants Bureau Inc., New York, 1964. (Cited on page 141.)

[212] Yu.P. Mel'nik, V.V. Pilipenko, A.S. Fomin, et al. Study of self-organized nuclear burning wave regime in fast reactor based on Th-U cycle. *Atomic Energy*, 107:288–295, 2009. (Cited on page 146.)

[213] A.S. Fomin, S.P. Fomin, Yu.P. Mel'nik, et al. Self-sustained regime of nuclear burning wave in safe fast reactor using mixed Th–U–Pu fuel cycle. In *Proc. of ICAPP 2010*, San Diego, CA, USA, June 13–17 2010. Paper 10302. (Cited on page 146.)

[214] S.P. Fomin, A.S. Fomin, Yu.P. Mel'nik, et al. Nuclear burning wave in fast reactor with mixed Th–U fuel. *Progress in Nuclear Energy*, 53:800–805, 2011. (Cited on page 146.)

[215] O.S. Fomin, S.P. Fomin, Yu.P. Mel'nik, et al. Specific mechanism of negative reactivity feedback in the nuclear burning wave reactor. In S. Monti, editor, *International Atomic Energy Agency (IAEA), Vienna: (Proc. IC FR-13, Paris, France, March 03–08, 2013)*, volume 46091111, pages 1–10, 2015. http://www-pub.iaea.org/MTCD/Publications/PDF/SupplementaryMaterials/P1665CD/Track3_Safety.pdf. (Cited on page 153.)

[216] H. Sekimoto and S. Miyashita. Startup of "CANDLE" burnup in fast reactor from enriched uranium core. *Energy Conversion and Management*, 47(17):2772–2780, 2006. http://www.sciencedirect.com/science/article/pii/S0196890406000495. (Cited on page 159.)

[217] O.S. Fomin, S.P. Fomin, Yu.P. Mel'nik, et al. Nuclear Burning Wave Reactor: Smooth Start-Up Problem. *Journal of KhNU #1041, physical series "Nuclei, Particles, Fields"*, 2:49–56, 2013. http://nuclear.univer.kharkov.ua/engl/fs.htm. (Cited on page 170.)

[218] A.S. Fomin, S.P. Fomin, Yu.P. Mel'nik, et al. Transient processes in the nuclear-burning-wave reactor. In *Proc. of "Global-2015"*, Paris, France, September 20-24 2015. Paper 5254. (Cited on page 170.)

université PARIS-SACLAY | ÉCOLE DOCTORALE PHENIICS

Titre: Effets de diffusion multiples sur la dynamique et le rayonnement des particules chargées rapide dans les cristaux. Les transitoires dans le réacteur à onde de combustion nucléaire.

Mots clés: canalisation, cristal courbé, moment magnétique anormal, polarisation dans le rayonnement, réacteur rapide, sécurité intrinsèque, onde de combustion nucléaire.

Résumé: Les effets cohérents dans l'interaction des particules à haute énergie avec les cristaux ouvrent de nouvelles opportunités d'accelaration et détection de particules. Les champs électromagnétiques efficaces presents daus les cristaux qui se présentent dans ce cas peuvent dépasser mille fois les champs qui sont maintenant réalisables dans les installations expérimentales.

La première partie de la thèse est consacrée à l'étude théorique des effets de diffusion multiples sur la dynamique et le rayonnement des particules chargées de haute énergie dans les cristaux. L'un des objectifs de cette étude est de trouver des conditions optimales pour effectuer la mesure du moment magnétique anormal du baryon Λ_c^+ au LHC. En raison de la courte durée de vie de cette particule, le seul moyen de fournir une telle mesure est d'utiliser un cristal courbé, qui peut imiter le champ magnétique de l'ordre de milliers de Tesla.

L'optimisation des paramètres du set up expérimental a été réalisée sur la base de la simulation par ordinateur du passage Λ_c^+ à travers un cristal courbé à l'aide du modèle de collisions binaires, en tenant compte de la diffusion incohérente sur les vibrations thermiques des atomes des noeuds en réseau et de la diffusion sur un sous-système électronique d'un cristal. Les résultats de la recherche menée dans la thèse démontre la possibilité d'effectuer une telle expérience au LHC et sont devenus la base de la proposition correspondante.

Les effets de diffusion multiple des électrons ultra relativistes et le rayonnement des positons dans les cristaux alignés sont également considérés dans la première partie de la thèse.

Il est également démontré que la distribution angulaire spectrale et les caractéristiques de polarisation du rayonnement diffèrent essentiellement des résultats de la théorie de Bethe–Heitler. Les conditions d'observation expérimentale de ces effets sont présentées.

La deuxième partie de la thèse est consacrée à l'étude des processus transitoires des réacteurs rapides fonctionnant dans un régime d'onde de combustion nucléaire auto-entretenue (OCN). C'est un nouveau concept de réacteurs de fission nucléaire avec la soi-disant "sécurité intrinsèque", dans laquelle le développement d'une réaction nucléaire à chaîne incontrôlable est impossible en raison des principes physiques du fonctionnement du réacteur. Les concepts prometteurs du réacteur OCN dans le cas de sa mise en œuvre permettent d'utiliser l'uranium appauvri et fournit le traitement des déchets radioactifs à longue durée de vie.

Cette étude est basée sur la résolution numérique de l'équation de diffusion non linéaire non stationnaire du transport de neutrons avec un ensemble d'équations de combustion pour les composants du carburant et les équations de la cinétique nucléaire pour les noyaux précurseurs des neutrons retardés, en utilisant une approche "effective multigroup". Le modèle du réacteur cylindrique homogène avec le combustible métallique des cycles de carburant U–Pu, Th–U et mixte Th–U–Pu est considéré dans le cadre du concept de flambage.

À la suite de ces études, l'existence du mode OCN dans le cas du combustible mixte Th–U–Pu et de ses avantages essentiels est démontrée; l'analyse détaillée d'un type spécial de rétroaction négative inhérente au régime OCN et sous-jacente à la "sécurité intrinsèque" d'un tel réacteur est effectuée; les scénarios d'un démarrage en douceur, d'un arrêt forcé et d'un redémarrage ultérieur du réacteur OCN sont développés.

Université Paris-Saclay
Espace Technologique / Immeuble Discovery
Route de l'Orme aux Merisiers RD 128 / 91190 Saint-Aubin, France

université PARIS-SACLAY | ÉCOLE DOCTORALE PHENIICS

Title: Multiple scattering effects on the dynamics and radiation of fast charged particles in crystals. Transients in the nuclear burning wave reactor.

Keywords: channeling, bent crystal, anomalous magnetic moment, radiation polarization, fast reactor, intrinsic safety, nuclear burning wave.

Abstract: The coherent effects in the high energy particle interaction with crystals open up new opportunities for accelerating and detecting techniques. The effective electromagnetic fields that arise in this case can exceed a thousand times the fields that are now attainable at experimental installations.

The first part of the thesis is devoted to the theoretical study of the multiple scattering effects on the dynamics and radiation of high energy charged particles in crystals. One of the goals of this study is to find optimal conditions to carry out the measurement of the anomalous magnetic moment of the baryon Λ_c^+ at the LHC. Due to the short lifetime of this particle the only way to provide such a measurement is to use a bent crystal, which can imitate the magnetic field of order of thousand Tesla.

The optimization of the parameters for an experimental setup was carried out on the basis of computer simulation of the Λ_c^+ passage through a bent crystal using the binary collisions model, taking into account incoherent scattering on thermal vibrations of atoms at lattice nodes, and scattering on an electronic subsystem of a crystal. The results of the research conducted in the thesis give an optimistic forecast for the possibility of carrying out such an experiment at the LHC and became the basis of the corresponding proposal.

The multiple scattering effects of ultra relativistic electrons and positrons radiation in aligned crystals are also considered in the first part of the thesis. This study is performed in the framework of classical electrodynamics approach for describing the relativistic particle radiation and the computer simulation of fast charged particles passing through a crystal using the above-mentioned model.

It is shown, that the spectral-angular distribution and the polarization characteristics of radiation essentially differ from the results of the Bethe–Heitler theory. The conditions for the experimental observation of these effects are presented.

The second part of the thesis is devoted to the study of transient processes in advanced fast reactor-breeder working in a self-sustained nuclear burning wave (NBW) regime. It is a new concept of nuclear fission reactors with the so-called “intrinsic safety”, in which the development of uncontrolled chain nuclear reaction is impossible due to the physical principles of reactor operation. The promising concepts of NBW reactor in the case of its implementation allows to utilize the depleted Uranium and provides the treatment of long-lived radioactive waste.

This study is based on numerical solving the non-stationary non-linear diffusion equation of neutron transport together with a set of the burn-up equations for fuel components and the equations of nuclear kinetics for precursor nuclei of delayed neutrons using effective multi-group approach. The model of cylindrical homogeneous reactor with metallic fuel of U–Pu, Th–U and mixed Th–U–Pu fuel cycles is considered in the framework of the buckling concept.

As a result of these studies the existence of the NBW mode in the case of mixed Th–U–Pu fuel and its essential advantages are demonstrated; the detailed analysis of a special kind of the negative reactivity feedback that is inherent to the NBW regime and underlies the “intrinsic safety” of such a reactor is performed; the scenarios of a smooth start-up, forced shutdown and subsequent restart of the NBW reactor are developed.

Université Paris-Saclay
Espace Technologique / Immeuble Discovery
Route de l’Orme aux Merisiers RD 128 / 91190 Saint-Aubin, France